DOE-ER-0313/65
Distribution
Categories
UC-423, -424

FUSION MATERIALS
SEMIANNUAL PROGRESS REPORT
FOR THE PERIOD ENDING

December 31, 2018

Prepared for
DOE Office of Fusion Energy Sciences
(AT 60 20 10 0)

DATE PUBLISHED: March 2019

Prepared by
OAK RIDGE NATIONAL LABORATORY
Oak Ridge, Tennessee 37831
Managed by
UT-Battelle, LLC
For the
U.S. DEPARTMENT OF ENERGY

FOREWORD

This is the sixty-fifth in a series of semiannual technical progress reports on fusion materials science activity supported by the Fusion Energy Sciences Program of the U.S. Department of Energy. It covers the period ending December 31, 2018. This report focuses on research addressing the effects on materials properties and performance of exposure to the neutronic, thermal and chemical environments anticipated in the chambers of fusion experiments and energy systems. This research is a major element of the national effort to establish the materials knowledge base for an economically and environmentally attractive fusion energy source. Research activities on issues related to the interaction of materials with plasmas are reported separately.

The results reported are the products of a national effort involving a number of national laboratories and universities. A large fraction of this work, particularly in relation to fission reactor irradiations, is carried out collaboratively with partners in Japan, Russia, and the European Union. The purpose of this series of reports is to provide a working technical record for the use of program participants, and to provide a means of communicating the efforts of fusion materials scientists to the broader fusion community, both nationally and worldwide.

This report has been compiled under the guidance of F. W. (Bill) Wiffen and Stephanie Melton, Oak Ridge National Laboratory. Their efforts, and the efforts of the many persons who made technical contributions, are gratefully acknowledged.

Daniel Clark
Research Division
Office of Fusion Energy Sciences

TABLE OF CONTENTS

TABLE OF CONTENTS

TABLE OF CONTENTS

1. FERRITIC/MARTENSITIC STEEL DEVELOPMENT

1.1 PROGRESS ON CASTABLE NANOSTRUCTURED ALLOY DEVELOPMENT—L. Tan and Y. Yang (Oak Ridge National Laboratory)

OBJECTIVE

Castable nanostructured alloys (CNAs) are being developed at Oak Ridge National Laboratory (ORNL) as a United States (U.S.) reduced-activation ferritic-martensitic (RAFM) steel. The alloys are engineered to contain an increased amount of stable nanoprecipitates and to be produced using conventional, affordable steelmaking methods. With the successful progress of developing the first-generation CNAs, second-generation CNAs are now being explored for further property improvements.

SUMMARY

A large commercial heat CNA7 of the first-generation CNAs was procured and tested, together with a small laboratory heat CC22 of the first attempted second-generation CNAs. In general, the CNAs showed enhanced yield strength, creep resistance, and Charpy impact toughness. The CNA7 had comparable or superior yield strength, creep resistance, and Charpy impact toughness compared with the small laboratory heat CNA4, suggesting the property sustainability and fabrication feasibility for the scale-up of the first-generation CNAs. The CC22 showed tensile properties and creep resistance comparable to CNA7, with impact toughness satisfactory although somewhat inferior to the first-generation CNAs.

PROGRESS AND STATUS

Introduction

Six small laboratory-scale heats (~1 lb. each) of the first-generation CNAs were fabricated and assessed at ORNL. They exhibited enhanced yield/tensile strength, impact toughness, and creep resistance. To check the scalability of the property improvements, a commercial heat of a first-generation CNAs was procured for comparison. Meanwhile, the first attempt at developing the second-generation CNAs was focused on elevated nitrogen alloying, which is in contrast to the primarily carbides that were engineered in the first-generation CNAs.

Experimental Procedure

A commercial heat (~60 lbs.) of a first-generation CNAs, designated CNA7, was procured from an industrial facility. It was fabricated by vacuum induction melting, followed by hot forging at 1100°C to a 0.75—in-thick plate. The plate was normalized at 1170°C for 20 minutes, water quenched and then tempered at 750°C for 1 hour with air cooling. A nitrogen-alloyed small laboratory-scale heat of a second-generation CNAs, designated CC22, was fabricated at ORNL by arc-melting and casting, followed by hot rolling at 1100°C to a 0.3-in-thick plate, normalized at 1170°C for 15 minutes and tempered at 750°C for 30 minutes. Type SS-3 miniature specimens and half-size Charpy specimens were machined from the alloys for tensile, creep, and Charpy impact tests in air.

Results

Figure 1 shows optical micrographs of CNA7 (a large commercial heat of a first-generation CNA) and CC22 (a small laboratory heat of a second-generation CNA). Tempered martensite developed in both alloys, however, CNA7 showed noticeably finer/denser lath structures.

Tensile tests were conducted at temperatures up to 700°C. The temperature-dependent yield strength in Figure 2a indicates comparable yield strength of CNA7, CNA4, and CC22, all of which are significantly higher (by ~170–200 MPa) than the yield strength of Eurofer97 and T91. Consistent with the enhanced yield strength, the creep resistance of the three CNAs was also noticeably enhanced compared to T91 as shown in Figure 2b. The Charpy impact toughness results, shown in Figure 2c, suggest excellent impact

toughness of CNA7, CNA4, and CC22, all superior to Grade 91 under the same sample geometry and orientation.

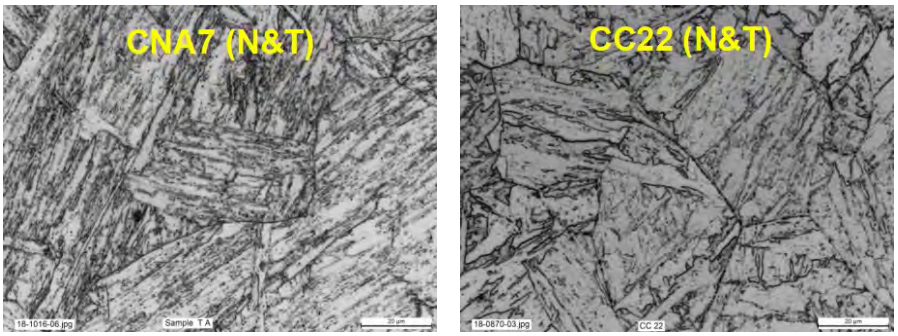

Figure 1. Optical micrographs of CNA7 and CC22, showing tempered martensite structures.

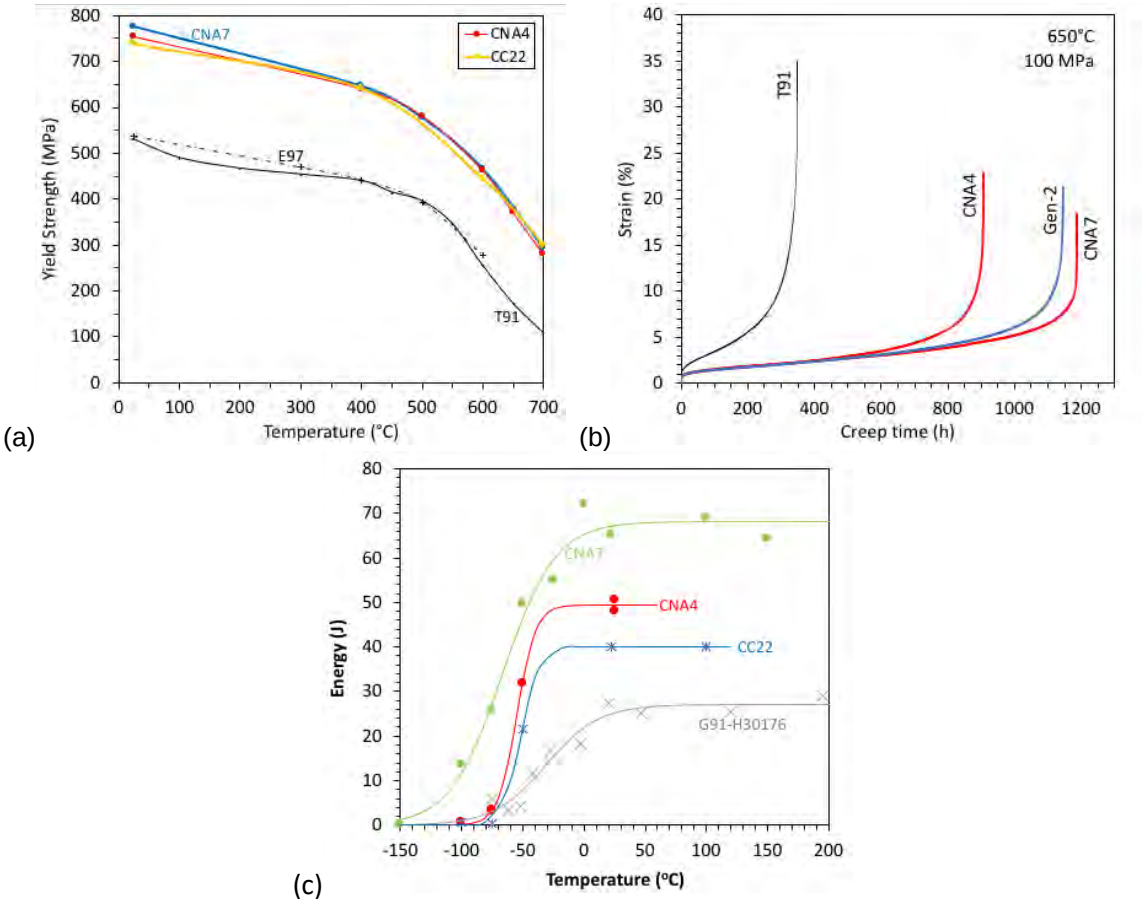

Figure 2. (a) Temperature-dependent yield strength of CNA7 and CC22 compared with CNA4, Eurofer97, and T91; (b) Creep curves of CNA7 and CC22 (Gen-2) compared with CNA4 and T91 tested at 650°C and 100 MPa; (c) Temperature-dependent Charpy impact absorbed energy of CNA7 and CC22 compared with CNA4 and Grade 91-heat 30176.

1.2 POST-IRRADIATION EVALUATION OF THE IRRADIATION TEMPERATURE AND VICKERS MICROHARDNESS FOR EUROFUSION M4CVN BEND BAR SPECIMENS—X. Chen, A. Campbell, R. Howard, A. Bhattacharya, J.W. Geringer, Y. Katoh (Oak Ridge National Laboratory), T. Graening (Karlsruhe Institute of Technology)

OBJECTIVE

The aim of this task is to determine the irradiation temperature and measure the irradiation hardening of EUROFusion M4CVN bend bar specimens machined from ten Eurofer97 steel variants. The neutron irradiation was performed in the High Flux Isotope Reactor (HFIR) at Oak Ridge National Laboratory (ORNL) with the planned irradiation condition of 300°C/2.5 displacements per atom(dpa).

SUMMARY

We have completed the post-irradiation evaluation (PIE) of the irradiation temperature and measured the Vickers microhardness for EUROFusion M4CVN bend bar specimens machined from ten Eurofer97 steel variants. Eight Eurofer97 variants experienced similar irradiation temperatures with average values in the range of 259 to 295°C. The resulting irradiation hardening was quite similar among variants E, H, L, O, and P with increases in the Vickers hardness values of 79 to 94. Variants J and K showed higher irradiation hardening with increases in the Vickers hardness values of 108 and 132, respectively. Variant I indicated less irradiation hardening with an increase of 61 in the Vickers hardness. Two variants, M and N, experienced a much higher irradiation temperature with an average value of 476°C and showed little irradiation hardening.

PROGRESS AND STATUS

Introduction

Eurofer97 is the European reference reduced activation ferritic martensitic (RAFM) steel for the first wall and blanket applications of early demonstration fusion power plants. During fusion plant operation, high neutron irradiation damage on first wall materials can cause irradiation embrittlement and reduce the fracture toughness of RAFM steels. Therefore, the irradiation effects on the fracture toughness of Eurofer97 is one of the core properties under the EUROFusion project. In this study, we performed PIE of the irradiation temperature and Vickers microhardness for EUROFusion M4CVN bend bar specimens machined from ten Eurofer97 steel variants, identified in Table 1. These results will be useful in selecting the optimal testing temperatures for the Master Curve fracture toughness testing of the bend bar specimens.

Experimental Procedure

Five rabbit capsules, identified as ES31-35, were used to irradiate ten Eurofer97 variants in the HFIR flux trap region. Each capsule contained four M4CVN bend bar specimens machined from two Eurofer97 variants and four SiC passive thermometry specimens for irradiation temperature determination after the irradiation. Figure 1 shows the section view of the capsule design [1]. The detailed irradiation matrix including specimen IDs is summarized in Table 2 with Figure 2 (a)-(e) showing the layout of bend bar and SiC specimens in each capsule [1]. One SiC temperature monitor specimen from each capsule was sectioned into three equal pieces as top, middle, and bottom, and they were used to determine irradiation temperature distribution along the axial length of each capsule. Figure 3 (a)-(e) show photos of SiC thermometry specimens after sectioning. The method for irradiation temperature determination using SiC thermometry specimens has been described in detail by Campbell et al. in Reference [2]. Once the irradiation temperatures were determined from three SiC cut pieces, the average irradiation temperature of the thermometry specimen was calculated as:

$$T_{avg} = (T_{top} + 2 \times T_{mid} + T_{bot}) / 4 \quad (1)$$

The calculation gives more weight to the middle thermometry piece. The rationale is based on the simulation results for temperature contours for the bend bar specimen irradiated at 300 °C (Figure 4), most of the specimen middle plane section (black rectangle area in Figure 4) stayed in the higher temperature region of the temperature scatter band. The middle plane section corresponds to the end of fatigue pre-cracking and cleavage fracture should also initiate here during fracture toughness testing. Therefore, irradiation temperature determination should focus in this area. Giving more weight to the middle thermometry determination, Equation (1) gives a more realistic estimation for the average irradiation temperature. Lastly, based on simulation results in Reference [1], the average irradiation temperature for the M4CVN specimen is 5 °C higher than the average irradiation temperature of the thermometry specimen from the same capsule.

Table 1. Summary of Eurofer97 steel variants. AQ: air quenched, WQ: water quenched, LT: low temperature application, HT: high temperature application

M-Code	Material type	Heat	Condition	Provider
E	EUROFER97/2	993391	980°C/0.5h + AQ + 760°C + AC (reference)	KIT
H	EUROFER-LT	J362A	1000°C/0.5h + WQ + 820°C + AC	KIT
I	EUROFER-LT	J363A	1000°C/0.5h + WQ + 820°C + AC	KIT
P	EUROFER-LT	J361A	1000°C/0.5h + WQ + 820°C + AC	KIT
L	EUROFER97/2	994578	1150°C/0.5h + AQ + 700°C + AC	CEA
J	EUROFER-LT	I196C	TMT:1250°C/1h and then rolling to a final rolling temperature of 850°C in 6 rolling steps with a reduction of 20-30% for each rolling pass, then AC.	SCK.CEN
			Q&T: 880°C/0.5h+WQ+750°C/2h+AC	
K	EUROFER-HT	I427A	TMT:1250°C/1h and then rolling to a final rolling temperature of 850°C in 6 rolling steps with a reduction of 20-30% for each rolling pass, then AC.	SCK.CEN
			Q&T: 1050°C/15min + WQ + 675°C/1.5h + AC	
M	EUROFER97/2	993391	1020°C/0.5h + AQ + 1020°C/0.5h + AQ +760°C/1.5h + AC (double austenitization)	ENEA
O	EUROFER-LT	VM2991	TMT: 1080°C/1h, cooling to 650°C and rolling, reduction 40% (from 30 mm to 18mm)	ENEA
			Tempering: 760°C/1h + AC	
N	EUROFER-LT	VM2897	920°C/1.5h + AQ + 920°C/1.5h + AQ + 760°C/1h + AC (double austenitization)	ENEA

Vickers microhardness testing was performed using a Mitutoyo HV-120 hardness tester in the hot cell as shown in Figure 5. We applied 1 kg force with 15 sec dwell time for each measurement. At least four measurements were performed at each notch location on a M4CVN bend bar specimen. The schematic for the location of the Vickers microhardness indentations is illustrated in Figure 6.

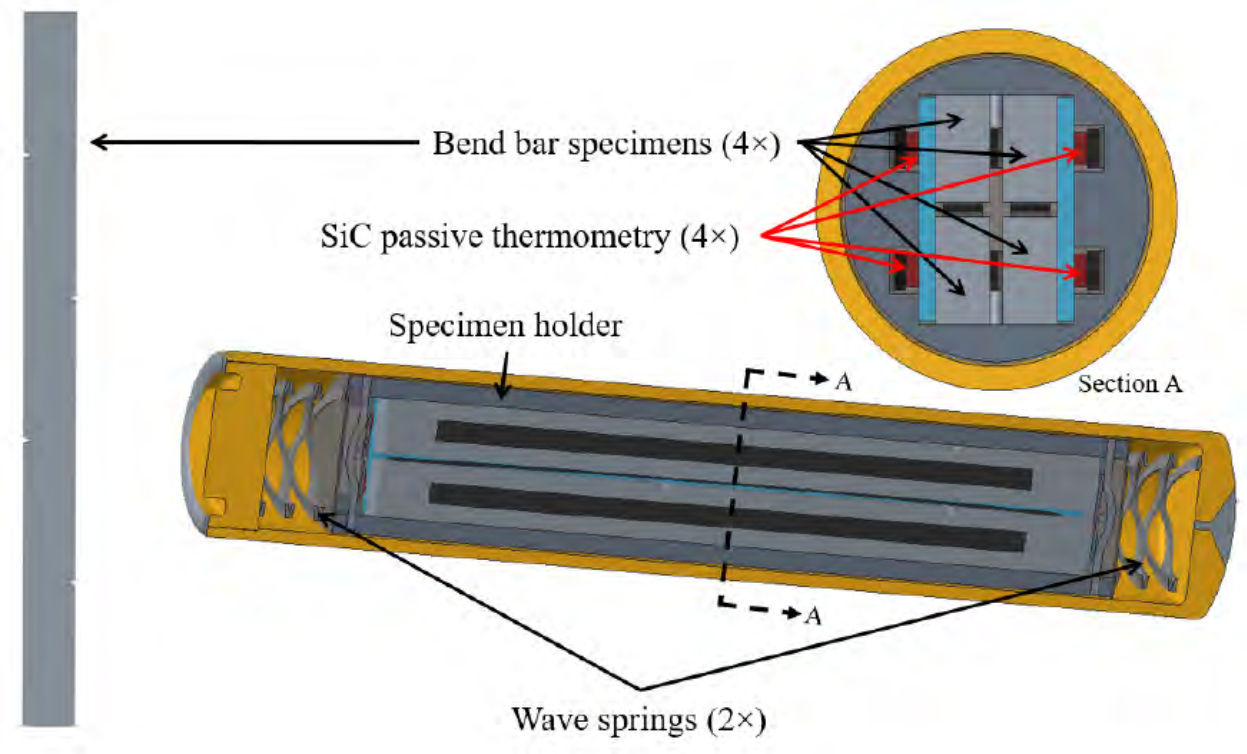

Figure 1. Section view of the M4CVN bend bar capsule [1].

Table 2. Irradiation matrix for M4CVN bend bar and SiC thermometry specimens

Capsule ID	M4CVN specimen ID	SiC specimen ID
ES31	E030	1
	E036	2*
	H000	4
	H001	41
ES32	I000	8
	I001	9*
	J000	10
	J004	11
ES33	K001	12
	K003	13
	L000	14*
	L001	15
ES34	M000	16*
	M001	17
	N000	18
	N001	19
ES35	O000	20*
	O001	21
	P000	22
	P001	23

*Used for irradiation temperature measurements.

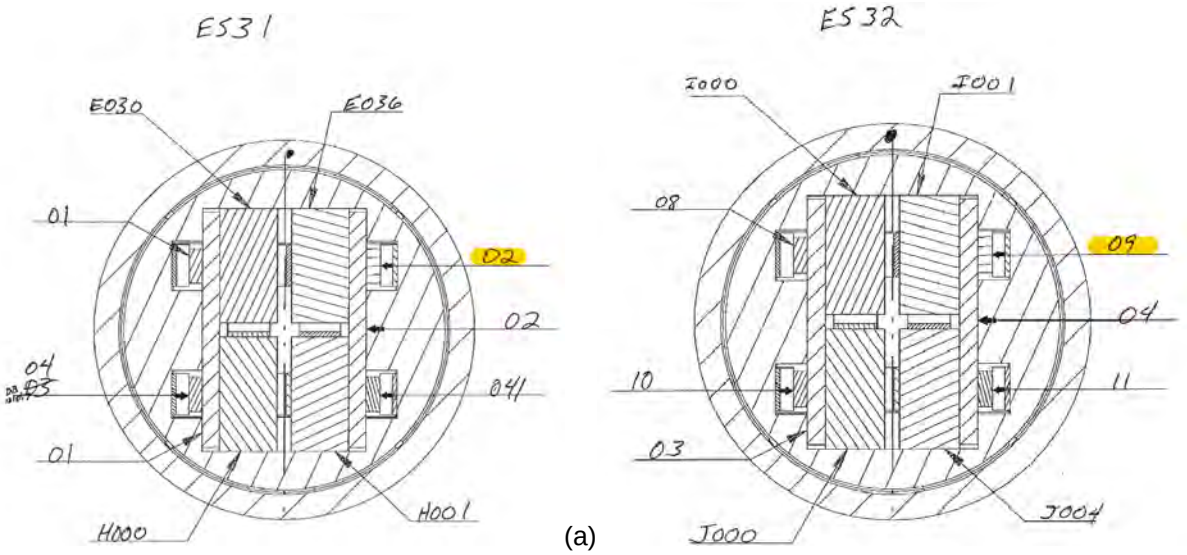
ES31
E030
E036
01
02
04
03
041
01
H000
H001
ES32
I000
I001
08
09
04
10
11
03
J000
J004

(a)
(b)

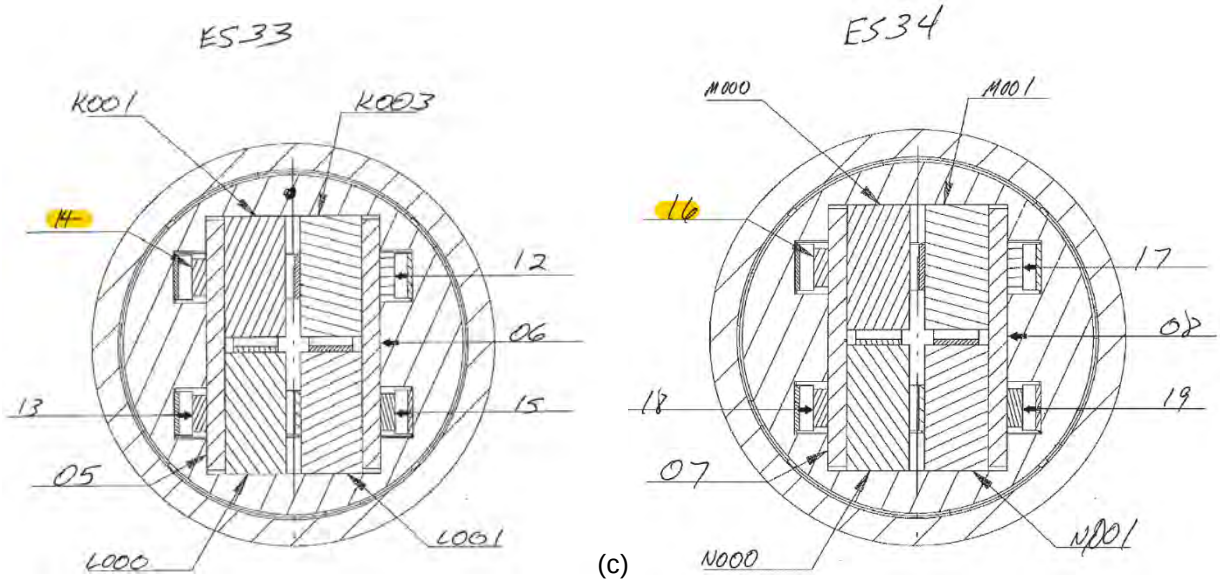
ES33
K001
K003
14
12
06
13
15
05
L000
L001
ES34
M000
M001
16
17
07
18
19
07
N000
N001

(c)
(d)

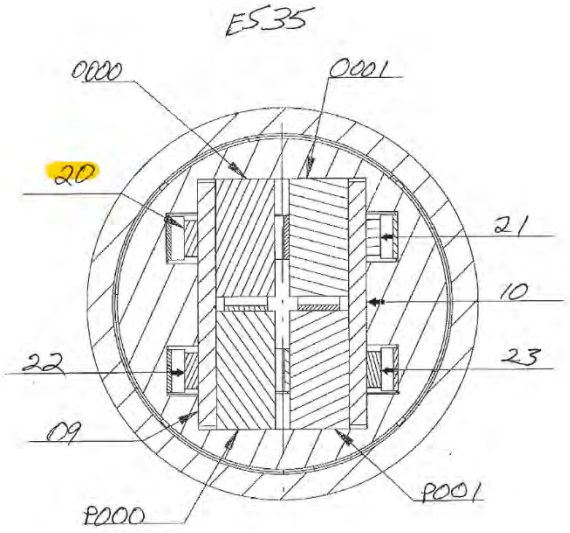

(e)

Figure 2. Layout of M4CVN bend bar and SiC thermometry specimens in each irradaition capsule: (a) ES31, (b) ES32, (c) ES33, (d) ES34, and (e) ES35. Yellow highlightings show the SiC specimens used for irradiation temperature measurements [1].

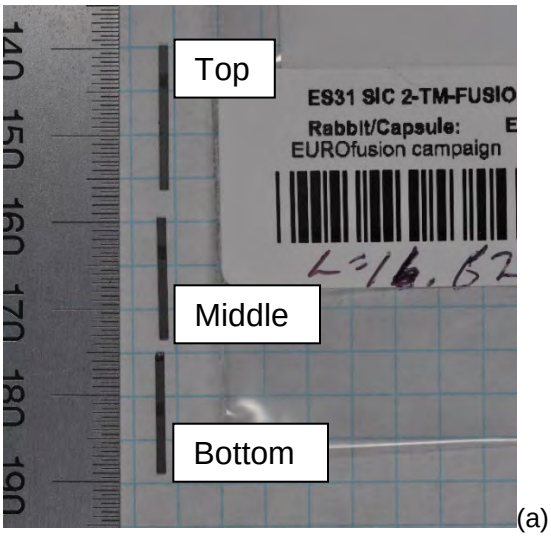

(a)

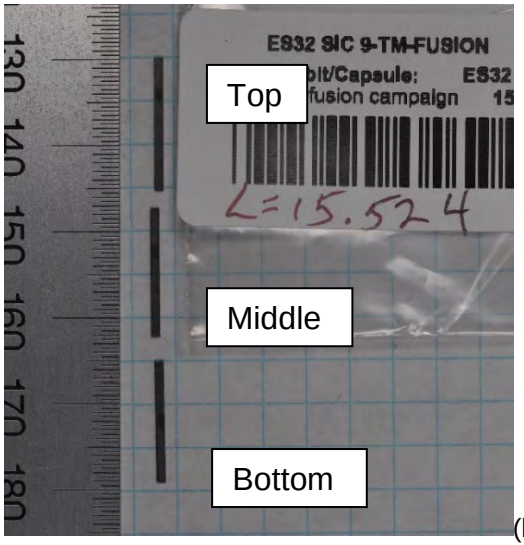

(b)

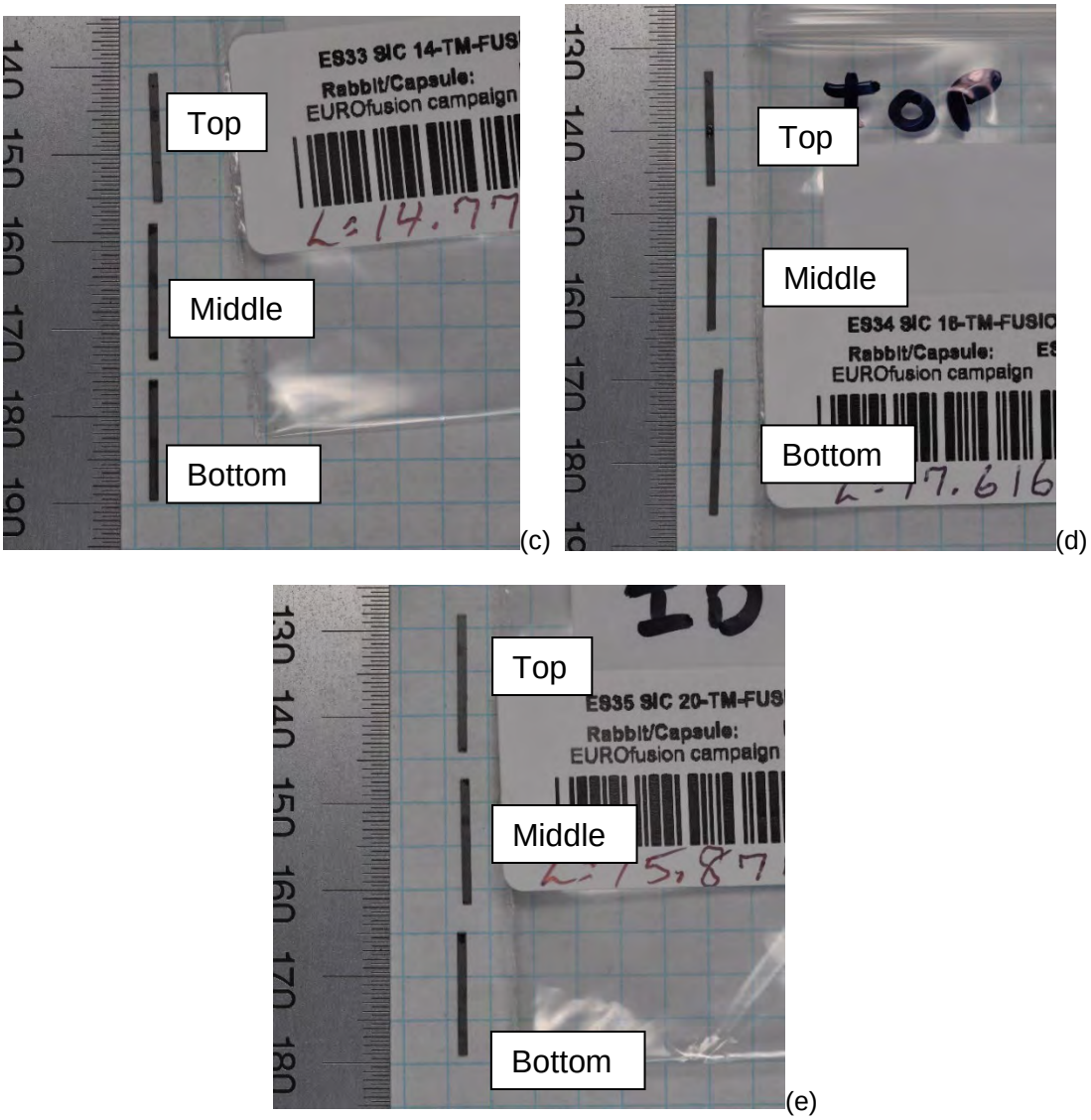

Figure 3. SiC specimens after sectioning for capsules: (a) ES31, (b) ES32, (c) ES33, (d) ES34, and (e) ES35.

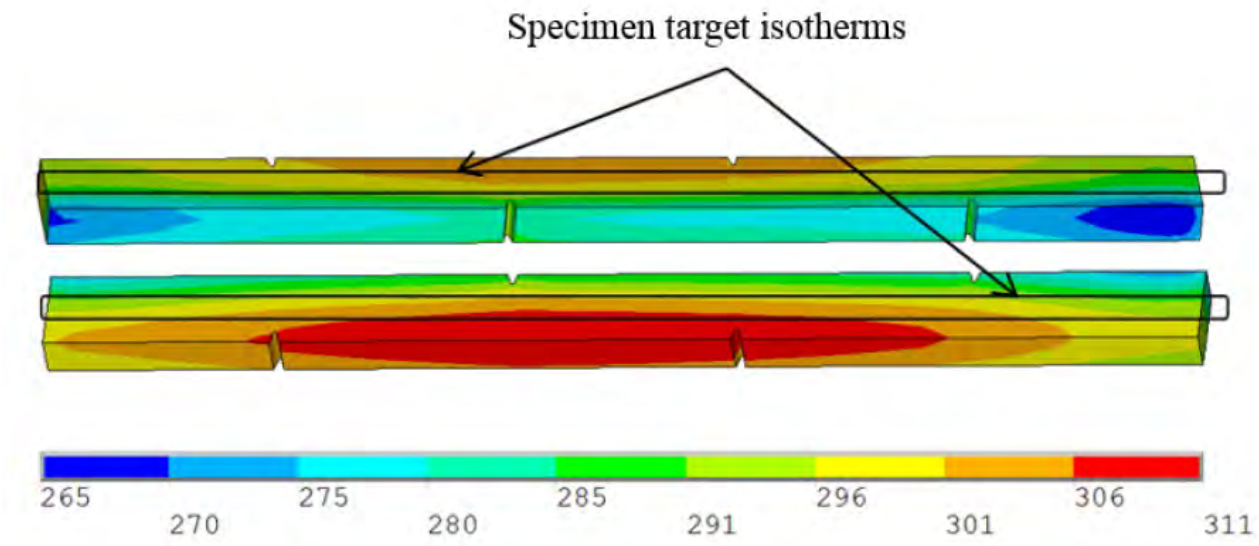

Figure 4. Temperature contour simulation for M4CVN bend bars with 300°C target irradiation temperature.

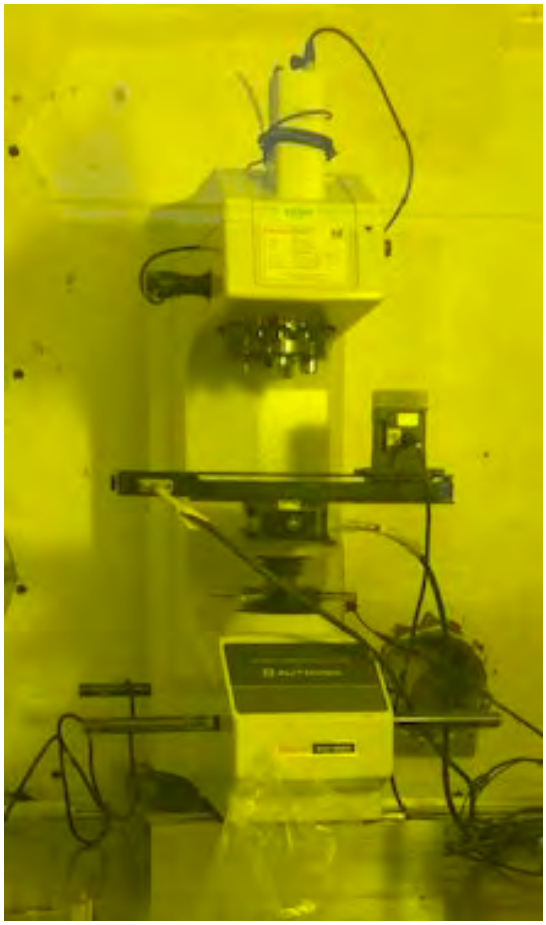

Figure 5. Mitutoyo HV-120 Vickers hardness tester in the hot cell with remote test control.

Figure 6. Vickers microhardness indentation pattern for a M4CVN bend bar specimen.

Results

The irradiation temperature for each SiC cut specimen is determined based on the deformation measurements made in a dilatometer as shown in Figures 7-11. For each test, the mean value of the minimum and maximum temperatures was used as the irradiation temperature for the cut thermometry specimen. Irradiation temperature determination from the three cut pieces of one thermometry specimen give the axial irradiation temperature distributions as shown in Figure 12 (a)-(e). Also shown in the figures are axial microhardness distributions given by measurements from four notches of each M4CVN bend bar specimen. Overall, the middle thermometry specimen gives higher irradiation temperature than the top and bottom thermometry specimens, which matches the simulation results in Figure 4. The microhardness results from four notches of the M4CVN bend bar specimen do not show an obvious trend and are relatively uniform across the length of the specimen.

Figure 13 summarizes the irradiation temperature and hardening of M4CVN bend bar specimens machined from ten Eurofer97 variants irradiated to 2.5 dpa. Error bars correspond to one standard deviation. For capsules ES31 and ES35, the average irradiation temperatures were similar and in the range of 276-295°C. The irradiation hardening resulted in similar increase in materials hardness values, ca. HV80, regardless of material types. Capsule ES32 had an average irradiation temperature of 278°C and materials in this capsule showed different amounts of irradiation hardening. Capsule ES33 had a slightly lower irradiation temperature of 259°C and materials irradiated in this capsule showed higher irradiation hardening. Capsule ES34 had significantly higher irradiation temperature than the design target (476°C vs. 300°C) and little irradiation hardening was observed for either material.

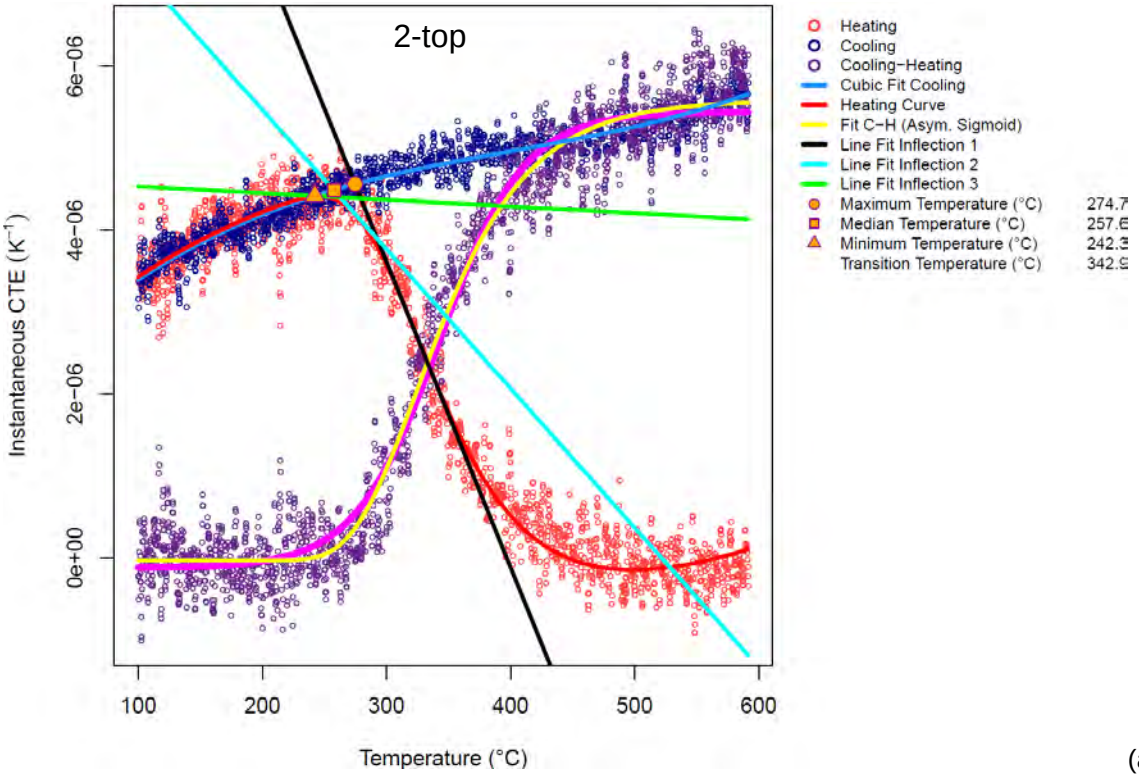
2-top
Instantaneous CTE (K^{-1})
0e+00
2e−06
4e−06
6e−06
100
200
300
400
500
600
Temperature (°C)
Heating
Cooling
Cooling−Heating
Cubic Fit Cooling
Heating Curve
Fit C−H (Asym. Sigmoid)
Line Fit Inflection 1
Line Fit Inflection 2
Line Fit Inflection 3
Maximum Temperature (°C) 274.7
Median Temperature (°C) 257.6
Minimum Temperature (°C) 242.3
Transition Temperature (°C) 342.9

(a)

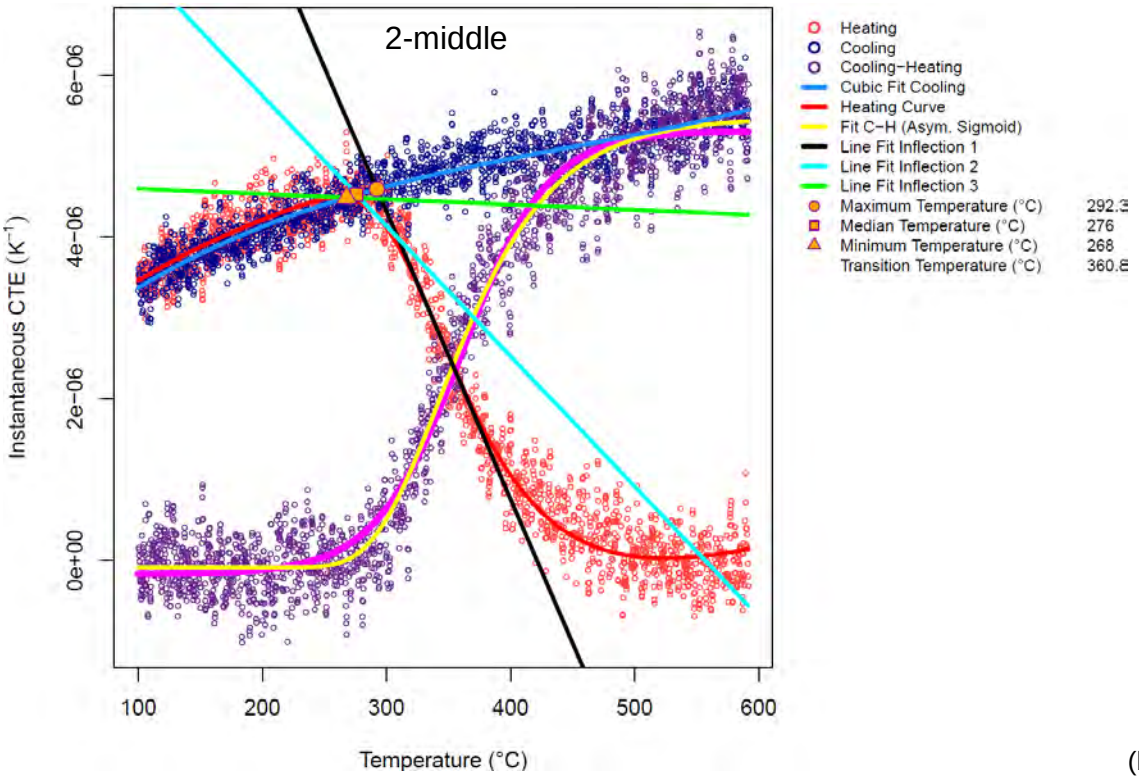
2-middle
Instantaneous CTE (K^{-1})
0e+00
2e−06
4e−06
6e−06
100
200
300
400
500
600
Temperature (°C)
Heating
Cooling
Cooling−Heating
Cubic Fit Cooling
Heating Curve
Fit C−H (Asym. Sigmoid)
Line Fit Inflection 1
Line Fit Inflection 2
Line Fit Inflection 3
Maximum Temperature (°C) 292.3
Median Temperature (°C) 276
Minimum Temperature (°C) 268
Transition Temperature (°C) 360.8

(b)

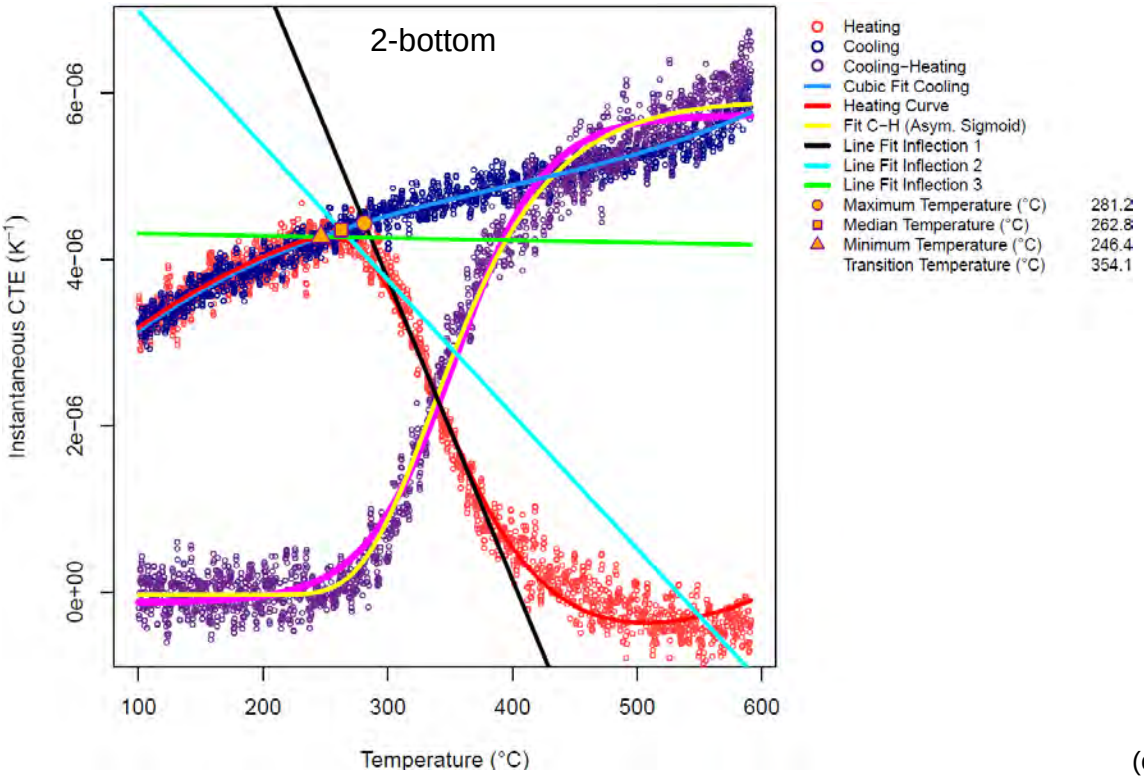

(c)

Figure 7. ES31 capsule thermometry specimen #2 irradiation temperature determinations: (a) top, (b) middle, (c) bottom.

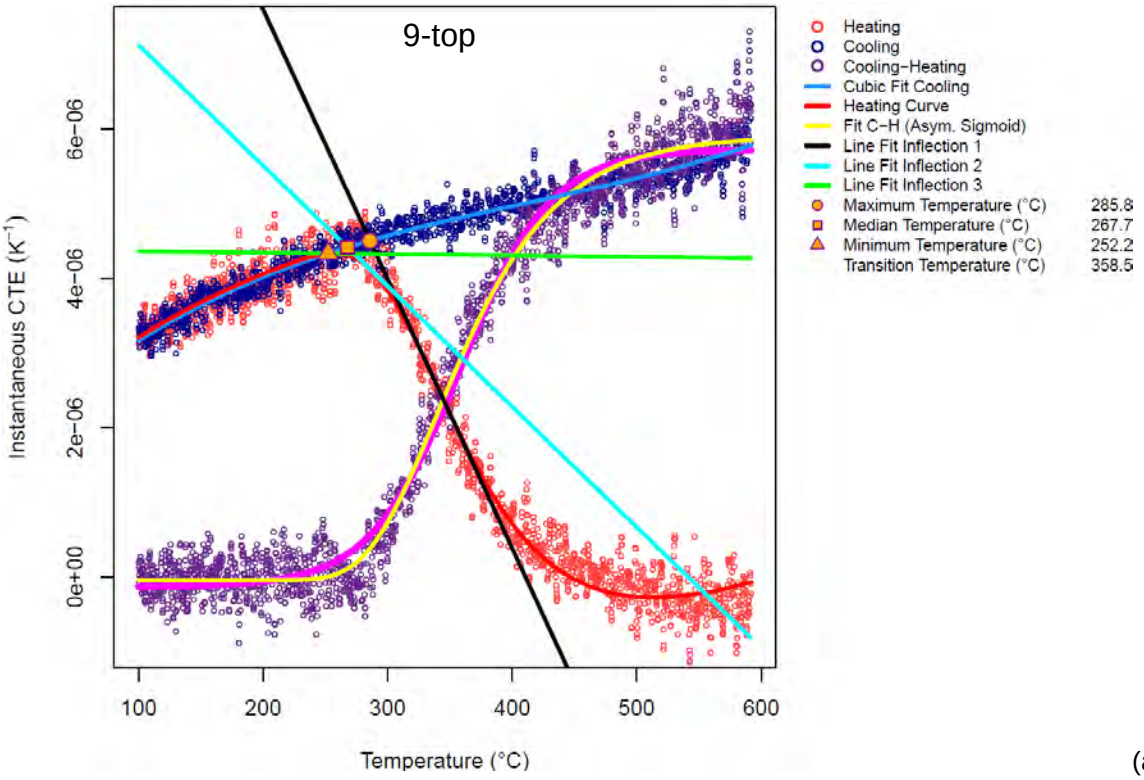

(a)

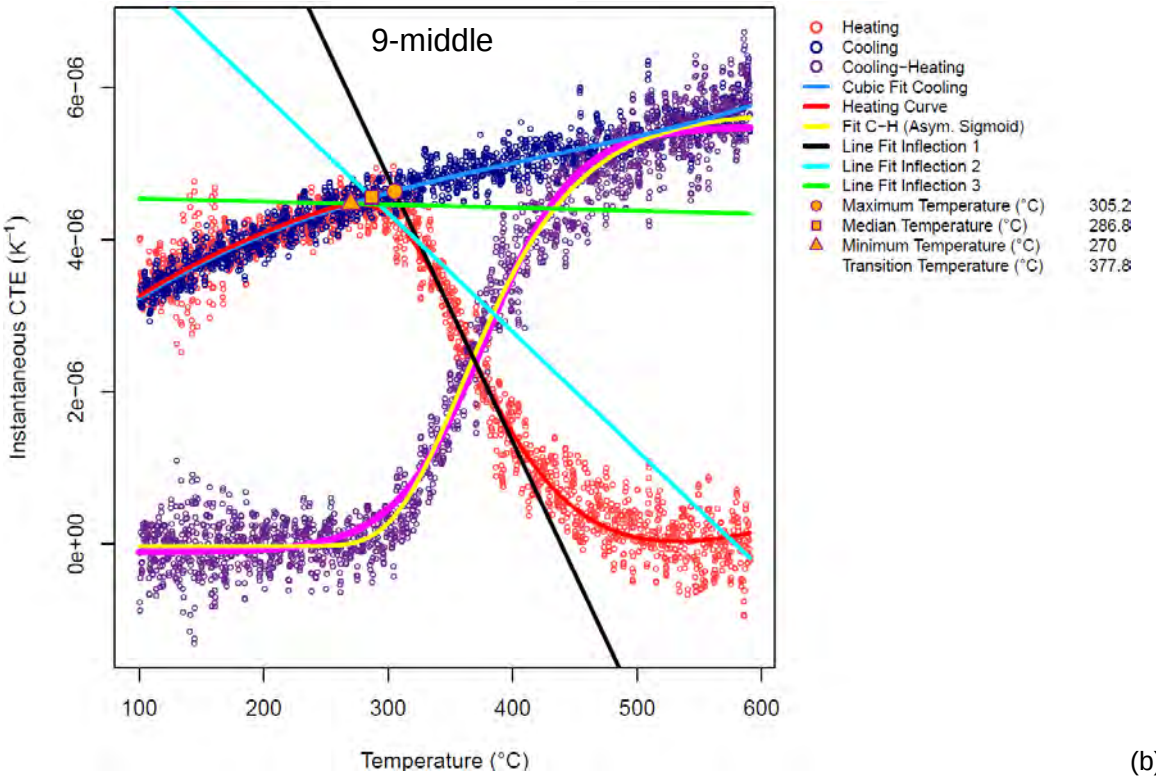

(b)

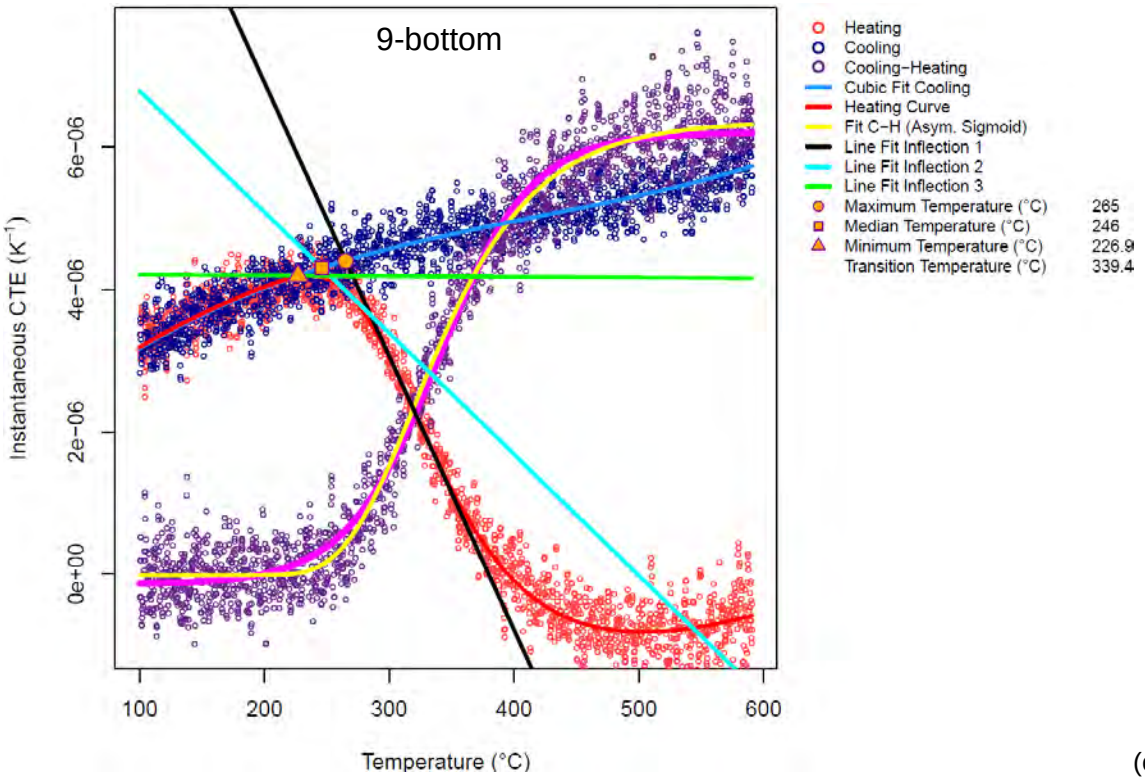

(c)

Figure 8. ES32 capsule thermometry specimen #9 irradiation temperature determinations: (a) top, (b) middle, (c) bottom.

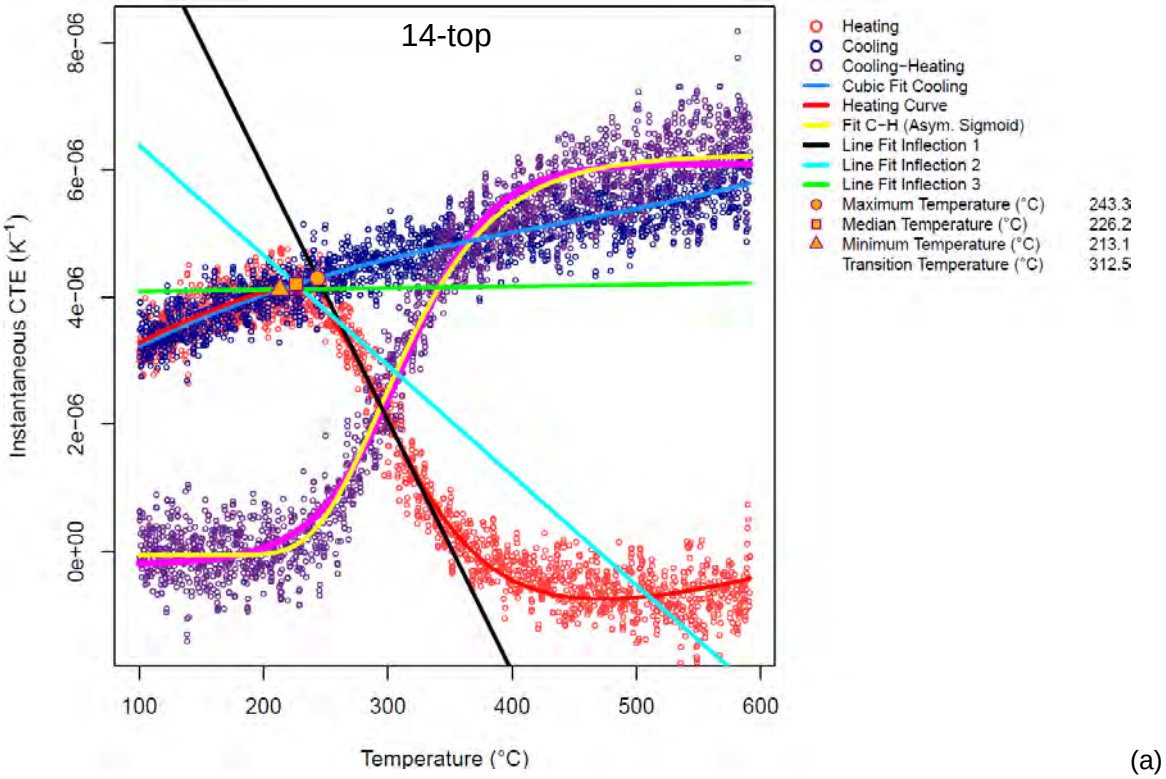
14-top
Instantaneous CTE (K^{-1})
0e+00
2e−06
4e−06
6e−06
8e−06
100
200
300
400
500
600
Temperature (°C)
Heating
Cooling
Cooling−Heating
Cubic Fit Cooling
Heating Curve
Fit C−H (Asym. Sigmoid)
Line Fit Inflection 1
Line Fit Inflection 2
Line Fit Inflection 3
Maximum Temperature (°C) 243.3
Median Temperature (°C) 226.2
Minimum Temperature (°C) 213.1
Transition Temperature (°C) 312.5

(a)

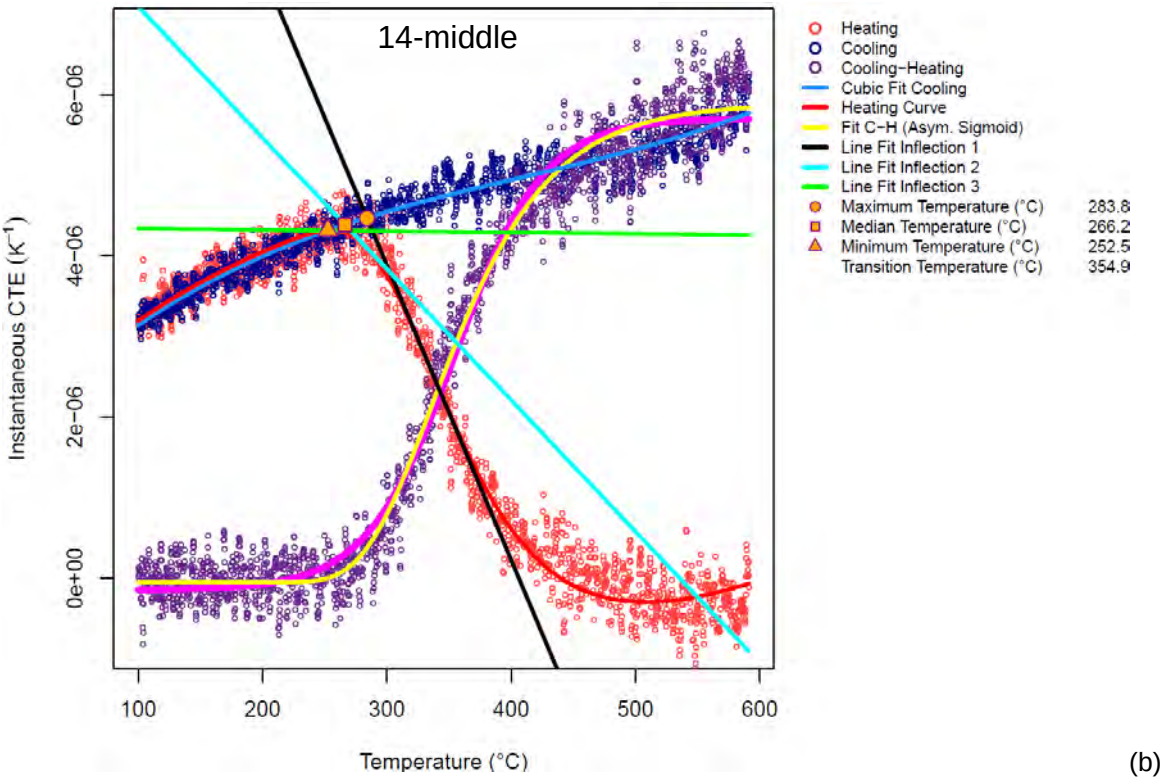
14-middle
Instantaneous CTE (K^{-1})
0e+00
2e−06
4e−06
6e−06
100
200
300
400
500
600
Temperature (°C)
Heating
Cooling
Cooling−Heating
Cubic Fit Cooling
Heating Curve
Fit C−H (Asym. Sigmoid)
Line Fit Inflection 1
Line Fit Inflection 2
Line Fit Inflection 3
Maximum Temperature (°C) 283.8
Median Temperature (°C) 266.2
Minimum Temperature (°C) 252.5
Transition Temperature (°C) 354.9

(b)

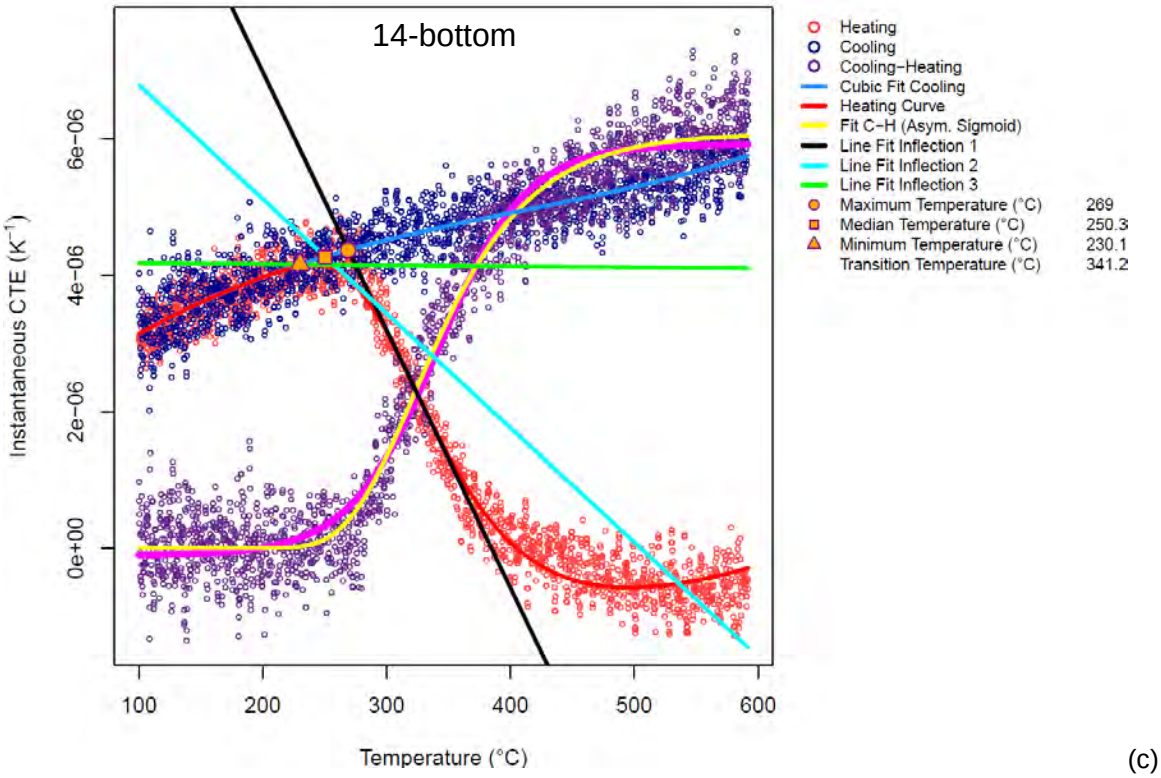

(c)

Figure 9. ES33 capsule thermometry specimen #14 irradiation temperature determinations: (a) top, (b) middle, (c) bottom.

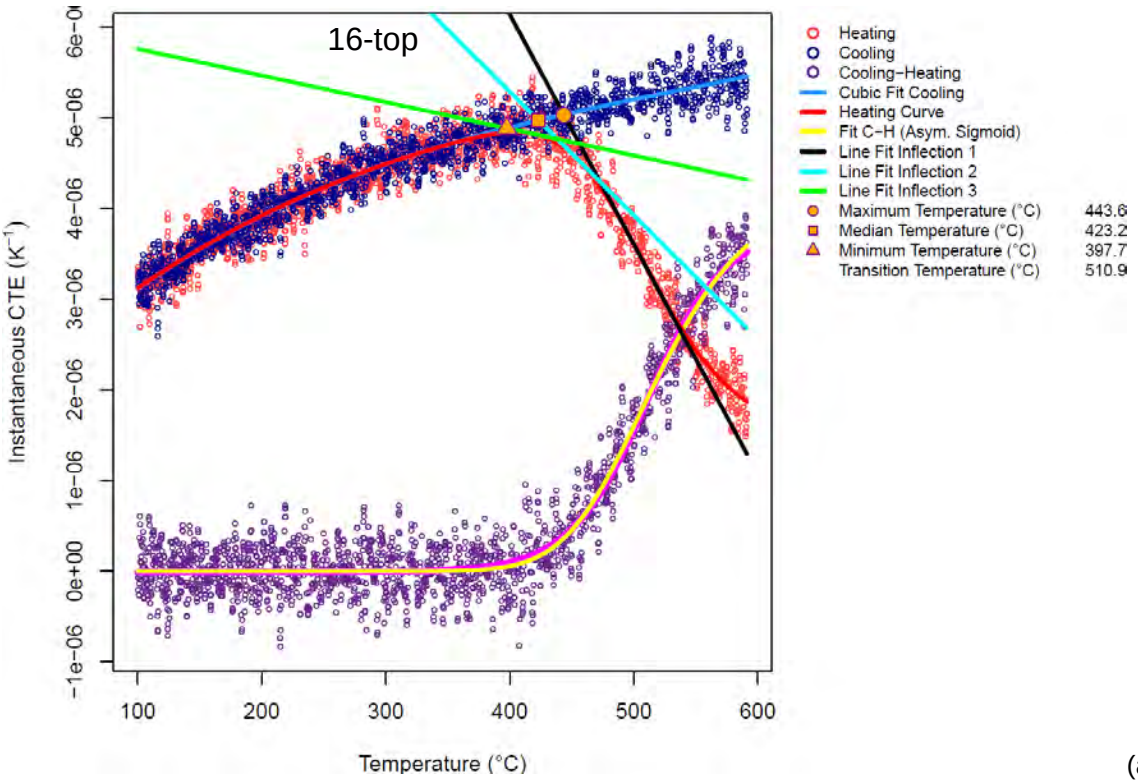
16-top
Instantaneous CTE (K⁻¹)
Temperature (°C)
Heating
Cooling
Cooling−Heating
Cubic Fit Cooling
Heating Curve
Fit C−H (Asym. Sigmoid)
Line Fit Inflection 1
Line Fit Inflection 2
Line Fit Inflection 3
Maximum Temperature (°C) 443.6
Median Temperature (°C) 423.2
Minimum Temperature (°C) 397.7
Transition Temperature (°C) 510.9

(a)

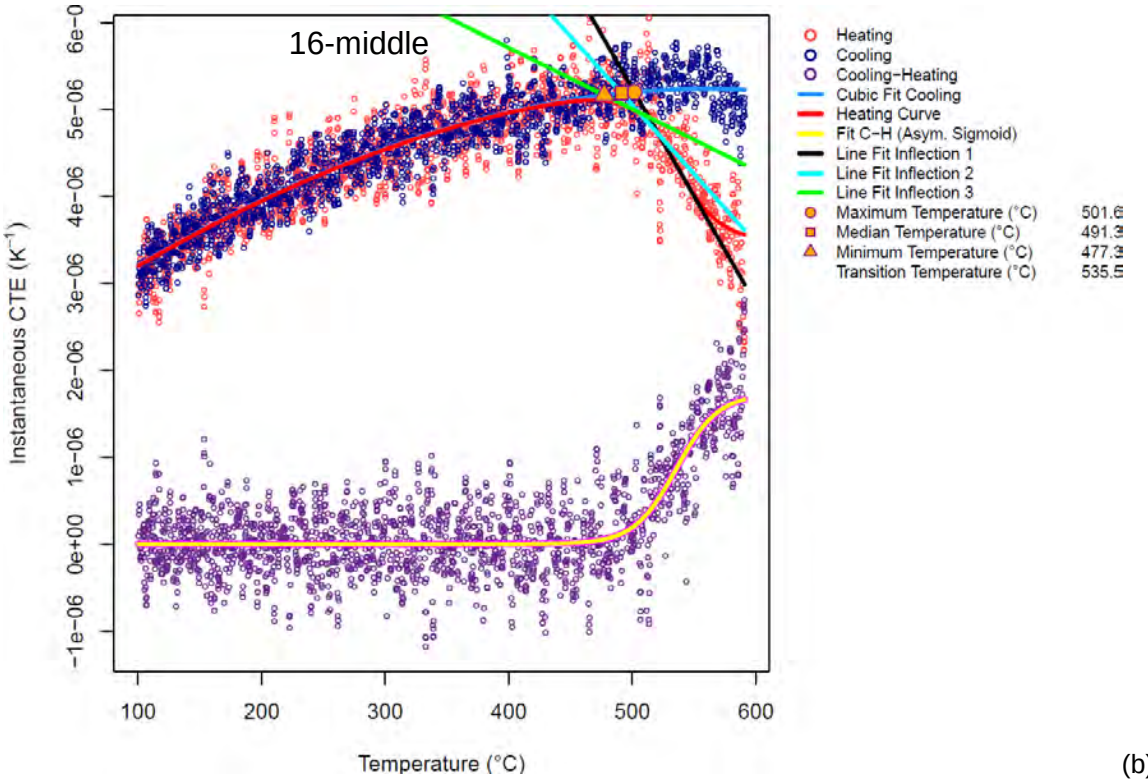
16-middle
Instantaneous CTE (K⁻¹)
Temperature (°C)
Heating
Cooling
Cooling−Heating
Cubic Fit Cooling
Heating Curve
Fit C−H (Asym. Sigmoid)
Line Fit Inflection 1
Line Fit Inflection 2
Line Fit Inflection 3
Maximum Temperature (°C) 501.6
Median Temperature (°C) 491.3
Minimum Temperature (°C) 477.3
Transition Temperature (°C) 535.5

(b)

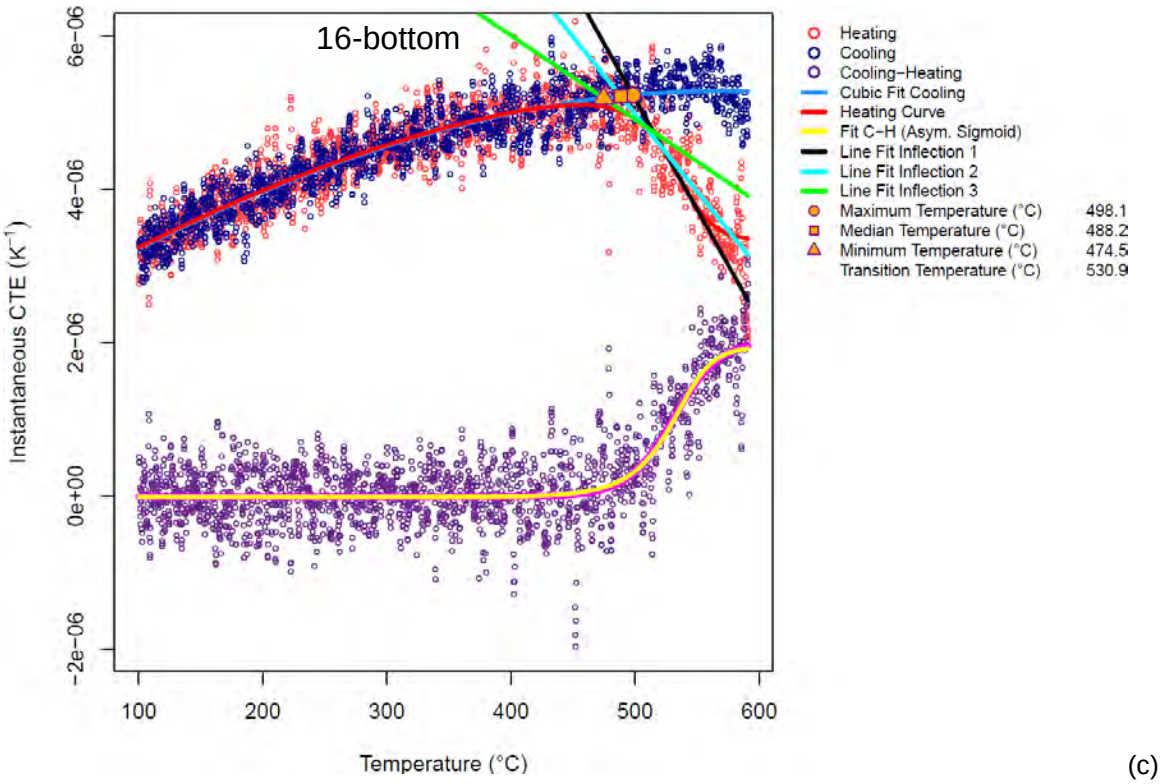

(c)

Figure10. ES34 capsule thermometry specimen #16 irradiation temperature determinations: (a) top, (b) middle, (c) bottom.

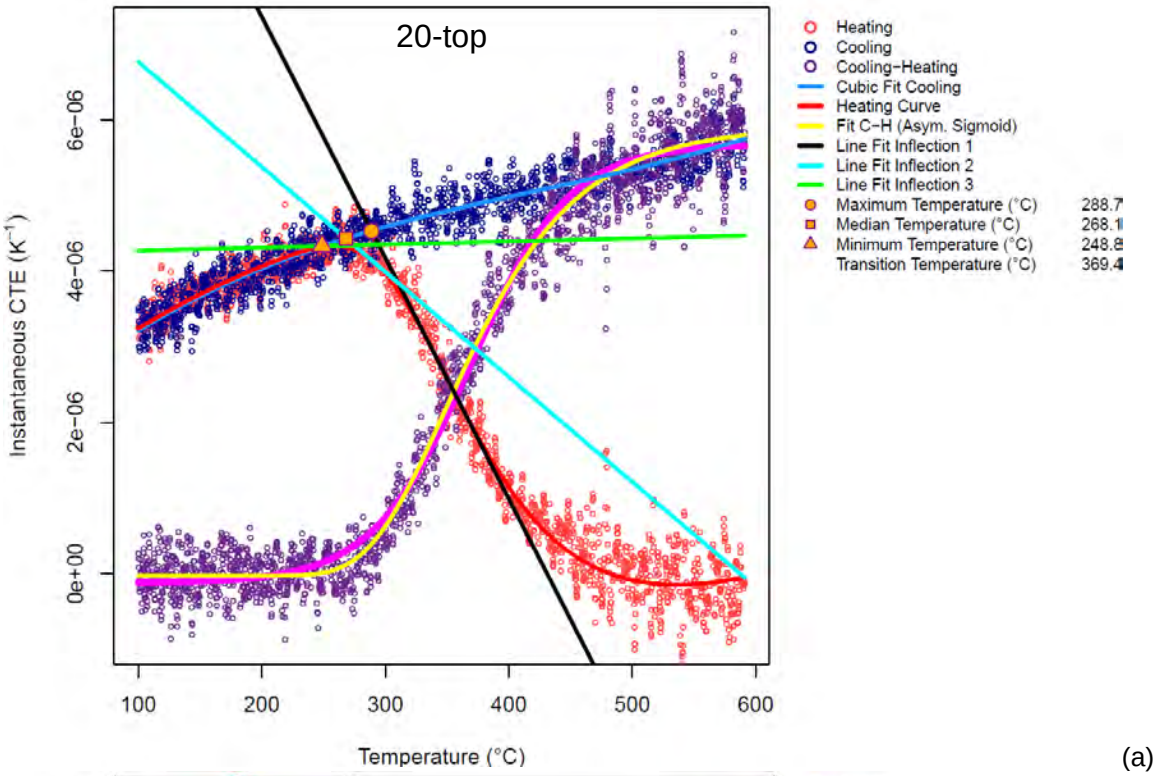
20-top
Heating
Cooling
Cooling−Heating
Cubic Fit Cooling
Heating Curve
Fit C−H (Asym. Sigmoid)
Line Fit Inflection 1
Line Fit Inflection 2
Line Fit Inflection 3
Maximum Temperature (°C) 288.7
Median Temperature (°C) 268.1
Minimum Temperature (°C) 248.8
Transition Temperature (°C) 369.4
Instantaneous CTE (K⁻¹)
0e+00
2e−06
4e−06
6e−06
100
200
300
400
500
600
Temperature (°C)

(a)

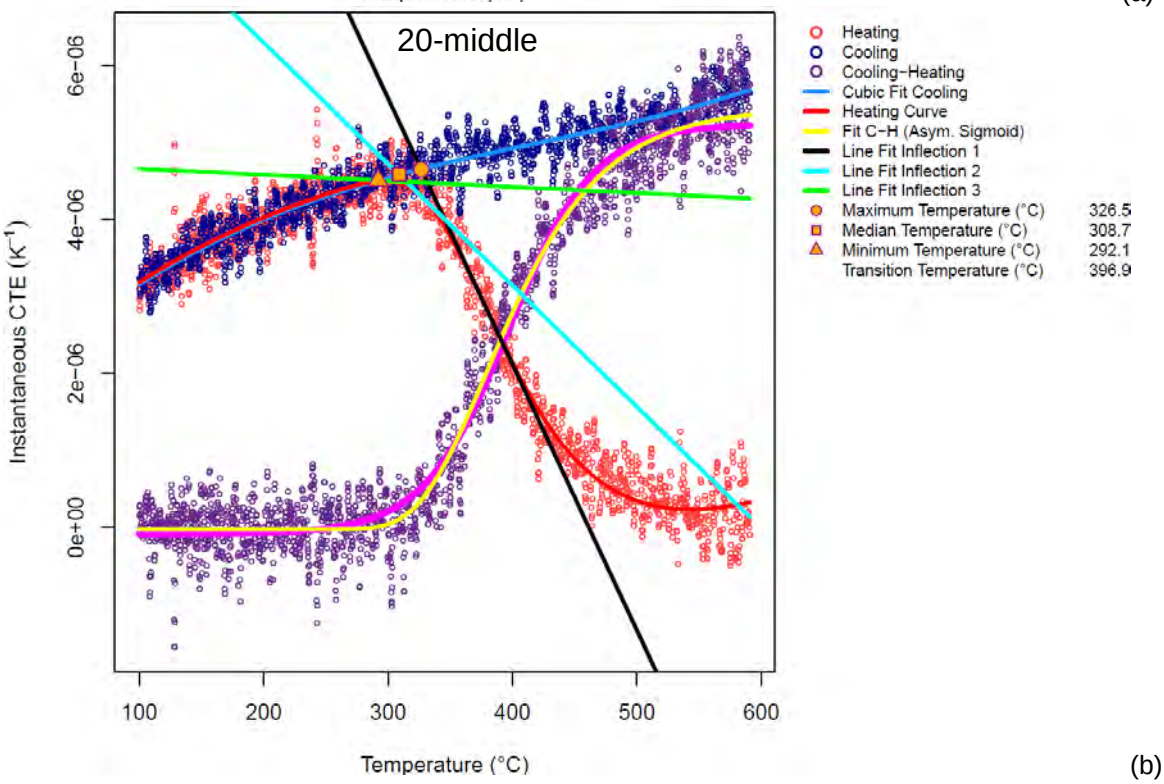
20-middle
Heating
Cooling
Cooling−Heating
Cubic Fit Cooling
Heating Curve
Fit C−H (Asym. Sigmoid)
Line Fit Inflection 1
Line Fit Inflection 2
Line Fit Inflection 3
Maximum Temperature (°C) 326.5
Median Temperature (°C) 308.7
Minimum Temperature (°C) 292.1
Transition Temperature (°C) 396.9
Instantaneous CTE (K⁻¹)
0e+00
2e−06
4e−06
6e−06
100
200
300
400
500
600
Temperature (°C)

(b)

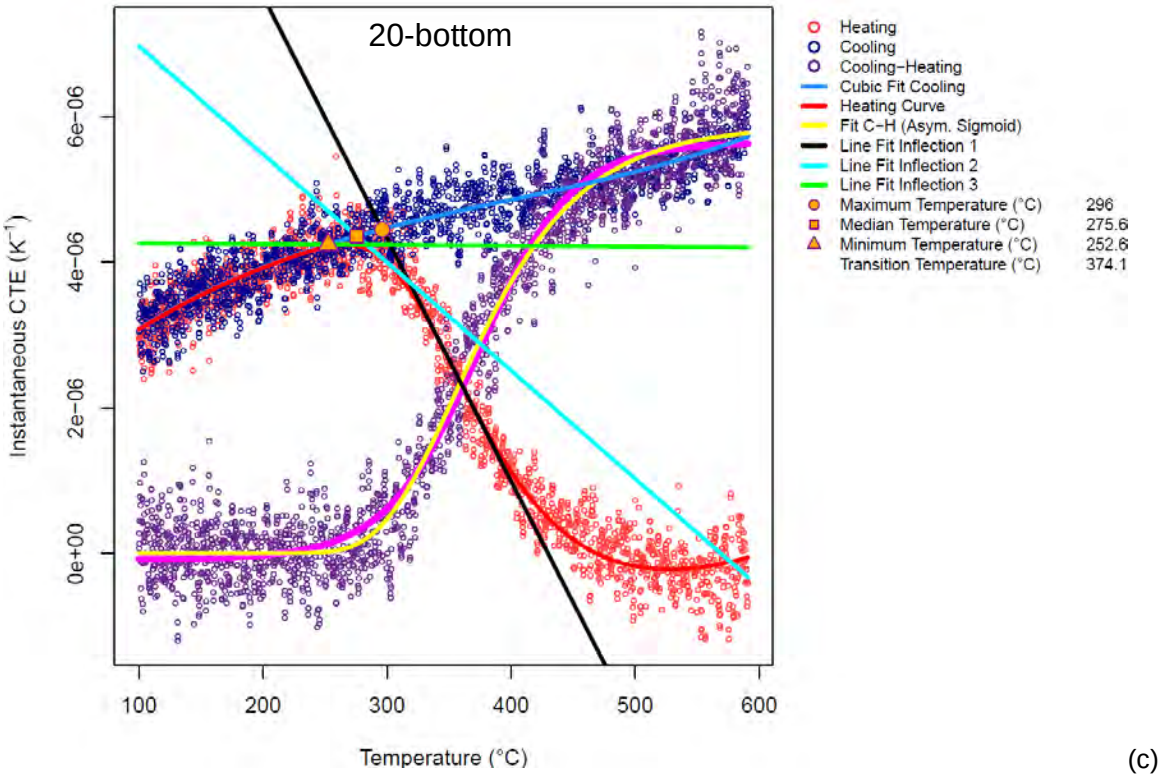

(c)

Figure 11. ES35 capsule thermometry specimen #20 irradiation temperature determinations: (a) top, (b) middle, (c) bottom.

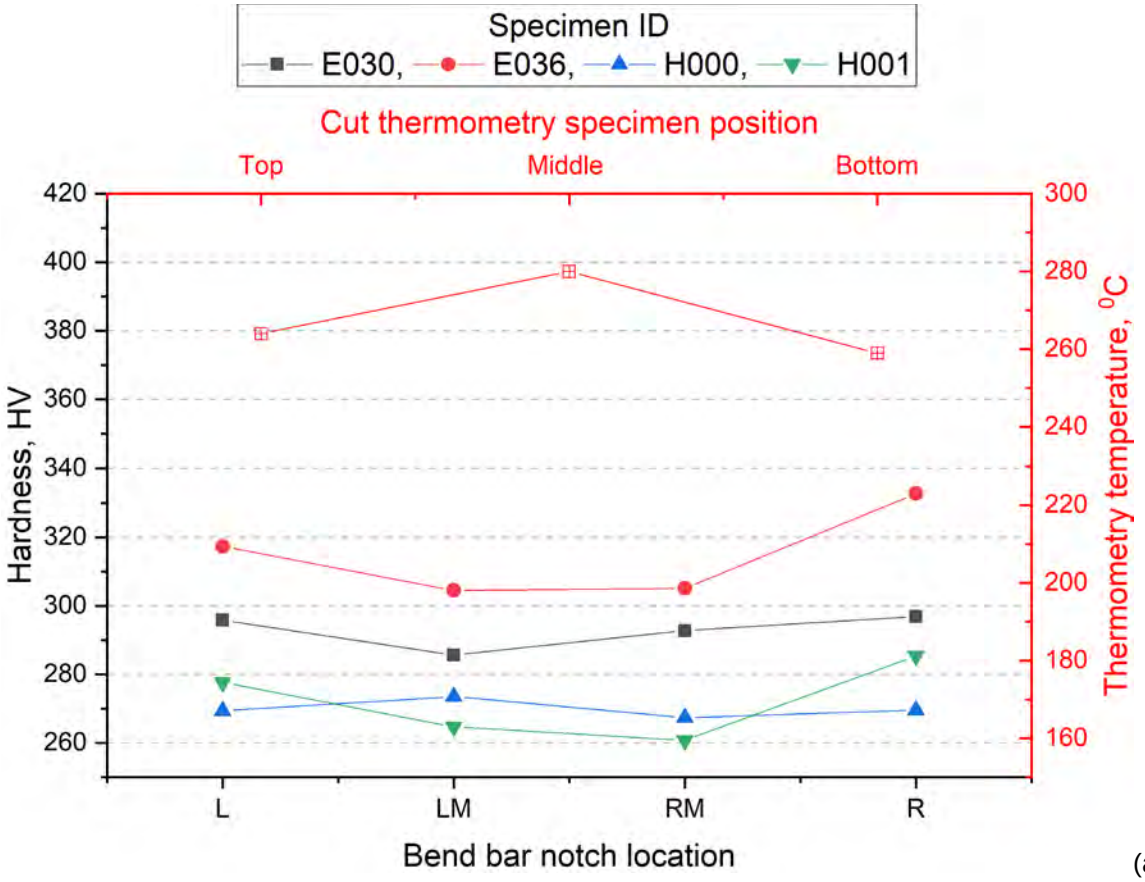
Specimen ID
E030,
E036,
H000,
H001
Cut thermometry specimen position
Top
Middle
Bottom
Hardness, HV
Thermometry temperature, °C
420
400
380
360
340
320
300
280
260
300
280
260
240
220
200
180
160
L
LM
RM
R
Bend bar notch location

(a)

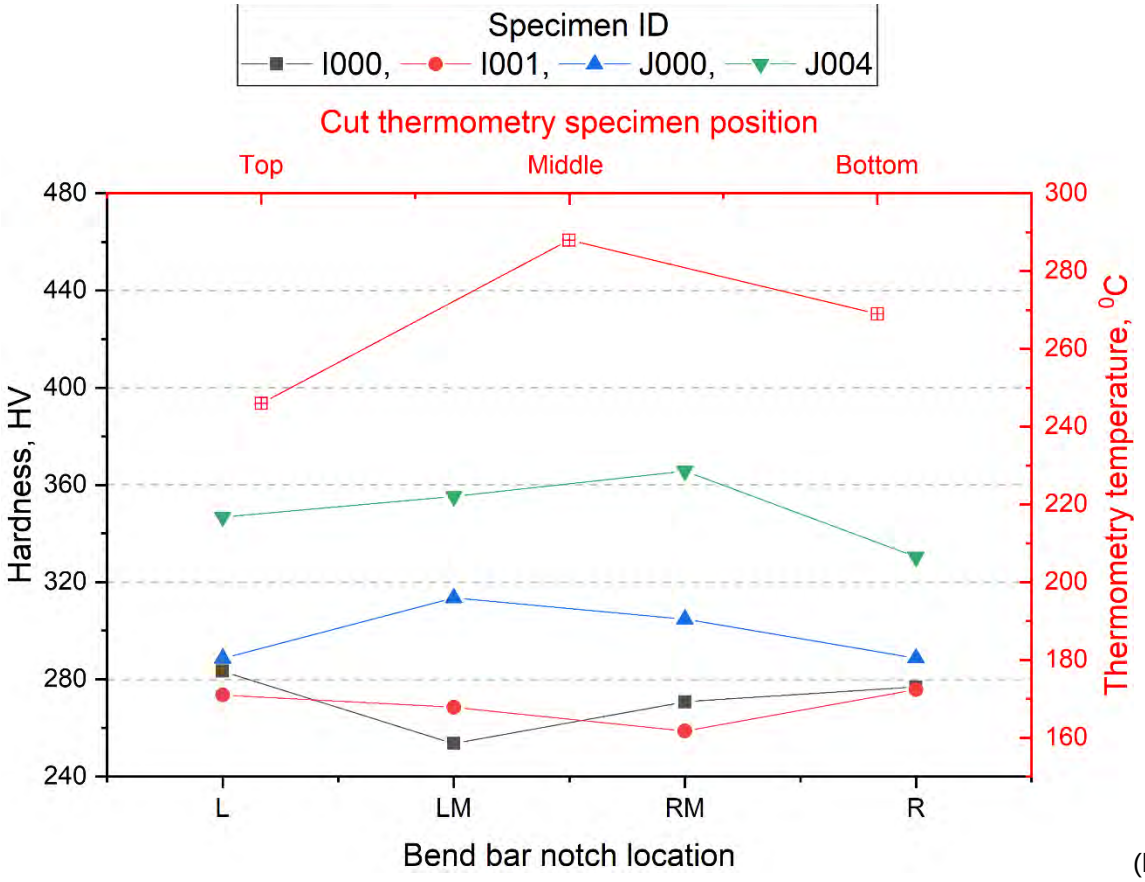
Specimen ID
I000,
I001,
J000,
J004
Cut thermometry specimen position
Top
Middle
Bottom
Hardness, HV
480
440
400
360
320
280
240
Thermometry temperature, °C
300
280
260
240
220
200
180
160
L
LM
RM
R
Bend bar notch location

(b)

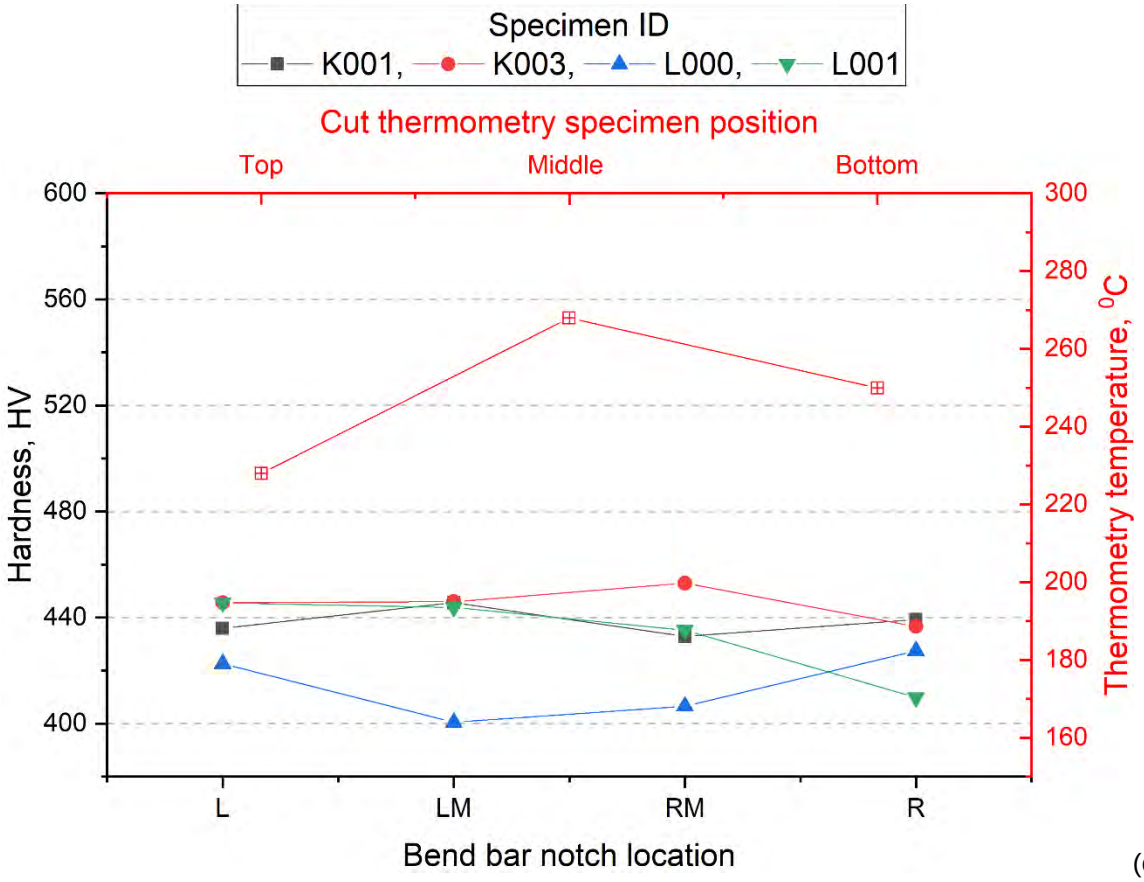
Specimen ID
K001,
K003,
L000,
L001
Cut thermometry specimen position
Top
Middle
Bottom
600
560
520
480
440
400
Hardness, HV
300
280
260
240
220
200
180
160
Thermometry temperature, °C
L
LM
RM
R
Bend bar notch location

(c)

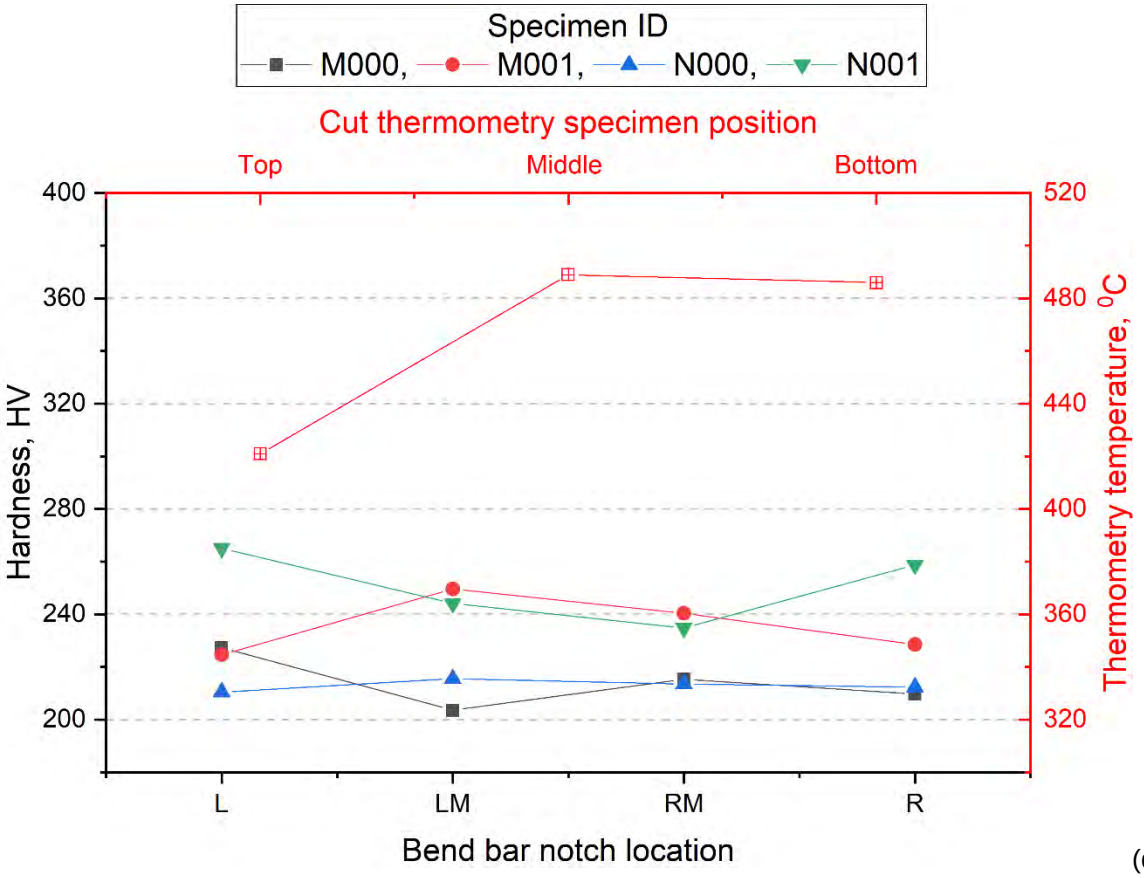
Specimen ID
M000,
M001,
N000,
N001
Cut thermometry specimen position
Top
Middle
Bottom
Hardness, HV
Thermometry temperature, °C
400
360
320
280
240
200
520
480
440
400
360
320
L
LM
RM
R
Bend bar notch location

(d)

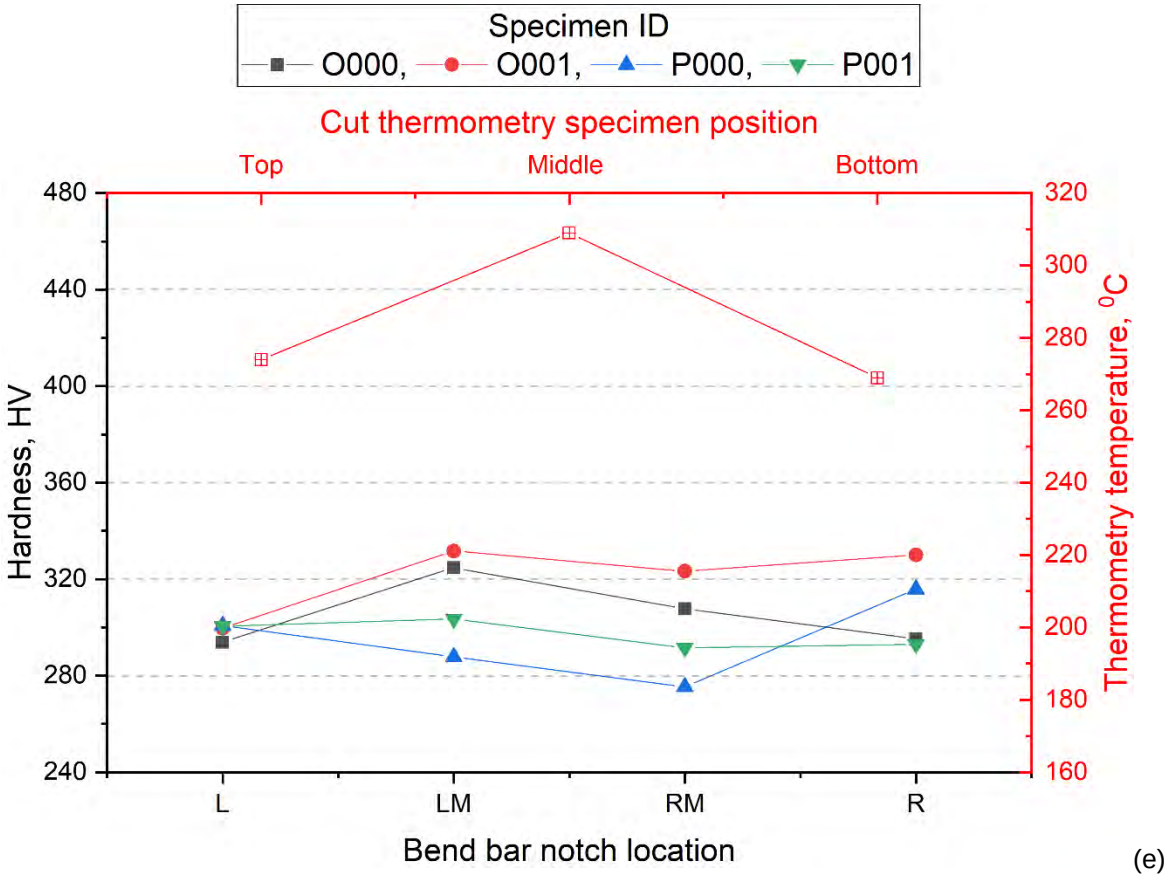

Figure 12. Axial irradiation temperature and microhardness distributions in capsules: (a) ES31, (b) ES32, (c) ES33, (d) ES34, and (e) ES35.

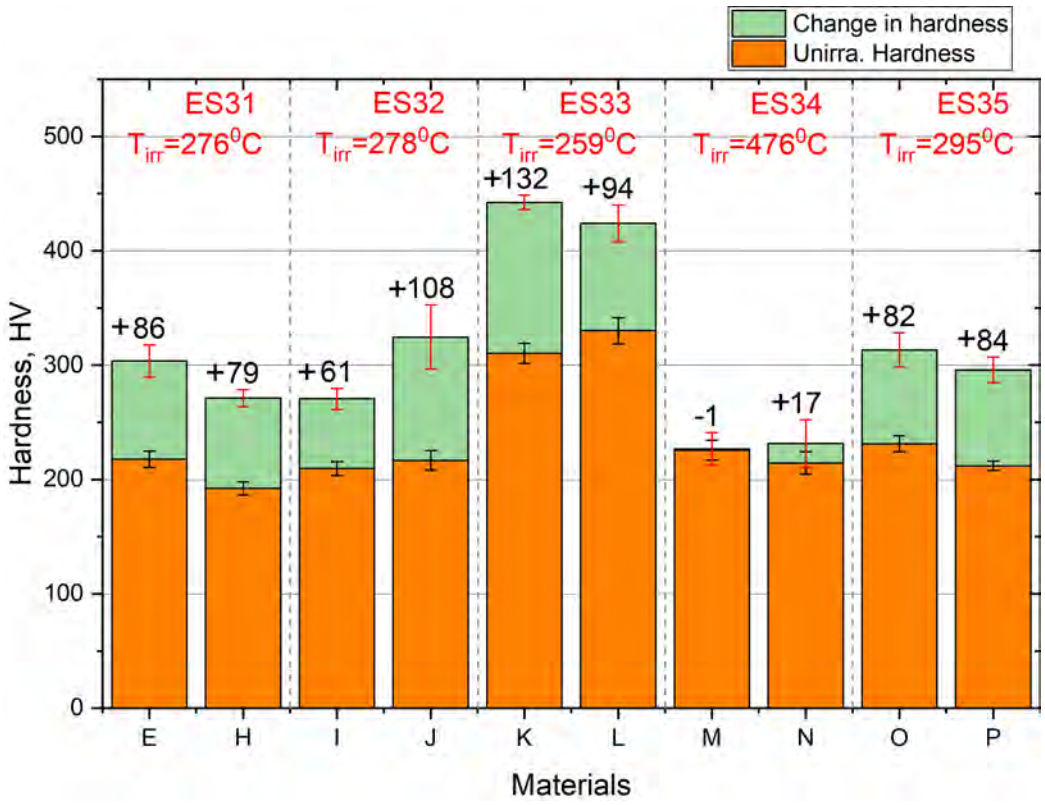

Figure 13. Summary of irradiation temperature and hardening for M4CVN bend bar specimens machined from ten Eurofer97 variants irradiated to 2.5 dpa.

References

[1] R.H. Howard, K.R. Smith, Development of a Flexible Design for Irradiation of Miniature Tensile and Charpy Test Specimens in the High Flux Isotope Reactor, ORNL/TM-2018/872, July 2018.

[2] A.A. Campbell, W.D. Porter, Y. Katoh, L.L. Snead, Method for analyzing passive silicon carbide thermometry with a continuous dilatometer to determine irradiation temperature, Nucl. Instruments Methods Phys. Res. Sect. B Beam Interact. with Mater. Atoms. 370 (2016) 49–58. doi:10.1016/j.nimb.2016.01.005.

1.3 CHARACTERIZATION OF HFIR IRRADIATED EUROFER97 STEEL VARIANTS FOR THE EUROFUSION PROGRAM—A. Bhattacharya, X. Chen, J.W. Geringer, Y. Katoh (Oak Ridge National Laboratory), T. Graening and M. Rieth (Karlsruhe Institute of Technology)

OBJECTIVE

Nine Eurofer97 steel variants having different chemistries, produced using non-standard manufacturing / processing routes, and a reference Eurofer97 steel were irradiated in High Flux Isotope Reactor (HFIR) to ~2.5 dpa at a planned temperature of 300±20 °C. The samples were irradiated as small-scale tensile specimens (type SS-J3) as a part of the EUROfusion program. This work details the irradiation-induced Vickers hardness increase of the steel variants and the temperature invariance of the steel hardness for irradiation temperatures between ~255-346 °C.

SUMMARY

It is now well-accepted that the operating temperature window for the fusion first-wall structural components constructed from Eurofer97 steels will be very narrow: between ~350-550°C [1,2]. The upper temperature limit arises from poor creep strength of Eurofer97 or any 9%Cr ferritic-martensitic (FM) steel in general [3]. The critical lower temperature limit is due to the well-known irradiation-induced embrittlement of FM steels inducing a positive shift in the ductile-brittle transition temperature (DBTT), primarily occurring for irradiation temperatures < 350°C [3]. To address these two critical issues, there is a need to improve Eurofer97 steel properties using a combinatorial approach of modifying the minor alloying chemistry and the processing route. In this context, nine Eurofer97 variants and a reference Eurofer97 were provided to Oak Ridge National Laboratory (ORNL) for pre-irradiation characterization, then neutron irradiations at HFIR to (i) screen the performance of the different steels and (ii) to generate mechanical properties of neutron irradiated baseline Eurofer97 for code qualification. These steels, in the geometry of SS-J3 specimens, were irradiated to a nominal dose of ~2.5 dpa, at target temperature of 300±20°C (International Thermonuclear Experimental Reactor [ITER] relevant conditions). The manufacturing/processing history of these steels is summarized in Table 1.

Post-irradiation SiC thermometry revealed the SS-J3 sample temperatures ranged from as low as ~250 °C to as high as ~346 °C. We performed Vickers hardness tests on the end tab sections of all the irradiated SS-J3 samples using 1 kg load, 15 s dwell time. Figure1 compares the hardness of the different steel families before (red symbols) and after the irradiation (blue symbols). All the steel families showed irradiation-induced increase in hardness. However, from Figure 1 it is evident that despite different manufacturing routes (and slight changes in chemistries) the increase in hardness due to irradiation for all the steel variants fell into a narrow range (between ΔHV= 65-100). Further, with irradiation temperatures between ~255-346 °C, each steel variant systematically showed similar hardness despite a change in the irradiation temperature (Figure 2).

Table 1. Summary of different Eurofer97 steel variants. AQ: air quenched, WQ: water quenched, LT: low temperature application, HT: high temperature application

M-Code	Material type	Heat	Condition	Provider
E	EUROFER97/2	993391	980°C/0.5h + AQ + 760°C + AC (reference)	KIT
H	EUROFER-LT	J362A	1000°C/0.5h + WQ + 820°C + AC	KIT
I	EUROFER-LT	J363A	1000°C/0.5h + WQ + 820°C + AC	KIT
P	EUROFER-LT	J361A	1000°C/0.5h + WQ + 820°C + AC	KIT
L	EUROFER97/2	994578	1150°C/0.5h + AQ + 700°C + AC	CEA
J	EUROFER-LT	I196C	TMT:1250°C/1h and then rolling to a final rolling temperature of 850°C in 6 rolling steps with a reduction of 20-30% for each rolling pass, then AC. Q&T: 880°C/0.5h+WQ+750°C/2h+AC	SCK.CEN
K	EUROFER-HT	I427A	TMT:1250°C/1h and then rolling to a final rolling temperature of 850°C in 6 rolling steps with a reduction of 20-30% for each rolling pass, then AC. Q&T: 1050°C/15min + WQ + 675°C/1.5h + AC	SCK.CEN
M	EUROFER97/2	993391	1020°C/0.5h + AQ + 1020°C/0.5h + AQ +760°C/1.5h + AC (double austenitization)	ENEA
O	EUROFER-LT	VM2991	TMT: 1080°C/1h, cooling to 650°C and rolling, reduction 40% (from 30 mm to 18mm) Tempering: 760°C/1h + AC	ENEA
N	EUROFER-LT	VM2897	920°C/1.5h + AQ + 920°C/1.5h + AQ + 760°C/1h + AC (double austenitization)	ENEA

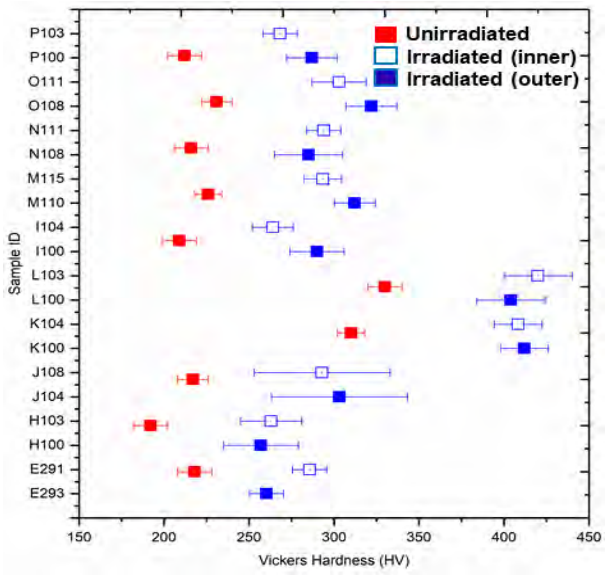

Figure 1. Vickers hardness of EUROfusion steels before and after 2.5 dpa neutron irradiations.

In FM steels, the severity of the irradiation-induced hardening and embrittlement depends on the (i) irradiation temperature and (ii) neutron dose. At a given irradiation temperature, it is well-known that irradiation-induced hardening/embrittlement in FM steels saturates around ~20-30 dpa. Similar hardness values of different steels over a wide irradiation temperature range between ~255-346°C suggests that there is negligible effect of the irradiation temperature on hardening in the current temperature range. This result is qualitatively consistent with saturation of DBTT with irradiation temperature in neutron irradiated Eurofer97 steels at T < 350°C [2].

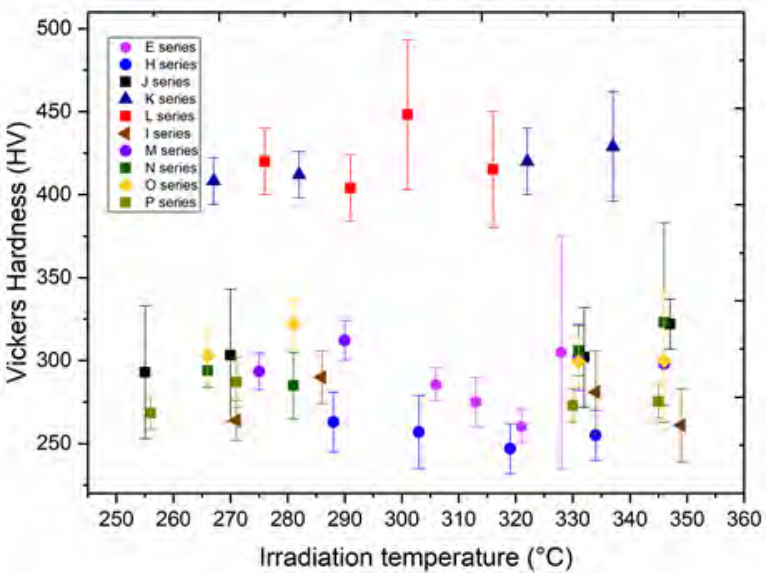

Figure 2. Vickers hardness versus irradiation temperature for the ten steel variants.

PROGRESS AND STATUS

Vickers hardness of ten EUROfusion steel variants irradiated in HFIR were evaluated using the hardness testing facility in the ORNL hot cell. Despite differing chemistries and manufacturing routes, the change in hardness of all the steel families irradiated to ~2.5 dpa lie within a very narrow range (between ΔHV= 65-100). Further, for irradiation temperatures between ~255-346°C, the hardness change in each steel family was negligible suggesting irradiation-temperature invariant hardening behavior for T<350°C. This is consistent with the invariance in DBTT shift of Eurofer97 for irradiation temperature <350°C.

In continuing work on this project, uniaxial tensile tests in the hot cells will be performed on these samples at room and the irradiation temperature., The testing will be followed by detailed state-of-art microstructure characterization at Low Activation Materials Development and Analysis (LAMDA) lab using conventional and analytical scanning transmission electron microscopy (STEM), high-throughput energy dispersive X-ray spectroscopy (EDX) and/or electron energy loss spectroscopy (EELS).

References

[1] F. Tavassoli, Eurofer steel, development to full code qualification, Procedia Eng. 55 (2013) 300–308. doi:10.1016/j.proeng.2013.03.258.
[2] D. De Meis, Structural Materials for DEMO R&D Status, RT/2015/25 (2011).
[3] R.L. Klueh, D.R. Harries, High-Chromium Ferritic and Martensitic Steels for Nuclear Applications, ASTM, Bridgeport, 2001. doi:10.1520/MONO3-EB.

1.4 DESIGN OF 3Cr-3WV BAINITIC STEEL FOR CROSS-WELD PROPERTY IMPROVEMENT—Y. Yamamoto (Oak Ridge National Laboratory)

OBJECTIVE

This work aims to develop new bainitic steels, based on 3Cr-3WV(Ta) steels originally developed at Oak Ridge National Laboratory (ORNL). The goal is mechanical properties of both base metal and weldments superior to those of existing commercial bainitic steels or ferritic martensitic (FM) steels, together with no requirement for post-weld heat treatment (PWHT). The target applications are high temperature structural components in fusion reactors such as the vacuum vessel, structural ring which supports the blanket modules, and magnet shields, to be used at or above the 400-500ºC range. Improvement of long-term creep properties by introducing additional fine, stable second-phase dispersions, as well as maintaining good weldability, is targeted via optimization of alloy composition and thermo-mechanical heat treatment.

SUMMARY

Alloy modification was pursued based on the 3Cr-3WV steel (Ta-free) combined with high Mn, low C, low Si, and additional B, to produce the expected improvement of creep performance and elimination of temper-embrittlement. Three lab-scale heats of new steels were prepared at ORNL. Evaluation by micro-Vickers hardness of as-normalized and normalized-and-tempered materials indicated comparable hardness to the original 3Cr-3WV steel despite the lower carbon contents in the new steels. Charpy impact toughness tests revealed adequate toughness in as-normalized and normalized-and-tempered materials (>40 J/cm^2 and >180 J/cm^2, respectively). No temper-embrittlement was observed in the new heats which could be due to the relatively lower Si addition (0.16 wt.%) than the previously evaluated heat. The gas tungsten arc weld of the new heats with a 3Cr-3WVTa steel weld filler metal has been completed. Map hardness analysis across the weldment was conducted and the results were summarized in conjunction with a newly proposed alloy design strategy.

PROGRESS AND STATUS

Introduction

Development of new bainitic steels was initiated under the Fusion Energy Materials Program in FY2014, as a modification of the original 3Cr-3WV(Ta) steels developed at ORNL [1, 2, 3]. The target applications include vacuum vessels or structural rings supporting the blanket modules in fusion reactor applications as in the conceptual United States (US) Fusion Neutron Sciences Facility (FNSF) [4]. The current alloy design strategy is to make the materials usable without PWHT (PWHT-free) to lower the capital cost of these large volume components. Potential concern in the characteristics of the PWHT-free components would be the property inhomogeneity of the as-welded material across the weldment. Such inhomogeneity needs to be minimized to avoid any premature failure attributed to itself (e.g. stress concentration). To solve the potential issue, an alloy design was proposed which focused on decreasing the hardness in the normalized condition without losing the high “hardenability” to promote the carbide-free acicular bainite ferrite formation. With this design strategy, a new heat “MSLC2” (Fe-3Cr-3W-0.2V-0.1Ta-2Mn-0.05C-0.5Si, in wt.%) was proposed with guidance from computational thermodynamics. The steel achieved tensile strengths comparable to the original 3Cr-3WVTa steel despite the low C content, which could be attributed to the formation of carbide-free acicular bainitic ferrite laths through the designed high hardenability. Relatively low hardness was also achieved in the as-normalized condition which led to the reduced cross-weld hardness inhomogeneity. The creep-rupture life of the modified steels at 550-600°C was comparable to the original 3Cr-3WVTa steels, and a slight improvement of the cross-weld creep properties was also found at 550°C. However, the Charpy impact toughness of the steel indicated a significant temper-embrittlement which could be attributed to the excess amount of Si (~0.5 wt.%).

Based on these results, another set of alloys with a new design strategy has been proposed; high Mn, low C, low Si, and a small amount of B. The boron addition in ferritic-martensitic steels is known to refine the

size of $M_{23}C_6$ type carbides and improve the thermal stability of the carbide which positively works stabilizing the martensite laths at the service temperatures and therefore the creep performance as well [5]. There is a concern about the potential helium-bubble formation due to transmutation of B in an irradiation condition, although the negative impact is believed to be sufficiently small or even negligible because the expected dose would be relatively low in the target components. In addition, the new alloys were based on Ta-free 3Cr-3WV steel in order to eliminate the combined effect of MC type carbide formation on the alloy modification. In this report, the selection of the alloy compositions through prediction of phase equilibrium and transformation kinetics are summarized, and the initial property screening results including micro-Vickers hardness and Charpy impact toughness are presented. The cross-weld hardness analysis of the gas tungsten arc welded (GTAW) materials are also discussed.

Results

Three alloy compositions based on 3Cr-3WV steel have been proposed, as shown in Table 1. The compositions of original 3Cr-3WV and previously prepared heat MSLC2 are also shown for comparison. The modifications include the additions of (1) 2 wt.% Mn, (2) 0.05 or 0.08 wt.% C, and (3) with 0.01 wt.% B. Note that the Si addition was kept the same as the original steel (0.16 wt.%) to avoid temper-embrittlement.

Table 1. Nominal composition of the steels in this study

Alloy	Nominal composition, wt.%									Remarks
	Fe	Cr	Mn	Si	Ta	V	W	C	B	
MLC02	91.59	3	2	0.16	-	0.2	3	0.05	-	High Mn, low C
MLC03	91.56	3	2	0.16	-	0.2	3	0.08	-	High Mn
MLC03B	91.56	3	2	0.16	-	0.2	3	0.08	0.01	High Mn, with B
Original 3Cr-3WV	93.14	3	0.4	0.16	-	0.2	3	0.1	-	Ta-free
Ref: MSLC2	91.15	3	2	0.50	0.1	0.2	3	0.05	-	Reference

The predicted phase equilibria of the original and modified steels are shown in Figure 1, calculated by JMatPro v.9. Compared to the original 3Cr-3WV, the high Mn + low C additions resulted in lowering the Ac1 (800°C for the original and 700-720°C for the modified steels). Among the predicted second-phases, M_6C carbide was dominant at ~600°C, and $M_{23}C_6$ or Laves-phase (Fe_2W) followed in the modified steels. Total amounts of carbides formed below Ac1 decreased with lowered C contents, and the B addition promoted small amount of boride formation. The effects of alloy modification on the transformation kinetics were discussed by using continuous cooling transformation (CCT) diagrams shown in Figure 2. The addition of 2 wt.% Mn resulted in lowering the bainite start temperature (Bs) from ~540°C to 480°C at a cooling rate of 10°C/s, which indicated higher hardenability compared to the original 3Cr-3WV steel. The addition of C in a range 0.05 to 0.08 wt.% did not change the bainite formation kinetics, although the pearlite start curve (Ps) shifted toward longer time with decreasing carbon content. Interestingly, the B addition resulted in slow bainite formation kinetics with the bainite start at ~380°C at 10°C/s. Although the mechanism is unclear, the calculation results indicate a positive effect of the B addition on the hardenability.

Three lab-scale heats (MLC02, MLC03, and MLC03B) were prepared by arc-melting with pure element feedstock, followed by drop-casting into a rectangle shape mold. The ingots with size 1” x 1” x 4” were homogenized at 1200°C in Ar cover gas for 2 h, followed by air-cooling to room temperature. The ingots were soaked at 1100°C in Ar cover gas for 30 min, thermo-mechanically processed (forging and rolling) to make plate-shape samples with 0.3” thickness, subsequently annealed at 1100°C in Ar cover gas for 30 minutes, and then air-cooled to room temperature (normalization). Part of the normalized plates were sectioned, and then tempered at 700°C in air for 1 h, followed by air cooling to room temperature. Figure 3 summarized the initial property screening, including micro-Vickers hardness and Charpy impact toughness tests conducted at room temperature. The as-normalized materials showed comparable hardness to the original 3Cr-3WV steel despite the lower carbon contents, indicating that the designed high hardenability

was successfully obtained. The hardness of the normalized-and-tempered materials increased compared to the original 3Cr-3WV steel, although the values were comparable. Charpy impact toughness tests revealed adequate toughness of the as-normalized and normalized-and-tempered materials (>40 J/cm^2 and >180 J/cm^2, respectively). As expected, no temper-embrittlement was observed in the new heats.

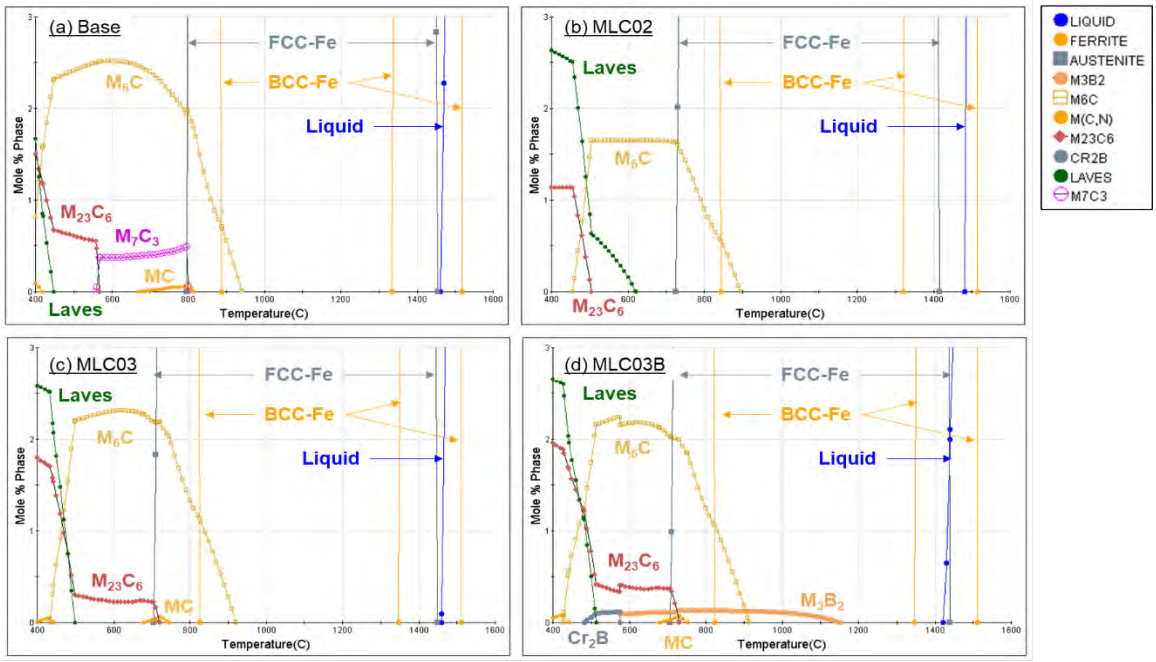

Figure 1. Phase equilibrium calculated by JMatPro v.9; (a) original 3Cr-3WV steel, (b) MLC02, (c) MLC03, and (d) MLC03B.

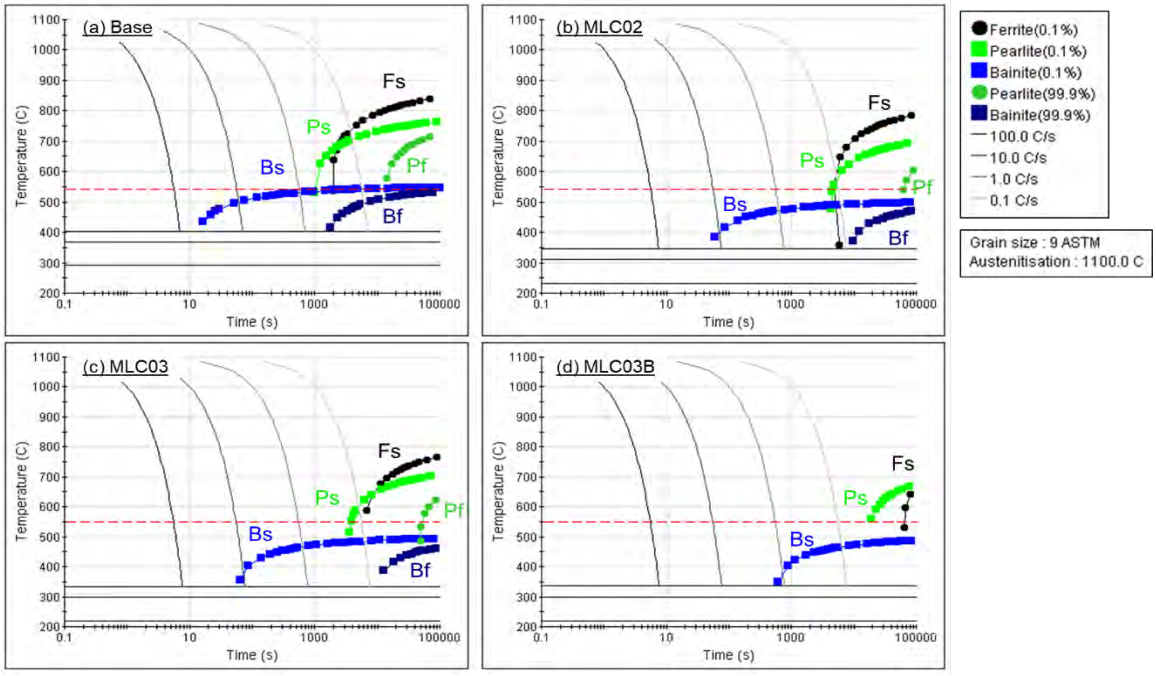

Figure 2. CCT diagrams calculated by JMatPro v.9; (a) original 3Cr-3WV steel, (b) MLC02, (c) MLC03, and (d) MLC03B. The red broken line corresponds to the bainite start temperature of the original 3Cr-3WV steel at a cooling rate of 10°C/s.

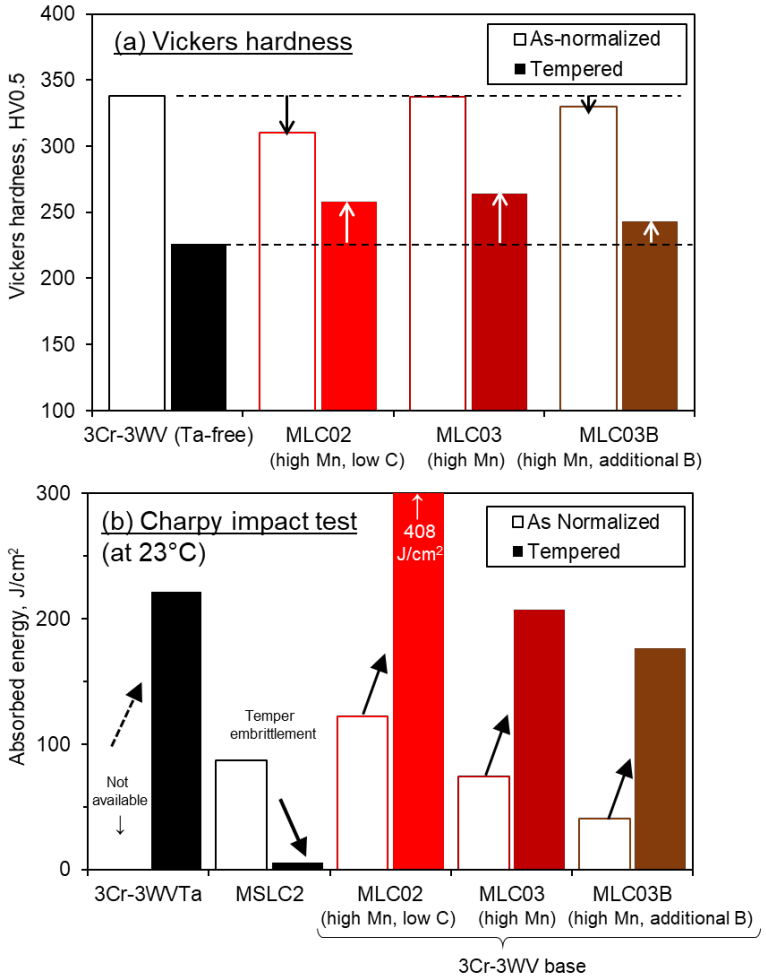

Figure 3. Comparison of properties among the 3Cr-3WV steels in normalized and tempered conditions; (a) micro-Vickers hardness, and (b) Charpy impact test results.

A manual GTAW was formed for each of the three new heats in the normalized-and-tempered condition. Original 3Cr-3WVTa steel material was used as a weld filler metal. The creep-rupture of the cross-weld specimens always occurred at the heat affected zone (HAZ) in the previous heat MSLC2, so that the improved stability of microstructure and mechanical properties at the HAZ would be the key to improving the cross-weld creep properties. Thus, the weld filler material with higher creep resistance than the base metal was selected, in order to control that the creep deformation would dominantly occur at the HAZ, not inside the weld metal.

Figure 4 illustrates cross-sectional views of the as-welded materials with a superimposed color contour map showing hardness distribution across the welds. The weld metal and the HAZ showed higher hardness than the base metal in all samples, because the regions were exposed above Ac3 so that most of the regions consisted of the as-normalized microstructure. The HAZ hardness in MLC02 with 2Mn-0.05C was in the range of 260-320HV which was relatively lower than the other heats (MLC03 with 0.08C and MLC03B with 0.08C-0.01B, 270-360 HV). This was attributed to the amount of the C addition, where the higher C content gave the higher hardness. There was no clear difference between MLC03 and MLC03B in the present results, although the high hardness region (>340HV) in MLC03B seemed wider than that in MLC03, which might be due to the higher MLC03B hardenability predicted in the transformation kinetics in Figure 2d. Because of the minimum hardness among all samples, MLC02 achieved the closest microstructure to the targeted alloy design with less inhomogeneous property distribution across the weld. The base metal and

cross-weld creep property evaluation of these heats has been initiated, and the results will be summarized in a future report.

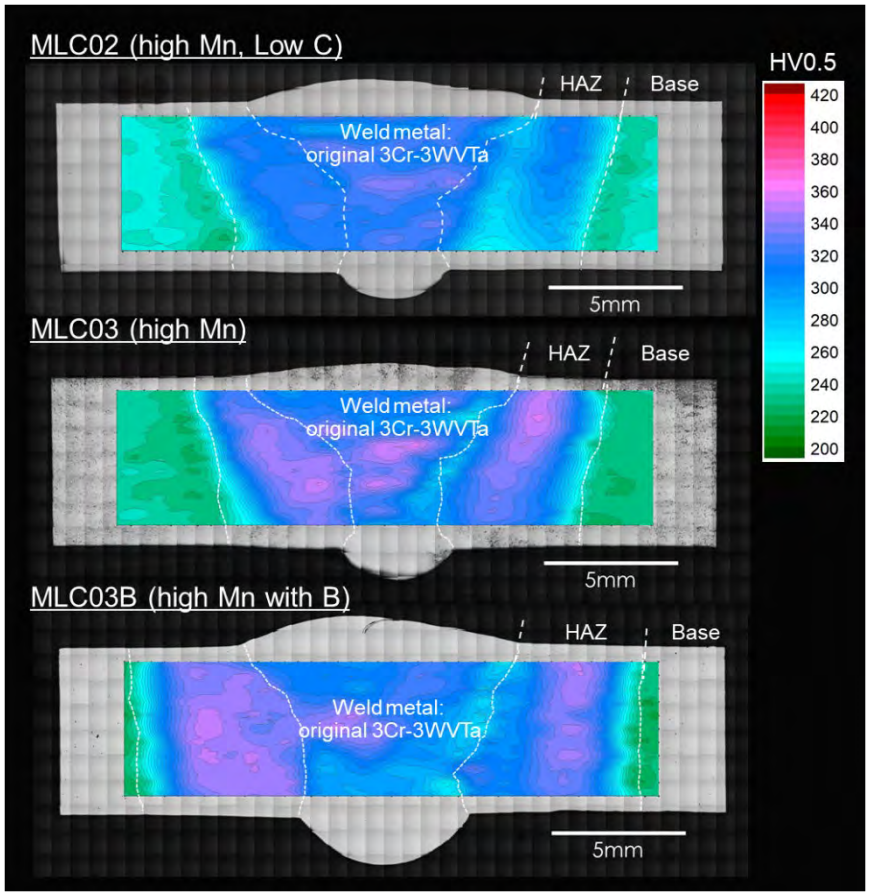

Figure 4. Color contour hardness map of cross-weld modified 3Cr-3WV steel plates with 3Cr-3WVTa weld filler metal

References

[1] R.L. Klueh, Elevated-Temperature Ferritic and Martensitic Steels and Their Application to Future Nuclear Reactors, ORNL/TM-2004/176, November 2004.

[2] R.L. Klueh, N.D. Evans, P.J. Maziasz, V.K. Sikka, Creep-rupture behavior of 3Cr-3W-V bainitic steels, International Journal of Pressure Vessels and Piping, 84 (2007) 29-36.

[3] M. Jawad, V.K. Sikka, Development of a New Class of Fe-3Cr-W(V) Ferritic Steels for Industrial Process Applications, ORNL/TM-2005/82, 2005, Oak Ridge National Laboratory

[4] L. El-Guebaly, et al., Design Challenges and Activation Concerns for Aries Vacuum Vessel, FUSION SCIENCE AND TECHNOLOGY, 64 (2013) 449-454.

[5] For example: N. Takahashi and T. Fujita: Tetsu-to-Hagané, 61 (1975), 2604-2616.

2. ODS AND NANOCOMPOSITED ALLOY DEVELOPMENT

2.1 IRRADIATION DAMAGE EFFECTS IN 14YW AND 14YWT FERRITIC ODS ALLOYS STUDIED BY ATEM AND APT—Karen Kruska, Danny J. Edwards, Jing Wang, Richard Kurtz (Pacific Northwest National Laboratory), T. Yamamoto, Y. Wu and G.R. Odette (University of California-Santa Barbara)

This is an Extended Abstract for a paper presented at NuMat2018

Oxide dispersion strengthened (ODS) alloys are being considered as a first wall blanket material for fusion reactors due to their exceptional performance at high temperatures. Nanoscale oxide particles dispersed in the matrix of the alloy not only enhance its strength, but also act as helium (He) traps. Without such a capturing mechanism, He build-up in bubbles could lead to void swelling, causing detrimental material degradation in plasma facing components and structural materials. The stability of these nano-oxide particles is important to ensure they remain viable traps over the lifetime of the component. In this study, we explore the long-term stability of ODS particles in two alloys under extreme conditions. We used ATEM and APT to analyze ODS particle size, density and composition in two ODS alloys before and after neutron irradiation in High Flux Isotope Reactor (HFIR). A novel cluster search algorithm developed at Pacific Northwest National Laboratory (PNNL) (OPTICS) was used to quantitatively evaluate ODS and α' phase particles.

Transmission Electron Microscopy (TEM) discs of ODS 14YW and nanostructured ferritic alloy 14YWT were irradiated in HFIR at Oak Ridge National Laboratory (ORNL) to a dose of 21.2 dpa at 500°C in the JP-27 experiment [1-3] as part of the in-situ helium injection (ISHI) experiment. The He was injected to 1230 atomic parts per million (appm) into the alloys by transmutation of a Ni-Al coating on each sample. The particle density in the 14WT is too coarse to effectively capture enough particles for statistical analysis using APT, but for the NFA 14YWT over 400 particles were analyzed in both the as-received and the irradiated samples. The particles in both alloys proved to be stable based on post-irradiation analysis by both TEM and APT, with some minor changes in density but exhibiting a stable average size. It was observed that the chemistry of the particles experiences a slight shift, likely due to Cr segregating to the ODS particles during irradiation [4]. α′ particles were found in both alloys after irradiation, at roughly comparable densities of ~5 x 10^{23} m^{-3} and average size of 4-5 nm. Localized variations exist in the α′ spatial distribution and that of the ODS particles in both alloys based on the APT analysis, but these variations are not as evident in the α′ when documented using elemental mapping on an aberration-corrected Japan Electron Optics Laboratory (JEOL) ARM200CF. The elemental mapping doesn't easily capture the α′ particles less than 3 nm, so the measured size distribution yields a larger average size than measured by APT.

The APT and ATEM proved to be complementary techniques for analyzing precipitates in these ODS materials, with APT more sensitive to smaller precipitates than ATEM and able to probe the chemistry of the nanoparticles more effectively. The ATEM can analyze a larger volume and better explore global spatial variations in the α′ particle distribution near intragranular oxy-carbo-nitrides and other interfaces. Using both techniques, we documented that the ODS particles were stable in both alloys under neutron irradiation at 500°C, with no apparent influence of He injection on the ODS particles or the α′. The APT did indicate Cr segregation to the ODS particles in the 14YWT, but this was not captured convincingly in the 14YW because of its coarser oxide distribution.

ACKNOWLEDGEMENTS

The work was performed at University of Connecticut, and at PNNL, which is operated by Battelle for the United States Department of Energy (U.S. DOE) under Contract DE-AC06-76RL0-1830. This research is funded by the U.S. DOE Office of Fusion Energy Sciences under contract DE-AC05-76RL01830. All computations were performed on PNNL's Institutional Resources (PIC).

References

[1] T. Yamamoto, G.R. Odette, L.R. Greenwood, Fusion Materials Semiannual Report 1/1 to 6/30/2005 DOE/ER-313/38, 2005, p. 95.

[2] T. Yamamoto, G.R. Odette, P. Miao, D.T. Hoelzer, J. Bentley, N. Hashimoto, H. Tanigawa, R. J. Kurtz, J. Nucl. Mater., 367-370 (2007) 399.
[3] R.J. Kurtz, G.R. Odette, T. Yamamoto, D.S. Gelles, P. Miao, B.M. Oliver, J. Nucl. Mater. 367-370 (2007) 417.
[4] J. He, F. Wan, K. Sridharan, T.R. Allen, A. Certain, Y.Q. Wu, J. of Nucl. Mater. 452 (2014) pp. 87-94.

3. CERAMIC COMPOSITE STRUCTURAL MATERIAL DEVELOPMENT

3.1 MULTISCALE EXPERIMENTAL CHARACTERIZATION OF COATINGS ON CERAMICS: A CASE STUDY OF TUNGSTEN ON SiC—Huaxin Li (Hefei University of Technology), Takaaki Koyanagi, Xunxiang Hu, Yutai Katoh (Oak Ridge National Laboratory)

Abstract of a manuscript submitted to Surface and Coatings Technology

State-of-the-art transmission Kikuchi diffraction (TKD) and high-speed nano-indentation were combined with glow-discharge optical emission spectroscopy (GDOES), transmission electron microscopy (TEM) and micro-cantilever testing to characterize microstructures and mechanical properties of coatings on a ceramic substrate. The goal was to develop a multiscale experimental characterization method to assess the coating/substrate couple. A tungsten coated silicon carbide substrate was the system used for this development. The combination of GDOES, TEM and TKD enabled precise phase identification in the system, while TKD provided superior spatial resolution for phase identification. Micro-cantilever tests were able to measure adhesion strength, with support from high-speed nano-indentation which enabled rapid modulus and hardness determination over relatively large areas.

3.2 NANO-SCALE MICROSTRUCTURE DAMAGE BY NEUTRON IRRADIATIONS IN A NOVEL BORON-11 ENRICHED TiB_2 ULTRA-HIGH TEMPERATURE CERAMIC—A. Bhattacharya, C. M. Parish, T. Koyanagi, C. M. Petrie, Y. Katoh (Oak Ridge National Laboratory), D. King, G. Hilmas, W. G. Fahrenholtz (Missouri University of Science and Technology), S. J. Zinkle (University of Tennessee)

Abstract of a manuscript published in Acta Materialia 165 (2019) 26-39

Ultra-high temperature transition-metal ceramics are potential candidates for fusion reactor structural/plasma-facing components. We reveal the irradiation damage microstructural phenomena in Boron-11enriched titanium diboride (TiB_2) using mixed-spectrum neutron irradiations, combined with state-of art characterization using transmission electron microscopy (TEM) and high resolution TEM (HRTEM). Irradiations were performed using High Flux Isotope Reactor at ~220 and 620 °C up to 2.4 × 10^{25} n/m^2 (E > 0.1 MeV). Total dose including contribution from residual Boron-10 (10B) transmutation recoils, was ~4.2 displacements per atom. The TiB2 is susceptible to irradiation damage in terms of dislocation loop formation, cavities and anisotropic lattice parameter swelling induced micro-cracking. At both 220 and 620 °C, TEM revealed dislocation loops on basal and prism planes, with nearly two orders of magnitude higher number density of prism-plane loops. The HRTEM, electron diffraction and relrod imaging revealed additional defects on {1010} prism planes, identified as faulted dislocation loops. High defect cluster density on prism planes explains anisotropic a-lattice parameter swelling of TiB2 reported in literature which caused grain boundary micro-cracking, the extent of which decreased with increasing irradiation temperature. Dominance of irradiation-induced defect clusters on prism planes in TiB_2 is different than typical hexagonal ceramics where dislocation loops predominantly form on basal planes causing c-lattice parameter swelling, thereby revealing a potential role of c/a ratio on defect formation/aggregation. Helium generation and temperature rise from residual 10B transmutation caused matrix and grain boundary cavities for the irradiation at 620 °C. The study additionally signifies isotopic enrichment as a viable approach to produce transition-metal diborides for potential nuclear structural applications.

4. HIGH HEAT FLUX MATERIALS AND COMPONENT TESTING

4.1 INFLUENCE OF SPECIMEN SIZE, DUCTILE PHASE PROPERTIES AND LARGE IMPURITY INCLUSIONS ON THE FRACTURE TOUGHNESS OF TUNGSTEN HEAVY METAL ALLOYS: WNiFe and WNiCu—M.E. Alam, G.R. Odette (University of California Santa Barbara)

OBJECTIVE

The objective of this research is to identify the effect of specimen size, ductile phase properties, and impurity inclusions on the room temperature fracture toughness of tungsten heavy alloys as divertor material.

SUMMARY

The tensile strength and fracture toughness properties of four ductile phase toughened (DPT) commercially available tungsten (W)-based heavy metal alloy composites (WNiFe), reinforced with 3 to 10 (wt.%) of a NiFe phase, were previously thoroughly characterized from room to liquid nitrogen (LN_2) temperatures. All the alloys manifested a sub-zero brittle-to-ductile transition temperature (BDTT) ranging from -25ºC to -150 ºC, depending on the amount of the ductile NiFe phase. However, these results are for small specimens (B=1.65mm, W=2B). While the results are largely consistent with American Society for Testing and Materials (ASTM) E1921 validity criteria, tests on specimens 3 and 6 times larger and thicker revealed that the 97 wt.% tungsten heavy alloy (WHA) fractured elastically, rather than ductile tearing, but at a $K_{Ic} \approx 4.5$ times higher than for monolithic W. In contrast, all the WHA at lower W experienced ductile tearing, showing little effect of size on K_{Jm}. Room temperature (RT) fracture toughness was also conducted on a 95W-3.5Ni-1.5Cu alloys to understand the effect of the ductile phase properties (Cu vs. Fe) on toughness.

PROGRESS AND STATUS

Introduction

Due to high melting temperature, good conductivity, low sputtering rate and high-temperature strength, W and its alloys, are currently considered the most promising candidates for plasma facing component for future fusion reactor divertor applications [1-4]. This application requires that structural W-based alloys and structures have sufficient fracture toughness to withstand the severe thermal-mechanical environment of a divertor. It is likely that monolithic W is intrinsically too brittle for this task. Previously a series of WNiFe (90, 92.5, 95 and 97 wt.% W with 7:3 = Ni:Fe) heavy metal alloys were shown to have much higher RT toughness (> 10x) and much lower BDTT temperatures (-150 to -25 ºC) than monolithic W (several hundred °C), depending on their ductile phase NiFe content [5-6]. However, these results are for relatively small specimens (thickness, B= 1.65 mm; W= 2B; S= 4W). Though these results are largely consistent with the ASTM E-1921 standard validity criteria due to the high yield strength and elastic moduli of the WHA, however, due to the complex physics of process-zone microcracking toughening, we have conducted toughness test on different size specimens, mostly 3 times larger and thicker for all WHA at RT. We have also conducted test on the 6x larger specimens of a selective alloy (95W-3.5Ni-1.5Fe) to check the size effects. Further, we have repeated these tests on a new alloy composition that contains 1.5Cu, instead of 1.5Fe for 95W WHA, to understand the effect of the ductile phase properties. Microstructural characterization, microhardness and tensile tests, all were also performed on this Cu-reinforced 95WNiCu WHA alloy.

Experimental Procedure

Five commercial (Mi-Tech Metals, Indianapolis, Indiana) liquid-phase sintered (LPS) WHA were received in the form of plates. Out of five, four of the WHAs contained 90, 92.5, 95 and 97 wt. % W with a balance of an initially 70% Ni and 30 %Fe phase, while the other one is 95W-3.5Ni-1.5Cu (wt.%). Other than the difference in size for 3PB bend bars, (which are 3 times ≈ 45x10x5mm, and 6 times ≈ 90x20x10mm larger than the original size), all the specimen preparations, characterization tools and analyzing procedures are same and can be found in references [5-6].

Results

Specimen size effect on RT fracture toughness

We have previously reported microstructural, tensile and fracture toughness (K_{Jm}) properties of small specimens from RT to liquid nitrogen (LN_2) temperature and can be found elsewhere [5-6]. While the RT K_{Jm} tests using specimen's dimensions of 16x3.3x1.65 mm that are nominally valid per ASTM standard E-1921 [6-7]. However, we have tested a limited number of specimens that are 3 and 6 times larger and thicker, dubbed medium (45x10x5mm), and large (90x20x10mm), respectively, and reported here. Note, like the small specimens, these were also fatigue precracked to a nominal a/W = 0.45-0.5 and four specimens have been tested for each alloy category at RT. Normalized for a/W = 0.5, the RT load-displacement (P-d) curves for the medium specimens are shown in Figure 1. Figure 2a shows representative P-d curves for the medium (for all 4 alloys) and large (only for 95WNiFe alloy) specimens, while their respective K_{Jm} values along with small specimens are plotted in Figure 2b and summarized in Table 1. The results of all the medium-sized (B= 5mm) specimens, except 97W, show stable crack growth (see Figure 1). The toughness, K_{Jm}, slightly decreases with increasing W loading up to 95W, however, they are still within the range of standard deviation (see Table 1 and Figure 2b).

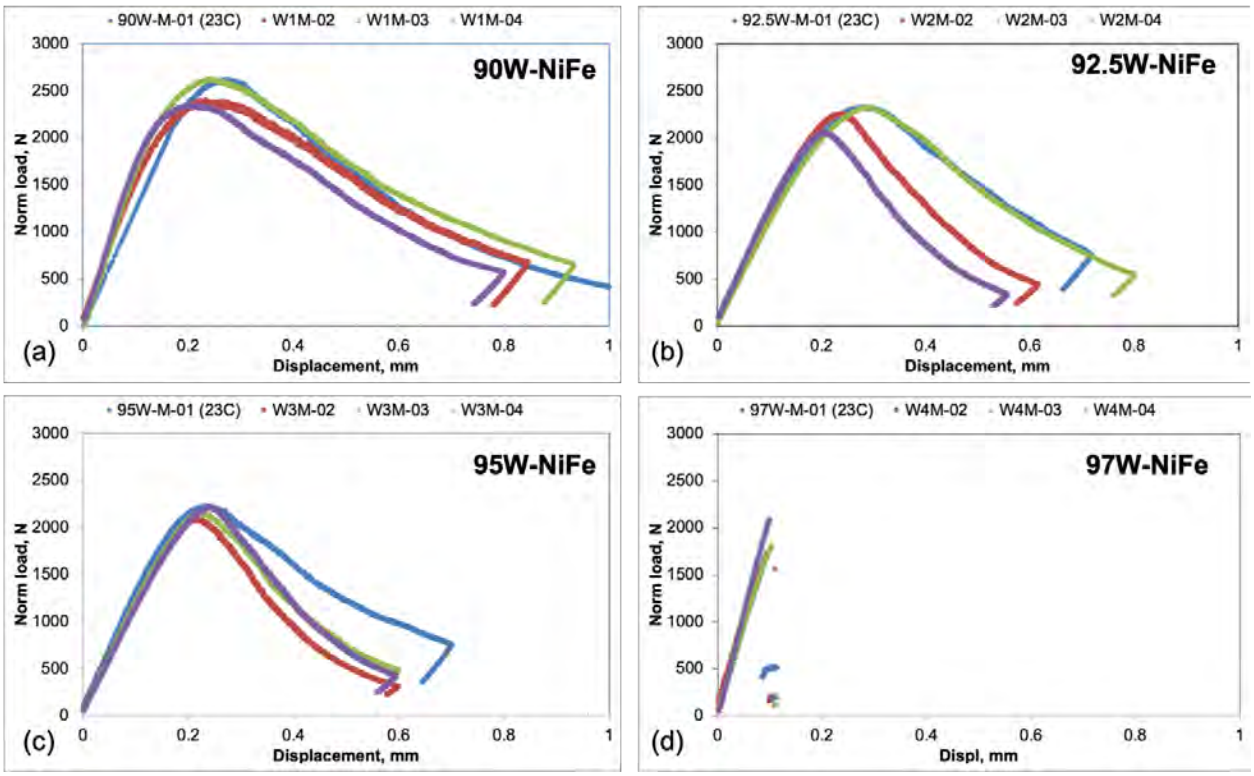

Figure 1. Normalized for a/W = 0.5, RT load-displacement (P-d) curves for medium-sized WNiFe WHA alloys of: (a) 90W; (b) 92.5W; (c) 95W; and, (d) 97W, respectively.

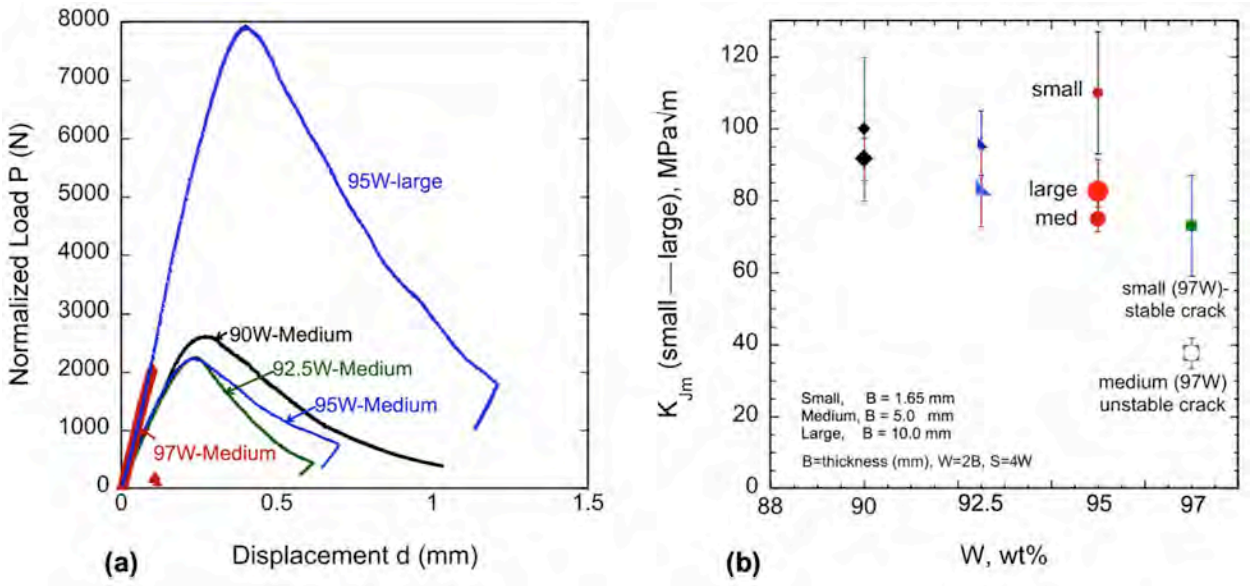

Figure 2. (a) Normalized to a/W=0.5, representative RT P-d curved for the medium and large specimens; and, (b) their K_{Jm} values (MPa√m).

Table 1. The room temperature K_{Jm} for the (90-97)W-NiFe and 95W-NiCu WHAs

Specimen size	K_{Jm} (MPa√m)				
	90W	92.5W	95W-NiFe	95W-NiCu	97W
Small	100 ± 20	96 ± 9	110 ± 17	-	73 ± 13
Med	92 ± 6	84 ± 11	75 ± 4	50 ± 6	38 ± 4
Large	-	-	82 ± 9	45 ± 1	-

Variation in average local fracture modes is minimal for the different size specimens for up to 95W (see Table 2). Unlike small 90-97W specimens (or medium specimens up to 95W), all the medium-sized 97W specimens show unstable crack growth (see Figures1-3 and [5]). The fractions of local fracture modes are also found different for the medium 97W specimens (see Table 2 and Figure 3a,f). While most of the literature, on tensile test data, claims that the higher ductile rupture (DR) and tungsten-cleavage (WC) fractions are better for the tensile ductility; however, our observation found somewhat opposite trend for WC, and similar for DR fraction for the WHA toughness. The highest amount of WC (~57%) was found for medium-sized 97W compared to other three WHA alloys (~5.4%) at RT and is responsible for lower K_{Jm}. Note, WC fraction is also relatively higher for smaller 97W compare to other small-sized WHA alloys (see Table 2). This observation is also consistent with the lower temperature toughness tests, discussed previously [5-6]. Though lower in fraction among all, still DR is one of the most important local modes for WHA ductility. Our observation refers that minimum 5 wt% ductile constituents (~10 area% of NiWFe DP, see Table 1 of [6]) is required to mitigate the strain constraint for larger specimens to stop unstable crack propagation. Lower fraction of DR (0.8%) is found for the medium-sized 97W, might be responsible for the lower K_{Jm}. However, the average K_{Jm} value (38 ± 4 MPa√m) for 97W is still ~ 4 to 5 times higher than the monolithic W toughness (8 ± 4 MPa√m).

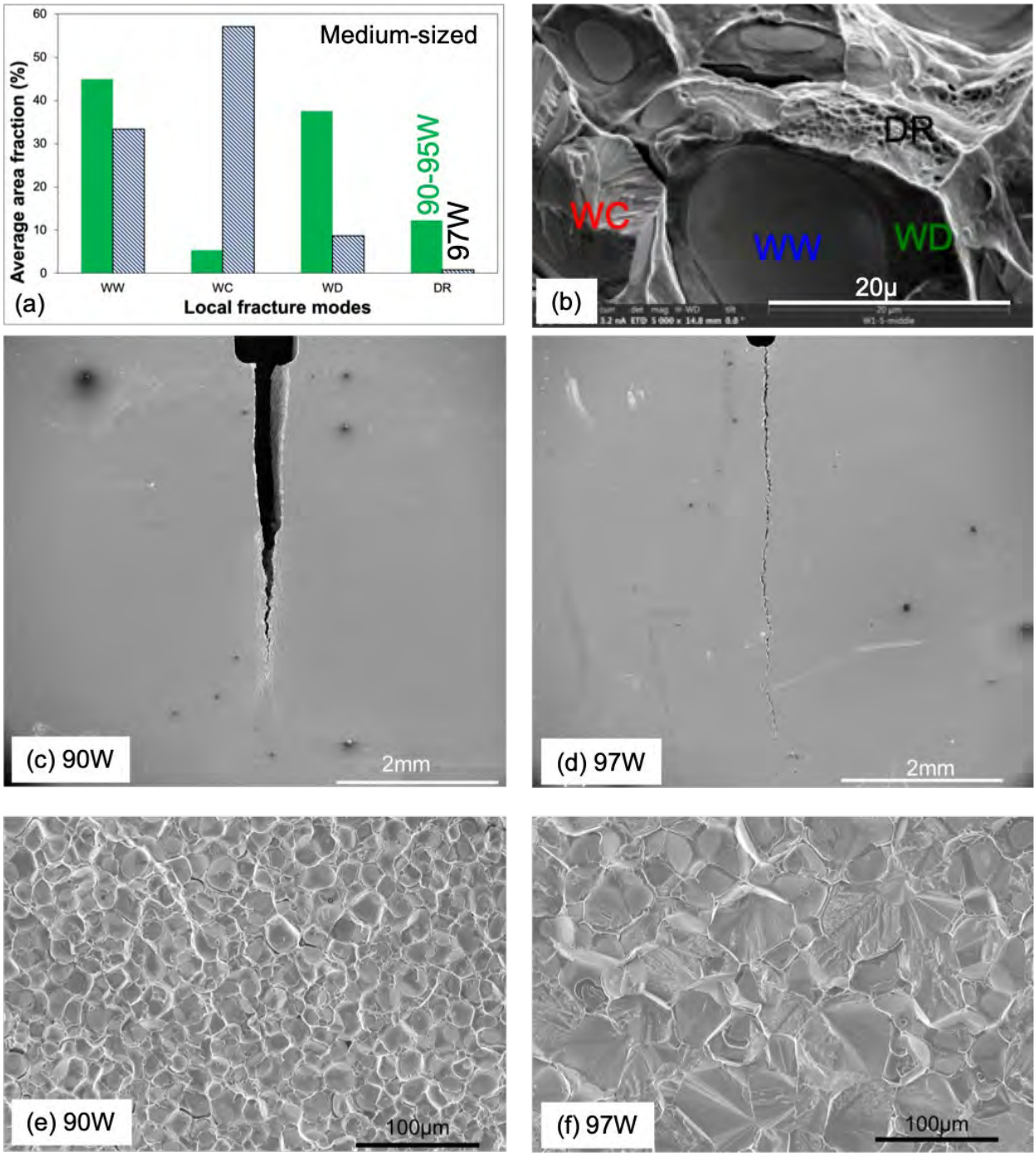

Figure 3. (a) Average local fracture modes for medium-sized specimens; (b) types of fracture modes. Low magnification scanning electron microscopy (SEM) images on side surface showing the stable and unstable crack propagation for the medium-sized RT toughness specimens of: (c) 90W, and (d) 97W alloys, respectively; whereas higher magnification SEM images from the fractured face showing: (e) mix of all local fracture modes for 90W; and (f) WC dominating facture for 97W. Here, WW = W-W separation, WC= W-cleavage, WD= W-DP interface decohesion, DR= ductile rupture.

Table 2. The percentage of local fracture modes from RT toughness fractographs

WHA's	Specimen Size	WW	WC	WD	DR
90W	Small	31.7	12.0	44.1	12.2
	Medium	45.1	3.4	36.2	15.3
92.5W	Small	37.1	10.9	40.5	11.5
	Medium	41.2	4.1	42.4	12.3
95W	Small	42.6	13.5	32.8	11.1
	Medium	48.4	8.6	34.0	9.0
	Large	33.3	6.5	46.9	13.3
97W	Small	67.2	17.6	10.8	4.4
	Medium	33.4	57.1	8.7	0.8

WW = W-W separation, WC= W-cleavage, WD= W-DP interface decohesion, DR= ductile rupture.

To verify the specimen size effect and maximum allowable W% compositions in DP phase to quantify WHA as a structural material, we have precracked (a/W ≈ 0.45-0.5) and tested additional four larger size 95W specimens (B=10mm, W=20mm) at room temperature. Two of the specimens show complete ductile tearing, while other two fractured unstably prior to yielding (see Figure 4a). However, big impurity inclusion (ferrous oxide, ~1000μm x 750μm), verified by energy-dispersive (EDS) point scan and mapping, were found at the crack tip for both cases, which we strongly believe is the main reason for unstable crack propagation, rather than W% or size effect (see Figure 4b-i for more details). However, this type of inclusion is only occupied ~ 0.0082% area of the total inspected surface area for 95W, which incidentally is found at the crack tip. Nevertheless, all four specimens show reasonably similar toughness that averaged ≈ 82 ± 9 MPa√m, and within the standard deviation range in between small and medium-sized 95W toughness. Note, local fracture modes for all ductile tearing 95W are also similar, irrespective of specimen size effect (see Table 2).

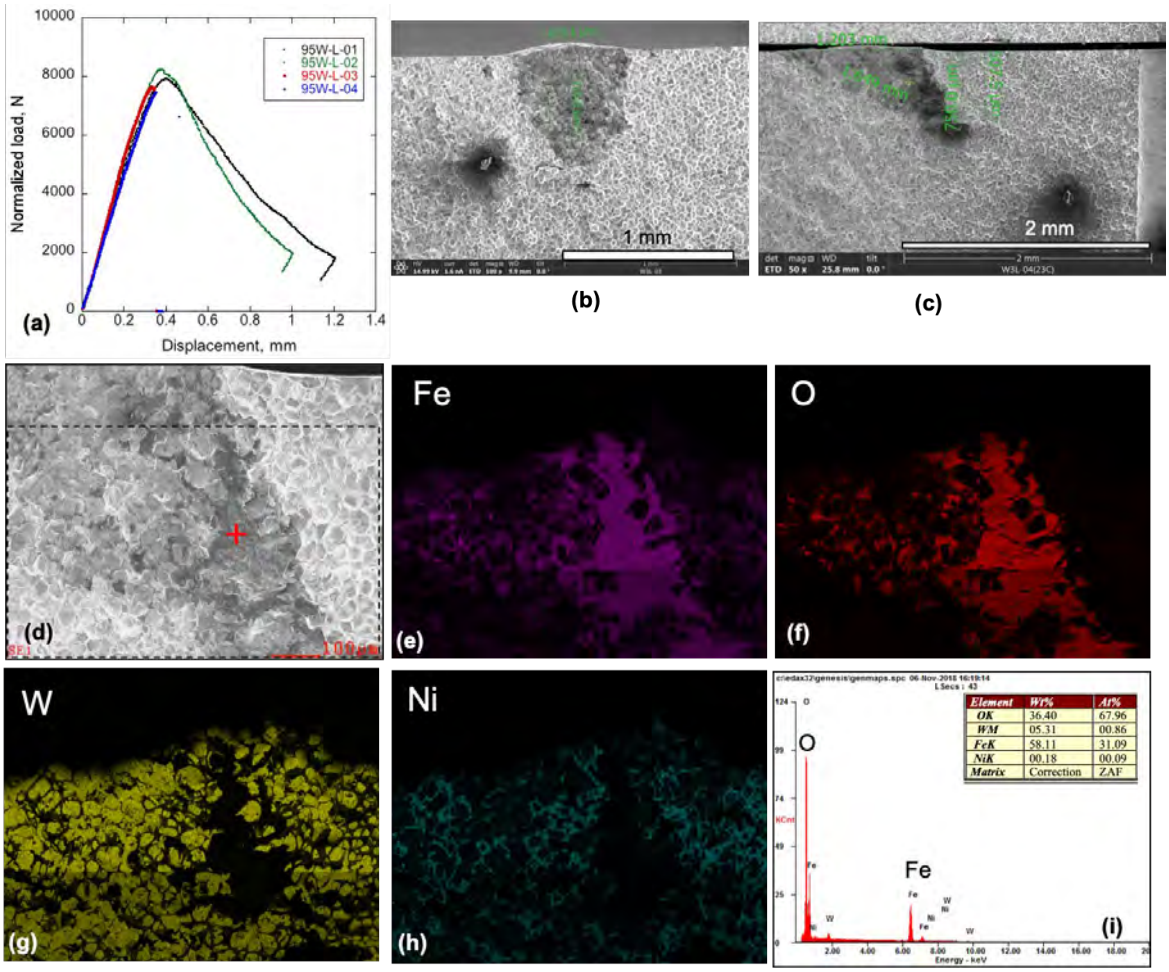

Figure 4. Images showing: (a) RT P-d curves for large 95W (B=10mm) specimens, normalized to a/W=0.5. Two of them show stable and other two show elastic fracture; (b-c) fractured surfaces with oxide inclusions (~1000µmx750µm, relatively larger black area on the top of the fractured surfaces) at the crack tip for the two elastically fractured specimens; and, (d-i) EDS mapping and point scan confirm oxide inclusions.

Damage Mechanisms

Like the smaller RT specimens [6], all the medium and large size specimens except 97W, show fairly similar side surface toughening mechanisms (see Figure 5). The W-particles are cleaved remotely, arrested and blunted by the DP at the process zone for up to 95W. Many individual W particles are widely stressed (see parallel slip lines on W particles), along the principal stress directions before fracture (Figure 5c). However, relatively more micro-cleaved W-particles linkage is observed for medium specimens versus the small specimens, and their numbers increase for higher W loading up to 95W (see Figure 5a-b and references [5-6]). On the other hand, medium-size 97W show no process-zone microcracking (see Figure 5d). Also, the RT toughness slightly decreases with W loading, up to 95%W, might be due to the decrease in NiWFe DP phase and DP thickness to W particle diameter (t/d) ratio for higher W% alloys (see Tables 1 and 1 in Reference [6]). The triaxial constraint is higher for the larger and thicker specimens, and the lower fraction of NiWFe DP affects the effective crack blunting ductility, and dilatation at the crack-tip process-zone, resulting reduced toughness. Indeed, an inadequate amount of DP in the 97W resulting elastic fracture. In this case, like the -196 ºC tests of small specimens, once initiated, the co-planar cracks immediately linked, without affecting the neighbouring W-particles (see Figure 5d, and references [5-6]).

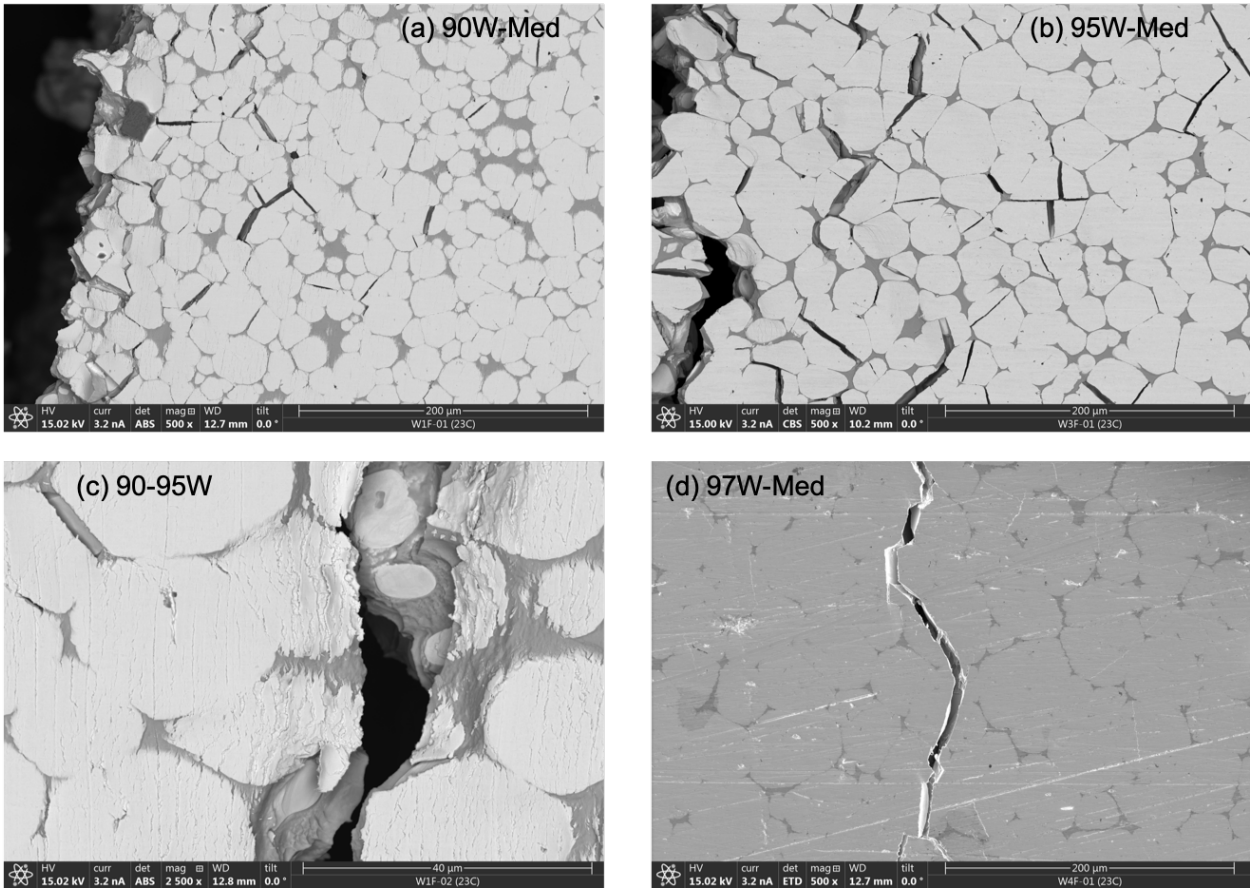

Figure 5. The SEM images showing side-surface damage mechanisms for medium-sized specimens of: (a) 90W; and, (b) 95W alloys, respectively, showing micro-cleaved W-particles observed in the side surface that are arrested and blunted by the DP phase. (c) numerous slip lines in the W-particles, aligned perpendicular to the principal stress direction for the 90 to 95W alloys; and, (d) very sharp crack propagation for medium-sized 97W specimens, without affecting the nearby W-particles.

Larger Impurity Inclusion Effects on the Microstructural and Mechanical Properties

Like WNiFe WHAs, WNiCu are widely used for similar applications. Therefore, we have conducted room temperature fracture toughness test on medium and large specimens on a 95W-3.5Fe-1.5Cu (wt.%) WHA following ASTM standard E-1921. We have also conducted basic microstructural, along with hardness and RT tensile tests. For the simplicity, unless otherwise stated, we now will address these 95W-3.5Ni-1.5Fe and 95W-3.5Ni-1.5Cu alloys as NiFe and NiCu WHA, respectively.

Microstructure

The SEM micrographs of the polished and etched 95W-NiFe and 95W-NiCu plates shown in Figure 6 reveal roughly spheroidal W particles (particle aspect ratio (PAR): 1.1 ± 0.2 for NiFe and 1.3 ± 0.3 for NiCu) surrounded by the interconnected honeycomb web structure of the ductile NiWFe and NiWCu phases, respectively. Multiple EDS X-ray spectroscopy scans show that the particles are close to 100% W in both plates. However, while the NiWFe DP is approximately 50%Ni, 30%W and 20%Fe (wt.%), the NiWCu DP is ~50%Ni, 40%W and 10% Cu (see Table 3 and Figure 7). Figure 6 and Table 3 also show that the W–particles are larger for NiCu WHA than the NiFe WHA (38μm vs 27μm). The W-W contiguity also increases for NiCu WHA, while NiWCu DP area fraction; DP web thickness, t; and t/d; all decreases compared to the NiFe WHA (Table 3). It is also very interesting to note that, while the smaller W-particles (black particles in Figure 6c) are relatively well dispersed in the NiWFe DP phase (white in Figure 6c) in the NiFe WHA, relatively larger W-particles for NiCu WHA are arranged in a cluster-like fashion (minimal white space

between W-particles), and forms pools of DP-phases (larger white area in Figure 6d). That is, there is a heterogeneous distribution of W in DP phase.

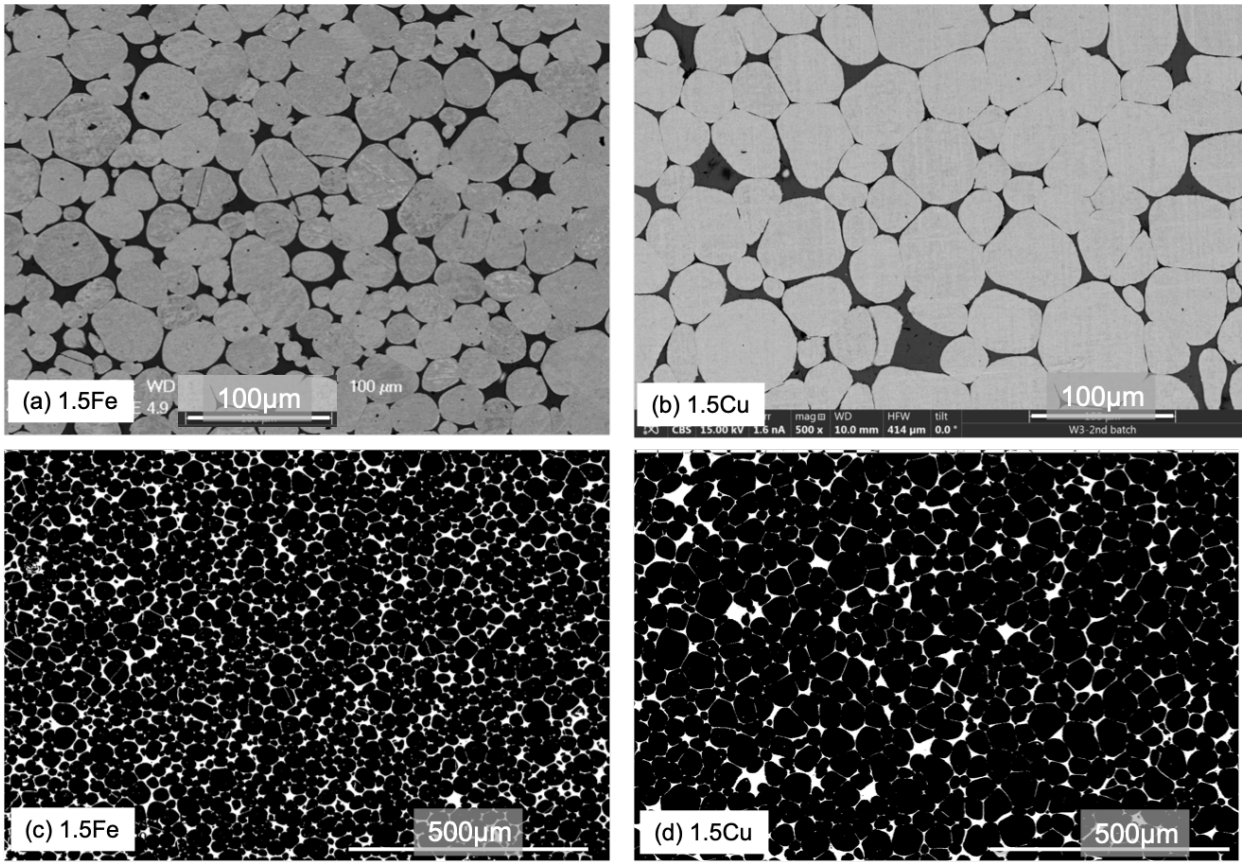

Figure 6. The SEM images of the W particles (gray) and the ductile NiWFe phase (dark) for: (a) NiFe 95W; and (b) NiCu 95W WHA, respectively. The binary black (W) and white (DP) images of: (c) NiFe, and (d) NiCu highlight the NiWFe and NiWCu honeycomb web, respectively. Note, W particles are smaller and relatively uniformly dispersed in the NiWFe DP (Figure c), however, they are relatively larger and form clusters of W (minimal to no white DP between W-particles) and pools of NiWCu DP phases (larger white area) for NiCu WHA (Figure d).

Table 3. The size and contiguity of W-particles, and the composition and morphology of the DP honeycomb web structure for 95W-NiFe and 95W-NiCu alloys

WHA	W particle size, μm	W-W Contiguity, C_w	Ni/W/(Fe or Cu), Wt.%	DP area fraction, %	DP thickness, t, μm	t/d, (μm/μm)
NiFe	27 ± 11	23.3	49/32/19	12.3	5.2	0.14
NiCu	38 ± 16	32.7	51/39/10	8.9	4.1	0.09

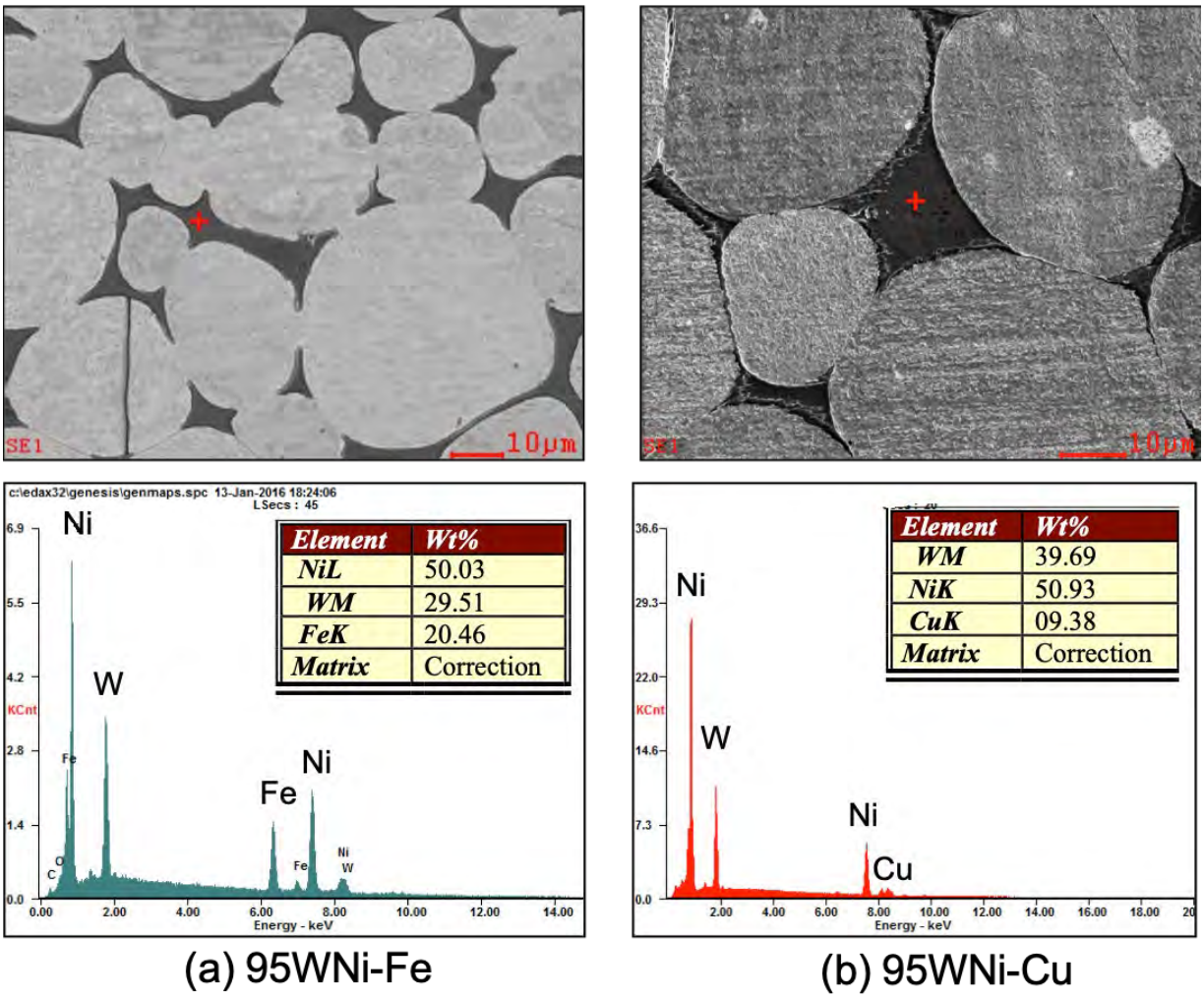

Figure 7. The EDS point scans showing Ni-rich: (a) ~50Ni-30W-20Fe; and, (b) ~ 50Ni-40W-10Cu DP for NiFe and NiCu 95W WHA, respectively.

Microhardness

The RT Vicker's microhardness (H_v) test on both the NiFe and NiCu WHA plates show that there is no to little variation of hardness between them (349 ± 7 kg_f/mm^2 for Fe vs 352 ± 10 kg_f/mm^2 for Cu), even though the particle size is different. Lower area fraction of softer DP phase for NiCu WHA might help to retain hardness level same as NiFe WHA (see Tables 3 and 4).

RT tensile tests

The RT engineering tensile stress-strain (s-e) curves are shown in Figure 8a-b for 95W-NiFe and 95W-NiCu WHA, respectively, and the results are summarized in Table 4. While the 0.2% yield strength (s_y) is relatively similar; however, the ultimate tensile strength (s_u); uniform (e_u); and total elongation (e_t) are much inferior for NiCu 95W than the NiFe 95 WHA (Table 4). Fracture, in all cases, takes place almost immediately after reaching ultimate tensile stress, at low e_u and e_t with virtually no necking.

Table 4. Room temperature mechanical properties of 95W-NiFe and 95W-NiCu WHA

Alloy	Microhardness, H_v, (kg_f/mm^2)	s_y (MPa)	s_u, (MPa)	e_u (%)	e_t (%)	K_{Jm} (MPa√m)
95W-NiFe	352 ± 10	600 ± 15	818 ± 10	7.3 ± 1	8 ± 1	89 ± 19
95W-NiCu	349 ± 7	620 ± 14	642 ± 25	1.0 ± 0.5	1.2 ± 0.5	47 ± 4

The SEM fractographs of RT tensile test on 95W-NiFe and 95W-NiCu WHA alloys are shown in Figure 8c-f. Side-surface observation for NiFe WHA shows micro-cleavage on W particles, infer transfer of load to the neighboring particles via well-bonded W-DP interface (see Figure 8c), whereas almost clean side surface for NiCu WHA indicates poor interfacial bonding between W-particles and NiWCu DP phase (see Figure 8d). These observations are further confirmed by the SEM images taken from the fractured face (Figure 8e-f). The SEM fractograph, shown in Figure 8e for 95W-NiFe WHA, reveals continuous DP network with strong W/DP interface with virtually no pores. The WC, WW and WD, all the dominating local fracture modes are found for NiFe WHA, with fewer DR [5-6]. However, NiCu WHA tensile fractograph reveals discontinuous DP network with poor interfacial bonding between W and DP, leaving many pore-like empty spaces between W particles (see Figure 8f). Local fracture modes are mostly dominated by WW, which is the weakest of all, with much lower WD, and others modes, responsible for lower ductility. These tensile results and fracture surface observations are quite consistent with the many other research groups results on NiCu WHA's [8-11]. However, our results additionally suggest following for reasons for the lower ductility NiCu WHA's: (i) larger W-particle size with lower DP area fraction; (ii) heterogeneous distribution of W-particles in the DP, forms more W-W particle clusters (higher C_w) and DP pools; (iii) poor interfacial bonding between W and NiWCu DP, confirmed by higher magnification (x50,000) SEM scan, not shown here; and, (iv) lower wettability of NiWCu DP, again confirmed by SEM scan (see insert of Figure 8f) that shows a small amount of DP present in-between two closely-spaced W-particles.

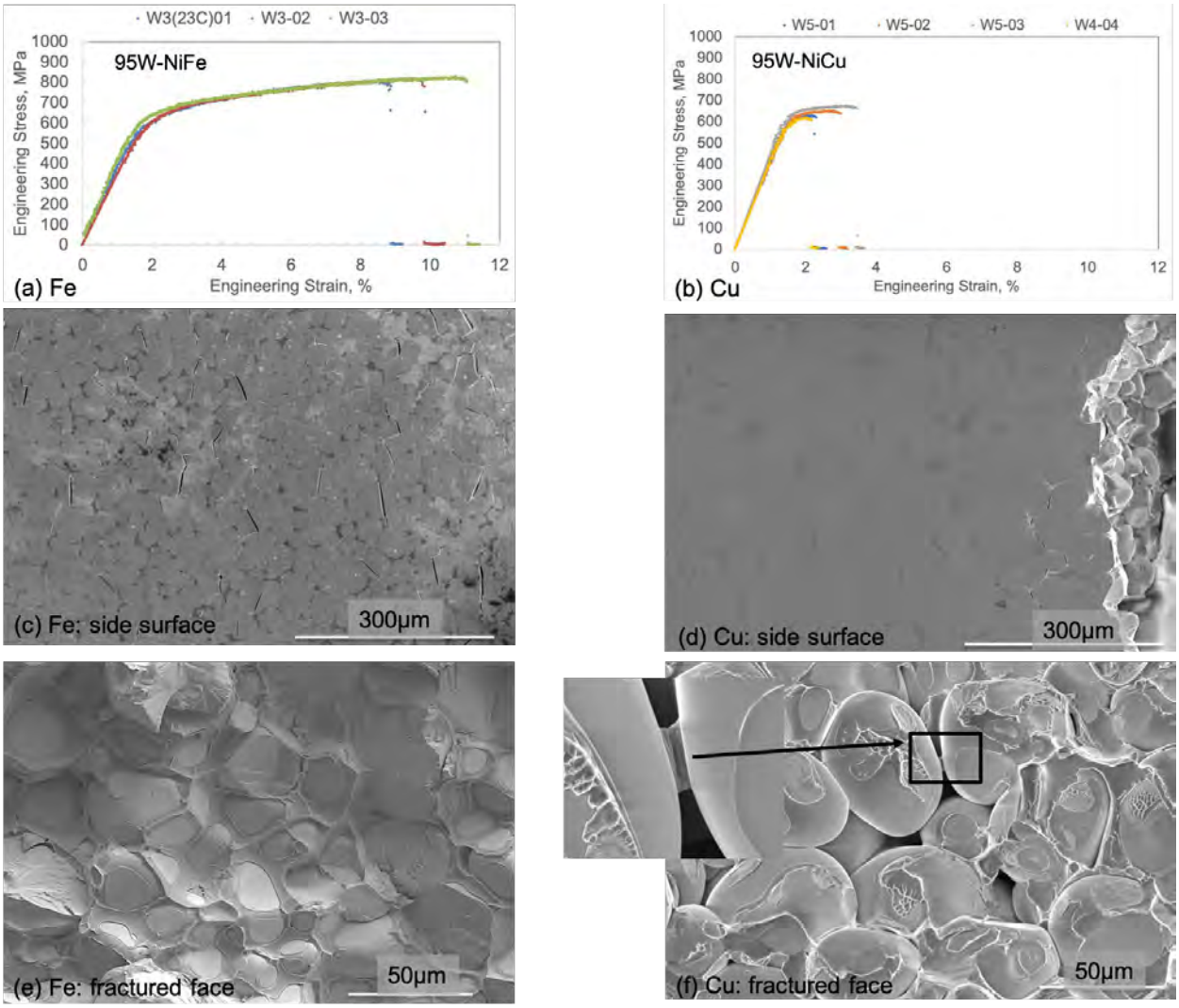

Figure 8. a) and b) RT tensile s-e for 95W-NiFe (left) and 95W-NiCu (right) WHA, respectively; and, tensile loaded side (c, d) and fractured (e,f) are shown for NiFe (left); and NiCu (right) WHA's, respectively.

RT fracture toughness

The RT fracture toughness tests on the medium and large NiCu 95W specimens have been conducted and their P-d curves are compared with NiFe 95W specimens, shown in Figure 9a. Again, all are fatigue precracked and the shown P-d curves are normalized for a/W= 0.5 (Figure 9a). It can be seen from Figure 9a that, for both medium and large specimens, NiCu WHAs experience much lower load before yielding, and post-yield load drop is much sharper than for the NiFe WHA. However, all of them show some stable crack growth. The average RT K_{Jm} for size-specific (Table 1), and size-independent (Table 4) 95W-NiFe and 95W-NiCu specimens are also included. Table 4 shows that the K_{Jm} for NiCu WHA is ~ half to that of NiFe WHA. Figure 9b shows the RT fracture toughness versus the tensile $\sqrt{e_t S_u}$ (scaling the energy needed to fracture tensile specimen) for the 95W-NiFe and NiCu WHA's follow a similar trend line.

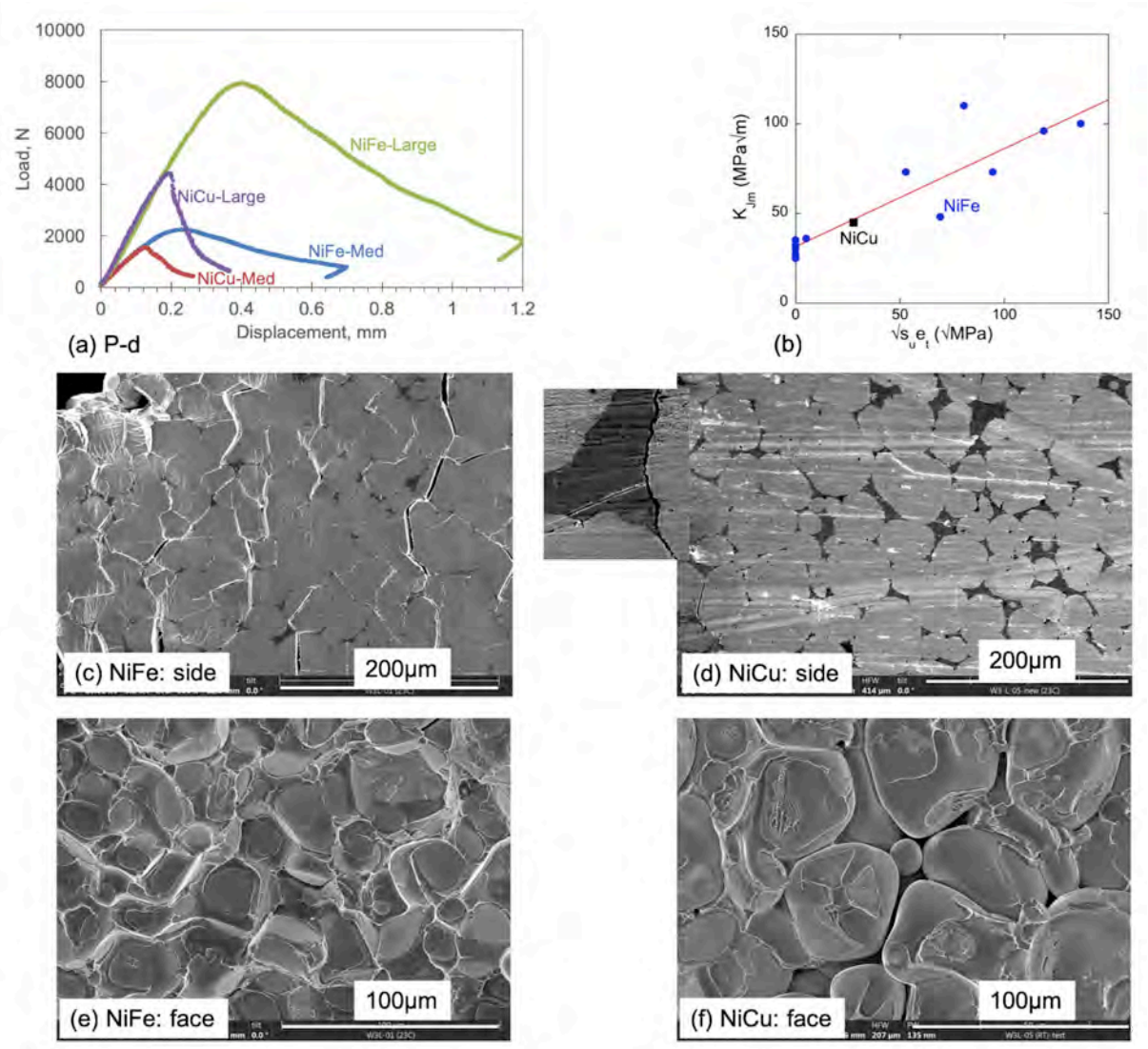

Figure 9. (a) RT P-d curves for the NiFe and NiCu medium and large WHA specimens; (b) fracture toughness vs. $\sqrt{s_u e_u}$; (c) fractured side surface for 95W-NiFe large specimen showing micro-cleavage W particles along with slip lines for deformed W-particles; (d) loaded side surface for the 95W-NiCu large specimens with minimal micro-cleavage and predominant crack propagation through WW and W-DP interface (see insert); (e) presence of all 4 local fracture modes for NiFe WHA; and, (f) the absence of DP between many of the W-particles for a NiCu WHA, respectively.

The side (Figure 9c,d) and face surface (Figure 9e,f) SEM images for the RT toughness tested NiFe- (left column) and NiCu (right column) 95W WHAs are shown in Figure 9c-f. Like RT tensile loaded fracture observation, fracture toughness specimens also reveal almost identical features (see Figures 8 and 9). Similar toughening mechanisms, as observed for the small and medium-size specimens, have also been observed for larger NiFe 95W specimens (i.e. micro-cleavage W particles that are arrested and blunted by DP; slip-lines on W-particles parallel to the crack propagation directions, helps to dissipate strain energy etc.), see details in Figures 5b-c and 9c and reference [6]. In contrast, irrespective of specimen size, NiCu WHA fails to show such strong dilatation toughening mechanism, and shows mostly WW particle separation with very few but sharp micro-cleaved W-particles (see Figure 9d). Like tensile fracture surface, toughness fracture surface for NiCu 95W also shows poor interfacial strength (insert of Figure 9d), pore-like features, lack of wettability/absence of DP between W-particles, discontinuous DP phase etc. (Figure 9f), responsible

for lower yield point, sharp load drops after yielding, and thus lower toughness. Nevertheless, they show somewhat stable crack propagation, even for the larger specimen, further convinced that the presence of ferrous-oxide impurity at the crack tip is only to blame for the unstable crack propagation observed for 2 of the large NiFe 95W specimens, and not to this 95W alloy composition or it's specimen size.

Ongoing and Future Work

- New WHA plates have been ordered and received. More toughness test on the even larger 3PB bars and compact tension specimens will be carried out.
- A controlled environmental set-up is nearly ready for the high temperature (600 to 800ºC) toughness testing.
- A multi-mechanism toughening model will be developed.
- Thermal shock tests will be performed on these WHA's.

Acknowledgement

We would like to acknowledge the support provided by the United States (U.S.) Department of Energy (DOE) through the Office of Fusion Energy Sciences (Pacific Northwest National Laboratory) Tungsten: 8-442520-22403-3 ROF02), and DOE-Fusion (8-442520-22419-3). The U.S. National Science Foundation supported California Nanoscience Institute provided facilities critical the success of this research.

References

[1] M. Rieth, S. L. Dudarev et al., Recent progress in research on tungsten materials for nuclear fusion applications in Europe, J. Nucl. Mater. 432 (2013) 482-500.

[2] P. Norajitra, R. Giniyatulin, W. Krauss, V. Kuznetsov, I. Mazul, I. Ovchinnikov, J. Reiser, M. Rieth, V. Widak, Current status of He-cooled divertor development for DEMO, Fusion Eng. Des. 84 (2009) 1429–1433.

[3] V. Philipps, Tungsten as material for plasma-facing components in fusion devices, J. Nucl. Mater. 415 (2011) S2–S9.

[4] J. Davis, V. Barabash, A. Makhankov, L. Plöchl, K. Slattery, Assessment of tungsten for use in the ITER plasma facing components, J. Nucl. Mater. 258–263 (1998) 308–312.

[5] M.E. Alam, S. Pal, K. Fields, G.R. Odette, Mechanical properties characterization of 90-97wt% WNiFe heavy alloys, DOE Fusion Reactor Materials Program Semiannual Progress Report, DOE/ER-0313/61 (2016) 73-82.

[6] M.E. Alam, G. R. Odette, "On new and remarkably powerful toughening mechanisms in W-NiFe heavy alloys", DOE Fusion Reactor Materials Program Semiannual Progress Report, DOE/ER-0313/64 (2018) 69-80.

[7] ASTM E1921-13a, Standard Test Method for Determination of Reference Temperature, T_o, for Ferritic Steels in the Transition Range, ASTM International, West Conshohocken, PA, 2013.

[8] D. V. Edmonds, P.N. Jones, Interfacial embrittlement in liquid-phase sintered tungsten heavy alloys, Metall. Trans. A. 10 (1979) 289–295.

[9] X. Gong, J. Fan, F. Ding, Tensile mechanical properties and fracture behavior of tungsten heavy alloys at 25-1100 °C, Mater. Sci. Eng. A. 646 (2015) 315–321.

[10] K. Hu, X. Li, X. Ai, S. Qu, Y. Li, Fabrication, characterization, and mechanical properties of 93W-4.9Ni-2.1Fe/95W-2.8Ni-1.2Fe/95W-2.8Ni-1.2Fe-1Al_2O_3 heavy alloy composites, Mater. Sci. Eng. A. 636 (2015) 452–458.

[11] J. Das, G. A. Rao, S.K. Pabi, Microstructure and mechanical properties of tungsten heavy alloys, Mater. Sci. Eng. A. 527 (2010) 7841-7847.

4.2 IN SITU ANALYSIS OF DAMAGE EVOLUTION IN ULTRAFINE GRAINED TUNGSTEN CONTAINING TITANIUM CARBIDE DISPERSOIDS—W.S. Cunningham, J.R. Trelewicz (Stony Brook University), O. El-Atwani, E. Esquivel, B. P. Uberuaga, S.A. Maloy (Los Alamos National Laboratory), M. Li (Argonne National Laboratory)

OBJECTIVE

Grain size refinement and alloying additions are two complementary approaches for enhancing the radiation tolerance of existing nuclear materials. Ultrafine grained tungsten alloyed with small amounts of TiC has been shown to exhibit promising mechanical behaviour and improved resistance to recrystallization embrittlement. The technical aim of this research is to map the radiation tolerance of these alloys through in-situ electron microscopy. To accomplish this objective, damage evolution was quantified under ion irradiation of ultrafine grained tungsten containing 1.1 wt.% of TiC nano-dispersoids.

SUMMARY

Defect evolution and radiation tolerance of ultrafine grained W-TiC alloy thin foils bombarded with 1 MeV Kr^{2+} ions at room temperature and 1073 K are quantified through in-situ transmission electron microscopy (TEM) experiments. A loop Burgers vector analysis confirmed the presence of <100> loops whose population increased at high temperature. Total damage generally scaled with the average loop size, which was higher at 1073 K and attributed to biased vacancy sink behaviour of the TiC dispersoids. By comparison, overall loop and void damage in pure tungsten was larger by a factor of six and two, respectively. The improved irradiation damage resistance in the W-TiC alloy is thus attributed to the effect of dispersoids in 1) the enhancement in annihilating defects and mutual defect recombination due to both dispersoids and a higher grain boundary density, and 2) decreasing the loop mobility, which resulted in shrinkage and annihilation of defect loops.

PROGRESS AND STATUS

The microstructure of the as-received W-TiC (1.1%) consisted of equiaxed grains as observed in the bright-field TEM image in Figure 1a with an average grain size of 290 nm from the distribution shown in Figure 1d. A TiC reflection was evident in the selected area diffraction pattern as was the ring diffraction pattern of tungsten. The vast majority of the TiC particles resided along the grain boundaries though a small fraction were also found within the grains with some clustering evident in Figure 1c. An electron back scatter diffraction (EBSD) analysis produced the grain boundary character map shown in Figure 1b, which indicated a large fraction of the boundaries were high-angle as confirmed in the grain boundary misorientation distribution depicted in Figure 1e. This behaviour is consistent with the high energy ball milling process employed to synthesize the starting powder for hot isostatic pressing. Vicker's microhardness of the sample in the as-received condition averaged 8 GPa; in contrast, a commercially available pure tungsten sample averaged 4.6 GPa, thus demonstrating the significant improvement in mechanical properties realized through the combination of grain refinement and alloying.

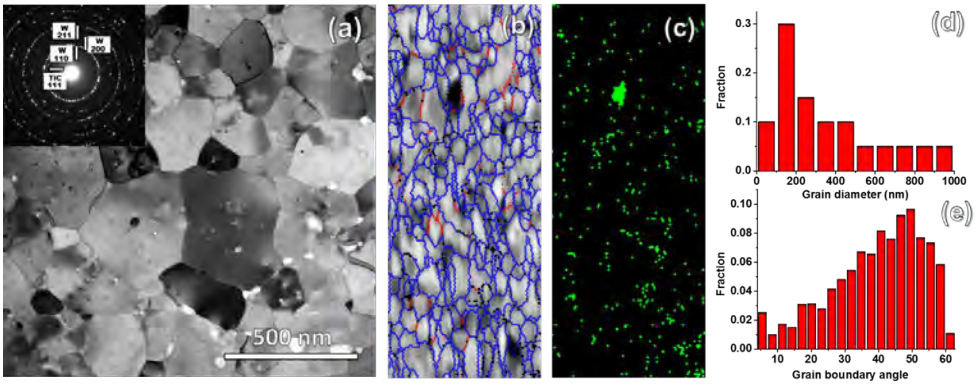

Figure 1. (a) Bright-field micrograph of the W-TiC sample showing TiC dispersoids on the grain boundaries as well as the grain matrices. (b) Grain boundary and (c) TiC phase map produced from an EBSD [001] inverse pole-figure map of the W-TiC sample, and corresponding (d) grain size and (e) grain boundary misorientation distributions.

In-situ irradiation employing 1 MeV Kr^{+2} ions at room temperature (RT) and 1073 K was conducted on the W-TiC sample with loop density, average loop area, and overall damage reported as a function of irradiation dose. Part of the scope of this study was to characterize the Burgers vector of the dislocation loops formed after irradiation and, in addition, estimate the fraction of glissile <111> loops and sessile <100> loops. The analysis was performed on the samples irradiated to 2 dpa at RT and 1073 K. Upon tilting to near the [001] zone axis between the g <200> and <100>, both 1/2<111> (in this study analysed as <111>) and <100> type dislocation loops were visible as demonstrated in Figure 2 for the sample irradiated to 2 dpa at RT. Using the <200> g vector, four variants of the <111> and one of <100> type are expected, while using the <110> g vector, two variants of <111> and <100> type are possible. The average density of the loops present was calculated for each condition and the estimated percentage of <111> loop variants was estimated to be 44% at RT and 32% at 1073 K.

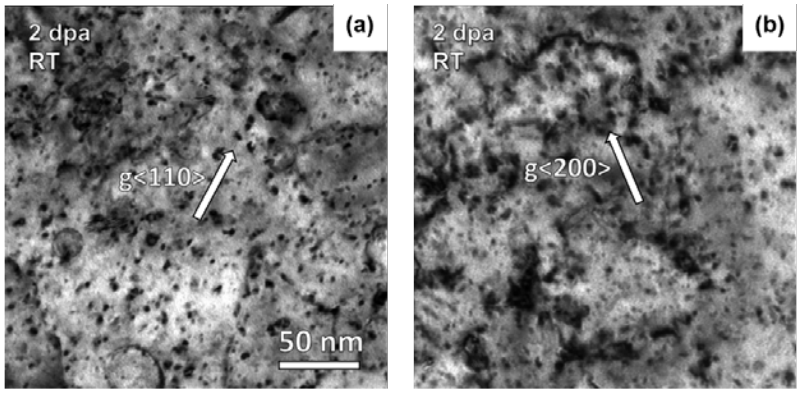

Figure 2. (a) Bright-field 2-beam TEM micrographs using the (a) <110> g vector and (b) <200> g vector for W-TiC irradiated at RT; micrographs have the same scale bar.

For irradiation damage quantification, still images were taken from the in-situ videos from which the average loop density and size (area) were determined for each dose; the product of these quantities were used as an estimate of the total damage. Measurements are quantified as a function of dose in Figure 3. The loop density in the samples irradiated at RT and 1073 K initially increased, reaching a maximum (within the studied dose range) at approximately 0.5 dpa and 0.4 dpa respectively, followed by a slight decrease and eventual plateauing of the loop density. The average area (size) of the loops appeared to cycle up and down with dose at both temperatures, but across all doses (within the confines of the total dose of this

study), the average area of the loops was larger at 1073 K. Consequently, the total damage was also greater across all doses for the sample irradiated at the higher temperature.

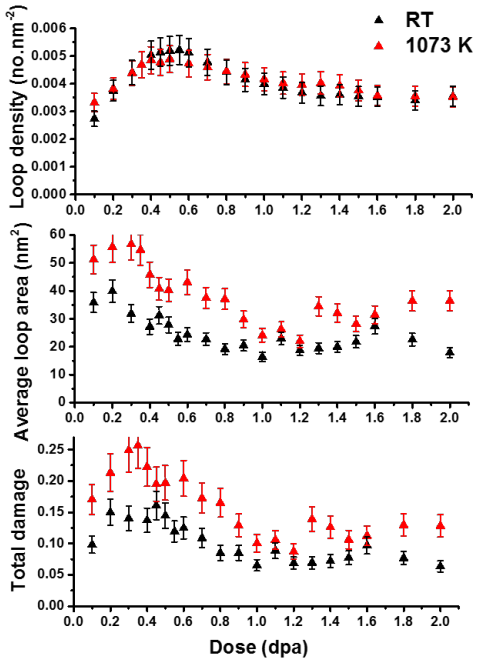

Figure 3. Loop density, area, and total damage as a function of dpa for RT and 1073 K in-situ irradiated W-TiC.

The loop density in Figure 3 was nearly identical for the samples irradiated at both RT and 1073 K, exhibiting an initial increase up to approximately 0.5 dpa and subsequent decrease. It is possible that this behaviour could have resulted from loop coarsening, as previously observed in heavy ion irradiated tungsten and iron[1, 2]. However, the peak in the average loop area at approximately 0.3 dpa and subsequent decrease together indicate that loop coarsening did not account for the decrease in the loop density in this case. The loop area also exhibited an explicit temperature dependence where, as noted above, the loops formed during irradiation at 1073 K were generally larger than those formed at RT. The total damage followed the same trend as the average loop area, suggesting that the loop area governed the behaviour after an initial incubation period in the W-TiC alloy. This indicates that, at high temperature, changes in loop area strongly influenced the irradiation damage mechanism.

Void formation was also observed in the sample irradiated at the elevated temperature of 1073 K as evident in the Fresnel under-focused image shown in Figure 4a. The average void density, average void area and change in volume (swelling determined from visible voids) were determined at the final dose of 2 dpa as the imaging conditions were unfavourable for in situ void quantification. The average void density was measured to be approximately 0.06 nm^{-2} with an average size (area) of 2.8 nm^2, collectively resulting in 0.22% swelling. The TiC dispersoids exhibited much lower damage relative to the surrounding tungsten grains as indicated by the absence of large defect loops and voids in Figure 4b. In addition, no apparent change occurred in the size of the dispersoids during irradiation. However, larger voids (~ 8-16 nm) were observed in the vicinity of the interface between the TiC dispersoids and the tungsten matrix in Figure 4b for bombardment at 1073 K only. In the coarse-grained tungsten sample, the void density, average area, and corresponding change in volume were 0.1 void·nm^{-2}, 3.80 nm^2, and 0.55% respectively, all of which were higher than the W-TiC alloy and indicative of an enhanced resistance to void damage and swelling.

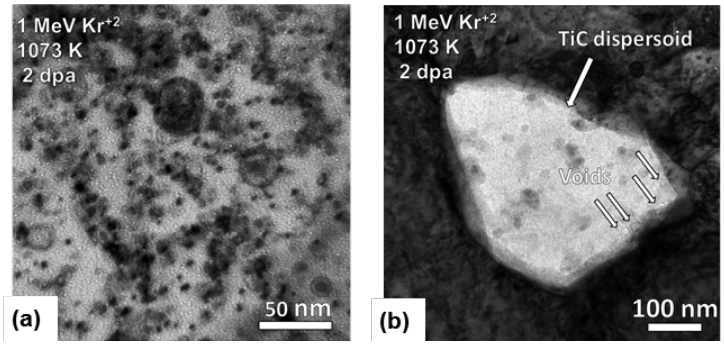

Figure 4: (a) Fresnel (under focused) and (b) bright-field TEM micrographs illustrating void behaviour after 2 dpa at 1073 K in both the tungsten grains and TiC dispersoids. Large voids are evident on the interface between the tungsten matrix and TiC particles as indicated in (b).

While isolating the dominant mechanism for any given condition is challenging due to the convolution of many effects, our in-situ measurements provide useful insights into the underlying physics governing the radiation tolerance of the W-TiC alloy. Based on the consistent loop densities across both irradiation temperatures and the combination of larger loop sizes and prevalence of voids in the dispersoid-matrix interface at 1073 K, the greater total loop damage at 1073 K relative to RT is attributed to enhanced interstitial and vacancy loop growth. Three mechanisms are postulated to contribute to this effect: (1) biased vacancy absorption by the dispersoid-matrix interfaces promoting interstitial loop growth; (2) reduced recombination of vacancies and interstitials promoting simultaneous interstitial and vacancy loop growth; (3) vacancy migration to vacancy loops promoting vacancy loop growth. We note these mechanisms are consistent with the behaviour in nanocomposite oxides where damage accumulation can be enhanced if one type of defect preferentially migrates to different regions of the material[3].

Future Work

With phase boundaries serving as biased vacancy sinks at high temperature, the damage tolerance should be enhanced by increasing the dispersoid-matrix interfacial area. In situ irradiation experiments will be leveraged to explore this effect in samples with different TiC volume fractions.

Acknowledgements

This work was led out of Los Alamos National Laboratory and supported by the U.S. Department of Energy (DOE), Office of Nuclear Energy under DOE Idaho Operations Office Contract DE-AC07- 051D14517 as part of a Nuclear Science User Facilities experiment. Research at Stony Brook University was supported by the DOE through Grant DE-SC0017899.

References

[1.] O. El-Atwani, E. Esquivel, M. Efe, E. Aydogan, Y. Wang, E. Martinez and S. Maloy, *Acta Materialia*, 2018.
[2.] O. El-Atwani, J. Nathaniel, A. Leff, K. Hattar and M. Taheri, *Scientific Reports*, 2017, **7**.
[3.] B. Pedro Uberuaga, E. Martinez, Z. Bi, M. Zhuo, Q. Jia, M. Nastasi, A. Misra and A. Caro, *Materials Research Letters*, 2013, **1**, 193-199.

4.3 THERMAL AND MECHANICAL PROPERTIES OF TUNGSTEN IN THE PHENIX COLLABORATION IRRADIATION—L.M. Garrison, Hsin Wang, Y. Katoh, W. Geringer (Oak Ridge National Laboratory), Takeshi Miyazawa (Tohoku University, Japan), Masafumi Akiyoshi (Radiation Research Center, Japan)

OBJECTIVE

The photon electron new heavy ion experiment (PHENIX) collaboration tungsten irradiation aims to expand the database on neutron irradiation data for tungsten materials.

SUMMARY

The High Flux Isotope Reactor (HFIR) RB*19J capsule included over 20 varieties of tungsten and had three temperature zones, nominally 500, 800, and 1200°C. Hardness tests have been completed on the unirradiated samples and irradiated samples from the 500°C and 800°C sub-capsules and are planned to continue for the highest temperature zone. Tensile tests were completed on the irradiated samples from the 500°C and 800°C sub-capsules, tested at temperatures of 500°C and 700°C respectively. Methods for signal noise control, sample coating, vacuum control, and small sample measurement were developed for the new LFA467HT thermal diffusivity instrument.

PROGRESS AND STATUS

The PHENIX program of the US-Japan collaboration has a goal of investigating tungsten for use in future fusion reactors. For this potential use, more information is needed about tungsten's response to neutron irradiation at fusion relevant conditions. To investigate this, the PHENIX collaboration prepared over 1500 tungsten samples for inclusion in the HFIR RB*19J irradiation capsule, including several varieties of single and polycrystalline tungsten and tungsten alloys. The materials are identified by a unique two symbol code for the RB*19J irradiation, which is also used here for tracking the many material varieties. The listing of material codes and description of the materials was reported previously [1].

Microhardness was measured with a Vickers indenter, 10 second dwell time, and 1000 gf load, giving the results shown in Figure 1. Most materials had a higher microhardness after irradiation in the 800°C sub-capsule than in the 500°C sub-capsule. The 800°C sub-capsule received a slightly higher neutron dose than the 500°C sub-capsule because of the location within the experiment in HFIR. Thus, the higher dose as well as higher temperature may have contributed to the increase in hardness for the 800°C sub-capsule samples. Materials 80, EE, and GE had the highest absolute hardness values. When the hardness is shown as a percentage change (Figure 2), materials 70, TE, and X0 had the largest increase.

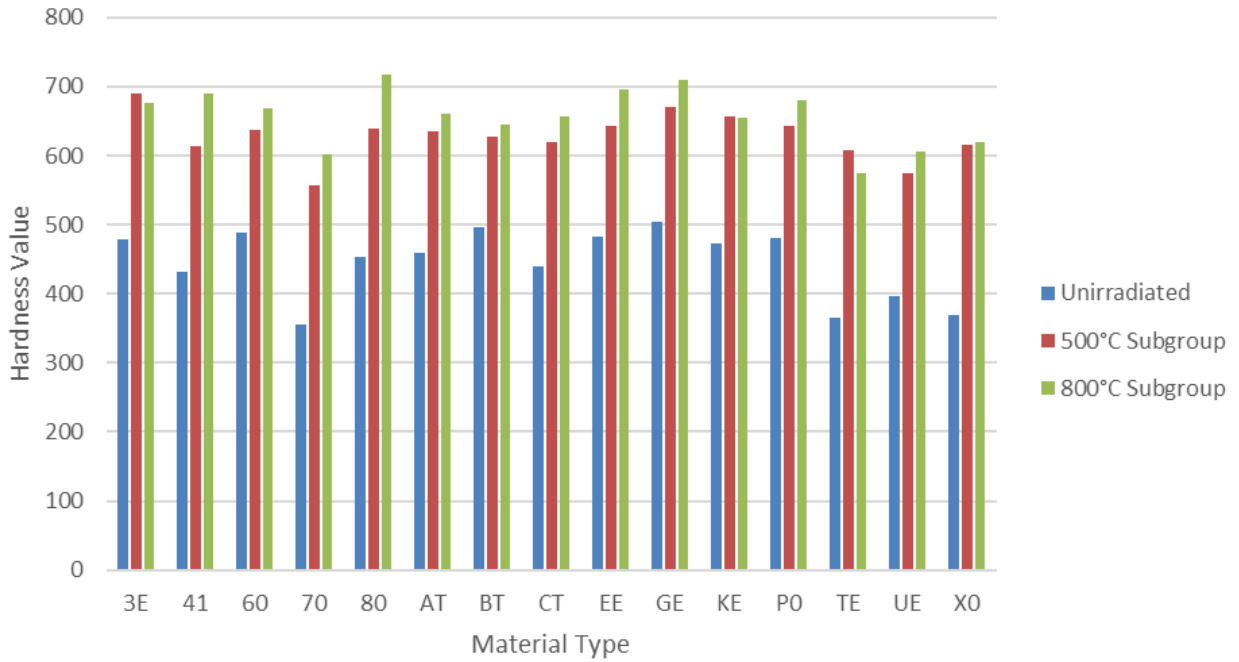

Figure 1. Vickers microhardness values of different tungsten materials irradiated in the RB*19J capsule.

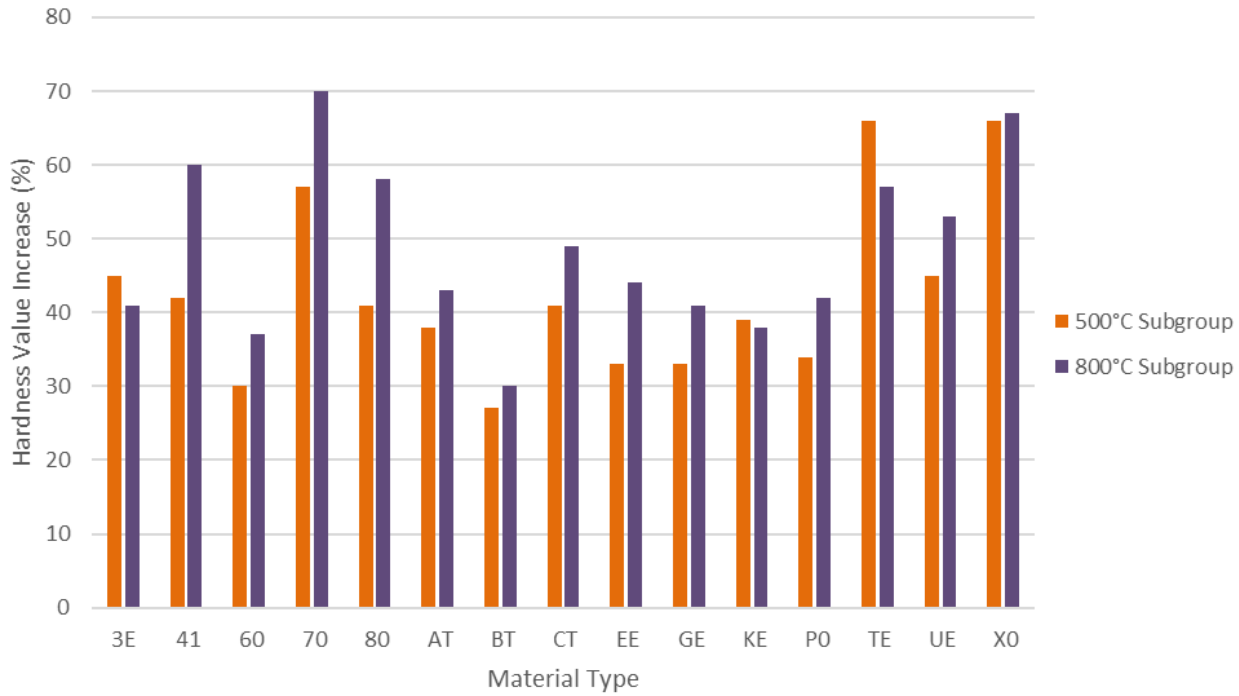

Figure 2. Percentage increase in hardness for tungsten materials irradiated in the RB*19J capsule.

All the tungsten materials included in this irradiation campaign are known to be brittle at room temperature, so tensile tests focused on the elevated temperature behavior of the materials. Materials irradiated in the 500°C and 800°C sub-capsules were tensile tested at temperatures of 500°C and 700°C respectively. A vacuum furnace tensile frame was used, so the crosshead motion was used to as the measure of strain.

The elastic strain (and machine compliance) has been subtracted and only the plastic strain is shown in Figure 3 for the example material AT, which was machined from a thick plate of unalloyed tungsten. The unalloyed tungsten lost significant ductility and was hardened by the irradiation.

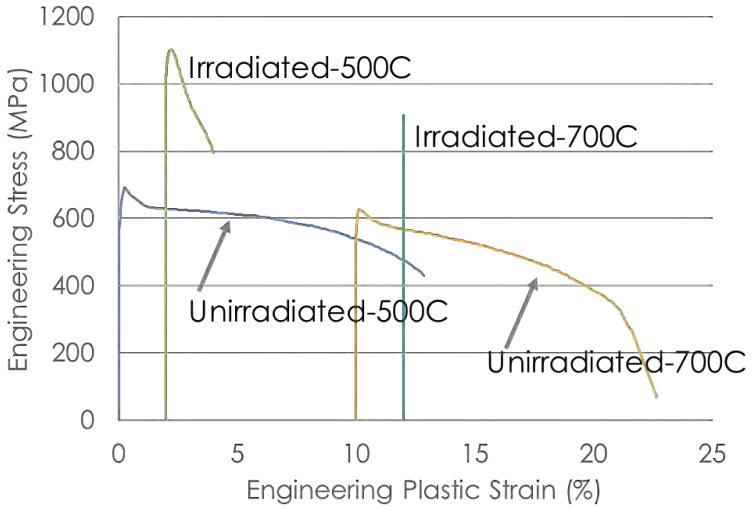

Figure 3. Tensile behavior of thick plate unalloyed tungsten (AT).

The LFA467HT thermal diffusivity instrument has four sample chambers, uses a xenon flash lamp to provide the heat pulse, and has a turbopump-roughing pump vacuum system. Because the pulse width is shorter (0.02 to 1.2 ms), thinner samples can be measured than in the previously used instrument. With the 3D analysis software, samples of different sizes were measured and gave the same thermal diffusivity value, as shown in Figure 4 for the example of SiC samples. The measurement of the PHENIX tungsten samples is more challenging than SiC because W oxidizes starting at ~400°C in a poor vacuum. Additionally, at temperatures above ~800°C, ripples in the measurement signal have been observed and are attributed to the graphite coating leaving the tungsten surface. The graphite coating is necessary so that the surface does not reflect the light flash. Additional calibration tests with the tungsten samples are underway.

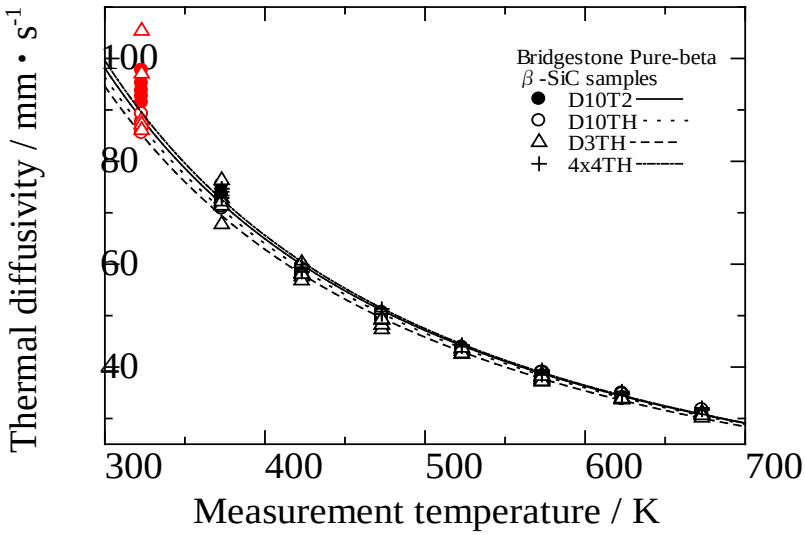

Figure 4. SiC samples of various geometries measured in the LFA467HT thermal diffusivity instrument.

References

[1] L.M. Garrison, Y. Katoh, N. Reid, E. Proehl, M. Fukuda. “MICROSTRUCTURE AND MECHANICAL PROPERTIES OF IRRADIATED PHENIX PROGRAM TUNGSTEN” – pp. 112-124 in Fusion Materials Semiannual Progress Report for the period ending June 30, 2017 (DOE-ER-0313/62)

5. MAGNETIC AND DIAGNOSTIC SYSTEM MATERIALS

No contributions this reporting period.

6. FUSION CORROSION AND COMPATIBILITY SCIENCE

6.1 LIQUID METAL COMPATIBILITY IN STATIC Li, Sn AND Sn-Li—J. Jun and B. A. Pint (Oak Ridge National Laboratory)

OBJECTIVE

The objective of this task is an initial evaluation of the maximum use temperature for structural steel compatibility with liquid Li, Sn and Sn-20Li for plasma wall applications, and to determine if a thermally grown surface oxide can significantly improve compatibility. For this application, Sn and Sn-Li offer much lower vapor pressures than Li but Li is known to be compatible at higher temperatures.

SUMMARY

A few additional 1000 h isothermal capsule experiments were conducted in Sn to better understand the role of alloy composition and pre-oxidation on compatibility at 400° and 500°C. Specimens of model alloys Fe-20Cr showed less mass loss than Fe-5Al but both were higher than commercial FeCrAlMo (alloy APMT). Pre-oxidation of Fe-20Cr improved its Sn compatibility at 400°C, similar to APMT. A pre-oxidized specimen of APMT also showed low mass gain at 500°C. Tensile specimens of APMT from previous capsule experiments showed embrittlement at room temperature after exposures to Sn or Sn-20Li at 400°C without pre-oxidation. Embrittlement was reduced in both environments with pre-oxidation at 1000°C to form α-Al_2O_3. Exposures at 600°C in Li showed no benefit of pre-oxidation.

PROGRESS AND STATUS

Introduction

To identify structural steels compatible with candidate liquid metals (LMs) for plasma facing components (PFC), F82H (Fe-8Cr-2W), a reduced activation ferritic martensitic (RAFM) steel, and Kanthal APMT, an alumina-forming Fe-20Cr-5Al-3Mo alloy, were exposed to static Sn and Sn-20Li (SnLi) at 400°C and Li at 600°C for 1000h [1]. Surprisingly, the APMT specimens with and without pre-oxidation showed much less mass loss than F82H in Sn and SnLi. Preoxidation at 1000°C was extremely effective in minimizing mass loss for APMT in Sn. The exposed APMT specimens included both coupons and 25 mm long tensile specimens, similar to those exposed to Pb-Li [2]. As APMT has more Cr and Al than F82H, another set of experiments was conducted in Sn at 400°C to determine if Cr or Al was more effective at reducing mass loss under these conditions. An Fe-20Cr specimen also was pre-oxidized to determine if a pre-formed Cr_2O_3 surface scale could improve Sn compatibility as well as Al_2O_3. Also, a pre-oxidized APMT specimen was exposed at 500°C to determine if pre-oxidation could enable higher temperature compatibility. The results of the room temperature tensile exposures from the earlier capsule experiments are also presented.

Experimental Procedure

The alloys exposed included Fe-20.3Cr-0.52La, Fe-5.4Al-0.18Hf and commercial alloy APMT (Fe-21.2Cr-4.8Al-2.8Mo-0.47Si-0.21Y-0.17Hf-0.11Zr). Some coupons were pre-oxidized in laboratory air for 2 h, APMT at 1000°C and Fe-20Cr at 800°C. Isothermal capsule experiments were conducted for 1000 h with specimens in inner Mo capsules (25 mm diameter x 75mm long) and outer type 304 stainless steel (SS) capsules to protect the Mo from degradation during the experiment. Shot of 99.999% purity Sn was loaded in an Ar-filled glove box and the specimen was attached to one end of the capsule with Mo wire. Exposures

in SnLi and Li were described previously [1]. The capsules were heated in box furnaces and the capsules were inverted at the end of 1000 h to allow the Sn to drain away from the specimen. After exposure, the pre-oxidized specimens showed no Sn residue. The bare specimens were covered with Sn and were cleaned using liquid Li at 250°C followed by liquid NH_3 to remove the Li. Previous capsule experiments [1] included 25 mm long, SS-3 type APMT tensile specimens. Those specimens were tested at room temperature with a 10^{-3} s^{-1} strain rate.

Results

Figure 1 shows the mass change results of the recent Sn-exposed specimens compared to some of the previous results. Bare specimens all suffered large mass losses at 400°C but all were minor compared to the 368 mg/cm^2 loss of the F82H specimen under the same conditions [1]. In contrast, the pre-oxidized Fe-20Cr and APMT specimens all exhibited much smaller mass changes at 400°C. A pre-oxidized APMT specimen was exposed for 1000 h at 400°C followed by 1000 h at 500°C and exhibited a small mass gain.

From the previous series of capsule experiments in Sn, Li and SnLi, APMT tensile specimens were tested at room temperature after 1000 h exposures. Figures 2 and 3 show the results of bare and pre-oxidized APMT specimens. For comparison, specimens also were annealed for 1000 h at 450°C in air to compare to specimens exposed in the Pb-Li loop [2]. Changes in the post-exposure yield and ultimate tensile strength (YS and UTS) as well as uniform and total plastic elongation (UPE and TPE) can be used to assess performance and detect embrittlement. Bare APMT specimens exposed to Sn and SnLi at 400°C showed a significant loss in ductility and increase in YS and UTS. However, pre-oxidized APMT did not show a similar loss in ductility after exposures to Sn or SnLi. Previously, such a loss was attributed to the formation of α' at temperatures below 500°C [2]. Consistent with that observation, a large ductility loss was observed for specimens annealed at 450°C but only a small ductility loss was noted for the specimens exposed to Li at 600°C. However, the 600°C exposure did result in an increase in YS and UTS, Figure 2.

Further work is in progress to characterize the tensile specimens and the specimens from the most recent capsule experiments.

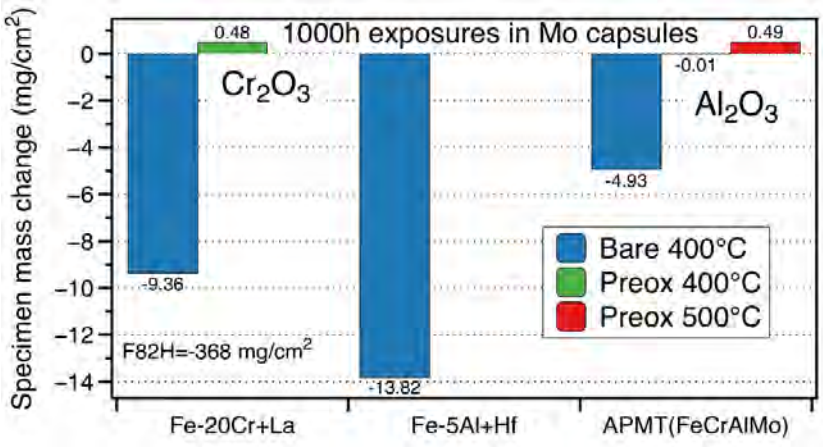

Figure 1. Mass change of tested alloy specimens after static Sn expoures. Fe-20Cr+La and APMT were tested with pre-oxidized and bare (no pre-oxidation) conditions.

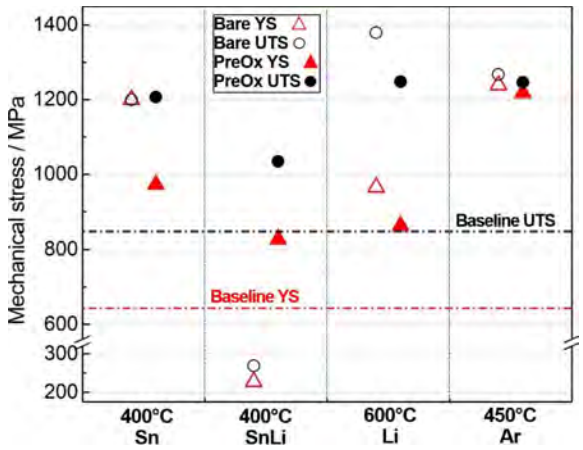

Figure 2. Measured yield and ultimate tensile strengths (YS and UTS) of APMT after liquid metal exposure and Ar annealing. The baseline YS and UTS values were obtained from as-produced bare APMT.

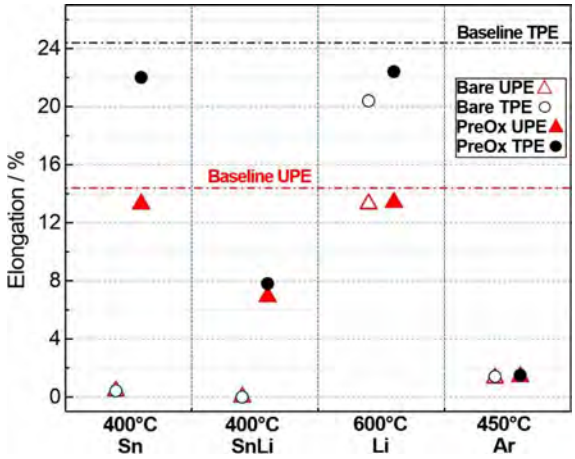

Figure 3. Measured uniform and total plastic elongations (UPE and TPE) of APMT after liquid metal exposure and Ar annealing. The baseline UPE and TPE values were obtained from as-produced bare APMT.

References

[1] B. A. Pint and J. Jun, ORNL/TM-2018/1072 (2018) 55.
[2] S. J. Pawel and K. A. Unocic, J. Nucl. Mater. 492 (2017) 41.

7. MECHANISMS AND ANALYSIS

7.1 MECHANICAL PROPERTIES AND RADIATION EFFECTS IN FUSION MATERIALS—Yury Osetskiy (Oak Ridge National Laboratory)

The purpose of this research is to understand low-level mechanisms of radiation damage and mechanical properties degradation of fusion materials under fusion irradiation conditions. We use molecular dynamics (MD) to study interactions between moving dislocations and materials obstacles important for fusion, including oxide particles, secondary phase precipitates, voids and Helium (He) filled bubbles. A large database of MD results has been accumulated and is now under treatment using theoretical models for materials plasticity. We are investigating a number of effects that include applied strain rate, ambient temperature and dislocation-obstacle interaction geometry. So far we have investigated the effects of obstacle type and strain rate on the dislocation-obstacle interaction mechanisms.

Several effects were observed and studied using large scale MD. Here we present examples of seven nm voids in Fe and Cu and rigid particle in Fe. Stress-strain, τ-ε, dependences, obtained in modeling edge dislocation ½<111>{110} in Fe and ½<110>{111} in Cu intersecting an obstacle through its equator under external applied strain, are presented in Figure 1. Strain rates from $1x10^5s^{-1}$ to $1x10^7s^{-1}$ were applied providing overall dislocation velocity from ~0.24 m/s to ~24 m/s and the ambient temperature was 300 K. Dislocation configurations corresponding to the critical strain are also shown in Figure 1 for each obstacle.

The analysis of the difference in τ-ε curves for different obstacles clarifies the difference in interaction mechanisms. The strong curvature of the dislocation line and the long, >90 nm, dipole of ½<111> screw dislocations can be observed in the case of the rigid obstacle in Fe. Moreover, the τ-ε curve demonstrates a significant softening before the dislocation is released from the obstacle. The intersection mechanism can be described as follows: the dislocation curves around the impenetrable obstacle and creates a screw dislocation dipole. With increasing strain deformation, the dipole is elongated until it annihilates due to screw segment attraction. Due to a high Peierls stress of the ½<111> screw dislocation, annihilation of screw segments is thermally activated and depends strongly on the dipole length. The strong dependence on the strain rate is due to an interplay between screw dislocation segment annihilation and elongation. A large Orowan shear loop, slightly above the inclusion size, is left around the inclusion and a few defects, vacancies and interstitial atoms are formed after the dipole recombination.

In the case of voids in Fe a screw dislocation dipole is also formed but its length is rather short, and the softening effect is much less pronounced. The interaction mechanism here is controlled by a competition between shear and screw segment mobilities. The mobility of screw segments is necessary for their cross-slip and recombination on the void surface rather than in the crystal bulk as observed for the rigid inclusion. As a result of the dipole recombination on the void surface, a large superjog is formed on the dislocation line which is equivalent of a few tens of vacancies absorbed from the void.

No softening was observed in the case of a dissociated ½110>{111} dislocation intersecting a void in Cu. The interaction mechanism here is pure shear without formation of any other defects.

Understanding these mechanisms helps in predicting temperature and strain rate effects in dislocation-obstacle interactions. This work is currently continuing.

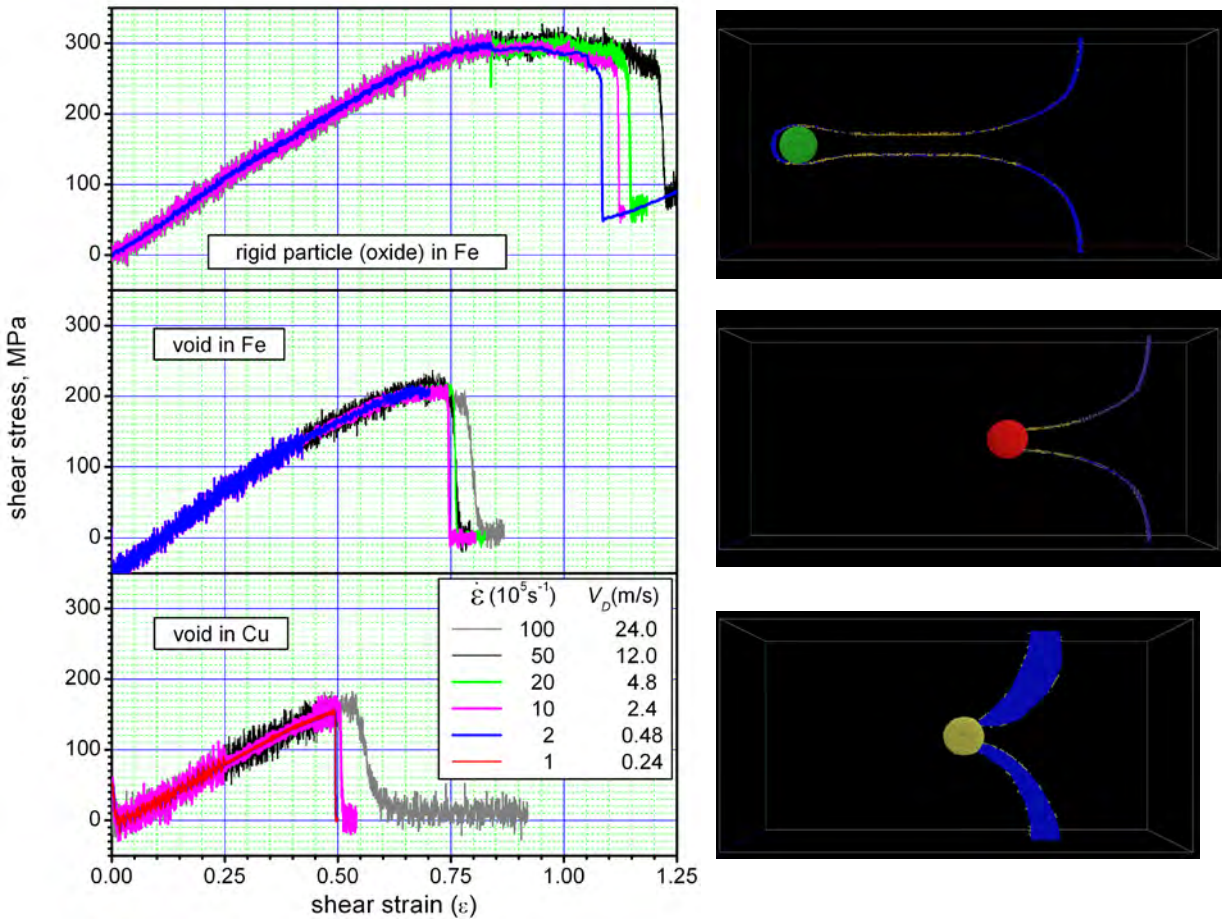

Figure 1. Stress-strain dependences (left) and the corresponding dislocation line shapes at critical strain (right) obtained in modeling ½<111>{110} edge dislocation interacting with rigid inclusion and void in Fe and ½<110>{111} edge dislocation interacting with void in Cu.

7.2 EQUILIBRIUM DISTRIBUTION OF POINT DEFECTS IN SYSTEMS WITH PRECIPITATES - Fe-Y-O AS A REPRESENTATIVE SYSTEM—G. D. Samolyuk, Y. N. Osetsky, (Oak Ridge National Laboratory, Oak Ridge, TN)

A recently proposed thermodynamic approach [1,2] allows estimation of the equilibrium defect distribution in multiphase system by minimizing the free energy of the system using a limited set of defects and microstructural characteristics calculated by DFT. In the current work the approach was extended to take into consideration defects at the interface of the precipitate and matrix. This approach now incorporates radiation induced defects, *i.e.* iron vacancies (V) and self-interstitials (I). Herein the equilibrium distribution of iron vacancies is investigated, as a typical irradiation induced defect. The new approach allows us to investigate the defect concentration as a function of both precipitate volume fraction and size distribution; it also includes specific orientation of the precipitate-matrix interface.

Previously, in the DFT calculations by Brodrick, Hepburn and Ackland [3], it was demonstrated that the ODS particle interface attracts V-defects and provides the defect sink. Initially, the (Y_2O_3+bcc Fe) system with vacancies in both the Y_2O_3 and bcc Fe phases, Y substitutions and O interstitials in Fe, Fe impurities and anti-site defects in Y_2O_3 has been considered [2]. The presence of the interface in this approach has been neglected. It was demonstrated that that the number of defects in both the Y_2O_3 and Fe matrix is very small (Figure 1 from the Reference [2]), guarantying stability of yttria in the Fe matrix.

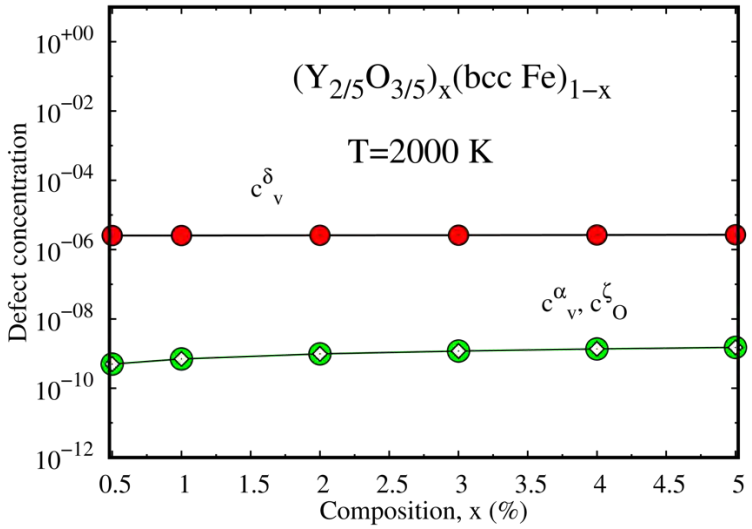

Figure 1. Equilibrium defect concentration in $(Y_{2/5}O_{3/5})_x(\text{bcc Fe})_{1-x}$ compound as a function of yttira fraction at T=2000K, where $\boldsymbol{c_V^{\delta}}$ corresponds to bcc Fe vacancies, $\boldsymbol{c_V^{\alpha}}$ - $\boldsymbol{\alpha}$ (oxygen site in Y_2O_3) site vacancy and $\boldsymbol{c_O^{\zeta}}$ – octahedral oxygen interstitial in bcc F.

The main defect corresponds to thermally activated vacancies in the Fe sublattice ($\boldsymbol{c_V^{\delta}}$). This finding allows us to neglect the rest of the defects and focus on the equilibrium distribution of iron vacancies.

Formalism

The ODS alloy is modeled as a pseudo-binary alloy $(Y_{2/5}O_{3/5})_x(\text{bcc Fe})_{1-x}$, which contains x fraction of yttria in the bcc Fe matrix. In the system of interest, the V-defects are considered as an excitations of the "perfect" (defect free) $(Y_{2/5}O_{3/5})_x(\text{bcc Fe})_{1-x}$, described by the Hamiltonian

$$H' = \sum_{\alpha} (\varepsilon_\alpha - \varphi_\alpha)\hat{n}_\alpha + \frac{1}{2}\sum_{\alpha,\beta} V_{\alpha\beta}\hat{n}_\alpha\hat{n}_\beta\,, \quad (1)$$

where the index α characterizes the iron vacancy position (either one of three layers from the bulk Fe Klim-Fe-O-Y [2] interface or "bulk" Fe), $\hat{n}_\alpha$ occupancy of the position by vacancy (1 or 0), $V_{\alpha\beta}$ is the interaction between vacancies. Using a standard thermodynamic approach, the equilibrium concentration of vacancies, c_α, could be obtained as an extremum of thermodynamic potential, Ω, over external field φ_α

$$c_\alpha = \langle\hat{n}_\alpha\rangle = {}^{\delta\Omega}/_{\delta\varphi_\alpha}\,, \quad (2)$$

where thermodynamic potential is defined as follow

$$\Omega = -T\ln\mathrm{Tr}\exp(-H/T), H = H' - \sum_{\alpha} \mu_{Fe}\hat{n}_{\alpha,Fe}\,, \quad (3)$$

where μ_{Fe} is Fe chemical potential and Tr denotes the sum over all possible configurations. μ_{Fe} is obtained from the requirement to preserve the $(Y_{2/5}O_{3/5})_x$(bcc Fe)$_{1-x}$ composition. In the presence of interactions $V_{\alpha\beta}$ the solution of equation (2) in nontrivial. Below, it is solved mean-field approximation (MFA). The original Hamiltonian (3) in MFA is reduced to the following form

$$H = \sum_{\alpha} (\varepsilon_\alpha - \varphi_\alpha - \mu_{Fe})\hat{n}_\alpha + \sum_{\alpha,\beta} V_{\alpha\beta}\hat{n}_\alpha c_\beta\,. \quad (4)$$

MFA allows obtaining a non-linear equation for vacancy concertation

$$c_\alpha = \frac{1}{Z_\alpha}\exp\left[-\frac{\varepsilon_\alpha - \varphi_\alpha - \mu_{Fe} + \sum_\beta V_{\alpha\beta}c_\beta}{T}\right], \quad (5)$$

where the partition function Z_α is defined as

$$Z_\alpha = 1 + \exp\left[-\frac{\varepsilon_\alpha - \varphi_\alpha - \mu_{Fe} + \sum_\beta V_{\alpha\beta}c_\beta}{T}\right]. \quad (6)$$

In order to preserve the $(Y_{2/5}O_{3/5})_x$(bcc Fe)$_{1-x}$ composition, the possible number of vacancy positions at the interface should be calculated. As was demonstrated, the energetically preferable interface corresponds to Klim-Fe-O-Y [2]. On the bcc Fe sites this interface corresponds to a $[111]$ plane. It can be built by the repetition of rectangles containing two atoms sites, as shown in Figure 2

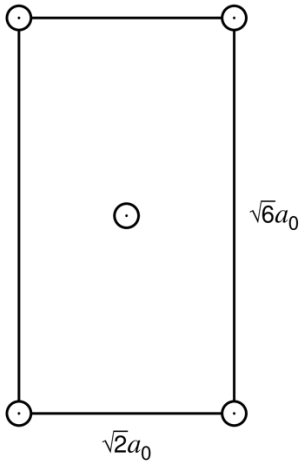

Figure 2. The smallest unit of a $[\mathbf{111}]$ plane cross section in bcc Fe with lattice parameter a_0.

The precipitate shape can be approximated as a cuboid with edges oriented as a $< 111 >$ planes of size $R \times R$. In this approach the number of possible vacancy positions at the interface in the first Fe plane is

$$n_1 = 6\frac{R^2}{\sqrt{2}a_0\sqrt{6}a_0}2 = 2\sqrt{3}\left(\frac{R}{a_0}\right)^2 = 2\sqrt{3}N_R^2 \quad (7)$$

If there are *m* precipitates with size *R* in the sample containing N^3 elementary cubes with two lattice sites (bcc lattice) the total number of available Fe lattice positions is $2N^3 - 2mR^3$. In this expression the number of precipitates could be expressed through composition, x,

$$x = m\frac{2N_R^3}{2N^3}. \quad (8)$$

From expressions (7) and (8) the number of Fe atoms in the sample can be obtained as

$$N_{Fe} = 2N^3(1-x) + N_V, \quad (9)$$

where N_V is number of iron vacancies. It's equal to the vacancy concentration multiplied by the number of possible vacancy positions at the interface and in the bulk, i.e.

$N_{Fe} = 2N^3(1-x) - 2\sqrt{3}N_R^2 m c_V^i - \left[2N^3(1-x) - 2\sqrt{3}N_R^2 m\right]c_V^b = 2N^3(1-x) - N_{Fe},$

where c_V^i is vacancy concentration at the interface, c_V^b is vacancy contribution in the bulk iron and N_{Fe} is total number of iron vacancies. Using Eq. (8) the last equation could be reduced to

$$\sqrt{3}\frac{x}{1-x}\frac{1}{N_R}c_V^i + \left(1 - \sqrt{3}\frac{x}{1-x}\frac{1}{N_R}\right)c_V^b = \langle c_V \rangle, \quad (10)$$

where $\langle c_V \rangle$ is averaged number of vacancies in the system.

.

Conclusions

The general thermodynamic approach to the calculation of the equilibrium distribution of defects in a nonuniform system with interfaces has been developed. It was then applied to the case of ODS Y_2O_3-Fe alloys. This then demonstrated that due to the large defect formation energies the ODS particles are extremely stable and the main defect correspond to Fe vacancies. Fe vacancies predominantly occupy the interface.

References

[1.] G.D, Samolyuk, B. Újfalussy and G.M. Stocks, "The distribution alloying elements in alnico 8 and 9 magnets: Site preference of ternary Ti, Fe, Co, and Ni additions in DO_3 Fe_3Al, Co_3Al, and Ni_3Al based intermetallic phases", J. Appl. Phys. 116 (2014) 173908.

[2.] G.D. Samolyuk and Y.N. Osetsky, "Thermodynamic approach to the stability of multi-phase systems: application to the Y_2O_3–Fe system", J. Phys.: Cond. Matter, 37 (2015) 305001 (9pp).

[3.] J. Brodrick, D.J. Hepburn, G.J. Ackland, "Mechanism for radiation damage resistance in yttrium oxide dispersion strengthened steels", J. Nucl. Matter. 445 (2014) 291-297.

7.3 A COUPLED RATE THEORY-MONTE CARLO MODEL OF HELIUM BUBBLE EVOLUTION IN PLASMA-FACING MICRO-ENGINEERED TUNGSTEN—Edward Gao, Nasr M. Ghoniem (University of California, Los Angeles)

This is an extended abstract of a paper published in Journal of Nuclear Materials (E Gao, NM Ghoniem, "A coupled rate theory-Monte Carlo model of helium bubble evolution in plasma-facing micro-engineered tungsten," Journal of Nuclear Materials 509 (2018) 577-590)

A multiscale model of helium bubble evolution in plasma-facing materials is developed. The model links different stages of helium bubble evolution: deposition, nucleation, growth, motion, and coalescence. Helium deposition is simulated with the Stopping and Ranges of Ions in Matter (SRIM) Monte Carlo program to give spatial information on helium and displacement damage distributions near the surface. This deposition profile is then introduced into a space-dependent rate theory of bubble nucleation and growth to describe the early stages of the distribution and size of helium bubbles. The coarsening stage of bubble evolution as a result of whole bubble motion, interaction, and coalescence is modeled by a new Object Kinetic Monte Carlo (OKMC) model, for which initial conditions are taken from the mean-field rate theory calculations. The model is compared to experimental data on low-energy helium plasma interaction with micro-engineered tungsten (W), and on high-energy helium ion deposition in flat W samples. The novel features of the multiscale model are: (1) space-dependent rate theory; (2) OKMC model of bubble motion in stress and temperature fields; and (3) application of the model to micro-engineered materials, and comparison with experiments on the same time-scale. At low helium ion energy, it is found that the mechanism of trap mutation is essential in achieving good agreement with experimental measurements. On the other hand, good agreement with experiments at high incident ion energy and temperature showed the importance of bubble coalescence and coarsening as main mechanisms. The results of the model are compared with experiments on flat W surfaces irradiated at high ion energy (30 keV), and with micro-engineered W, where the surface is coated with high-density micro-pillars at low ion energy (around 100 eV). The predicted average bubble radius and density are in qualitative agreement with experimental results.

We simulated these events in an OKMC model that is coupled with the rate theory of bubble nucleation and growth. A sketch of the various physical processes that are included in the multiscale model is shown in Figure 1. A flowchart of the entire components of the multiscale model is shown in Figure 1, where the implantation phase is simulated with the SRIM binary collision Monte Carlo code [1], the nucleation/growth stage is modeled with an extension of the mean-field rate theory [2, 3], and finally the coalescence and motion stage is modeled with a new OKMC code that we developed specifically for plasma-implanted helium, following our own earlier work [4, 5]. A sketch of the multiscale model is shown in Figure (2), and details can be found in our recent publication [6].

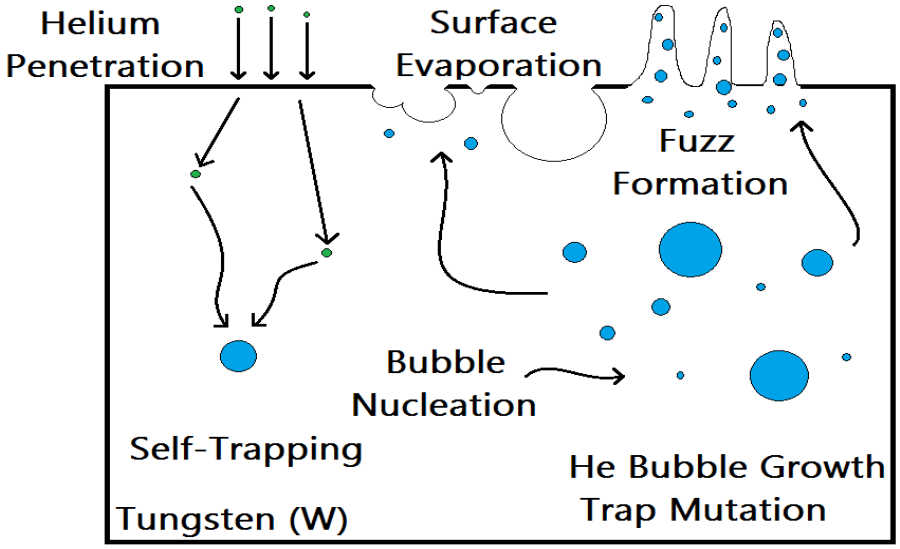

Figure 1. Overview of bubble evolution as helium (green) ions penetrates the tungsten surface to form subsurface gas bubbles (blue) due to trapping effects that eventually return to the surface as micro-scale perforations and tendrils (fuzz).

The developed multiscale framework for the simulation of helium bubbles in plasma-irradiated W was able to capture the entire evolution process over experimental time scales (e.g. 30 minutes for 100 eV helium ion irradiation on angled tungsten surfaces). Past modeling attempts, such as molecular dynamics, cluster dynamics, and Monte Carlo have been limited to modeling either incubation, nucleation, or growth of these helium bubbles, but not the entire process. By applying the multiscale approach, we were able to simulate the behavior of subsurface bubbles in tungsten.

Application of the multiscale model to low-energy helium ion irradiation of micro-engineered W, where the sample surface is covered with a dense forest of W micro-pillars revealed the important effects of ion incidence angle on bubble evolution. It is found that at steep angles of ion incidence (near grazing), the backscattering coefficient becomes so large, and the implantation depth so shallow that virtually no bubbles form near the surface. This is consistent with our experimental observations of the lack of bubbles or fuzz on the sides of cylindrical pillars exposed to low-energy plasma. The predicted average bubble radius is found to be within 26.0% - 44.2% of experimental observations, and the concentration is on the same order of magnitude. Furthermore, the model shows that the mechanism of trap-mutation is the main controlling factor in bubble growth during low energy helium exposure.

At high helium ion energy (e.g. 30 keV), the mechanism of trap-mutation ceases to be important because of the abundance of vacancies produced by collision cascades. The average bubble radius was found to be close to experimental data at three different temperature and fluence; the difference being in the range 2.8% to 9.8%. However, the bubble concentrations are over-estimated by 36.6% - 61.0%. It is confirmed that at high-energy and at temperatures above 1000 K, the key mechanism of bubble growth is by coalescence. The coalescence process is modeled by an elastic interaction that drives nearby bubbles to move towards one another to reduce energy. Large bubbles resulting from coalescence are found to be in thermodynamic equilibrium achieved between the internal pressure and the surface tension. The closeness of such large bubbles to the surface results in the porous structure that is experimentally observed.

References

[1] J. F. Ziegler, M. D. Ziegler, J. P. Biersack, Srim–the stopping and range of ions in matter (2010), Nuclear Instruments and Methods in Physics Research Section B: Beam Interactions with Materials and Atoms 268 (11-12) (2010) 1818–1823.

[2] N. M. Ghoniem, J. N. Alhajji, D. Kaletta, The effect of helium clustering on its transport to grain boundaries, Journal of Nuclear Materials 136 (2-3) (1985) 192–206.

[3] N. Ghoniem, Nucleation and growth theory of cavity evolution under conditions of cascade damage and high helium generation, Journal of nuclear materials 174 (2-3) (1990) 168–177. [4] S. [4] Sharafat, A. Takahashi, K. Nagasawa, N. Ghoniem, A description of stress driven bubble growth of helium implanted tungsten, Journal of Nuclear Materials 389 (2) (2009) 203–212.

[5] A. Takahashi, S. Sharafat, K. Nagasawa, N. Ghoniem, Kinetic monte Carlo simulation of helium-bubble evolution in ODS steels, in: Effects of Radiation on Nuclear Materials and the Nuclear Fuel Cycle: 24th Volume, ASTM International, 2010.

[6] E Gao, NM Ghoniem, “A coupled rate theory-Monte Carlo model of helium bubble evolution in plasma-facing micro-engineered tungsten,” *Journal of Nuclear Materials* **509**, 577-590, 2018.

7.4 BUBBLE FORMATION IN HELIUM-IMPLANTED NANOSTRUCTURED 14YWT AND CNA FERRITIC ALLOYS AT ELEVATED TEMPERATURES—Yan-Ru Lin, Steven J. Zinkle (University of Tennessee, Knoxville) David T. Hoelzer, Lizhen Tan (Oak Ridge National Laboratory)

OBJECTIVE

The objective of this task is to study the cavity size and density in several Helium (He) implanted nanostructured materials with different starting dispersoid sink strengths. The He in irradiated materials can cause low temperature hardening, void swelling and high temperature grain boundary embrittlement. These effects may be mitigated by increasing the nanocluster number density as He trapping sites to control the bubble size or to shield He from the grain boundaries.

SUMMARY

Cavity formation was examined in a series of materials ranging from pure Ni to complex alloys containing high dispersoid number densities following He implantation to ~7000 appm at 500 and 700°C. Electron energy loss spectroscopy (EELS) was used to characterize the size and density of nanoparticles in 14YWT and cast nanostructured ferritic alloy (CNA) materials. The He bubbles were found in pure Ni implanted at 500 and 700°C. However, no bubbles were found in the He implanted 14YWT and the CNA3 alloy at 500°C and 700°C.

PROGRESS AND STATUS

The 275 keV He ions were used to irradiate Ni, 14YWT-SM10 alloy [1] and CNA3 [2] alloy at 500 and 700°C with the fluence of 1.28 x 10^{20} m^{-2}. The chemical compositions of the two alloys are listed in Figure 1. The peak radiation damage and He concentration were roughly 0.3 dpa and 7000 appm, respectively. The Stopping and Range of Ions in Matter (SRIM) simulation results of both materials are shown in Figure 1. The orange curve shows the dpa (displacement per atom) profile, while the green curve is the implanted He atom concentration.

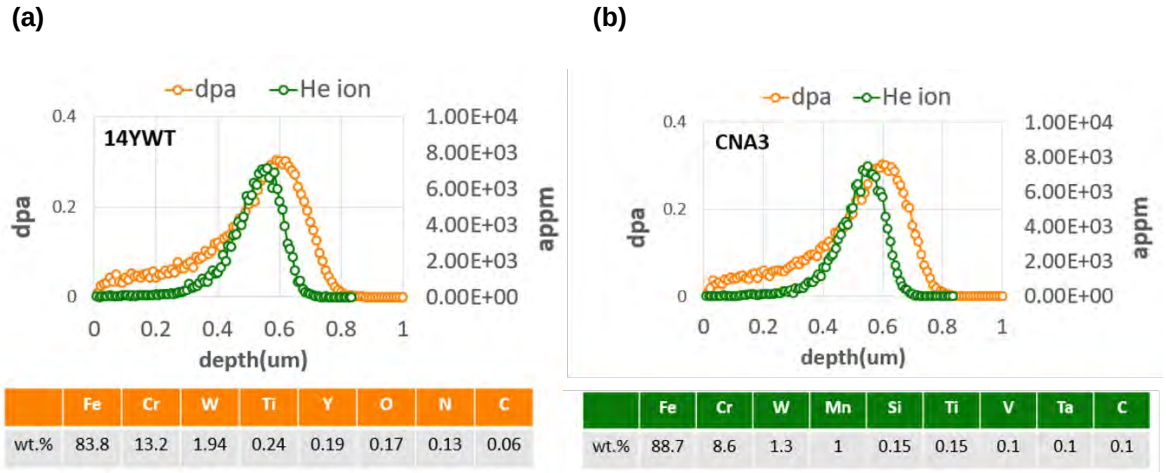

	Fe	Cr	W	Ti	Y	O	N	C
wt.%	83.8	13.2	1.94	0.24	0.19	0.17	0.13	0.06

	Fe	Cr	W	Mn	Si	Ti	V	Ta	C
wt.%	88.7	8.6	1.3	1	0.15	0.15	0.1	0.1	0.1

Figure 1. The ion concentration and dose with depth profile of (a) 14YWT and (b) CNA3.

Based on the transmission electron microscopy (TEM) EELS results **(**Figure 2.), the nanoclusters in 14YWT were mainly enriched in titanium, yttrium and oxygen. The density and diameter of the 14YWT nanoclusters were 1.12 x 10^{23} m^{-3} and 2.42 nm, respectively. In addition, other Ti-Ni-O rich precipitates were also observed with diameter ~10nm, as showed in Figure 3. In Figure 3, a chromium-enriched shell was observed around a nanocluster.

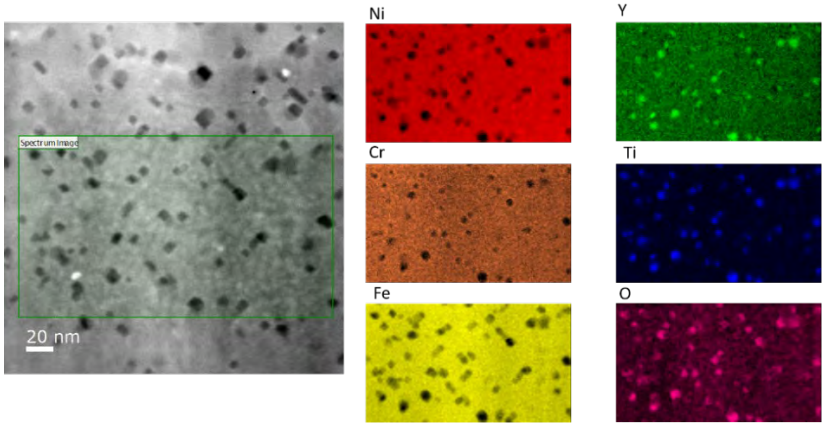

Figure 2. EELS results of 14YWT.

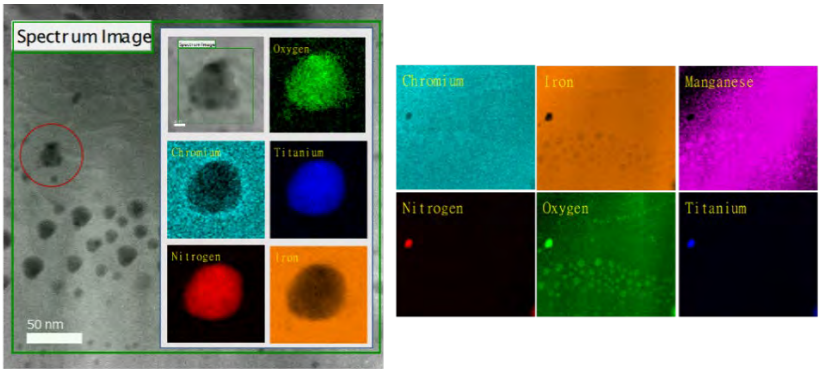

Figure 3. Ti-Ni-O rich precipitate in 14YWT.

For the TEM image (Figure 4.) of CNA3 materials, the density and diameter of the nanoclusters were 1.08 x 10^{23} m^{-3} and 4.68 nm, respectively. The nanoclusters in CNA3 are mostly TaC and MX precipitates (M: Ta/V, X: C/N).

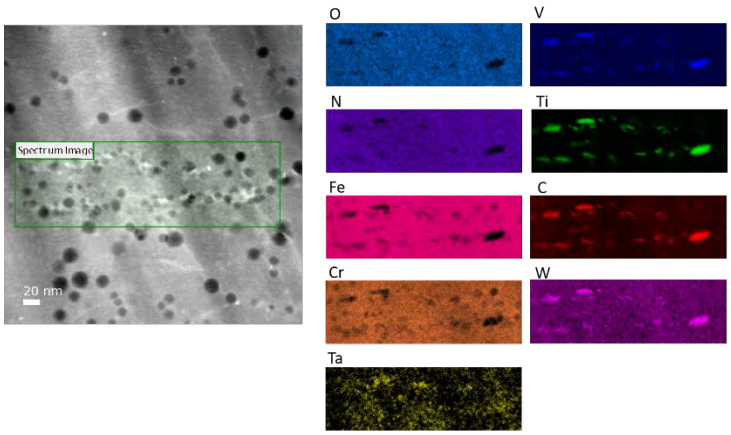

Figure 4. The EELS results of CNA3.

As shown in Figure 5, He bubbles were found in the implanted pure Ni at 500 and 700°C. From 500 to 700°C, the average bubble size increased from 5.5nm to 8.7nm. On the contrary, bubble density decreased from $8.7\times10^{22}/m^3$ to $1.3\times10^{22}/m^3$ with elevated temperature. Bubbles were not visible in the implanted CNA3 and 14YWT alloys at either 500 or 700°C, using conventional through focus imaging under kinematic contrast conditions at magnifications of 300KX in foils with thickness near 100 nm. This implies that the average diameter of any He-vacancy clusters in these alloys is <2 nm.

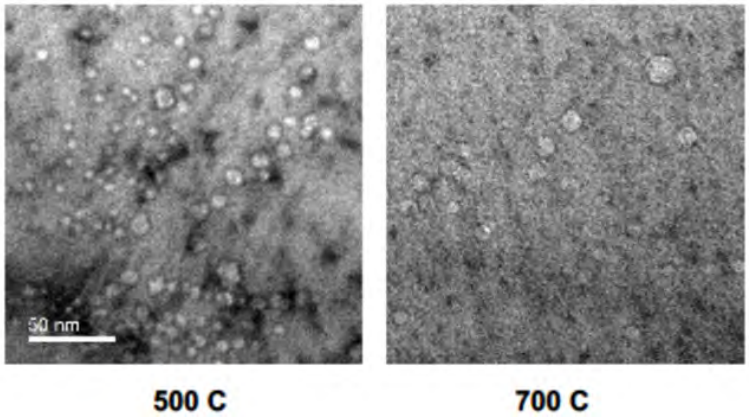

Figure 5. TEM images of He bubbles in Ni at 500 and 700°C.

Future Plans

The He implantation results of the 14YWT and CNA3 material at temperature above 700°C would be valuable to understand the bubble formation behavior. In addition, utilizing the Intermediate Voltage Electron Microscopy - Tandem Facility at Argonne National Laboratory can provide important results of the interaction between helium bubbles and nanoclusters at elevated temperatures. Dynamic monitoring of the evolution of bubble formation and their interaction with nanoclusters in 14YWT and CNA3 will provide direct observation to explain the morphological difference in the bubble-nanocluster complex between the two materials. Lastly, annealing the He implanted samples from 500°C to higher temperatures (above 700°C) under in-situ TEM, could provide information on the helium binding energies of these nanoclusters.

References

[1] M.K. Miller, K.F. Russell, D.T. Hoelzer, "Characterization of precipitates in MA/ODS ferritic alloys," *Journal of Nuclear Materials,* vol. 351, pp. 261-268, 2006.

[2] L. Tan, L.L. Snead, Y. Katoh, "Development of new generation reduced activation ferriticmartensitic steels for advanced fusion reactors," *Journal of Nuclear Materials,* vol. 478, pp. 42-49, 2016.

7.5 ALPHA-PRIME (α') PRECIPITATE FORMATION IN ION IRRADIATED Fe18Cr ALLOYS—Y. Zhao, S. Zinkle (University of Tennessee), A. Bhattacharya (Oak Ridge National Laboratory)

OBJECTIVE

This work investigates the effect of dose rate and temperature on the α' precipitate clustering behavior in binary Fe-Cr alloys after heavy ion irradiation at different temperatures and dose rates.

SUMMARY

High purity FeCr alloys with Cr content ranging from 0-18 wt. % Cr were irradiated with 8 MeV Fe ions to midrange doses of 0.35 or 3.5 dpa at 350 and 450°C at damage rates of 10^{-5} and 10^{-4} dpa/s. Definitive evidence for the formation of α' precipitates was confirmed in the Fe18Cr specimens irradiated at 450 °C to a dose of 0.35 dpa with dose rates of both 10^{-5} and 10^{-4} dpa/s by transmission electron microscope (TEM) energy-dispersive X-ray spectroscopy (EDS) mapping. The precipitates formed after low dose rate irradiation have a larger size than that from higher dose rate irradiation.

PROGRESS AND STATUS

Introduction

Binary Fe-Cr alloys are simple representatives of Ferrite-Martensitic steels which are structural material candidates for Gen. IV fission and fusion reactors. For Cr levels >8-9% and irradiation temperatures below ~480°C, these alloys suffer from neutron irradiation-induced/enhanced embrittling Cr-rich α' precipitation. The Cr-rich clusters were reported to form in alloys with 9-18% Cr at 300 °C or higher temperature when the dose was as low as 1.82 dpa [1, 2]. However, the literature regarding α' formation in FeCr alloys after high dose rate ion irradiations are limited [3,4]. The responsible mechanism for the lack of α' precipitation following heavy ion irradiation is uncertain but may involve the ballistic dissolution of precipitate nuclei along with insufficient time to renucleate the precipitates due to the high damage rates associated with typical ion irradiations.

The FeCr specimens were received from Commissariat à l'énergie atomique (CEA), Saclay France, in the shape of cylinders. Their chemical composition and grain size information are summarized in Table 1. The samples were cut into 3-mm diameter and 1 mm thick disks with electronic discharge machining (EDM), followed by mechanical grinding and polishing to a thickness of approximate 0.35 mm with one mirror surface. After that, the as-polished samples were shipped to Michigan Ion Beam Laboratory (MIBL), where they were irradiated by 8 MeV Fe at conditions listed in Table 2. The damage and Fe concentration profiles are calculated with Stopping and Range of Ions in Matter (SRIM) 2008 in the simple KP mode as shown in Figure 1. The flux and fluence of injected ions are calculated based on the damage at mid-range. The displacement energy of the target was set to be 40 eV. The preliminary analysis of the irradiated samples has focused on the Fe-18%Cr specimens irradiated at 450°C to a midrange dose of 0.35 dpa.

Table 1. Chemical composition and grain size of as-received FeCr specimens

specimen	element concentration							
	Cr (wt. %)	Cr (at. %)	C (ppm)	S (ppm)	O (ppm)	N (ppm)	P (ppm)	grain size (μm)
pure iron	<2 ppm		4	2	4	1	<5	183
Fe3Cr	3.05	3.27	4	2	6	2		390
Fe5Cr	5.4	5.78	4	3	6	2	<5	68
Fe8Cr	7.88	8.41	5	2	7	2		320
Fe10Cr	10.1	10.77	4	4	4	3	<5	82
Fe12Cr	11.63	12.38	5	2	4			500
Fe14Cr	14.25	15.15	5	7	4	5	<10	141
Fe18Cr	17.97	19.05	7	2	6	5		650
Fe25Cr	24.97	26.33	4	1	3	3		570

Table 2. Preliminary irradiation matrix. All materials were irradiated in a single sample holder (containing 9 TEM disk specimens) for each irradiation condition.

Ion Species	**Mid-range / Peak dose (dpa)**	**Fluence (ions.cm^{-2})**	**Flux/mid-range dose rate (ions.cm^{-2}.s^{-1} / dpa.s^{-1})**	**Temper-atures (°C)**	**Estimated time (h)**
8 MeV Fe ions	0.35/ 0.84	8.83×10^{14}	2.52×10^{11} /10^{-4}	350 450	0.97
8 MeV Fe ions	3.50/ 8.41	8.83×10^{15}	2.52×10^{11} /10^{-4}	350 450	9.72
8 MeV Fe ions	0.35/ 0.84	8.83×10^{14}	2.52×10^{10} /10^{-5}	450	9.72

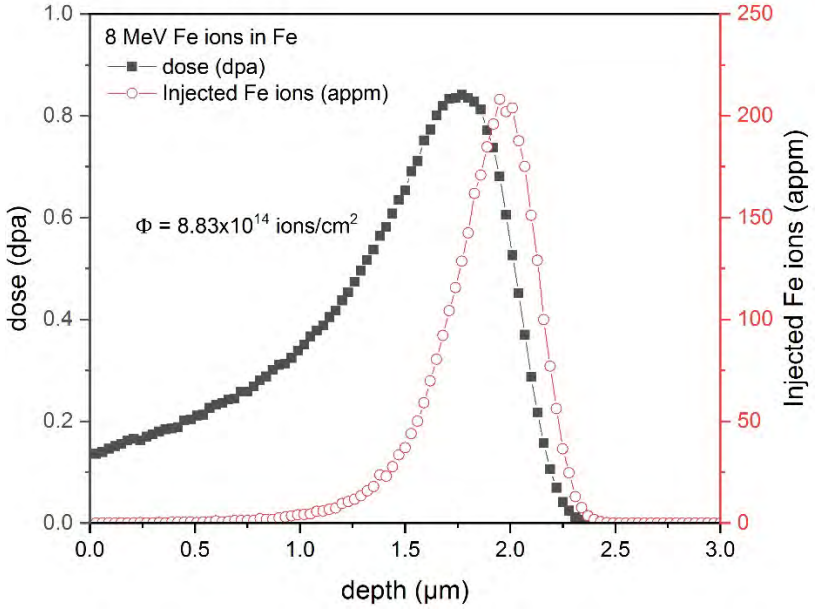

Figure 1. The SRIM based estimates of the depth profile of displacement damage in dpa and implanted Fe ions concentration in pure Fe with 0.35 dpa at mid-range (~1.0 micron depth).

Two of the irradiated Fe18Cr samples irradiated at 450°C to a midrange dose of 0.35 dpa (10^{-5} dpa/s and 10^{-4} dpa/s) have been characterized by TEM EDS with the FEI Talos F200X S/TEM at Oak Ridge National Laboratory (ORNL). The presence of α' precipitates was confirmed in both samples. The results from the mid-range (~1μm) region are given in Figure 2. The precipitates formed after low dose rate irradiation have a larger size than that from higher dose rate irradiation. The formation of network dislocations and flower-shaped dislocation loops has been observed in the Fe18Cr sample irradiated at the high dose rate. Besides, atom probe tomography (APT) results reveal the radiation-induced features exhibit enhanced segregation by C and N solute and are decorated with Cr-rich clusters.

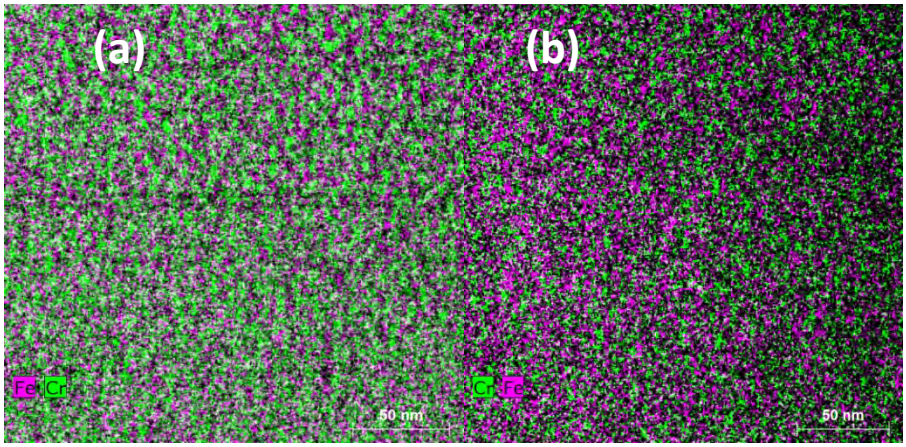

Figure 2. The EDS mapping from the mid-range of 450°C, 0.35 dpa ion irradiated Fe18Cr samples. (a) 10^{-5} dpa/s, (b) 10^{-4} dpa/s.

Heat treatments aiming at forming α' precipitates with various sizes and atomic concentrations have been carried out on some of the as-received Fe18Cr and Fe25Cr samples at 500 °C for 100, 300 and 900 hours

respectively. The formation of α' precipitates in Fe18Cr heat treated for 300 hours has been confirmed from the results of EDS mapping.

Future Work

- The presence or absence of α' precipitates in all the ion irradiated Fe14Cr and Fe18Cr samples will be checked with EDS and then quantified by APT examination. The effect of ballistic dissolution will be evaluated based on these results.
- The defect cluster and network dislocation microstructure in the irradiated Fe14Cr and Fe18Cr specimens will be characterized by TEM. The segregation of Cr to dislocations and dislocation loops will also be checked with TEM-EDS.

References

[1] Bachhav, M., et al. (2014). "α′ precipitation in neutron-irradiated Fe–Cr alloys." Scripta Materialia 74: 48-51.

[2] Reese, E. R., et al. (2018). "On α′ precipitate composition in thermally annealed and neutron-irradiated Fe- 9-18Cr alloys." Journal of Nuclear Materials 500: 192-198.

[3] Hardie, C. D., et al. (2013). "Effects of irradiation temperature and dose rate on the mechanical properties of self-ion implanted Fe and Fe–Cr alloys." Journal of Nuclear Materials 439(1-3): 33-40.

[4] Tissot, O., et al. (2016). "Influence of injected interstitials on α′ precipitation in Fe–Cr alloys under self-ion irradiation." Materials Research Letters 5(2): 117-123.

7.6 CAVITY DENUDED ZONE IN NEUTRON-IRRADIATED COPPER—Yan-Ru Lin and Steven J. Zinkle (University of Tennessee, Knoxville)

OBJECTIVE

The objective of this task is to systematically study the void and bubble denuded zone widths at planar sinks such as grain boundaries and surfaces in neutron and ion irradiated Cu materials at different dose, dose rate, and temperature.

SUMMARY

We confirmed that the denuded zone width of cavities adjacent to grain boundaries was dependent on temperature, damage rate, material and defect type (void or bubble). The temperature dependence of the width of the void denuded zone is proportional to exp(-Em/4KT), where Em is the vacancy migration energy. The denuded zone width is also proportional to $P^{-1/4}$, where P is the displacement damage rate. Furthermore, the corresponding denuded zone width for helium (He) bubbles was found to be much smaller than that for voids. In addition, localized peak swelling zones were observed in specimens with low sink strength, which can be interpreted as evidence for 1D gliding interstitial clusters. The importance of 1D gliding interstitial clusters disappears for high cavity (sink) strengths above ~$10^{14}/m^2$.

PROGRESS AND STATUS

Samples of pure Cu and copper containing ~100 appm ^{10}B were irradiated at a damage rate of $2x10^{-7}$ dpa/s in a mixed spectrum reactor to a dose of ~1 dpa at 182 to 500°C in heated temperature-controlled capsules that were continuously monitored with thermocouples. Following irradiation, the specimens were examined by transmission electron microscopy to characterize the cavity and other radiation induced defect microstructures. Details of the irradiation and characterization techniques, along with a summary of the average cavity sizes and densities are given elsewhere [1, 2].

Near grain boundaries and incoherent twin boundaries, void denuded zones were observed for the pure Cu specimens irradiated at 220 to 350°C, as shown in Figure 1. The average width of the denuded zones at various temperatures is given in Table 1. Both Figure 1 and Table 1 indicate that void denuded zone width gradually increased from 342 nm at 220°C to 751 nm at 350°C.

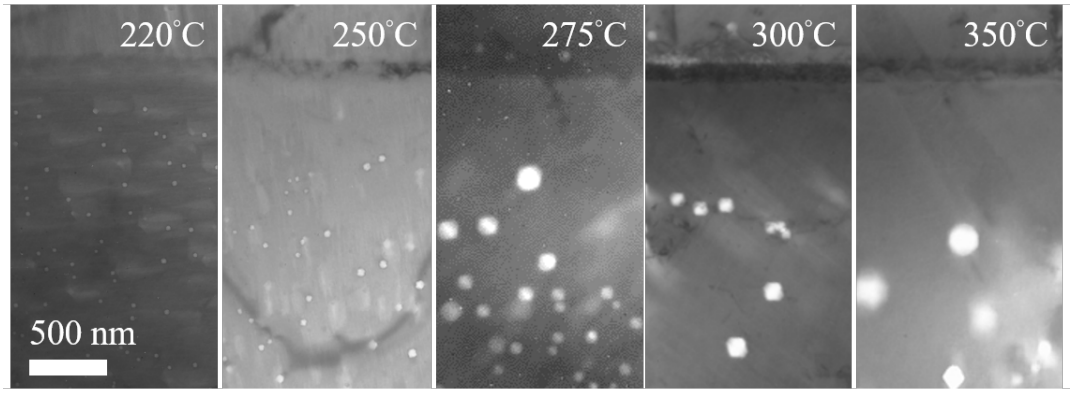

Figure 1. Grain boundary void denuded zone in neutron irradiated Cu at 220-350℃.

Table 1. Temperature dependence of void denuded zone widths at grain boundaries for neutron irradiated Cu

Temperature (℃)	Void DZ Width (nm)
220	342 ± 87
250	433 ± 89
275	606 ± 61
300	689 ± 97
350	751 ± 135

For the neutron irradiated copper-boron alloys, both voids and bubbles were observed. As shown in Figure 2, He bubbles (indicated by orange arrows) could be observed in the void denuded zones. This indicates that bubbles have their own denuded zone width that is smaller than the void denuded zone. According to our results shown in Table 2, similar to the increment of void denuded zones, the bubble denuded zone width increased also with elevating temperatures (from 32 nm at 182°C to 580 nm at 500°C). However, the quantitative value of the denuded zone width for He bubbles at any given temperature was much smaller than that for voids. The He bubble denuded zone width for boron-doped copper irradiated with fission neutrons at 182-350°C were about 2-6 time smaller than the corresponding void denuded zone width.

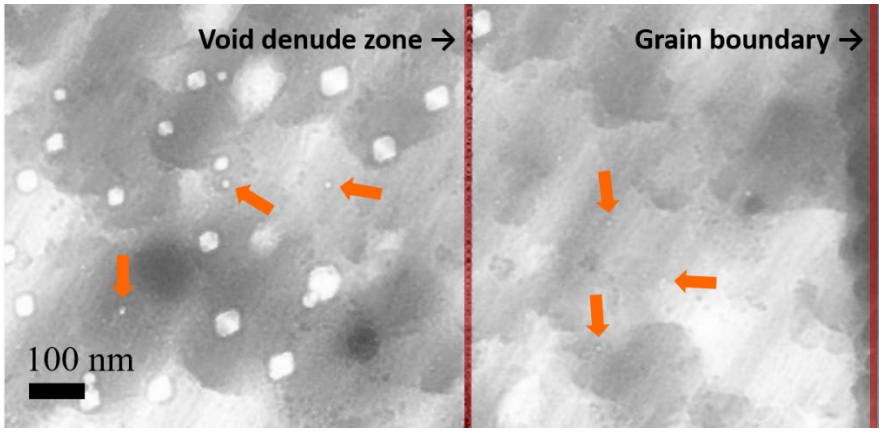

Figure 2. Voids and He bubbles in neutron irradiated Cu-B alloy at 250℃.

Table 2. Cavity denuded zone width of neutron irradiated Cu-B alloy

Temperature (℃)	Bubble DZ Width (nm)	Void DZ Width (nm)
182	32 ± 10	225 ± 20
250	102 ± 59	535 ± 80
350	420 ± 124	809 ± 37
400	593 ± 162	1784 (only one)
500	580 ± 184	--

In order to compare these results with other studies that have reported denuded zones in copper, we used the predicted dependence of cavity denuded zones (L_V) on damage rate and temperature, $L_V \sim (D_V/P)^{1/4}$ where $D_V=D_0\exp(E_m/kT)$ is the vacancy diffusivity, E_m is the vacancy migration enthalpy and P is the damage rate [3], to produce a comprehensive overview as shown in Figure 3. Comparing our results with previous studies [1, 2, 4-8], Figure 3 shows that the void denuded zone width of neutron and self-ion irradiated Cu (including the Cu-B alloy) are all distributed near the same fitted line (red-dashed line). The slope of this line gives E_m=0.72 eV, which agrees with the experimental data and the theoretical value of Cu vacancy migration energy (~0.7 eV). Conversely, the shorter bubble denuded zone width data from the neutron-irradiated Cu-B specimens were fitted by two blue-dashed lines with a transition point at ~350°C. The calculated migration energy value below 350°C was 1.26 eV. Above 350°C in the high-temperature regime, the migration energy reduced to 0.32 eV. Both values differ from the Cu vacancy migration energy. The Cu-B He bubble result (~100 appm He/dpa) is comparable to the He ion implantation study, which also showed a smaller bubble denuded zone width (~200 nm) at 450°C. In other words, in the presence of He atoms, the bubble denuded zone next to the grain boundary is much smaller than the case for voids. Recent density functional theory (DFT) calculations indicate that He-vacancy complexes can migrate by several mechanisms with different energy barriers [9]. This suggests that the migration of He-vacancy complexes or He clusters may dominate the formation of the bubble denuded zone width.

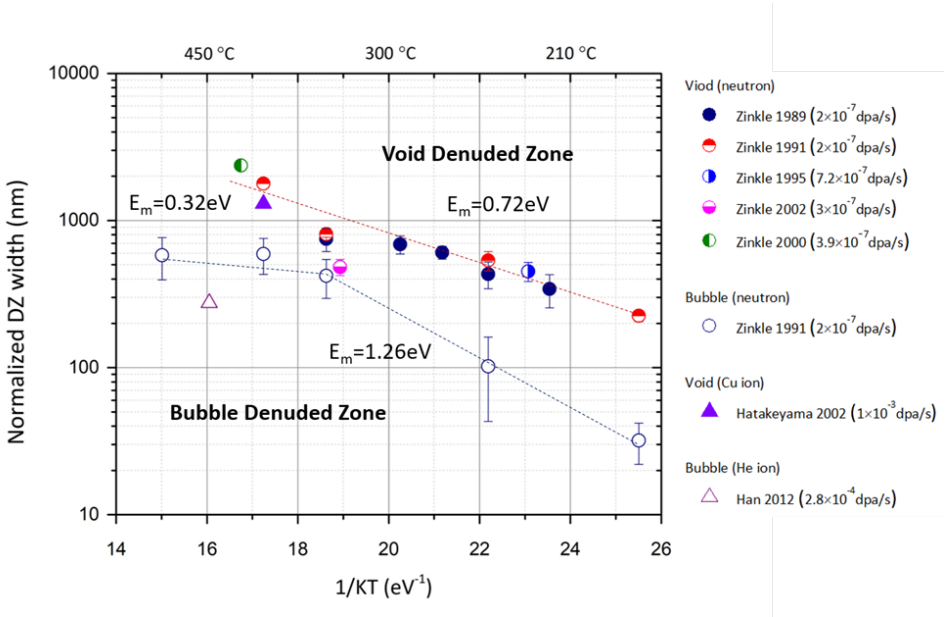

Figure 3. Void denuded zone (DZ) width vs. inverse temperature for irradiated Cu.

In addition, localized peak void swelling zones were observed adjacent to the void denuded zone along the grain boundary. This peak zone swelling has been claimed to be associated with 1D migration of small interstitial clusters produced during irradiation that more easily escape to the grain boundary than 3D migrating defects such as vacancies, causing a localized peak in the vacancy supersaturation [10]. However, in this study, these peak swelling transition regimes were only observed in the neutron-irradiated pure Cu specimens at 275, 300 and 350°C. Such regimes were not found in any of the irradiated Cu-B specimens, nor in the pure Cu specimens irradiated at temperatures below ~275°C. Because of the microstructural evolution of defects at elevated temperatures, this phenomenon might be correlated with the sink strength of the irradiation-induced defects, such as dislocation loops, voids or stacking fault tetrahedra (SFT) [1, 2]. Here, we calculated the defect sink strengths in the neutron irradiated pure Cu and Cu-B specimens irradiated at 250-350°C (Table 3). For the specimens without the peak swelling zones (Cu at 250°C, and Cu-B alloy at 250 and 350°C), the sink strengths were all above or very close to 10^{14} m^{-2}. As

for Cu at 275, 300 and 350°C, where the peak swelling zone was observable, the cavity sink strengths are in the order of 10^{13} m^{-2}. This suggests that when the cavity sink strength is above ~10^{14} m^{-2}, the high sink strength may suppress the 1D gliding of the interstitial clusters.

Table 3. Defect sink strengths in neutron irradiated Cu

Temperature (℃)	Cu		Cu-B alloy	
	Void (m^{-2})	Dislocation loop + SFT (m^{-2})	Void + bubble (m^{-2})	Dislocation loop + SFT (m^{-2})
250	$5.46x10^{13}$	$2.01x10^{15}$	$2.02x10^{14}$	$1.09x10^{15}$
275	$3.82x10^{13}$	$5.02x10^{14}$	--	--
300	$3.68x10^{13}$	$7.54x10^{13}$	--	--
350	$2.29x10^{13}$	$3.82x10^{13}$	$8.90x10^{13}$	$2.43x10^{13}$

In conclusion, cavity denuded zones were observed adjacent to surfaces and grain boundaries in irradiated copper and Cu-B. The denuded zone width was dependent on temperature, damage rate, material and defect type (void or bubble). The He bubble denuded zone width is about 2-6 times smaller than the void denuded zone width for comparable irradiation conditions. Furthermore, a transition regime with localized peak swelling was identified next to the denuded zone for specimens with low sink strength. When the sink strength is above ~10^{14} m^{-2}, 1D glide diffusion of interstitial clusters is apparently suppressed and the peak swelling zone is not evident. It is important to recognize and quantify the denuded zone width to avoid artifacts in analysis of irradiated materials. In addition, quantification of the defect-free zone width can provide insight on mobility (activation energy) for controlling defect species.

In addition to copper, other metals such as nickel exhibit the same exponential relationship on temperature for the cavity denuded zone width [11, 12]. From analysis of plots of the normalized void denuded zone widths of ion irradiated Ni vs. 1/kT, the slope of the Arrhenius plot implies a vacancy migration energy of Em=1.4 eV, which agrees with the commonly accepted literature value although some studies recommend a lower value near 1.0-1.1 eV [13].

Future Plans

We intend to collect the results of previous studies on bubble and void denuded zones of other materials and examine the dependence of the width of cavity denuded zone on temperature, dose rate, and vacancy migration energy.

References

[1] S. Zinkle and K. Farrell, "Void swelling and defect cluster formation in reactor-irradiated copper," *Journal of Nuclear Materials, v*ol. 168, pp. 262-267, 1989.
[2] S. Zinkle, K. Farrell and H. Kanazawa, "Microstructure and cavity swelling in reactor-irradiated dilute copper-boron alloy," *Journal of Nuclear Materials,* no. 179-181, pp. 994-997, 1991.
[3] N.Q. Lam, S.J. Rothman, R. Sizmann, Steady-state point-defect diffusion profiles in solids during irradiation, *Radiation Effects*, 23, pp. 53-59, 1974.
[4] W. Han, M. Demkowicz, E. Fu, Y. Wang and A. Misra, "Effect of grain boundary character on sink efficiency," *Acta Materialia,* vol. 60, pp. 6341-6351, 2012.
[5] S. Zinkle and L. Snead, "Microstructure of copper and nickel irradiated with fission neutrons near 230˚C," *Journal of Nuclear Materials, v*ol. 225, pp. 123-131, 1995.

[6] S. Zinkle, N. Hashimoto, D. Hoelzer, A. Qualls, T. Muroga and B. Singh, "Effect of periodic temperature variations on the microstructure of neutron-irradiated metals," *Journal of Nuclear Materials,* Vols. 307-311, pp. 192-196, 2002.
[7] M. Hatakeyama, H. Watanabe, M. Akiba and N. Yoshida, "Low void swelling in dispersion strengthened copper alloys under single-ion irradiation," *Journal of Nuclear Materials ,* Vols. 307-311, pp. 444-449, 2002.
[8] S. Zinkle and Singh, "Microstructure of Cu-Ni alloys neutron irradiated at 210C and 420C to 14 dpa," *Journal of Nuclear Materials, v*ol. 283-287, pp. 306-312, 2000.
[9] C. Gonzalez, "Migration mechanisms of helium in copper and tungsten," *Journal of Material Science,* vol. 49, pp. 8127-8139, 2014.
[10] H. Trinkaus, B.N. Singh, M. Victoria, Microstructural evolution adjacent to grain boundaries under cascade damage conditions and helium production, *Journal of Nuclear Materials*, 233, pp. 1089-1095, 1996.
[11] J. Westmoreland, J. Sprague, F. Smidt jr. and P. Malmberg, "Dose rate effects in nickel-ion-irradiated nickel," *Radiation Effects*, vol. 1-2, no. 26, pp. 1-16, 1975.
[12] M. Shaikh, "Void denudation and grain boundary migration in ion-irradiated nickel," *Journal of nuclear material*, vol. 187, no. 3, pp. 303-306, 1992.
[13] W.G. Wolfer, Fundamental Properties of Defects in Metals, in: R.J.M. Konings (Ed.) *Comprehensive Nuclear Materials*, Elsevier, Amsterdam, pp. 1-45, 2012.

7.7 ADVANCED-STEM-BASED DEEP LEARNING FOR SEMANTIC SEGMENTATION OF DEFECTS IN STEELS

—Yuanyuan Zhu (University of Connecticut), Graham Roberts, Rajat Sainju, Brian Hutchinson, Richard J. Kurtz, Mychailo B. Toloczko, Danny J. Edwards, and Charles H. Henager, Jr. (Pacific Northwest National Laboratory)

This is an Extended Abstract of a paper in preparation for journal submission

The effort to obtain statistically meaningful quantification of a variety types of extended irradiation defects, such as dislocation lines and loops, voids and bubbles, and various types of precipitates, is a labor-intensive and time-consuming task. In this work, we developed a novel deep convolutional neural network (DCNN) model, called *DefectNet*, for robust and automated semantic segmentation of three crystallographic defects including line dislocations, precipitates, and voids commonly observed in structural metals and alloys [1,2]. Defect semantic segmentation in transmission electron microscopy (TEM) micrographs is a challenging deep learning task due to the nature of the image itself. Unlike everyday photographs, the interpretation of image contrast in TEM micrographs is usually not straightforward; multiple contrast mechanisms often contribute to the observation of defect features. Here, we aim at resolving this image-induced challenge by optimizing the image quality. In previous work, we established an experimental protocol for a diffraction contrast imaging scanning transmission electron microscopy (DCI STEM) technique and tailored it specifically for imaging defects in popular iron-based structural alloys [3]. Thus, the *DefectNet* was trained over a small but high-quality DCI STEM defect image sets of a HT-9 martensitic steel before and after neutron irradiation for 111.8 dpa at 412 ^{o}C. The performance of the resulting model for each defect was assessed quantitatively by standard semantic segmentation evaluation metrics, and the resulting defect density and size measurements were compared to that from a group of human experts.

Typical semantic segmentation evaluation metrics show excellent prediction performance of the *DefectNet*, with an overall averaged pixel accuracy of 94.61±1.13%, precision of 72.12±2.73%, recall of 79.22±3.27%, and region intersection over union (IU) of 61.79±2.13%, comparable to state-of-the-art deep learning semantic segmentation algorithm. To translate these machine learning performances into more practical materials evaluations, defect quantification including dislocation density, number density, diameter, and diameter standard deviation of precipitates and voids were carried out based on the deep learning predicted defect maps. Compared with the defect quantification results produced by human experts, computer-based analysis is overall more accurate and reproducible. Taking dislocation density for example, *DefectNet* yielded a percent error of ~ 4%, whereas, an averaged error of ~ 20% was produced by six human experts. In particular, due to the large number of relatively small precipitates in one image, the human quantification of precipitate number density proved less reliable, with an average error of ~ 45%, while *DefectNet* yielded an error around ~ 10% on average. Lastly, when comparing the time efficiency of the quantification methods, *DefectNet* wins by a large margin. For defect quantification that typically takes at least half an hour even for an expert, with a good model *DefectNet* can produce more reproducible and reliable quantification in a few seconds. This work demonstrates the feasibility of using deep learning algorithms for fast and accurate defect quantitative analysis. Meanwhile, several key issues related to the extended irradiation defects in nuclear structural alloys after high-dose irradiation were identified. Plans are under development to fully transfer the success of *DefectNet* to high throughput quantification of extended irradiation defects.

Acknowledgements

The work was performed at University of Connecticut, and at Pacific Northwest National Laboratory (PNNL), which is operated by Battelle for the United States Department of Energy (U.S. DOE) under Contract DE-AC06-76RL0-1830. This research is funded by the U.S. DOE Office of Fusion Energy Sciences under contract DE-AC05-76RL01830. All computations were performed on PNNL's Institutional Resources (PIC).

References

[1] G. Roberts, S.Y. Haile, R. Sainju, D. Patel, D. J. Edwards, B. Hutchinson and Y. Zhu. *in preparation.*

[2] Y. Zhu, G. Roberts, D. J. Edwards, R. J. Kurtz. *Semi-annual Progress Report* DOE/ER-0313/64 (June 2018).

[3] Y. Zhu, C. Ophus, M. B. Toloczko, D. J. Edwards, *Ultramicroscopy* **193**, 12-23 (2018).

8. MODELING PROCESSES IN FUSION SYSTEM MATERIALS

8.1 RFITML: REVERSE FITTING WITH MACHINE LEARNING FOR IMPROVING INTERATOMIC POTENTIALS—W. Setyawan and Charles H. Henager Jr. (Pacific Northwest National Laboratory)

OBJECTIVE

Fitting a classical interatomic potential often involves large number of trial sets, from which the "best" set is selected. The objective of this research is to develop a computational framework to explore the feasibility of using machine learning to improve the current "best" set by utilizing the available trial sets.

SUMMARY

A computational framework (RFITML) has been developed that utilizes machine learning (ML) technique to model property-parameter relationship of interatomic potentials. The RFITML was tested using training data from previously generated trial sets of Re embedded-atom method (EAM) potential, referred to as dataset1. The dataset1 was found to be unsuitable for this purpose because the knot positions of a series of cubic polynomials used in the EAM parametrization vary among trial sets, resulting in non-monotonic knots in the predicted set of parameters obtained by evaluating the trained ML model. Force-matching (FM) fits were subsequently performed to generate new training data, referred to as dataset2. In dataset2, the knot positions were fixed. Nevertheless, tests of RFITML using dataset2 so far resulted in un-physical pair interaction and the electronic density. The results indicate that the parametrization used in these tests is too prone to un-physical behaviors. Future studies may include examining the dataset for "bad" sets to be excluded from the ML fit, researching different deep neural networks, and testing using a new dataset with a simple analytical parametrization.

PROGRESS AND STATUS

Dataset1

In previous reports, we developed an EAM potential for point defect studies in tungsten-rhenium (W-Re) systems. The potential was recently published in Reference [1]. The potential reproduces Re defect formation energies in W, binding energies of Re to self-interstitial clusters in W, and the convex-hull of formation energies of structures in σ and χ Re-W phases reasonably well. The potential also predicts a Re melting temperature (3130 K) much closer to the experimental value (3459 K) than a previously published Re potential [2] (4836 K). Nevertheless, the predicted elastic constants of hcp Re need improving [1]. Note that the potential was not directly fit to target properties, but rather through a FM method. The FM method is selected over a conventional property-fit method because the former uses only first-principles forces, energies, and stresses, making it suitable for automated/high-throughput approaches of potential development. In addition, disordered and liquid structures are readily incorporated in a FM method to fit the potential far beyond the ground state configuration. Consequently, FM potentials typically exhibit better transferability than property-fit potentials. Large number of trial sets (1000 sets of Re potential and 500 sets of Re-W potential) was generated during the potential development. These original sets constitute dataset1.

In this report, we explore the idea of using ML on the existing trial sets to improve the "best" potential among these trial sets. The ML is typically used to model parameter-property relationships. We employ a reverse ML to obtain a property-parameter relationship, i.e. the properties of the trial sets are used as inputs while the potential parameters of the trial sets are used as outputs. Once a ML model has been trained using the trial sets, it is used to predict a "target" set of parameters given a set of target properties. The "worst" set in the trial sets is subsequently replaced by the "target" set, and the process is repeated until a new "best" set is obtained or until the needed improvement is achieved. In this research, a computational framework is developed to automate the iteration process.

Before we describe the RFITML, we describe the parametrization of the EAM potential for convenience. The pair interaction is a series of cubic polynomials:

$$\phi(r) = \sum_{i=1}^{15} f_i(r_i - r)^3 \theta(r_i - r) \quad (1)$$

where θ is a Heaviside step function. The atomic density is also a series of cubic polynomials:

$$\rho(r) = \sum_{i=1}^{4} g_i(x_i - r)^3 \theta(x_i - r), \text{ for } r \geq r_{min}$$
$$r = r_{min}, \text{ for } r < r_{min} \quad (2)$$

The embedding energy uses an analytical function:

$$F(\rho) = c_1\sqrt{\rho} + c_1\rho + c_2\rho^2 \quad (3)$$

RFITML Framework

The framework consists of a Unix daemon (named *rfitmld*) and a set of Unix, batch, and Python scripts. The scripts are responsible for running POTFIT, LAMMPS, and ML codes, while *rfitmld* manages the overall framework. The force-matching fit of the potentials was previously performed using the POTFIT code. In this framework, it is employed to convert potential parameters in a trial set to a LAMMPS-formatted potential file. The LAMMPS is used to calculate the properties of a trial set via molecular dynamics (MD) simulations. Currently, TensorFlow is used as the ML code.

The first version of RFITML has been completed. It is designed to manage the framework by monitoring the presence of certain files called state files. The main state files are *state_run_ml*, *state_run_potfit,* and *state_run_lmp.* These state files signal *rfitmld* to invoke Unix scripts *run_ml.sh*, *run_potfit.sh*, and *run_lmp.sh*, respectively. In turn, these scripts submit the batch scripts *qml*, *qpotfit*, and *qlmp* to perform ML, *potfit*, and LAMMPS tasks, respectively. The cycle of the framework is *state_run_ml* → *state_run_potfit* → *state_run_lmp* and loops back. Once *rfitmld* is launched, a user typically creates *state_run_ml* file to start performing a ML task. However, a user can choose to start whichever task by creating the appropriate state file. Subsequently, *rfitmld* proceeds to the next task by creating the appropriate state file automatically. An iteration counter is incremented every time *run_ml.sh* is invoked.

Once *rfitmld* is launched, a user can manually interrupt, cancel, or resume iterations by creating corresponding state files without exiting the daemon. A user can also exit the daemon by creating a *state stop* file. A user specifies a walltime, number of iterations, convergence criterion, and how the error is calculated, i.e. as a mean-absolute-error (mae) or as a root-mean-squared-error (rmse), in an input file named *rfitml.in*. A walltime is the maximum runtime allowed for *rfitmld*. Specifying a walltime prevents the daemon from running indefinitely. For convenience, *rfitml.in* is re-read at every iteration, allowing the user to adjust those variables during runtime.

A Python script named *ml.py* has been developed to perform the ML tasks. It uses Keras, a Python deep learning library, with the TensorFlow backend to build, train, and evaluate a neural network ML model. Note that *rfitmld* and *ml.py* do not depend on the type (e.g. EAM or other potential types), the parameters, and the properties of the potential. On the other hand, the scripts associated with POTFIT and LAMMPS need to be modified by the users based on their needs. For convenience, the framework comes with an example directory containing all the necessary files and scripts.

The trial sets of the Re potential are used as training data to test RFITML. The list of 19 properties with their target values and weights is presented in Table 1. A user specifies target properties and weights in *prop.target* file. The weights are used to calculate the error of a set with respect to the target properties as follows

$$e_j = (p_j - q_j)/q_j \quad (4)$$

$$mae = \frac{\sum_{j=1}^{L} w_j |e_j|}{\sum_{j=1}^{L} w_j} \quad (5)$$

$$rmse = \sqrt{\frac{\sum_{j=1}^{L} w_j e_j^2}{\sum_{j=1}^{L} w_j}} \quad (6)$$

where p_j is property-j, q_j is target property-j, e_j is relative error of property-j, w_j is the error weight of property-j, and L is the number of properties. The 19 properties are used as input nodes in the neural network, forming an input layer. Three hidden layers are constructed with each layer consisting of 64 nodes with an *ReLu* activation function employed in each node. All potential parameters, except the cutoff distance, for a total of 42 parameters, are used as output nodes forming an output layer. The ML model is successfully trained, and subsequently used to predict parameters based on the target properties. It was found that because the knot positions of the cubic polynomials used in the pair interaction and the electron density function vary among the training data, the predicted parameters contain non-monotonic knots. Therefore, new training data are needed.

Table 1. List of properties for the Re EAM potential. The weights are used to calculate the error of a trial set with respect to the target values. Data labelled with (Exp.) are from experiments, while the rest are *ab initio* data from our calculations. E_c is cohesive energy, E_f is point defect formation energy. Interstitial positions C to BC are depicted in [1]. Units are Å, eV, and GPa.

Property	Target	Weight	Property	Target	Weight
a	2.761 (Exp.)	1	E_f [Vac]	3.08	1
c/a	1.614 (Exp.)	1	E_f [C]	6.52	1
E_c [hcp]	8.03 (Exp.)	10	E_f [O]	8.13	1
E_c [hcp-fcc]	0.06	10	E_f [S]	6.53	1
E_c [hcp-bcc]	0.31	10	E_f [T]	6.52	1
C_{11}	613 (Exp.)	1	E_f [BO]	7.41	1
C_{33}	683 (Exp.)	1	E_f [BS]	8.09	1
C_{12}	270 (Exp.)	1	E_f [BT]	Relaxed to BO	1
C_{13}	206 (Exp.)	1	E_f [BC]	Relaxed to BO	1
C_{44}	163 (Exp.)	1			

Dataset2

Efforts are then shifted to performing the FM fit again. The "best" set from previous results (dataset1) is taken as a starting point with the pair interaction and embedding function are set close to zero by scaling their strength by a factor of 100 to minimize a bias towards converging to the same local minimum. The knot positions are fixed. In this fit, we also experiment with using only the liquid structures to fit the potential. Six liquid structures under various strain tensors are used. Each structure contains 64 atoms, therefore a total of 6*64*3 forces, 6 energies, and 6*6 stresses is used to fit the potential. The factor 3 in the number of forces is because there are 3 components for every force vector. Likewise, the factor 6 in the number of stresses is because there are 6 components for energy stress tensor. The FM fit is performed using force:energy:stress weight ratio of 1:1920:320. This ratio corresponds to an effective weight ratio of 1:10:10, i.e. an energy and a stress component are intended to be 10 times more important than a force component. In an FM, simulated annealing is employed to explore the parametric space. For each parameter, a new value is randomly sampled from within the allowed range. In POTFIT, we found that even though a random sampling is used, the parameters are iterated sequentially, i.e. the random sampling is performed for parameter 1, followed by parameter 2, and so on. This procedure introduces a bias which favors parameters

located earlier in the parameter array. To eliminate this, we modified POTFIT so that the parameters are also selected randomly.

The total number of trial sets in the dataset2 is 1447. For each set, the properties are evaluated and the error is calculated using the property weight previously presented in Table 1. This error is referred to as property error to distinguish it from the FM fit error. Figure 1 shows plots of property rmse versus FM total, force, energy, and stress rmse. The FM total rmse is weight-averaged over the force, energy, and stress rmse based on the weight ratio given in the previous paragraph. No correlations are observed. However, the set with the smallest FM total error has a property error that is close to the minimum property error. This indicates that it is possible to get a good potential set with the FM method using only liquid structures. Set-962 represents the set with the minimum FM total rmse (rmse_FM) of 287.8 arbitrary unit. Set-762 represents the overall best set with the minimum property rmse (rmse_prop) of 36.5%. Set-762 also represents the overall best set with the minimum property mae (mae_prop) of 25.6%. The properties of set-962 and set-762 are shown in Table 2.

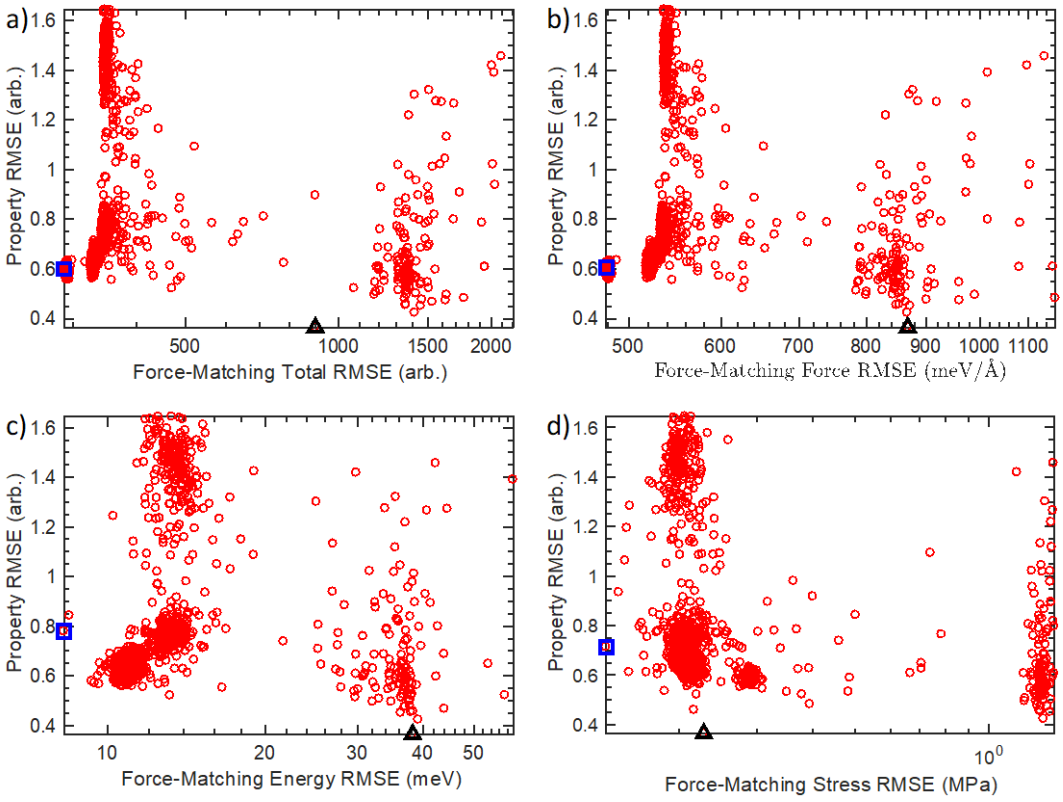

Figure 1. Scatter plot of root-mean-squared-error (rmse) of properties of trial sets in dataset2 with respect to target properties as a function of a) total, b) force, c) energy, and d) stress rmse from the FM fit. The plot is gathered from 1447 sets. The data point marked with a rectangle denotes the set with the minimum FM rmse, while the one marked with a triangle denotes the set with the minimum property rmse.

Visualizing Dataset2

To reveal correlations among the properties, they are plotted against each other. First, we study the correlations among the formation energies of an SIA at various sites. Figure 2 shows these correlations. In all plots, a linear correlation is observed. Therefore, to study correlations with other properties, one representative site suffices. This representative site is chosen to be site C since it is also the most stable site for an SIA (E_f = 6.52 eV). Before we move on to study the correlations with other properties, in Figure 2, the data points plotted as red squares represent the target properties. If only the SIA formation energies

are considered in the property rmse (called rmse_SIA), the best set is set-305 with rmse_SIA of 7.0%. The properties of set-305 are shown in Table 2.

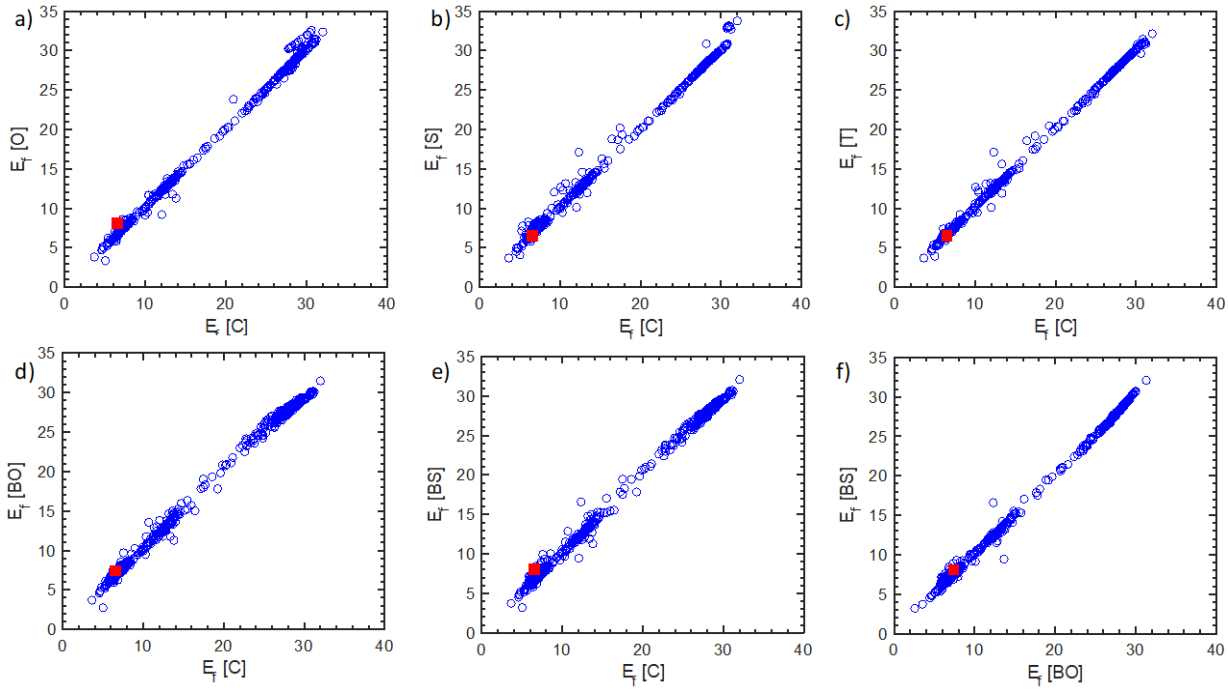

Figure 2. Scatter plots of formation energy (E_f in eV) of a self-interstitial atom in hcp Re at various sites from 1447 trial sets in dataset2. Data points plotted as red squares denote the target values.

Table 2. List of properties for the Re EAM potential from selected sets in dataset2. Target properties labelled with (Exp.) are from experiments, while the rest are *ab initio* data from our calculations. E_c is cohesive energy, E_f is point defect formation energy. Interstitial positions C to BC are depicted in [1]. Units are Å, eV, and GPa. Set-962, set-762, set-305, and set-628 represent the sets with the minimum rmse_FM, rmse_prop, rmse_SIA, and rmse_moduli, respectively (see text for description).

Property	Target	set-962	set-762	set-305	set-628
a	2.761 (Exp.)	2.731	2.863	2.734	2.712
c/a	1.614 (Exp.)	1.641	1.501	1.665	1.5901
E_c [hcp]	8.03 (Exp.)	7.63	7.98	7.81	7.24
E_c [hcp-fcc]	0.06	-0.003	0.03	-0.02	0.02
E_c [hcp-bcc]	0.31	0.10	0.21	0.14	0.11
E_f [Vac]	3.08	2.27	2.20	2.22	2.38
E_f [C]	6.52	6.94	7.23	6.82	9.81
E_f [O]	8.13	6.94	7.58	6.82	9.59
E_f [S]	6.53	6.94	6.93	6.84	10.38
E_f [T]	6.52	6.94	6.93	6.84	9.34
E_f [BO]	7.41	7.05	7.04	7.50	9.73
E_f [BS]	8.09	7.06	6.92	7.50	9.14
E_f [BT]	Relaxed to BO	7.05	7.04	7.50	9.14
E_f [BC]	Relaxed to BO	7.06	6.93	7.50	9.23
C_{11}	613 (Exp.)	569	583	631	513
C_{33}	683 (Exp.)	588	932	587	642
C_{12}	270 (Exp.)	371	403	449	285
C_{13}	206 (Exp.)	317	512	382	216
C_{44}	163 (Exp.)	84	225	86	216

Figure 3 shows the scatter plots among the elastic moduli. The target values are plotted as red squares. There are no obvious correlations among the elastic moduli, except between C_{12} and C_{13} where they show some degree of linear correlation. Set-628 represents the set with the minimum rmse of the elastic moduli with rmse_moduli of 16.8%. The properties of set-628 are shown in Table 2.

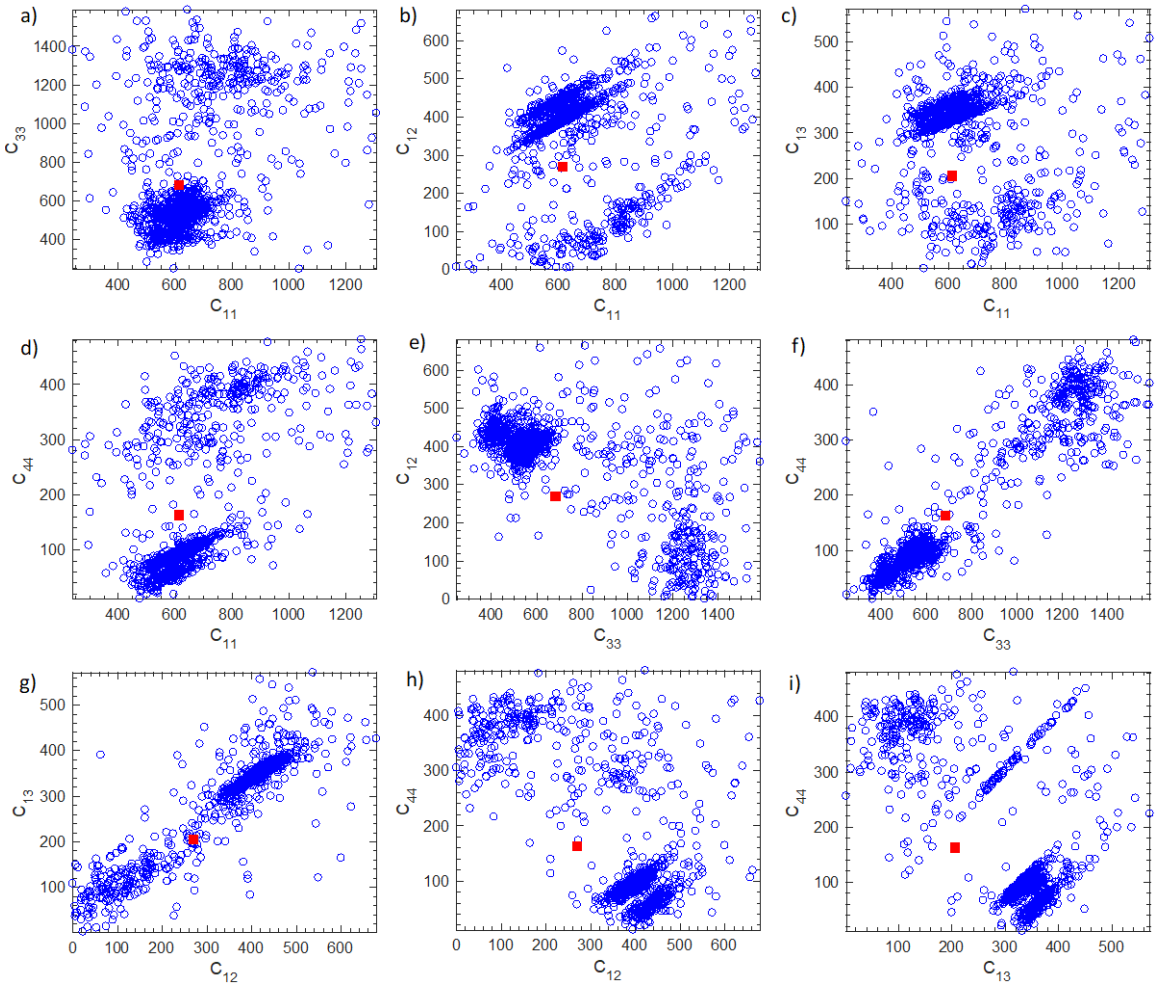

Figure 3. Scatter plots of elastic moduli (in GPa) of hcp Re from 1447 trial sets in dataset2. Data points plotted as red squares denote the target values.

Figures 4-5 show scatter plots among *a*, *c/a*, E_c [hcp], E_c [hcp-fcc], E_c [hcp-bcc], E_f [Vac], and E_f [C]. Some correlations are observed among *a*, E_c [hcp], E_f [Vac], and E_f [C]. No correlations are found between elastic moduli and any of the other properties (not shown).

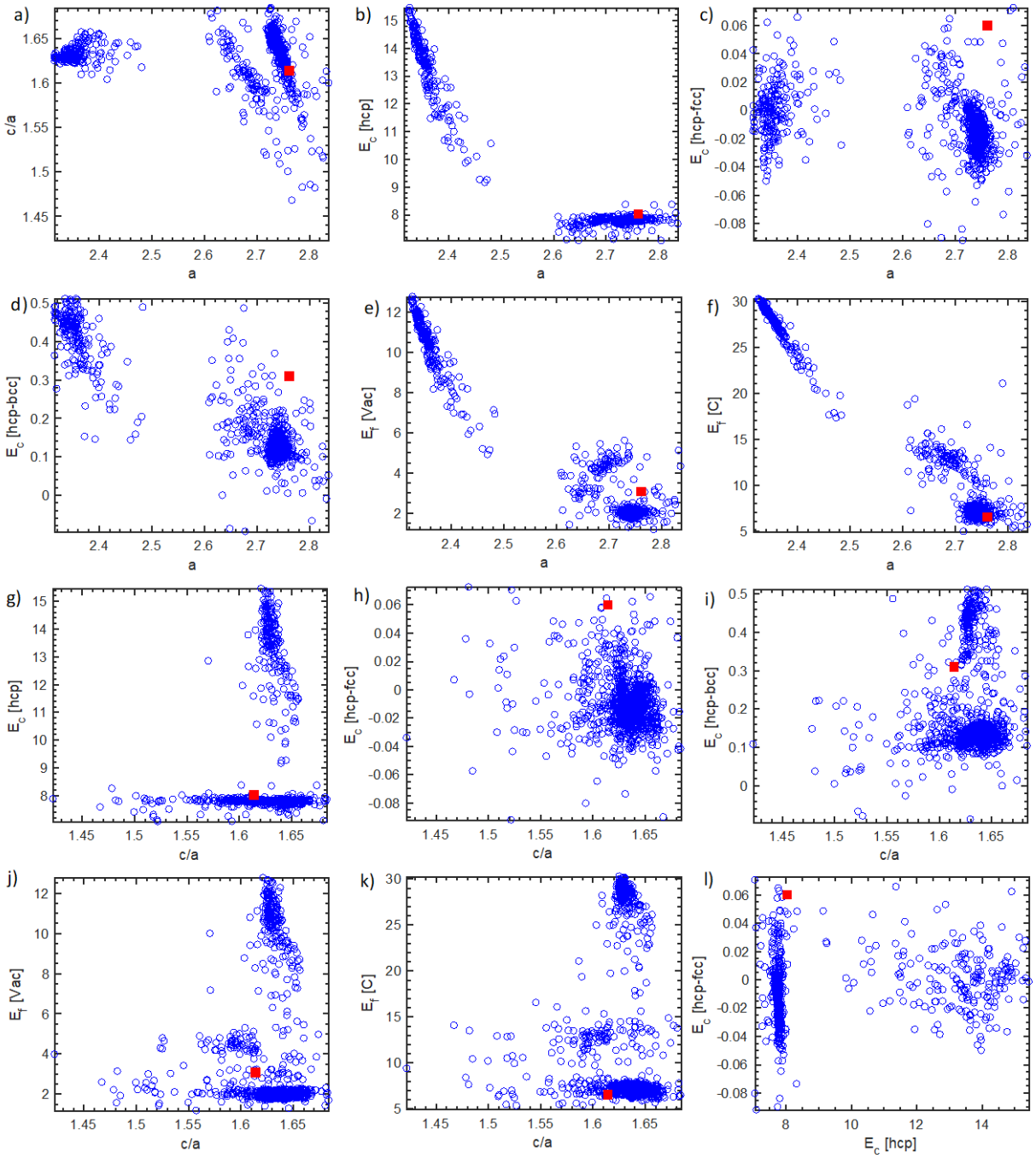

Figure 4. Scatter plots of selected properties from 1447 trial sets in dataset2. Data points plotted as red squares denote the target values.

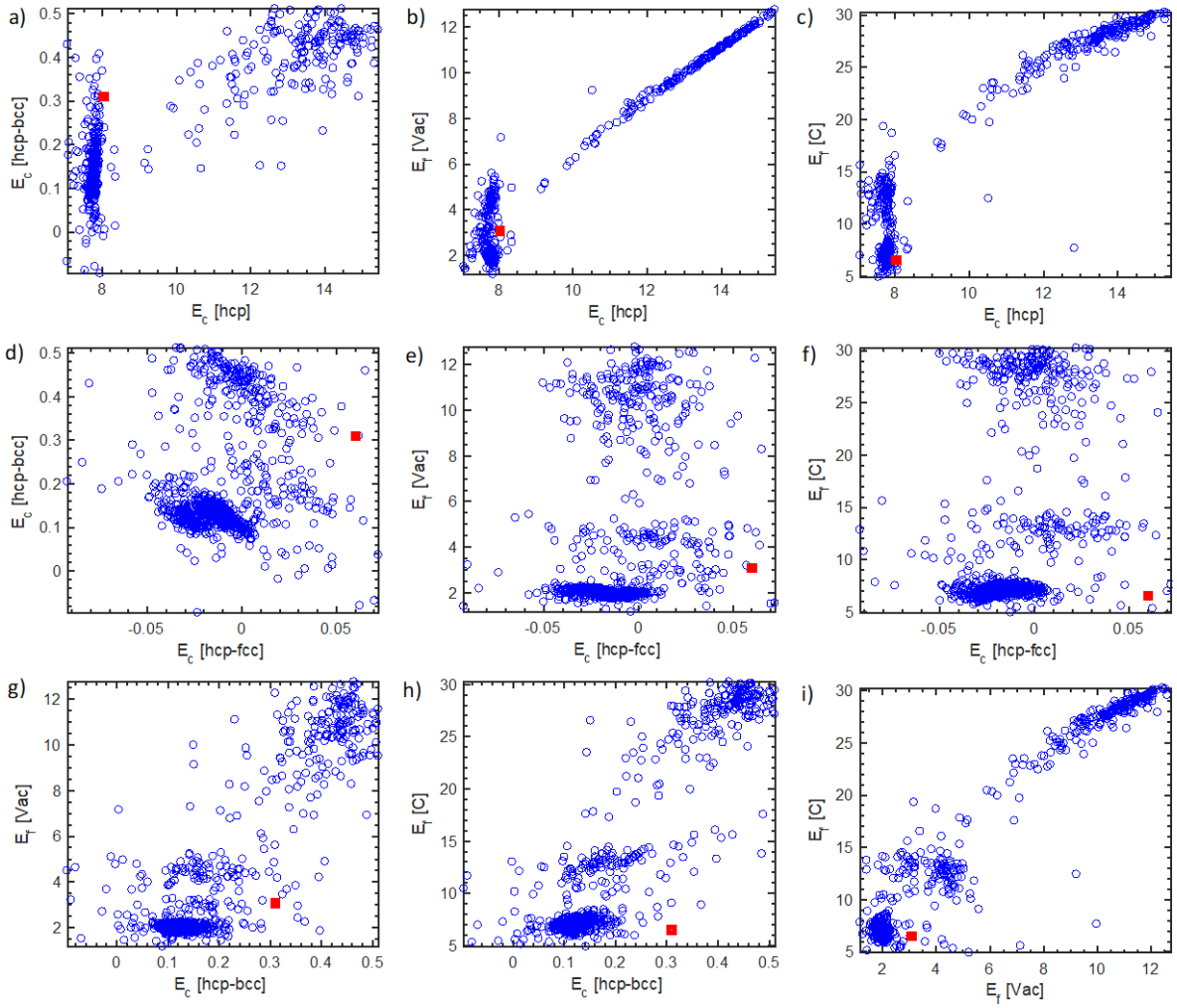

Figure 5. Scatter plots of selected properties from 1447 trial sets in dataset2. Data points plotted as red squares denote the target values.

Neural Network Architecture

Let N_s, L, and M be the number of sets in the dataset, the number of properties, and the number of potential parameters, respectively. Figure 6 shows the schematic of the deep neural network (DNN) model architecture. The architecture is a fully-connected network consisting of, in this example, two hidden layers with L property nodes forming the input layer and M parameter nodes forming the output layer. The nodes in each hidden layer are activated using an activation function, e.g. the rectified linear unit (*ReLU*) function. Users can modify the architecture of the network (e.g. number of hidden layers, the number of nodes in each hidden layer, and the activation function) in the script *ml.py*. As a general guidance in designing the optimum architecture, the number of training variables (N_v) in the DNN model should not exceed N_s to avoid overfitting.

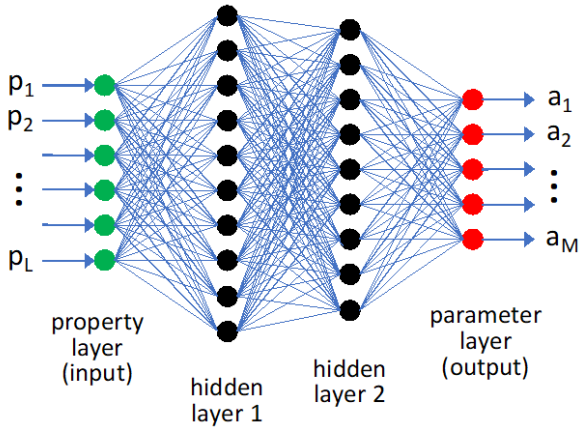

Figure 6. Schematic of a fully-connected deep neural network model used in RFITML where the properties and parameters of an interatomic potential are used as the input and output layer, respectively. The nodes in each hidden layer are activated using an activation function. Users can modify the architecture of the network and the activation function by editing the machine learning script *ml.py* in RFITML.

Training variables consist of weight variables (not to be confused with property error weights) and bias variables. For example, consider a model with two hidden layers: layer 1 with N_1 nodes and layer 2 with N_2 nodes. Each node in a layer (except the input layer) has as many weight variables as the number of nodes in its preceding layer plus one bias variable. Therefore, in this example,

$$N_v = (L+1)N_1 + (N_1+1)N_2 + (N_2+1)M \tag{7}$$

where the first, second, and third terms are the number of variables in layer 1, layer 2, and the output layer, respectively. If all the hidden layers have the same number of nodes (N), the number of training variables become

$$N_v = (L+1)N + (H-1)(N+1)N + (N+1)M \tag{8}$$

where H is the number of hidden layers.

Another general approach to avoid overfitting is to use a portion of the dataset (e.g. 90%) for training and the rest for validation. In this case, the number of training variables in Equations 7 and 8 should be less than the number of sets used for training rather than the whole dataset. In our framework, training a DNN model implies performing a regression to determine the weight and bias variables that minimize the training error. In *ml.py*, users can directly modify various hyper parameters of the regression as well as what portion of the dataset used for validation.

We consider 1302 (90% of 1447) sets dataset2 for training and the rests (145 sets) for validation. In dataset2, knot positions of the series of cubic polynomials used in the pair interaction and the electron density function are fixed. The potential parameters to be optimized with RFITML are f_1 to f_{15} in the pair interaction, g_1 to g_4 in the electron density, and c_1 to c_3 in the embedding energy for a total of M = 22 parameters. The number of properties is L = 19. Equation 8 indicates that for H = 2, 3, and 4, N must be equal to or smaller than 20, 16, and 14, respectively. Figures 7-9 show test potentials obtained with example combinations of H and N. It is found that the shapes of the pair interaction and electronic density function can vary considerably between different test runs, this is also true even for the same H and N. This indicates that the potential parametrization (Equations 1-3) particularly the series of cubic polynomials in the pair interaction and electron density are prone to un-physical shape, hence behaviors. As a result, none of these test potentials yield a stable hcp crystal. Future studies may include examining the dataset for “bad” sets to be excluded from the machine learning fit, researching different DNNs, and testing using a new dataset with a simple analytical parametrization.

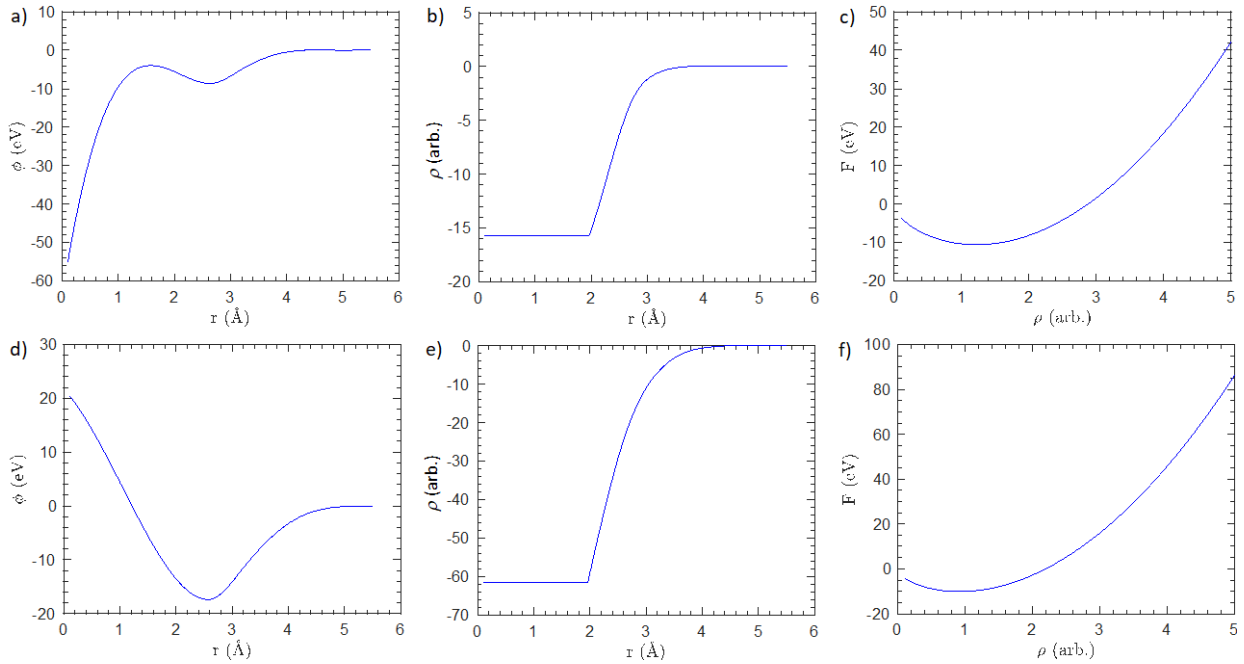

Figure 7. Example potentials obtained with 2 hidden layers, with the number of nodes per layer of 16 (panels a), b), and c)) and 20 (panels d), e), and f)).

For 3 hidden layers, Equation 8 indicates that *N* must be smaller than 17.

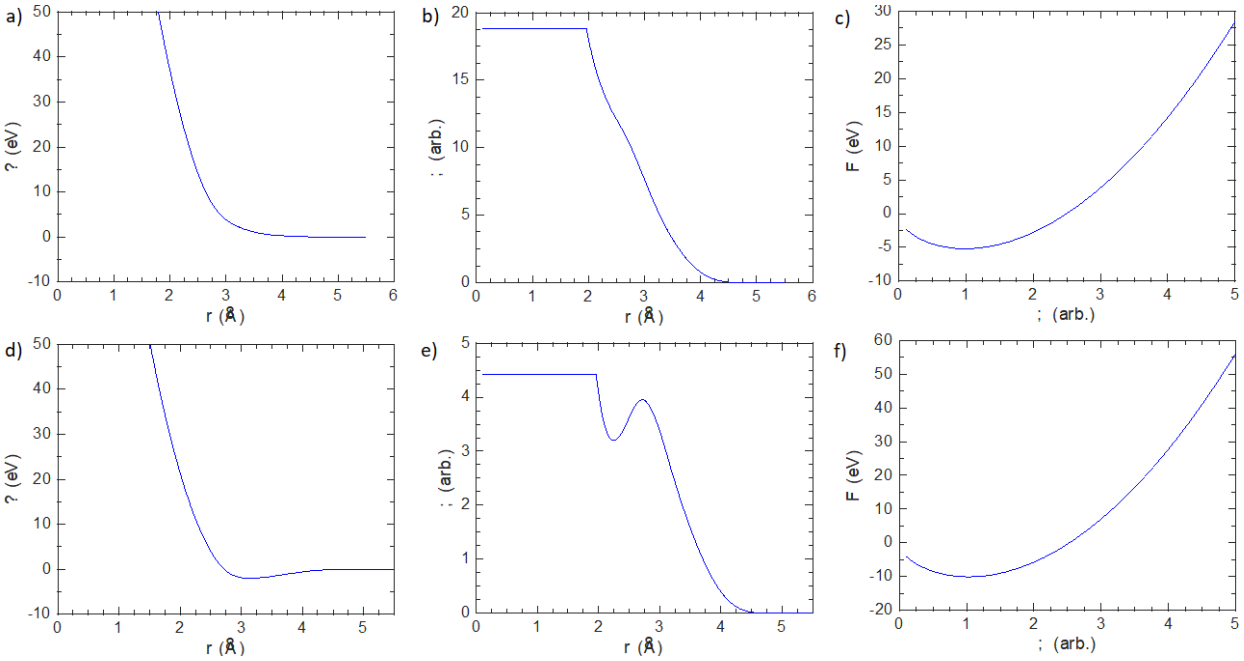

Figure 8. Example potentials obtained with 3 hidden layers, with the number of nodes per layer of 16 (panels a), b), and c)) and 14 (panels d), e), and f)).

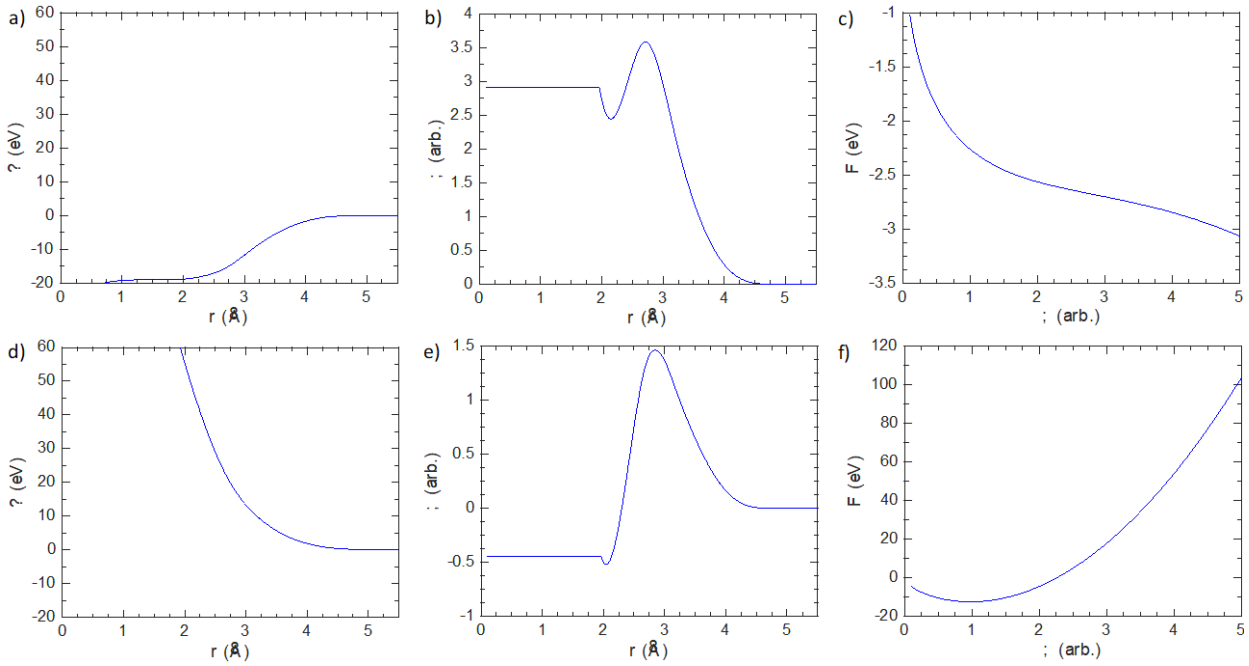

Figure 9. Example potentials obtained with 4 hidden layers, with the number of nodes per layer of 14 (panels a), b), and c)) and 12 (panels d), e), and f)).

Acknowledgements

This research has been supported by the United States Department of Energy, Office of Science, Office of Fusion Energy Sciences (DE-AC05-76RL0-1830).

References

[1] W. Setyawan, N. Gao, R. J. Kurtz, *Journal of Applied Physics* 123 (2018) 205102.
[2] G. Bonny, et al., *Journal of Applied Physics* 121 (2017) 165107.

8.2 THREE-DIMENSIONAL MODELING OF THE EFFECTS OF HELIUM BUBBLES ON THE ROOM-TEMPERATURE STRESS-STRAIN BEHAVIOR OF AN IRON BICRYSTAL BY A MECHANISTIC FINITE ELEMENT APPROACH INFORMED BY MOLECULAR DYNAMICS DATA—B.N. Nguyen, R.J. Kurtz (Pacific Northwest National Laboratory)

OBJECTIVE

The objective of this study is to investigate the effects of helium (He) bubbles on the stress-strain behavior of an iron (α-Fe) bicrystal by a mechanistic finite element (FE) approach using a continuum damage mechanics (CDM) description of the material behavior informed by molecular dynamics (MD) data. The approach models an α-Fe bicrystal system in which the elastic-plastic crystals finely discretized in three-dimensional (3D) finite elements (FE) are connected one to another by cohesive elements. The He bubbles at the GB are explicitly modeled through an equivalent hollow sphere under internal pressure and located in the middle of the modeling domain. Previously, MD and FE analyses of this bicrystal system subjected to uniaxial tensile loading and internal He pressure at 5 K and room temperature (RT) were performed using the LAMMPS software and ABAQUS FE package, respectively. The effects of the He bubbles on the RT stress-strain behavior have been further studied to complete the validation of this modeling approach.

SUMMARY

First, MD analyses of the single crystal and bicrystal lattice configurations ({Σ11 <110> {332} orientation) were performed to compute the uniaxial tensile responses of the α-Fe single crystal and GB. The MD results were then used in FE analyses of the same systems to identify parameters for the CDM constitutive relations for the crystal and the traction-separation law for the GB modeled by cohesive elements. Next, a 3D FE model of the α-Fe bicrystal system with an imperfect GB subjected to uniaxial tensile loading was developed. This model includes an equivalent hollow sphere representing the system with two vacancies under internal pressure in the middle of the GB to model the effects of pressurized He bubbles at RT on stress, strain and damage distributions. Finally, MD stress/strain data of the same bicrystal system with He bubbles were compared to the corresponding FE results to further validate this approach that had been validated previously for the same system at 5 K.

PROGRESS AND STATUS

Background

Ferritic/martensitic steels are considered to be prime candidate materials for structural applications in future fusion reactors [1]. In such applications, these materials are exposed to high-energy neutrons leading to He generation due to transmutation reactions. Formation of He is of particular concern because it can cause hardening and increases in the ductile-to-brittle transition temperature (DBTT) [2-3] and swelling as a result of nucleation and growth of He bubbles [4]. The He also weakens GBs by lowering the GB cohesive stress or by promoting nucleation, growth and coalescence of GB cavities, which can lead to intergranular fracture at high temperature [5]. As it is very difficult to experimentally quantify the effects of nano-scale He bubbles on material integrity, computational methods such MD simulations have been very helpful to elucidate the degradation mechanisms associated with He bubble formation. Although there are a significant number of atomistic studies of He in bulk α-Fe e.g., [6-27], work on He at α-Fe GBs is less extensive [28-38]. Our previous report [39] has shown that a promising and efficient approach to model the effects of He on the material integrity is by FE modeling of an α-Fe bicrystal system in which CDM is used to describe the constitutive behavior of α-Fe and cohesive elements are used to model the GB behavior. In [39], this mechanistic approach was validated through full 3D MD and FE analyses of such a system with perfect and imperfect GB at 5 K and subjected to uniaxial tensile loading. A preliminary study of the He bubble effects at RT was also conducted in [39]. In this report, we have completed the validation of the developed approach by additional analyses of the RT behavior of the same bicrystal system subjected to pressurized He bubbles and uniaxial tensile loading.

Model Development

We refer to our previous report [39] for the details of the FE models developed for analyses of the α-Fe bicrystal systems containing the clean GB (without He bubbles) (Figure 1a) and the GB involving two vacancies depicted by an equivalent hollow sphere occupied by He at a given pressure (Figures 1b and

1c). In these models the two crystals were connected one to another by cohesive elements. The dimensions of the modeling domains are 8 nm x 8 nm x 25 nm. In these models, the vertical displacements of the bottom boundaries were fixed while uniform vertical displacement loadings were incrementally applied on the top surfaces. The loading for the model with He bubbles (Figure 1b) also involved the prescribed internal pressure ramping up to a maximum value at the first loading step before application of the vertical displacement at the next loading step. Figure 1b illustrates a vertical section through the model with an imperfect GB showing the location of the equivalent hollow sphere that is further illustrated in Figure 1c. The constitutive parameters of the elastic-plastic damage model describing the α-Fe stress-strain behavior at RT were identified in our previous report [39]. In addition, the model with the clean GB (Figure 1a) was used to identify the material parameters for the traction-separation law describing the GB [39]. Subsequently, the same set of model parameters for the crystal and GB was used in all the analyses to determine the He bubbles effect on the stress-strain response of the *as-formed* bicrystal system at RT.

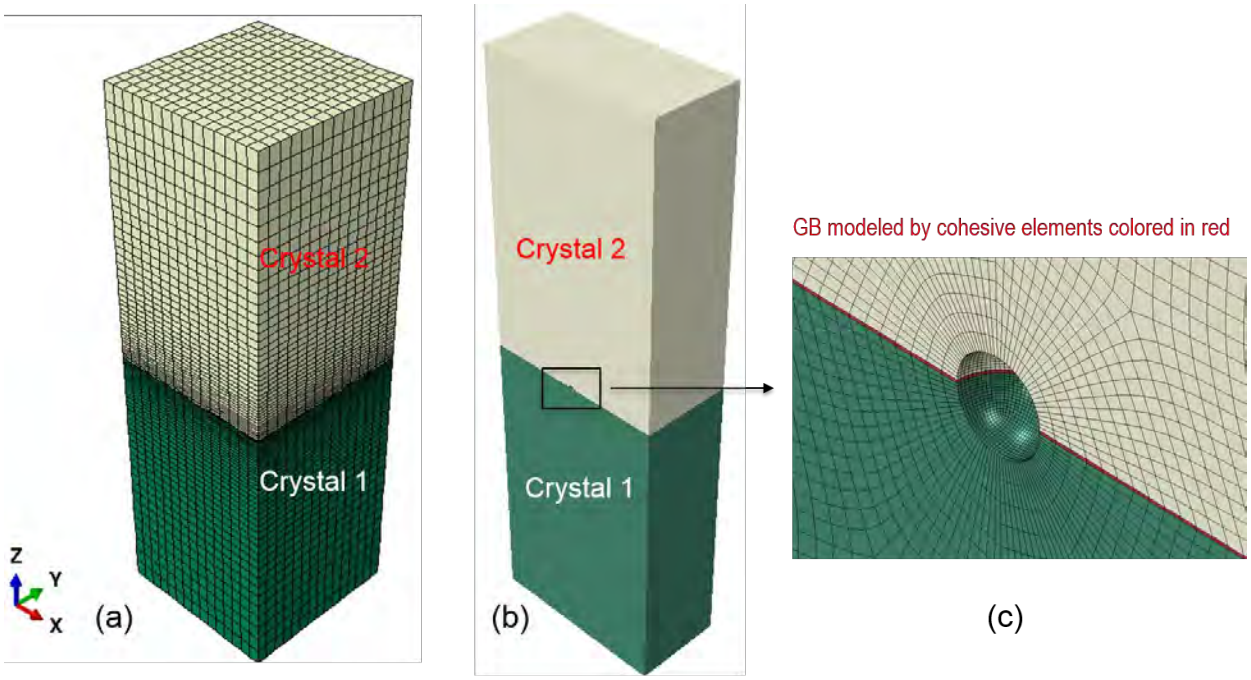

Figure 1. The 3D FE models for the α-Fe bicrystal system subjected to uniaxial tensile loading in the vertical direction (z-direction) – (a) model with clean GB, (b) a vertical cross section of the model with two vacancies depicted by an equivalent hollow sphere occupied by He, and (c) a magnified view showing the hollow sphere region.

Results

In this work, the elastic-plastic model with isotropic hardening and isotropic damage available in the ABAQUS material model options was used for the crystals while cohesive elements were used to describe the behavior of the GB. In the FE model with an imperfect GB, He pressure was applied inside the hollow sphere incrementally to a prescribed level during the first loading step. At the next loading step, while maintaining the He pressure at the maximum prescribed level, uniform vertical displacements were applied on the top model boundary incrementally until the system completely failed.

Figure 2a shows the damage distribution (depicted by the failure indicator) at the onset of total failure (fracture stress σ_r = 11.71 GPa) of the bicrystal system with imperfect GB subjected to 0 GPa He pressure and uniaxial loading at RT. Failure of this system at RT was caused by failure of the GB as illustrated in Figure 2b that shows the GB normal traction stress (S_{zz}) reached the fracture level of 11.71 GPa and started dropping to zero in the region surrounding the hollow sphere. However, at this loading level, ductile damage in the crystals was still moderate as indicated by the failure indicator much less than 1. In our previous report [39], we have found that failure of this system without He bubble pressure at 5 K was caused by

fracture of both the GB and surrounding crystals. For higher He pressures, we found the same fracture mode for the bicrystal system at RT as at 5 K [39] as illustrated in Figures 3a and 3b (compared to the results at 5K reported in [39]) that show the contours of damage and fracture in this system at total failure at RT for 10 and 25 GPa He pressure, respectively. These figures show that failure of the system is caused by fracture of the GB and crystal material surrounding the hollow sphere.

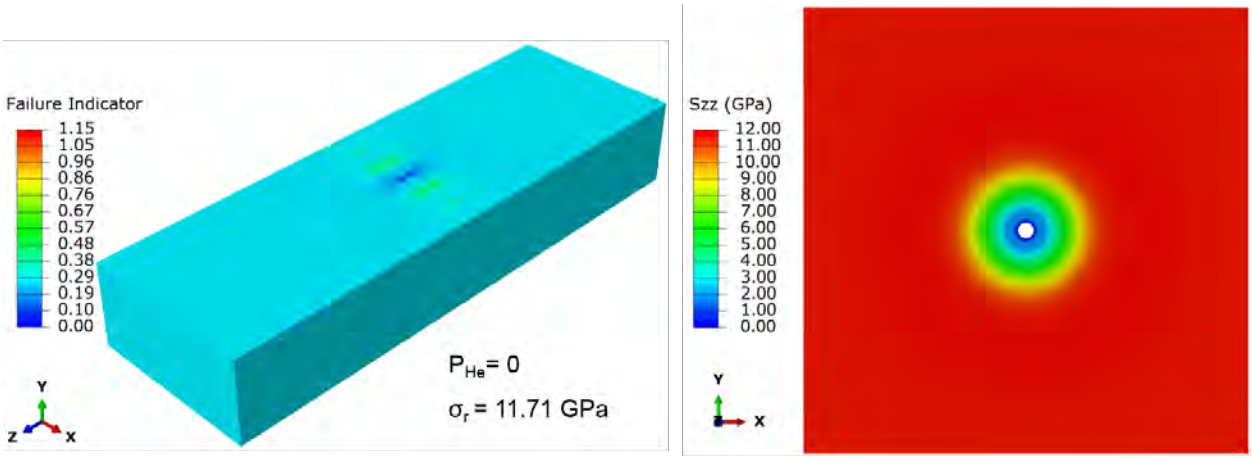

(a) (b)

Figure 2. (a) Damage distributions (viewed through a central cross section along the z-direction) depicted by the failure indicator for 0 GPa He pressure, and (b) Contour of the normal traction stress on the GB at the onset of total failure in the bicrystal system with 2 vacancies at RT.

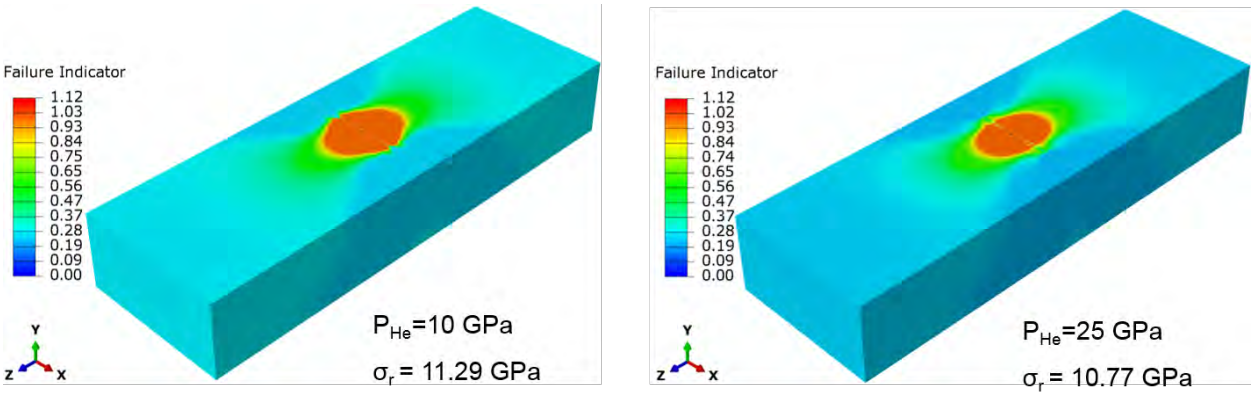

(a) (b)

Figure 3. Damage distributions (viewed through a central cross section along the z-direction) depicted by the failure indicator (1: failed, 0: undamaged) for (a) 10 and (b) 25 GPa He pressure in the bicrystal system with 2 vacancies at RT.

Finally, the effects of He bubbles on the stress-strain response of the bicrystal system at RT are illustrated in Figures 4a, 4b and 4c. Figure 4a shows the CDM predicted fracture stress versus applied strain for increasing levels of He pressure in the system. As observed in 5 K results [39], the presence of vacancies at the GB reduces the system strength and ductility. However, such reductions are less important at RT than at 5 K. With increasing He pressure, a gradual reduction of both failure strain and strength are also

found at RT as illustrated in Figures 5b and 5c, but beyond 26 GPa He pressure, the strength and failure strain reductions are more significant. Figuers 5b and 5c show a good agreement between CDM and MD results also reported on these figures.

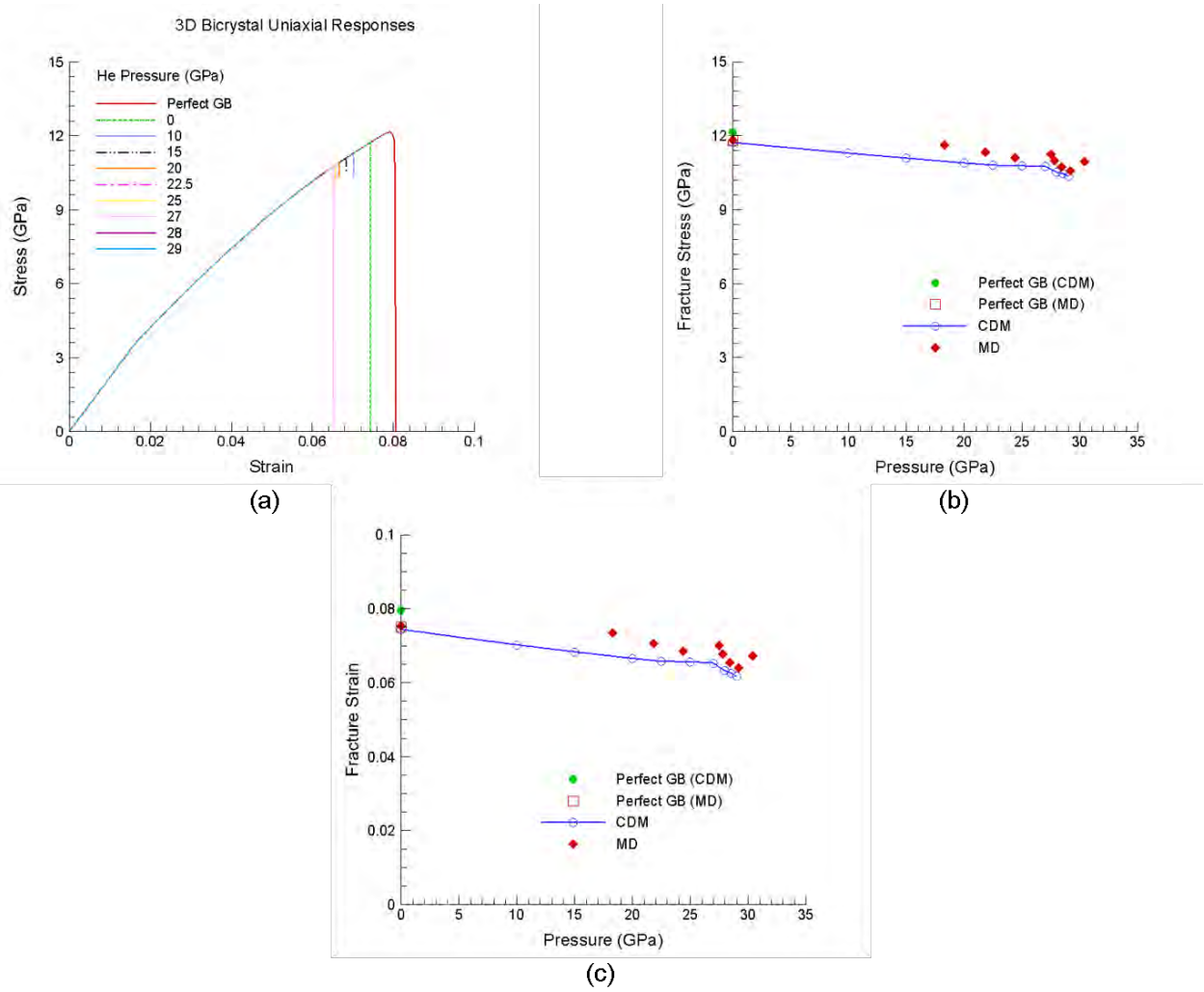

Figure 4. (a) Uniaxial stress-strain responses predicted by CDM FE analysis, (b) strength and (c) failure strain as a function of the He bubble pressure for the α-Fe bicrystal system at RT predicted by CDM FE and MD analyses.

Conclusions

During this report period, the mechanistic FE approach informed by MD data was further developed and validated to investigate the effects of He bubbles on the RT stress-strain behavior of an α-Fe bicrystal system. The results show an important effect of He pressure that reduces material ductility and strength significantly. Our model predictions show as good agreement with MD results at RT as at 5 K previously reported [39]. The developed approach appears to be very efficient in terms of computation time compared to MD simulations. Thus, it can serve as a very good complimentary approach to MD simulations to study He bubbles or other radiation-induced effects on material integrity.

Future Work

We are preparing a journal article to describe the approach and modeling results.

References

[1] A. Kohyama, A. Hishinuma, D.S. Gelles, R.L. Klueh, W. Dietz, K. Ehrlich, J. Nucl. Mater. 233–237 (1996) 138–147.
[2] N. Baluc, R. Schaublin, C. Bailat, F. Paschoud, M. Victoria, J. Nucl. Mater. 283–287 (2000) 731–735.
[3] X. Jia, Y. Dai, J. Nucl. Mater. 323 (2003) 360–367.
[4] F.A. Garner, Materials Science and Technology, Vol. 10A, VCH, Germany, 1994 (Chapter 6).
[5] H. Trinkaus, J. Nucl. Mater. 133–134 (1985) 105–112.
C.C. Fu, F. Willaime, Phys. Rev. Lett. 92 (17) (2004) 175503.
[6] Yang, L., F. Gao, Z.Q. Zhu, S.M. Peng, X.G. Long, X.S. Zhou, H.L. Heinisch, R.J. Kurtz, X.T. Zu, J. Nucl. Mater. 441 (2013) 6.
[7] Yang, L., H.Q. Deng, F. Gao, H.L. Heinisch, R.J. Kurtz, S.Y. Hu, Y.L. Li, X.T. Zu, Nucl. Inst. Meth. Phys. Res. B 303 (2013) 68.
[8] Heinisch, H.L., Gao, F., Kurtz, R.J., Phil. Mag. 90 (2010) 885.
[9] Yang L., Zu, X.T., Gao, F., Peng, S.M., Heinisch, H.L., Kurtz, R.J., Physica B 405 (2010) 1754.
[10] Yang L, XT Zu, F Gao, HL Heinisch, RJ Kurtz, Nucl. Inst. Meth. Phys. Res. B 267 (2009) 3046.
[11] Zu XT, L Yang, F Gao, SM Peng, XG Long, HL Heinisch, RJ Kurtz, Phys. Rev. B 80 (2009) 0541041.
[12] Yang, L., Zu, X.T., Wang, Z.G., Gao, F., Wang, XY, Heinisch, H.L., Kurtz, R.J., Nucl. Inst. Meth. Phys. Res. B 265 (2008) 541.
[13] Pu, J., Yang, L., Gao, F., Heinisch, H.L., Kurtz, R.J., and Zu., X.T., Nucl. Inst. Meth. Phys. Res. B 266 (2008) 3993.
[14] Yang, L., Zu, X.T., Wang, Z.G., Gao, F., Heinisch, H.L., Kurtz, R.J., Wang, X.Y., Liu, K.Z., J. Nucl. Mater. 374 (2008) 437.
[15] Yang, L., Zu, X.T., Wang, Z.G., Yang, H.T., Gao, F., Heinisch, H.L., Kurtz, R.J., J. of App. Phys. 103 (2008) 063528.
[16] Yang, L., Zu, X.T., Xiao, H.Y., Gao, F., Heinisch, H.L., Kurtz, R.J., Wang, Z.G., and Liu, K.Z., Nucl. Inst. Meth. Phys. Res. B 255 (2007) 63.
[17] Yang, L., Zu, X.T., Xiao, H.Y., Gao, F., Heinisch, H.L., and Kurtz, R.J., Physica B 391 (2007) 179.
[18] Heinisch, H.L., Gao, F., and Kurtz, R.J., J. Nucl. Mater., 367 (2007) 311.
[19] Heinisch, H.L., Gao, F., Kurtz, R.J, Le, E.A., J. Nucl. Mater. 351 (2006) 141.
[20] Yang, L., Zu, X.T., Xiao, H.Y., Gao, F., Heinisch, H.L., Kurtz, R.J., Liu, K., App. Phys. Lett. 88 (9) (2006) 091915.
[21] Yang, L., Zu, X.T., Xiao, H.Y., Gao, F., Liu, K., Heinisch, H.L., Kurtz, R.J., Yang, S.Z., Mater. Sci. Eng. A 427 (2006) 343.
[22] T. Seletskaia, Yu.N. Osetsky, R.E. Stoller, G.M. Stocks, J. Nucl. Mater. 351 (2006) 109–118.
[23] K. Morishita, R. Sugano, B.D. Wirth, J. Nucl. Mater. 323 (2003) 243–250.
[24] L. Ventelon, B. Wirth, C. Domain, J. Nucl. Mater. 351 (2006) 119–132.
[25] G. Lucas, R. Schäublin, J. Phys.: Condens. Matter 20 (2008) 415206.
[26] N. Juslin, K. Nordlund, J. Nucl. Mater. 382 (2008) 143–146.
[27] G. Lucas, R. Schäublin, J. Nucl. Mater. 386–388 (2009) 360–362.
[28] Deng, H.Q., W.Y. Hu, F. Gao, H.L. Heinisch, S.Y. Hu, Y.L. Li, R.J. Kurtz, J. Nucl. Mater. 442 (2013) S667.
[29] Heinisch HL, F Gao, RJ Kurtz, in proceedings ASTM 23rd Symposium on Effects of Radiation on Materials, (2009) 190.
[30] Gao F, HL Heinisch, RJ Kurtz, J. Nucl. Mater. 386 (2009) 390.
[31] Kurtz RJ, HL Heinisch, F Gao, J. Nucl. Mater. 382 (2008) 134.
[32] Gao, F., Heinisch, H.L., and Kurtz, R.J., J. Nucl. Mater. 367 (2007) 446.
[33] Heinisch, H.L., F. Gao, R.J. Kurtz, J. ASTM Inter. 4 2007).
[34] Gao, F., Heinisch, H.L., Kurtz, R.J., J. Nucl. Mater. 351 (2006) 133.
[35] Kurtz R.J., Heinisch H.L.,, J. Nucl. Mater. 329-333 (2004) 1199.
[36] T. Suzudo, H. Kaburaki, M. Yamaguchi, J. Nucl. Mater. 417 (2011) 1102–1105
[37] T. Suzudo, T. Tsuru, M. Yamaguchi, H. Kaburaki, J. Nucl. Mater. 442 (2013) S655–S659.
[38] D. Terentyev, X. Hea, A. Serra, J. Kuriplach, Comp. Mater. Sci. 49 (2010) 419–429

[39] Nguyen B.N., R.J. Kurtz, in Fusion Materials Semiannual Progress Report For the Period Ending June 30, 2018, Ch. 8.4, p. 151 ed. FW Wiffen and S Melton, Oak Ridge National Laboratory, Oak Ridge, TN.

8.3 DEVELOPMENT OF A CRYSTAL PLASTICITY BASED DEFORMATION PROCESSING MODEL FOR 14YWT NFA—S. Pal, M. E. Alam, I. J. Beyerlein, G. R. Odette (University of California, Santa Barbara)

OBJECTIVE

The objective of this work is to develop a calibrated model to predict texturing and damage development in 14YWT NFAs based on an in-depth experimental characterization for a sequence of deformation steps that were used to calibrate the Visco-Plastic Self-Consistent (VPSC) crystal plasticity code for evaluating other processing paths.

SUMMARY

Extensive microstructure, texture and hardness characterization of the hot hydrostatically extruded 14 YWT NFA-1 tube, produced from hot extruded and cross-rolled mother plate, reveal that hot hydrostatic extrusion heals the preexisting microcracks without sacrificing the ferrite grain sizes, dislocation density, Y-Ti-O nano-oxides size, volume fraction, density and hardness of the hot cross-rolled alloy plate. However, hydrostatic extrusion transforms the <100> ND texture of cross-rolled plate to a mix of dominant <111> and weak <100> texture in the tube, produces favorable shear texture components of {112}<110> and {111}<110> and suppress the high volume fraction of detrimental {100}<110> texture component of α-fiber, that exists in the cross-rolled plate, by enforcing a shear dominated deformation. Proper parameterization results in VPSC calculated textures for the three sequential deformation processing conditions of hot extrusion, hot cross-rolling, and hot hydrostatic extrusion which is in good agreement with the experimentally observed data. This calibrated VPSC model is used to predict the possible texture evolution during a forging process, showing it to be a viable deformation processing path for the 14YWT-NFA alloy.

PROGRESS AND STATUS

Introduction

Nanostructure ferritic alloys (NFA) have outstanding properties [1–4]. University of California, Santa Barbara (UCSB) collaborated with Los Alamos National Laboratory (LANL) and Oak Ridge National Laboratory (ORNL) to develop a best practice 55 kg batch of a 14Cr NFA (FCRD NFA-1) processed by hot extrusion followed by hot cross-rolling and annealing. The microstructure, texture and mechanical properties characterization of the extrusion and cross-rolled plate were reported previously [4-7]. The as-processed alloy has a near-record strength-toughness combination with a very low DBTT of ≈ -175ºC [5,6]. Unfortunately, the cross-rolled plate contains a large population of microcracks normal to the plate short-thickness direction, running parallel to the plate faces. The microcracks originate during the hot cross-rolling at dislocation pile-ups that form {001} low angle subgrain boundaries. The sub boundaries are the microcrack fracture paths, associated with a high-volume fraction of brittle cleavage α-fiber texture component with {001} planes parallel to the plate surfaces, containing <110> crack propagation directions. Residual stresses produced during cross-rolling, and presence of the high volume fraction of the low cleavage toughness {001}<110> texture component, result in microcrack formation when the plate cools below DBT [7]. The microcracks retard further defect-free processing. We have previously described texture evolution during hot extrusion and hot cross-rolling. Here we extend the characterization of these plane strain dominated conditions, to a shear dominated hot hydrostatic extrusion step. We use experimental data for each processing step, hot extrusion → hot cross-rolling → hot hydrostatic extrusion (HyE) of thin-walled tubing [8], to parameterize the VPSC crystal plasticity code so that it can be applied to other arbitrary deformation processing sequences.

The HyE leads to significant change in the texture components compared to the cross-rolled plate. The dominant <100>∥ND texture, formed during hot cross-rolling, transforms to a mix of weak <100> and dominant <111> texture in the through-thickness direction of the tube. Aydogan et al. reported that hydrostatic extrusion also introduces a high population of low angle subgrain boundary [9]. The VPSC

code was parameterized by this data to establish, for the first time, a relation between texture development and the evolved stress state during deformation.

Experimental Procedure

The details of NFA-1 powder processing and deformation processing of the hot-cross-rolled plate has been described elsewhere [5–7]. The nominal composition of the alloy is 14Cr-3W-0.4Ti-0.3Y and balance Fe. HyE of thin-walled tubing at 815°C was carried out at Case Western Reserve University [8,9]. Figure 1a shows a schematic diagram of the hot-hydrostatically extruded tube, where hydrostatic-extrusion direction (HyED) is parallel to the extrusion direction of the mother plate. The radial direction (RD) is perpendicular to the HyED direction, and with lower symmetry is roughly equivalent to the thickness ND direction of the hot cross-rolled plate.

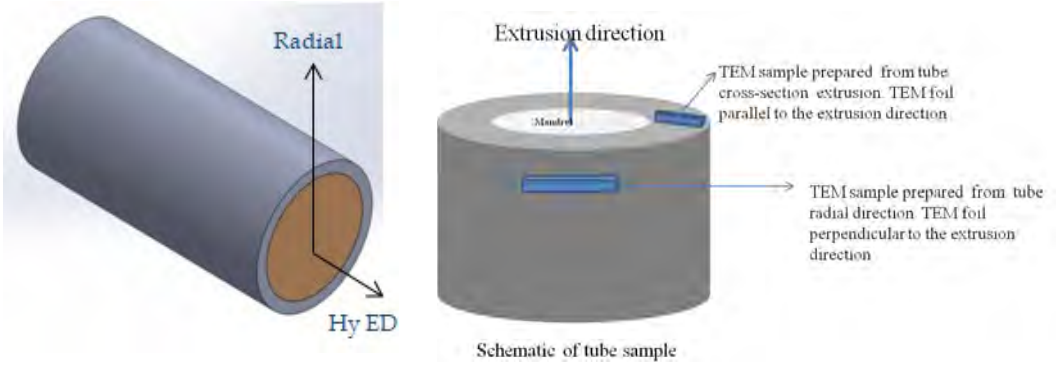

(a) (b)

Figure 1. a) A schematic of the hydrostatically extruded tube showing the different sample directions; and, b) a schematic showing the locations along different plane view sections (orientations) of the HyE tube, from where transmission electron microscopy (TEM) lamellas were extracted.

Microstructure, texture and hardness measurements of the tube were performed on small test pieces cut from both the HyED and RD plane view sections of the tube using electrical discharge machining (EDM). Microstructure characterization was performed on a FEI-XL40 scanning electron microscope (SEM) and FEI-Titan 300kV TEM. The dislocation density of the as-processed tube was also determined using TEM. Thin TEM foils were prepared inside an FEI Helios600 focused ion beam (FIB) microscope using lift out methods. The TEM foils were extracted from both the HyED and RD plane view sections, and their respective locations are shown in Figure 1b. The size, number density, volume fraction and composition of the NOs were analyzed using a Cameca 3000 HRX 3D-local electrode atom probe (LEAP), run in laser mode at 1nJ of laser energy and 35-45 K specimen temperature. A 3D reconstruction of LEAP data was performed using Cameca Integrated Visualization and Analysis Software (IVAS) software. The APT samples were prepared from the HyED plane view section of the tube using FIB-lift out method. Details of the LEAP sample preparation method from a bulk specimen using FIB was given elsewhere [10]. The texture of the as-processed tube was characterized using electron backscatter diffraction (EBSD) technique using an FEI Quanta SEM equipped with an Oxford instrument EBSD camera and HKL software for EBSD data acquisition and processing. Further data processing, and, texture component, grain size, grain aspect ratio, and grain boundary characteristics quantification were performed using MTEX code [11]. Vicker's microhardness of the tube was characterized using a LECO M-400A semiautomatic micro-hardness tester at a 500 g load. A Hysitron Triboscan nanoindenter, attached with a Berkovich tip, was used to measure the nanohardness of the tube. The nanohardness data was analyzed using Oliver-Pharr method [12], as well as SEM measurements of the indent dimensions. Prediction of texture development of NFA alloy during deformation processing was calculated using VPSC modeling technique, originally developed by Lebensohn, Tome et al. [13].

Results

Previous reports on 14YWT NFA-1 alloy plate show elongated pancake-shaped grains with an average size of ≈0.54 ± 0.34μm, and aspect ratio of ≈2.7 ± 1.6 [5]. The microstructure consists of: 1) multimodal size distributions dominated by sub-micrometer size grain; 2) strings of Ti/Y rich impurity phase (inclusions) aligned towards in the primary deformation directions; 3) 2-5 nm Y-Ti-O nano-oxides; and, numerous microcracks, ranging from 1-100 μm, in planes parallel to the plate faces running in the primary deformation directions [5–7]. Notably, as shown in Figure 2, SEM micrographs of the cross-section of the HyE tube do not exhibit any microcracks. That is the microcracks are healed under HyE, resulting in a defect-free tube.

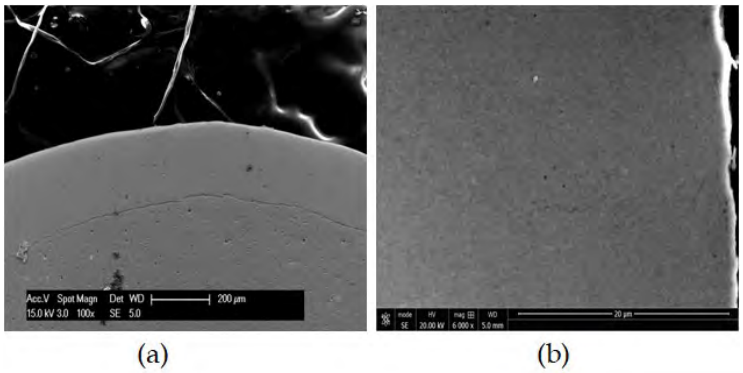

Figure 2. The SEM micrographs of NFA-1 tube; a) a low magnification image of the cross-section of the HyE tube; and, b) a high magnification image of the marked region in Figure 2a.

The EBSD scan inverse pole figures in Figure 3 show a moderate texture intensity of <110> α-fiber along the HyED, along with a mix of dominant <111> and some <100> in the RD. Similar textures for the HyE tube, using both neutron and EBSD techniques, were reported by Aydogan et al. [9].

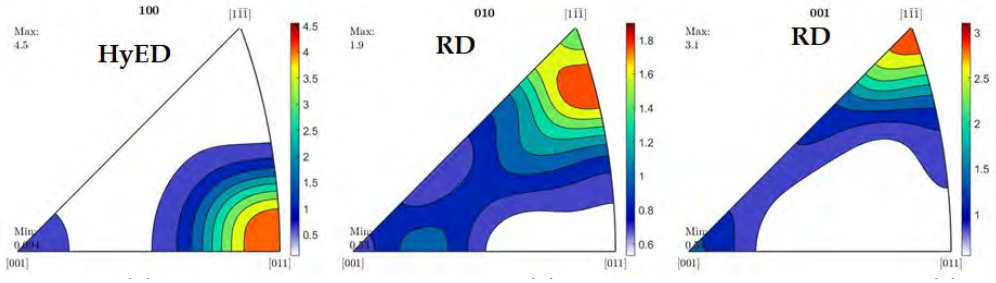

Figure 3. The IPFs of HyE tube: a) the HyED plane view; b) and c) the RD plane (equivalent to the thickness direction of the cross-rolled plate) views.

Figure 4 shows the IPF imaging maps along the HyED and RD plane view sections of the tube, respectively, where the inset color coding represents different crystallographic direction. A majority of the green color, representing <110> direction, is observed along the HyED plane view section. A mixture of red (<100>) and blue (<111>) are observed on the RD plane view section IPF. Quantitative measurements of grain size, grain aspect ratio, and volume fraction of different grain boundary (GB) populations were extracted from the IPF maps using the MTEX code [11]. A misorientation criterion of 15° was chosen to define the low versus high angle grain boundaries. Figure 5 shows that the HyE produces a large fraction of low angle grain boundaries, consistent with the results of Aydogan et al. [9]. Grain sizes and grain aspect ratio data are shown in Figure 6. About 80 to 90% of the grains have a mean diameter of ≈ 0.48 μm. The HyE process significantly reduces the volume fraction of α-fiber and increases the

amount of γ-fiber, which is beneficial for forming processes. The respective volume fractions of the α and γ fiber after cross-rolling and HyE are shown in Table 1.

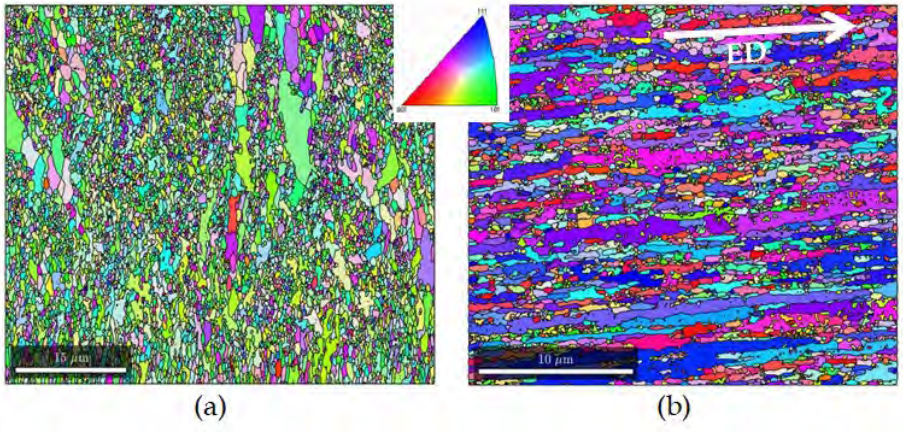

Figure 4. The IPF maps of HyE tube: a) the HyED plane view; and, b) the RD plane view.

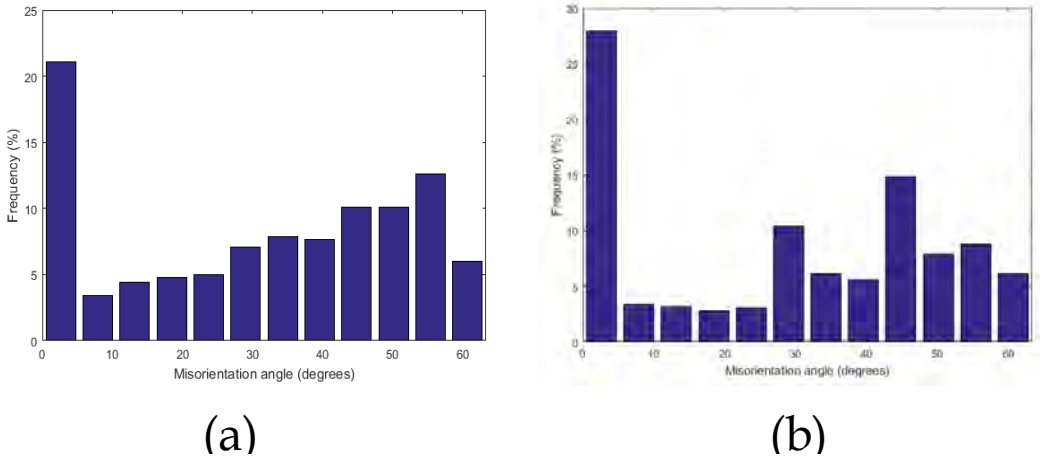

Figure 5. The GB misorientation angle distribution calculated using MTEX code from the EBSD data for the: a) HyED plane view; and, b) RD plane view sections of the tube.

Table 1. The volume fractions of α and γ fiber in the cross-rolled plate and hydrostatically extruded tube

Deformation processing	Vol. frac. of α-fiber	Vol. frac. of γ -fiber
Cross-rolled plate	44.8 %	9.96 %
Hydrostatically extruded tube	19.09	17.11

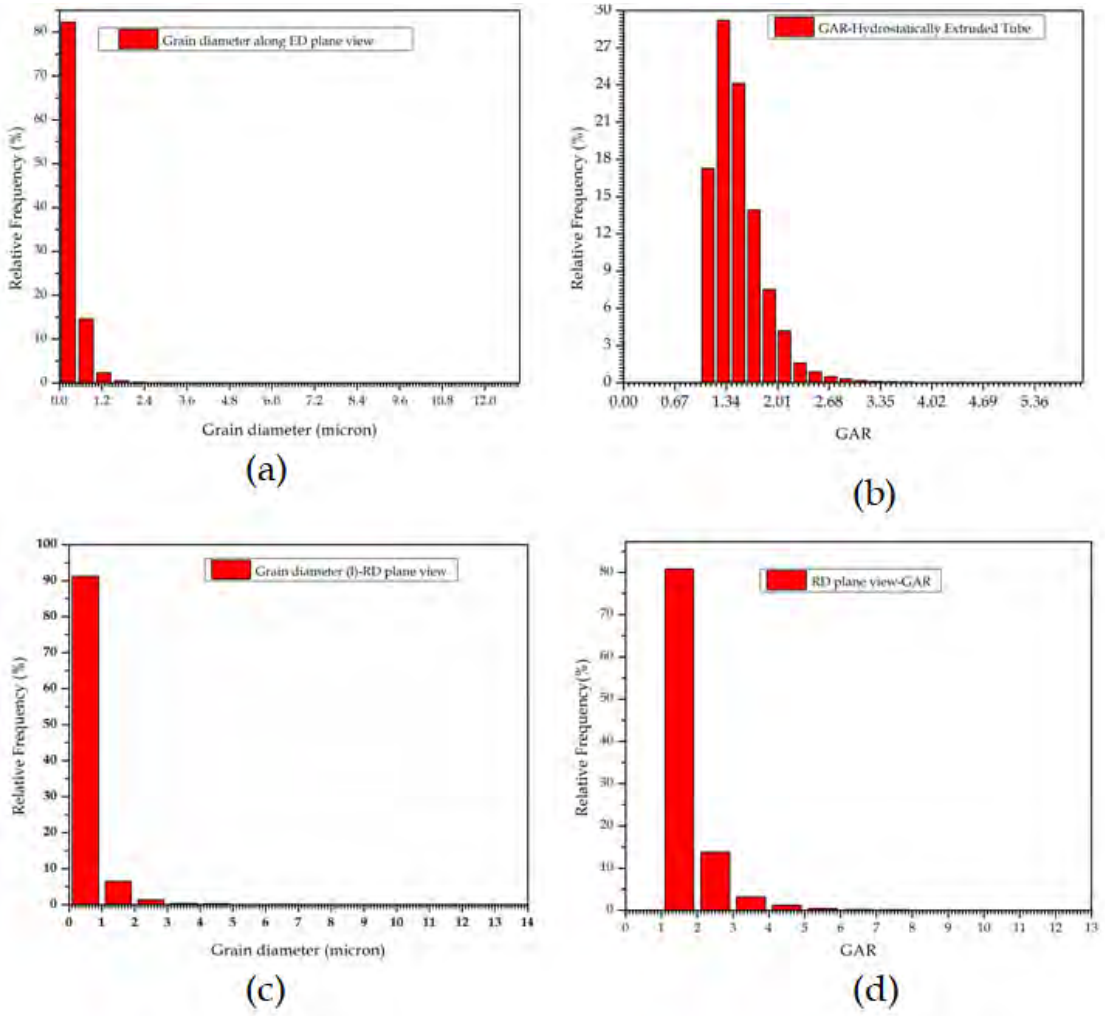

Figure 6. a) grain size distribution, b) grain aspect ratio distribution plots for the HyED plane view section; c) and d) plots of grain size and grain aspect ratio distribution for RD plane view section, respectively.

A more quantitative texture quantification of the HyE tube was performed using orientation distribution function (ODF), that previously showed that hot cross-rolling led to the formation of high-volume fraction of {001}<110> brittle texture components. The ODF maps of the RD plane view section of the tube shows a maximum texture intensity around the {112}<110> and {111}<110> texture components when compared to the ideal ODF plots of same φ_2 sections for bcc-Fe, as shown in Figures 7c and d.

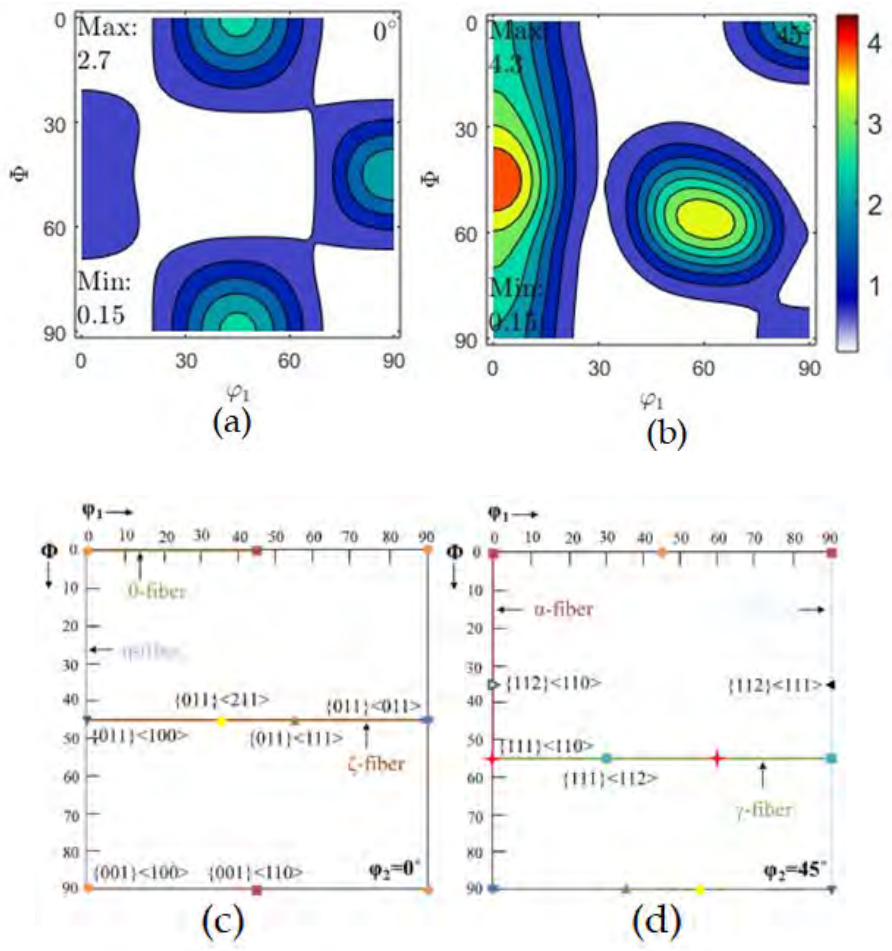

Figure 7. The 2D-ODF sections plots of the RD plane sections of the HyE tube a) φ_2 =0° section; b) φ_2 = 45° section; c) and d) ideal ODF plots for bcc-Fe at φ_2 =0 and 45° sections showing the locations of different texture components.

Transmission electron microscopy observations

The EBSD data shows that HyE alters the texture of the as-processed tube in the through-thickness radial direction and also affects grain size and morphology. The HyE also heals the microcracks in the cross-rolled plate more and introduces a high population of low angle grain boundaries.

The BF-TEM images in Figure 8 show a high dislocation density and low angle grain boundary is observed in the TEM images of Figure 6. The dislocation density was determined from different sets of bright field images for the same locations at different two-beam conditions. Average dislocation density of the foil has been measured under two-beam conditions. Assuming the dislocations are randomly oriented, their densities are given by $\rho = 2N_dM/Lt$. Here, N_d is the number of intersections that a random straight test line laid on a TEM image makes with the dislocations, L is the length of the test line, t is the thickness of the foil and M is the magnification of the micrograph. To minimize dislocation orientation effects, the intersections were counted using two concentric circles instead of straight lines [14]. The foil thickness was determined using the convergent beam electron diffraction (CBED) technique. Representative two beam BF image for (002) reflections for the two beam-condition and corresponding CBED pattern are shown in Figure 9.

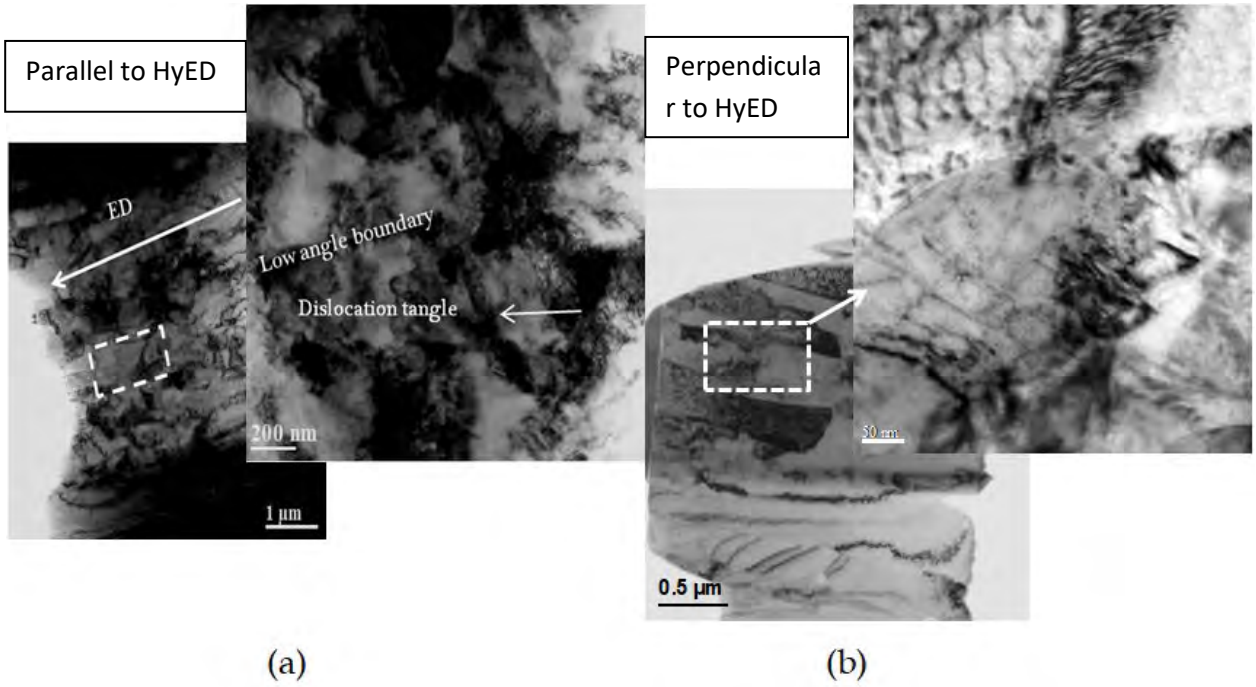

Figure 8. Both the low and high magnification bright-field TEM image of the tube: a) the hydrostatic extrusion direction is parallel to the TEM foil; and, b) the hydrostatic extrusion direction is perpendicular to the TEM foil.

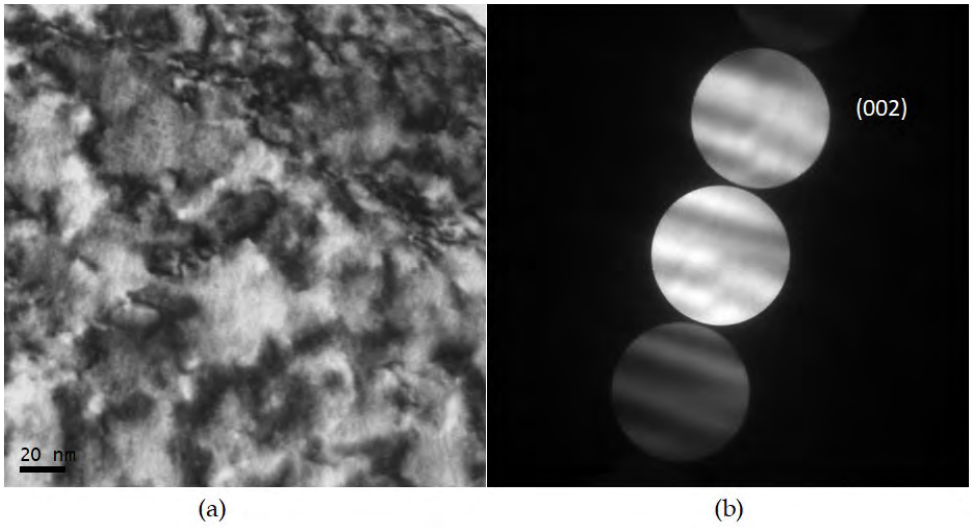

Figure 9. a) A two- beam condition BF-TEM image for the (002) reflection; b) a CBED pattern showing the alternative dark and white bands within the (000) and (002) reflections (the (002) disk is marked in Figure b).

The measured value of dislocation density in the TEM foils is 0.9 ± 0.42 X 10^{15} m/m^3 which is similar to those previously measured dislocation in the NFA plate [4]. Thus, HyE does not decrease the high dislocation density already present in the hot cross-rolled alloy plate.

APT analysis

As illustrated in Figure 10, NOs were identified in the reconstructed data using both iso-concentration surfaces and the maximum separation distance methods for the solute ions of interest, namely, Y, Ti and O, including their complex ionic forms like TiO and YO [15]. The NO average radius (<r>), volume fraction (f_v %), number density (<N>) were calculated from the APT reconstruction based on the method described by Cunningham et al. [4]. The average size (<r>), volume fraction (f_v %) and number density (N) of NOs in the hydrostatically extruded tubes are shown in Table. 2. Bulk average composition of the alloy and NOs are shown in Tables 3 and 4. The NO compositions include only the Y, Ti and O fractions as the nominal Fe and Cr are believed to be artifacts, although some Cr is segregated to the matrix side of the interface.

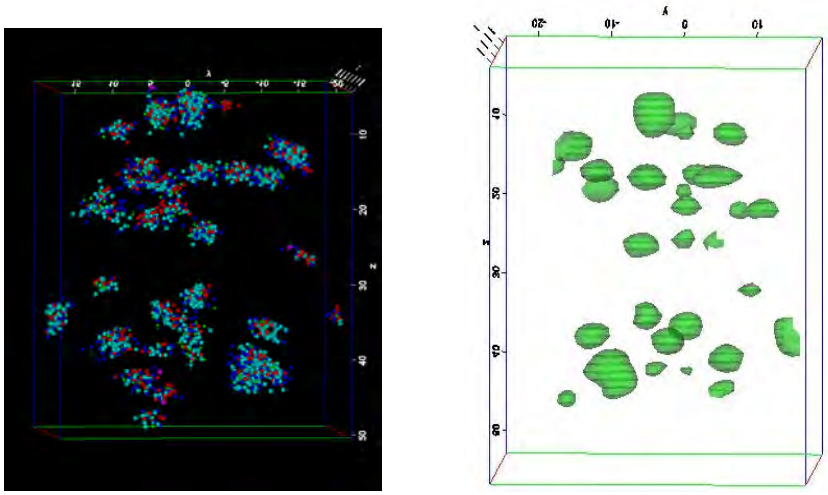

(a) (b)

Figure 10. a) Nano-cluster identified using the maximum separation method algorithm; b) TiO iso-surface reconstruction from the same tip.

Table 2. The average volume fraction (f_v), number density (N) and average size (<r>) of the nano-oxides

	f_v (%)	**N (/m^3)**	**<r> (nm)**
HyE tube 1	0.23 ± .0.098	2.709 ± 2.815 X10^{23}	1.43 ± 0.41
HyE tube 2	0.16 ± .0.03	6.52 ± 5.44 X10^{22}	1.79 ± 0.11

Table 3. The bulk composition of the hydrostatically extruded tube

Elements	**Fe (at.%)**	**Cr (at.%)**	**Ti (at.%)**	**Y (at.%)**	**W (at.%)**
HyE Tube 1	83.99 ± 0.71	14.77± 0.55	0.27 ± 0.09	0.08 ± 0.03	0.66 ± 0.18
HyE Tube 2	84.48± 0.71	13.80± 0.42	0.43 ± 0.27	0.22± 0.13	0.59± 0.02

Table 4. The composition of NOs in the hydrostatically extruded tubes

Elements	Fe (at.%)	Cr (at.%)	Ti (at.%)	Y (at.%)	O (at.%)
HyE Tube 1	65.23 ± 7.05	17.27 ± 0.42	8.71 ± 2.62	2.27 ± 0.76	6.01 ± 1.86
HyE Tube 2	62.96 ± 4.36	17.78 ± 1.10	12.95 ± 1.10	2.87 ± 0.35	14.45 ± 2.75

Comparing previously reported data of NOs size, volume fraction and number density [4,16,17] with our present observation (see Table 2), it can be concluded that HyE process does not affect the NOs characteristics as well as statistics in the as-processed tube.

Hardness

Vickers micro-hardness (H_v) of the hot-cross-rolled plate is ≈ 366 ± 30 kg_f/mm^2 [5]. This is similar to the Hv ≈ 379 ± 20 kg_f/mm^2 observed for the HyE tube. Therefore, it has been observed that HyE does not change the hardness of the alloy. The nano-hardness of the tube was measured at five different loads, 4, 6, 8, 10 and 15mN, to determine the indentation size effect. Figure 11a shows the load versus hardness data, which saturates at ≈ 8mN load. The typical indentation depth at 8mN applied load is ≈ 200 nm. Therefore, nanoindentation measurements across the tube cross-section at a 10mN load, with an indentation depth well above 200 nm.

Figure 11b plots the nanohardness values across the cross-section of the tube, which are approximately constant at ≈ 4.6 GPa. However, it has been observed that when we convert the Vickers scale hardness unit to GPa, the measured average microhardness value of the HyE tube along the thickness is ≈ 1GPa lower than the measured nanohardness value. In order to resolve this difference, both the micro and nano indentation were observed using a SEM, as shown in Figure 12. The hardness value for both cases were determined using the formula, $H_v = P/(24.5d^2)$, where H_v is the hardness, P is the applied load and d is the penetration depth of the indenter. The d for Vickers hardness is one-seventh of the measured diagonal of the square impression. Similarly, for the Berkovich tip, the penetration depth is one-seventh of the measured vertices separation distances of the triangular shape impression. As shown in Table 5, the measured nano and microhardness values by measuring the indentation impression are much closer to one another. Optical measurement of the standard Vickers diagonal length is larger than the values for the SEM measurements. Hence, the H_v from the microhardness tester is lower compared to that obtained by measuring the indent diagonal in SEM.

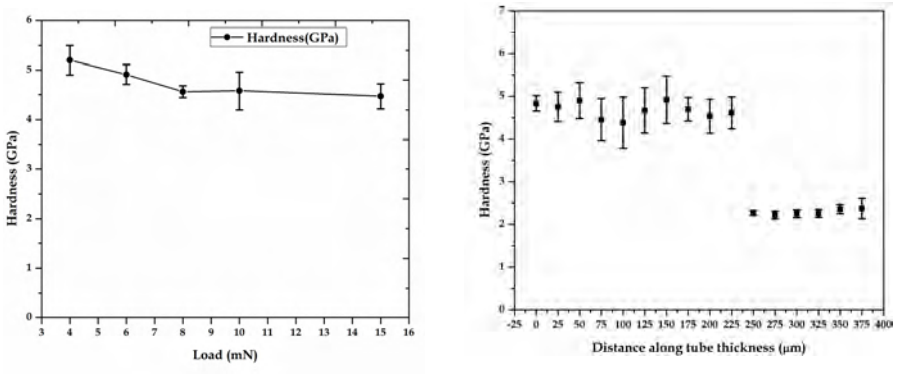

Figure 11. a) Nanohardness measured at different loads, and b) hardness variation across the thickness of the HyE tube. The lower values are for the mandrel.

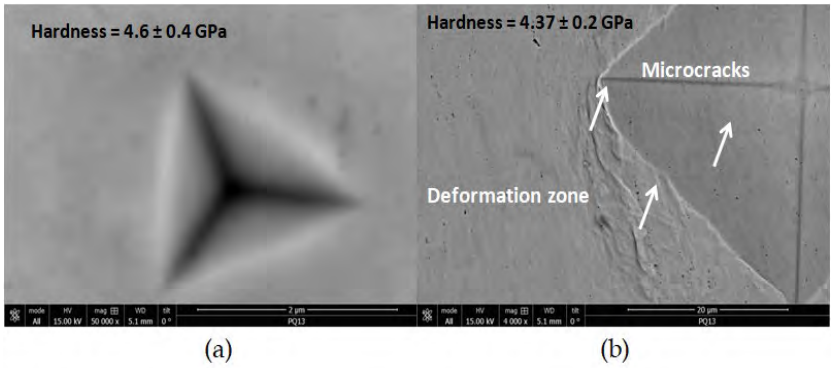

Figure 12. SEM images of the indents: a) nanoindentation; and, b) microindentation.

Table 5. Micro- and nanohardness measurements

NFA-1	Nano-hardness (GPa) Oliver-Pharr	Nano-hardness (GPa) SEM	Micro-hardness (GPa) OM	Micro-hardness (GPa) SEM
HyE Tube 1	4.58 ± 0.58	4.61 ± 0.4	3.72 ± 0.2	4.37 ± 0.16
HyE Tube 2	4.42 ± 0.59	4.48 ± 0.2	3.58 ± 0.19	4.24 ± 0.1

VPSC modeling

In VPSC scheme, each grain and orientation is considered as a visco-plastic inclusion embedded in a homogeneous effective visco-plastic medium (HEM), that represents average properties of all grains or orientations. The response of the medium need not to be known previously; rather, it is adjusted 'self-consistently' to coincide with the average response of all the orientations constituting the aggregate, where, the interaction between the aggregate and HEM scales with their relative stiffness. Numerically generated 1000 random crystallographic orientations were used for the calculation, assuming a pencil glide deformation mode of bcc-Fe, intermediate stiffness scheme between the aggregate-HEM interaction, a low value of strain hardening exponent (n=20), zero latent hardening and Voce type strain-hardening during the deformation. A similar type of approach has recently been used to simulate the occurrence of strong α-fiber in severely cold-rolled low carbon steel [18]. The Voce hardening parameters are determined by fitting the 800℃ uniaxial tensile test data of NFA-1 [5,19]. The VPSC was performed by imposing three sequential processes of hot-extrusion, hot-cross-rolling, and hot-hydrostatic extrusion on the initial random orientation. Each of the three processes in the calculation is defined by applying three different strain rate tensors in the VPSC code, as given below: $\dot{u}=\begin{bmatrix}1 & 0 & 0\\ 0 & -0.5 & 0\\ 0 & 0 & -0.5\end{bmatrix}$ for hot-extrusion, $\dot{u}=\begin{bmatrix}1 & 0 & 0\\ 0 & -0.35 & 0\\ 0 & 0 & -0.65\end{bmatrix}$ for hot cross-rolling, and, $\dot{u}=\begin{bmatrix}1 & 0 & 0\\ 0 & -0.5 & 0.05\\ 0 & 0.05 & -0.5\end{bmatrix}$ for hydrostatic extrusion.

At first, canned NFA-1 powder is consolidated by hot-extrusion to produce a square-shaped billet bar which is further cross-rolled perpendicular to the extrusion direction to produce a plate. During consolidation and cross-rolling, the NFA is confined within the mild steel can. In the case of hot-extrusion, a negative value of 0.5 is assigned for ε_{22} and ε_{33} strain rate components. The ε_{22} and ε_{33} strain rate components have same value due to square shape cross-section of the extruded billet, whereas

reduction in cross-sectional area after extrusion is indicated by a negative strain along both the y and z-direction compared to the ε_{11} principal strain along the x or extrusion direction. The alloy is deformed up to a uniform von Mises strain of 1.4. Figures 13a and b show φ_2 =0 and 45°section of the experimentally measured ODF plots of hot-extruded billet bar, respectively. Calculated texture for the hot-extrusion of NFA-1 alloy is shown for the same φ_2 =0 and 45°sections of the ODF plots in Figures 13 c and d.

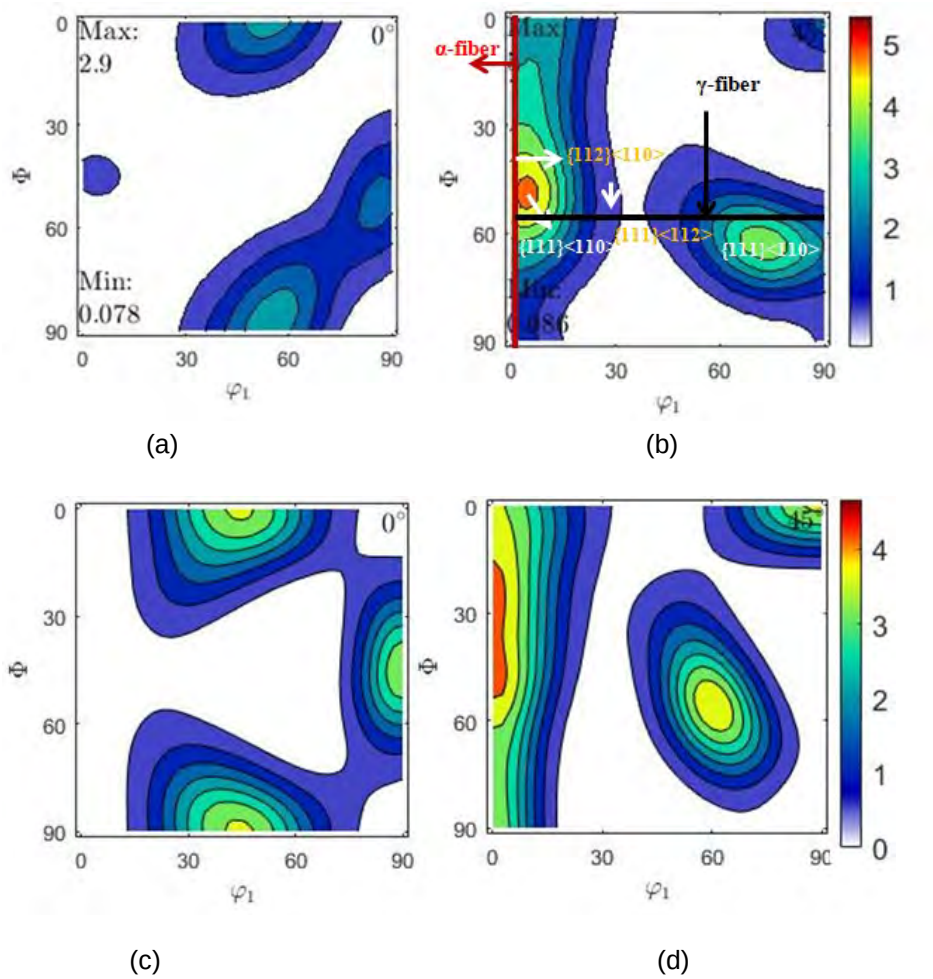

Figure 13. a) and b) show the φ_2 =0 and 45°section of the experimentally measured ODF of the hot-extruded billet bar. c) and d) shows the φ_2 =0 and 45°section of the ODF obtained from VPSC simulation of the hot-extrusion of NFA-1 alloy.

Figures 13 c and d indicates that calculated texture for the hot-extrusion process matches quite well with the experimentally measured ODFs of the hot-extruded billet bar, as seen in Figures 13a and b. Experimentally measured and calculated texture of the hot-extruded NFA-1 alloy shows the highest texture intensity at around {112}<110> and {111}<110> (comparing with the ideal bcc ODF shown in Figures 7c and d); however, calculated ODF shows a more uniform spreading of texture intensity around {112}<110> texture components; see Figure 13d.

Texture development during cross-rolling was simulated by deforming the hot extruded orientations produced by the VPSC simulation of hot extrusion of initial random orientations, with a von Mises strain of 0.7. For simulation of a rolling operation; typically the ε_{22} value is always chosen as zero, and, ε_{33} is considered as equal to ε_{11} in magnitude, but opposite in sign. However, for the present case, the hot

cross-rolling is performed perpendicular to the extrusion direction of the billet bar, which is still confined inside the mild steel can. Therefore, $\varepsilon_{22} = 0$ is not a valid assumption for the present case. Hence, we have chosen $\varepsilon_{22} = -0.35$ and $\varepsilon_{33} = -0.65$ based on the final dimensions of the rectangular cross-section of the rolled plate. Due to the constraint imposed by the mild steel can on the NFA-1 square billet, we observed non-zero strain along all principal directions. A schematic of the cross-rolling of NFA-1 is shown in Figure 14.

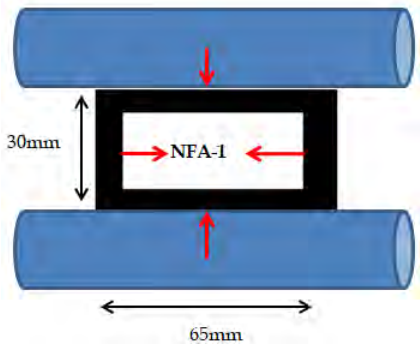

Figure 14. A schematic of the rolling process shows a rectangular cross-section of the plate.

The corresponding experimentally measured and calculated texture ODF plots for the cross-rolled NFA-1 plate are shown in Figure 15.

A high-volume fraction (≈44 %) of the {001}<110> texture component of the α-fiber is observed in both the experimentally measured and calculated ODF of cross-rolled NFA-1 alloy.

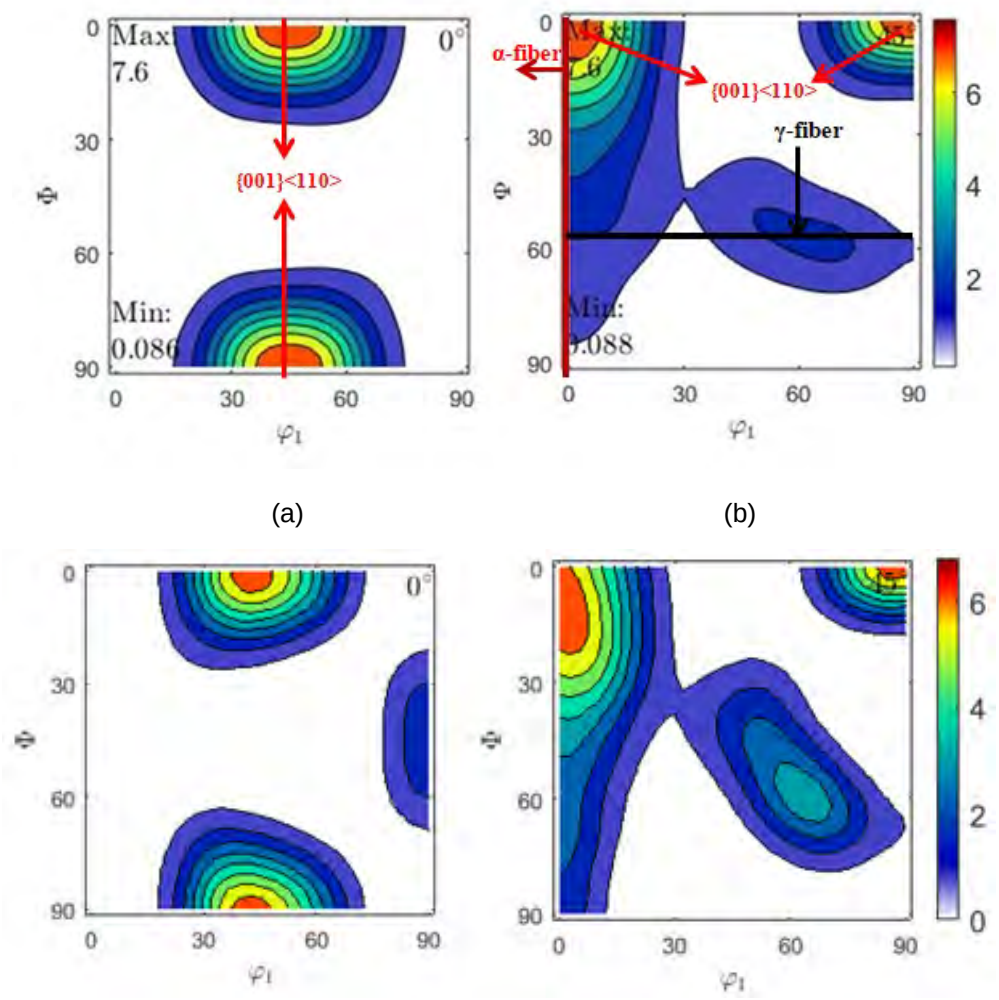

Figure 15. Experimentally measured ODFs are shown in: a) for φ_2 =0, and b) φ_2 = 45°sections, whereas their simulated ODF are shown in: c) and, d) at φ_2 =0 and φ_2 = 45°, respectively, for the hot-extruded and cross-rolled plate.

The VPSC simulation of hydrostatic extrusion (see Figure 16) of the cross-rolled plate mandrill-mounted mother tube was performed by adding the suitable strain rate tensor in the VPSC code, based on the previously reported result that during the hydrostatic extrusion process, shear stresses operate in the through the thickness direction of the extruded material, along with an applied hydrostatic compressive stress [20].

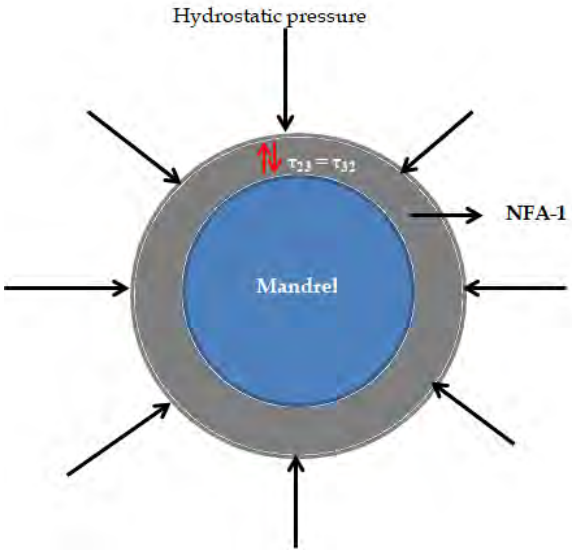

Figure 16. A schematic cross-section of the hydrostatically extruded tube. The directions of the applied stresses are also shown.

Therefore, we have introduced small but non-zero shear stress (τ_{23}= τ_{32} =0.05) component in the y-z plane or plane perpendicular to the extrusion direction. The strain rate tensor used for deforming the cross-rolled orientations can be written as, $\dot{u} = \begin{bmatrix} 1 & 0 & 0 \\ 0 & -0.5 & 0.05 \\ 0 & 0.05 & -0.5 \end{bmatrix}$. The cross-rolled orientations are deformed up to a von Mises strain of 1.4 during hydrostatic extrusion. When we consider the three deformation processes together, like HyE tube formation from the NFA-1 powder, the total von Mises strain imposed during the calculation is ≈ 3.5.

The ODF plots of the calculated texture for hydrostatic extrusion of NAF-1 alloy are shown in Figure 17.

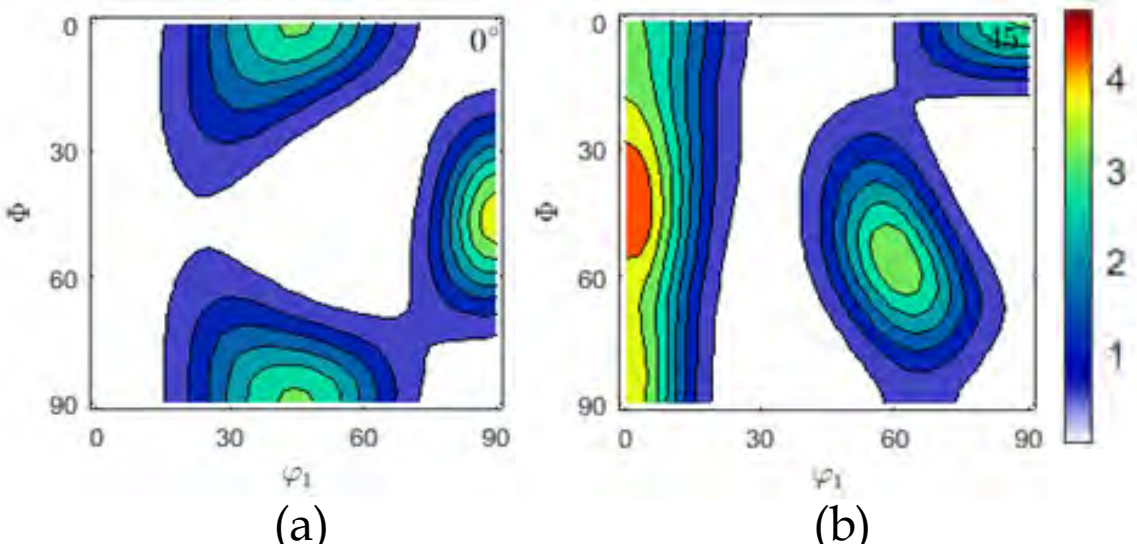

Figure 17. Calculated ODF sections for a) φ_2 =0 degree; b) φ_2 =45 degree using VPSC scheme for hydrostatic extrusion of NFA-1 alloy.

When we compare Figure 17 with the ODF maps obtained from the experimentally measured texture of the HyE tube, shown in Figures 7a and b, it can be concluded that VPSC calculations successfully predict the texture development of the NFA-1 alloy using hydrostatic extrusion.

VPSC modeling of forging of NFA-1 powder

In the previous section, we have calibrated our VPSC model with the experimentally measured texture for the hot-extruded, cross-rolled and hot-hydrostatically extruded NAF-1 alloy. It has been observed that calculated ODFs using VPSC model match quite well with the experimentally observed texture for the hot extruded billet bar, cross-rolled plate, and hydrostatically extruded tube. Formability and mechanical anisotropy of the as-processed alloy largely depends on the crystallographic texture of the as-finished product. Hence, texture prediction using the VPSC scheme for different deformation processing conditions can lead us to optimize the processing route for this alloy and serve as a guideline for selecting the most viable deformation processing path.

Here, forging is chosen as an alternative processing route, and texture development of the alloy is predicated using the VPSC modeling technique. Forging process in the VPSC code is defined using the following strain rate tensor $\dot{u}=\begin{bmatrix}0.5 & 0 & 0\\ 0 & 0.5 & 0\\ 0 & 0 & -1\end{bmatrix}$. A total von Mises strain of ≈3.5 is applied to the initial random orientation at 7 successive steps with a step size of 0.5 strain per step. Near about the same magnitude of total strain (≈3.5) has been applied in case of hydrostatic extrusion. Apart from the strain rate tensor, other parameters used for the simulation of forging process are kept the same, that was used in the simulation of the texture development during hydrostatic extrusion. The simulated texture for the forging process is shown in Figure 18 with φ_2 =0 and 45° sections of the ODF.

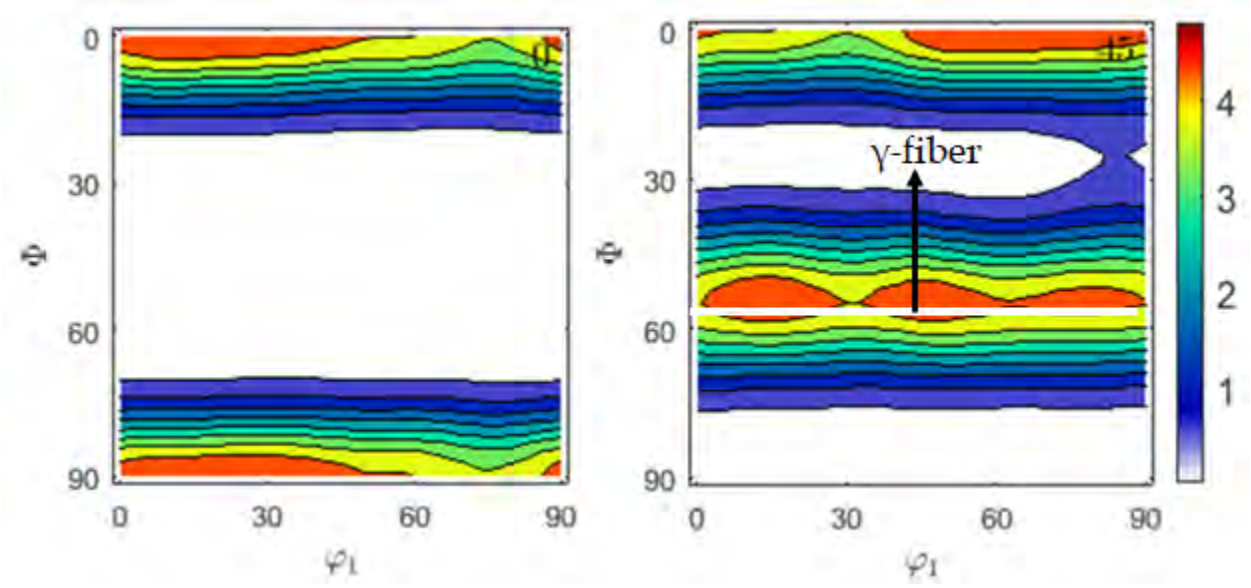

(a) (b)

Figure 18. The 2D-ODF sections plots of the VPSC calculated texture of NFA-1: a) φ_2 = 0-degree section; b) φ_2 = 45-degree section.

A strong γ-fiber (<111>∥ ND) is observed when the NFA-1 alloy is subjected to forging, as marked in Figure 18b. Highest texture intensity is observed at {111}<110> and {112}<110> texture components along with the {001}<100> 'Goss' texture component. Locations of all possible texture components at φ_2 =0 and 45º sections of an ideal ODF of bcc-Fe are shown in Figures 7c and d. The overall calculated

volume fraction of α and γ-fiber produced during forging is ≈ 15.65 and 21.3 %. A higher volume fraction of γ-fiber with the highest texture intensity at {111}<110> and {112}<110> suggests that forging could be used as a possible alternative processing path for the NFA-1 alloy.

Conclusions

Conclusions of the present work are the following:

- Hydrostatic extrusion completely heals the pre-existing microcracks and produces a defect-free tube without altering the ferrite grain sizes (≈ 0.5 μm) and its dislocation density (≈ 0.5 $X10^{15}$ m/m^3).
- Hydrostatic extrusion does not change the average size, number density and volume fraction of the Y-Ti-O nano-oxides present in the as-processed alloy.
- As-processed tube displays a very high value of hardness (≈ 4.5 GPa), the same as the cross-rolled plate that qualitatively indicates, the tube may also have a tensile strength value, like same as the cross-rolled NAF-1 plate.
- Shear dominated hydrostatic extrusion process reduces the volume fraction of α-fiber and increase γ-fiber's proportion in the as-processed tube, compared to the cross-rolled plate. Increase in the soft γ-fibers indicates good formability. Hence, the optimal processing routes for the alloy will be such that the final texture should contain a minimum volume fraction of α-fiber and maximum volume fraction of γ-fiber without sacrificing its mechanical properties.
- Development of strong α-fiber during cross-rolling occurs due to the constrained deformation of the billet bar within the mild steel can; whereas, dominant shear stress in the plane perpendicular to the hydrostatic extrusion direction during hydrostatic extrusion produces more γ-fibers than the α-fiber. The deformation mechanism is strongly affected by cross-slip systems, especially where latent hardening of a slip system is restricted by slip activity on other system.
- Simulation of the texture development of NFA-1 alloy powder upon hot forging produces a strong γ-fiber texture, suggesting forging could be an attractive alternative defect-free processing route for NFA-1 alloy.

Future work:

The VPSC will be coupled with a finite element code to model deformation and fracture of NFA in specific geometries. These tools will be used to explore other deformation processing routes to fabricate fusion reactor components. Emphasis will be on coupling to a developing high-temperature database.

Acknowledgments

We acknowledge the U.S. Department of Energy (US DOE) through the Office of Fusion Energy Sciences (DE-FG03-94ER54275) for financial support. The DOE Office of Nuclear Energy provided support for the tube study via a subcontract from LANL. We also acknowledge Dr. David Hoelzer (ORNL) for providing the as extruded and cross-rolled material, and Dr. Stuart Maloy and Prof. J.J. Lewandowski for supplying hydrostatically extruded tube.

References

[1] G.R. Odette, M.J. Alinger, B.D. Wirth, Recent Developments in Irradiation-Resistant Steels, Annu. Rev. Mater. Res. 38 (2008) 471–503.
[2] G.R. Odette, Recent Progress in Developing and Qualifying Nanostructured Ferritic Alloys for Advanced Fission and Fusion Applications, JOM. 66 (2014) 2427–2441.
[3] G.R. Odette, On the status and prospects for nanostructured ferritic alloys for nuclear fission and fusion application with emphasis on the underlying science, Scr. Mater. 143 (2018) 142–148.
[4] N. Cunningham, Y. Wu, D. Klingensmith, G.R. Odette, On the remarkable thermal stability of nanostructured ferritic alloys, Mater. Sci. Eng. A. 613 (2014) 296–305.
[5] M.E. Alam, S. Pal, K. Fields, S.A. Maloy, D.T. Hoelzer, G.R. Odette, Tensile deformation and fracture properties of a 14YWT nanostructured ferritic alloy, Mater. Sci. Eng. A. 675 (2016).

doi:10.1016/j.msea.2016.08.051.
[6] M.E. Alam, S. Pal, S.A. Maloy, G.R. Odette, On delamination toughening of a 14YWT nanostructured ferritic alloy, Acta Mater. 136 (2017).
[7] S. Pal, M.E. Alam, S.A. Maloy, D.T. Hoelzer, G.R. Odette, Texture evolution and microcracking mechanisms in as-extruded and cross-rolled conditions of a 14YWT nanostructured ferritic alloy, Acta Mater. 152 (2018).
[8] S. Pal, M.E. Alam, G.R. Odette, S.A. Maloy, D.T. Hoelzer, J.J. Lewandowski, Microstructure, Texture and Mechanical Properties of the 14YWT Nanostructured Ferritic Alloy NFA-1 BT - Mechanical and Creep Behavior of Advanced Materials, in: I. Charit, Y.T. Zhu, S.A. Maloy, P.K. Liaw (Eds.), Springer International Publishing, Cham, 2017: pp. 43–54.
[9] E. Aydogan, S. Pal, O. Anderoglu, S.A. Maloy, S.C. Vogel, G.R. Odette, J.J. Lewandowski, D.T. Hoelzer, I.E. Anderson, J.R. Rieken, Effect of tube processing methods on the texture and grain boundary characteristics of 14YWT nanostructured ferritic alloys, Mater. Sci. Eng. A. 661 (2016) 222–232.
[10] K. Thompson, D. Lawrence, D.J. Larson, J.D. Olson, T.F. Kelly, B. Gorman, In situ site-specific specimen preparation for atom probe tomography, Ultramicroscopy. 107 (2007) 131–139.
[11] F. Bachmann, R. Hielscher, H. Schaeben, Texture Analysis with MTEX – Free and Open Source Software Toolbox, Solid State Phenom. 160 (2010) 63–68.
[12] W.C. Oliver, G.M. Pharr, An improved technique for determining hardness and elastic modulus using load and displacement sensing indentation experiments, J. Mater. Res. 7 (1992) 1564–1583.
[13] R.A. Lebensohn, C.N. Tomé, A self-consistent anisotropic approach for the simulation of plastic deformation and texture development of polycrystals: Application to zirconium alloys, Acta Metall. Mater. 41 (1993) 2611–2624.
[14] M.R. Staker, D.L. Holt, The dislocation cell size and dislocation density in copper deformed at temperatures between 25 and 700°C, Acta Metall. 20 (1972) 569–579.
[15] D. Vaumousse, A. Cerezo, P.J. Warren, A procedure for quantification of precipitate microstructures from three-dimensional atom probe data, Ultramicroscopy. 95 (2003) 215–221.
[16] M.J. Alinger, G.R. Odette, D.T. Hoelzer, On the role of alloy composition and processing parameters in nanocluster formation and dispersion strengthening in nanostuctured ferritic alloys, Acta Mater. 57 (2009) 392–406.
[17] N.J. Cunningham, Study of the structure, composition, and stability of yttrium-ti-oxygen nm-scale features in nano-structured ferritic alloys, University of California Santa Barbara, 2012.
[18] S. Takajo, C.N. Tomé, S.C. Vogel, I.J. Beyerlein, Texture simulation of a severely cold rolled low carbon steel using polycrystal modeling, Int. J. Plast. 109 (2018) 137–152.
[19] E. Voce, Analysis of Stress Strain Curves, J. R. Aeronaut. Soc. 59 (1955) 442.
[20] J.D. Rigney, S. Patankar, J.J. Lewandowski, Properties of monolithic and composite NiAl processed by hydrostatic extrusion and vacuum hot-pressing, Compos. Sci. Technol. 52 (1994) 163–172.

8.4 MODELING DUCTILE-PHASE TOUGHENED TUNGSTEN FOR PLASMA-FACING MATERIALS BY A MULTISCALE MICROSTRUCTURAL APPROACH: EXPERIMENTAL VALIDATION OF THE NICKEL-IRON-TUNGSTEN TENSILE TEST ANALYSIS—B.N. Nguyen, C.H. Henager, Jr., R.J. Kurtz (Pacific Northwest National Laboratory)

OBJECTIVE

The objective of this study is to investigate the deformation behavior of ductile phase toughened tungsten (W) materials such as tungsten-nickel-iron (W-Ni-Fe) composites using a multiscale microstructural approach that involves a dual-phase model where the constituent phases (i.e., W and Ni-Fe) are finely discretized in finite elements and are described by a continuum damage mechanics (CDM) model. This approach which had previously been developed [1-2] is suitable for modeling deformation, cracking, and crack bridging for W-Ni-Fe, and other ductile phase toughened W-composites, or more generally, any multi-phase composite structure where two or more phases undergo cooperative deformation in a composite system. During the current reporting period, we validated this approach for W-Ni-Fe specimens subjected to tensile loading. Model predictions were compared to corresponding experimental results for crack patterns and stress-strain response. In addition, this modeling capability can be used as a tool to investigate hypothetical W-Ni-Fe microstructures to increase strength and ductility of these composites.

SUMMARY

A promising approach to increasing fracture toughness and decreasing the ductile-brittle transition temperature (DBTT) of a W-alloy is by ductile-phase toughening [3-4]. In this approach, a ductile phase is included in a brittle matrix to increase the overall work of fracture for the composite material. Previously, Pacific Northwest National Laboratory (PNNL) had developed a multiscale microstructural approach to study DPT of W and validated it through analyses of W-copper (Cu) and W-Ni-Fe bend bar tests [1-2]. References [1-2] show that such an approach is very robust and is able to capture the bridging mechanism responsible for increased strength, toughness, and ductility. This report describes recent applications of this approach to simulate tensile loading of W-Ni-Fe specimens. Model predictions for stress-strain response and crack patterns as a function of loading agree well with the corresponding experimental results. The developed approach can be used as a tool to optimize DPT-W composites with regard to strength and fracture toughness for fusion energy applications.

PROGRESS AND STATUS

Background

The W and W-alloys are the solid materials of choice for plasma-facing components (PFCs) of future fusion reactors, such as the International Thermonuclear Experimental Reactor (ITER) and Demonstration Power Plant (DEMO), due to their high melting point, strength at high temperatures, high thermal conductivity, low coefficient of thermal expansion, and low sputtering yield [5-8]. However, W and most W-alloys exhibit rather low fracture toughness and a high DBTT that would render them as brittle materials during reactor operations [6,8-9]. The DBTT for unirradiated W-alloys typically ranges from 573K to 1273K (300˚C to 1000˚C), and in a reactor environment radiation hardening would further elevate this range [8,10-11]. The W-alloys toughened by engineered reinforcement architectures, such as DPT are strong candidates for PFCs. The principle of DPT is illustrated in Figure 1, which shows an actual and schematic illustration of ductile bridging ligaments stretching across an open crack in a W matrix material [1]. The W-Cu was a DPT composite for model development purposes only, and there is an important need to develop other W-alloys employing DPT mechanisms to achieve high-strength and high-toughness W-composites meeting fusion energy application requirements. Our efforts have moved in this direction and have focused on applying the developed approach to simulate tensile loading of W-Ni-Fe specimens. Tensile tests were conducted on W-Ni-Fe specimens to determine the material stress-strain response and crack pattern development for model validation.

Model Development

The W-Ni-Fe material (90-wt% W, 7-wt% Ni, 3-wt% Fe) studied in this work has a lamellar-like microstructure as presented in Figure 2a that shows the Ni-Fe phase embedded in nearly parallel W-phase regions [2]. The nominal W volume fraction is about 0.8. This microstructure is repeated in the thickness

direction (out-of-plane direction). During this report period, our efforts focused on the experimental validation of the tensile test analysis of specimens made from this composite. The central part of the W-Ni-Fe tensile specimen which is away from the grips and does not include the entailed portions is 5-mm long, 1.1-mm wide and 0.25-mm thick. As the specimen was subjected to uniform tensile loading, only a representative domain located on the symmetry axes and covering the half of the specimen width was modeled and discretized in 2D finite elements based on a digital image using the OOF2[1] software. The 2D FE model (Figure 2b) containing the dual-phase microstructural domain was created using the method reported in [1] that captured the constitutive behaviors of W and of the Ni-Fe alloy described by an elastic-plastic damage model. During this report period, experimental tensile tests were performed on these specimens to obtain the material stress-strain responses and the development of damage and crack patterns as a function of loading for the model parameter identification and model validation.

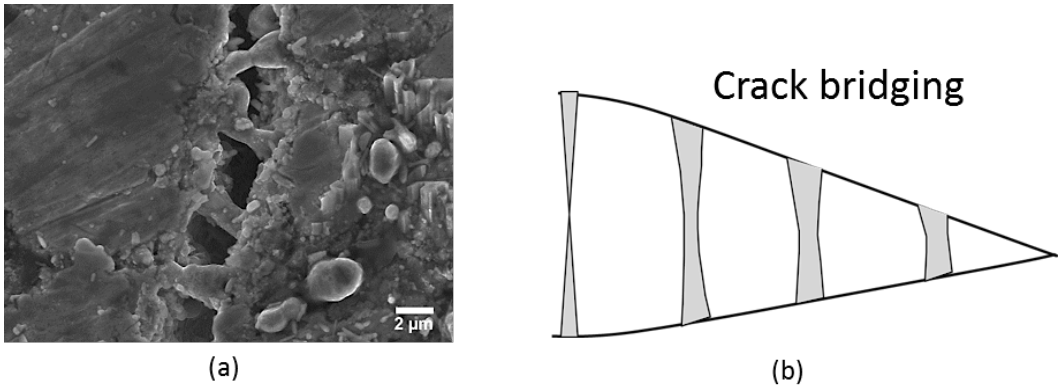

Figure 1. a) Scanning electron microscope (SEM) images of a crack in W-Cu tested at 632˚C in argon showing Cu ligaments bridging a crack. b) A steady-state bridging zone shown schematically in 2D [1].

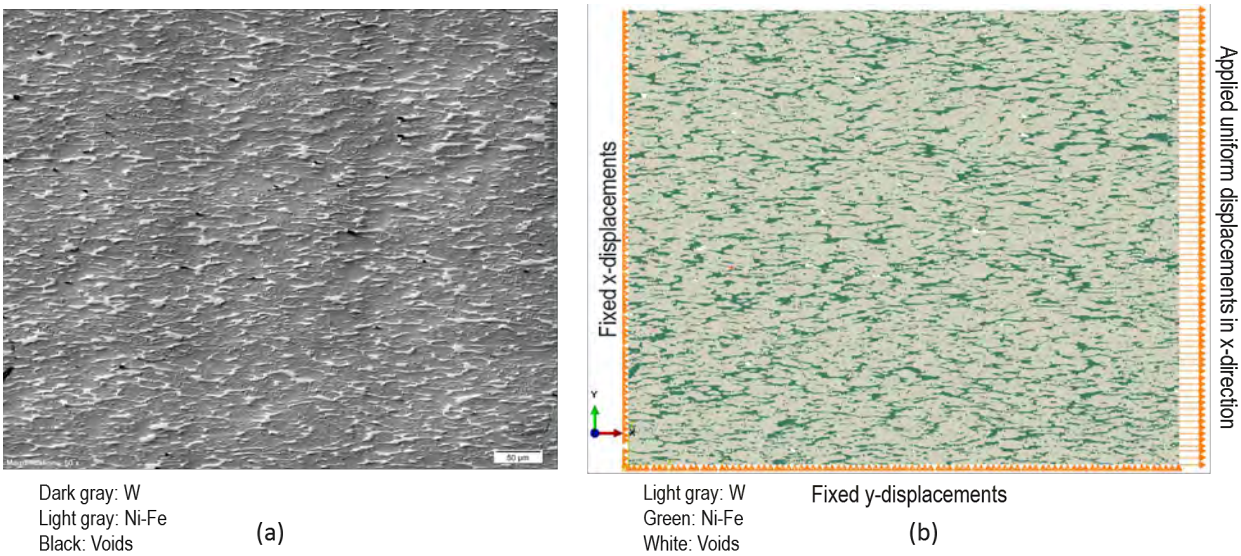

Figure 2. (a) The as-formed dual-phase microstructure from a tensile specimen, (b) The associated FE model with boundary conditions for analysis.

[1]Software developed at the National Institute of Standards and Technology.

Results

The 2D plane-stress model (Figure 2b) of the W-Ni-Fe specimen subjected to tensile loading was analyzed using the elastic-plastic damage model to describe the constitutive behaviors of W and Ni-Fe phases in the microstructural domain. A series of FE analysis was first conducted to identify the constitutive parameters for the model. The identification process started from using typical mechanical properties of W and of Ni alloys. The constitutive parameters were then adjusted through FE analyses until the predicted stress-strain response and loading-dependent damage pattern development agree with corresponding experimental results. Damage is quantified by a damage indicator that varies from 0 to 1. If the failure indicator is equal to 1, total failure (or fracture) causing crack propagation occurs and is captured by a vanishing element method [12,1]. Figure 3 shows the predicted stress-strain response that agrees very well with the corresponding experimental data also reported on this figure.

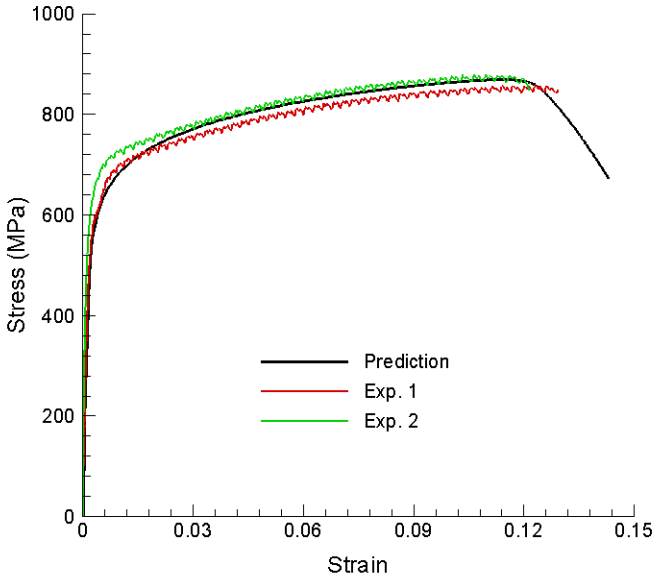

Figure 3. Predicted tensile stress-strain response for the studied W-Ni-Fe composite compared to the corresponding experimental data.

Figures 4a and 4b illustrate the predicted damage distributions and crack patterns at 0.04 and 0.12 overall strains, respectively. At 0.04 strain, significant damage has already been accumulated in the composite (Figure 4a). At this loading level, damage has preferentially developed inside the Ni-Fe regions (see Figure 2 for the regions) and from the pre-existing voids where stress concentrations were important and could break the W elements. However, at 0.12 strain that corresponds to about the elongation limit, many macrocracks were formed by the linking-up of failed Ni-Fe and W elements. Indeed, to propagate a crack needed to break the adjacent W elements as clearly illustrated in Figures 5a and 5b. Figure 5a shows a magnified view of a local area inside the microstructural domain where the crack linking-up directions are indicated. Figure 5b shows that macroscopic cracks were formed by the linking-up of failed Ni-Fe and W elements. The predicted crack patterns and failure mechanisms have been confirmed experimentally in Figures. 4c and 4d that show the SEM images of a tested sample region at 0.04 and 0.125 overall strains. This region roughly corresponds to the size of the studied microstructure domain illustrated in Figure 2. Furthermore, Figure 5c shows an SEM of a local crack that propagated through W regions adjacent to Ni-Fe regions and appears similar to the predicted crack paths in Figure 5b.

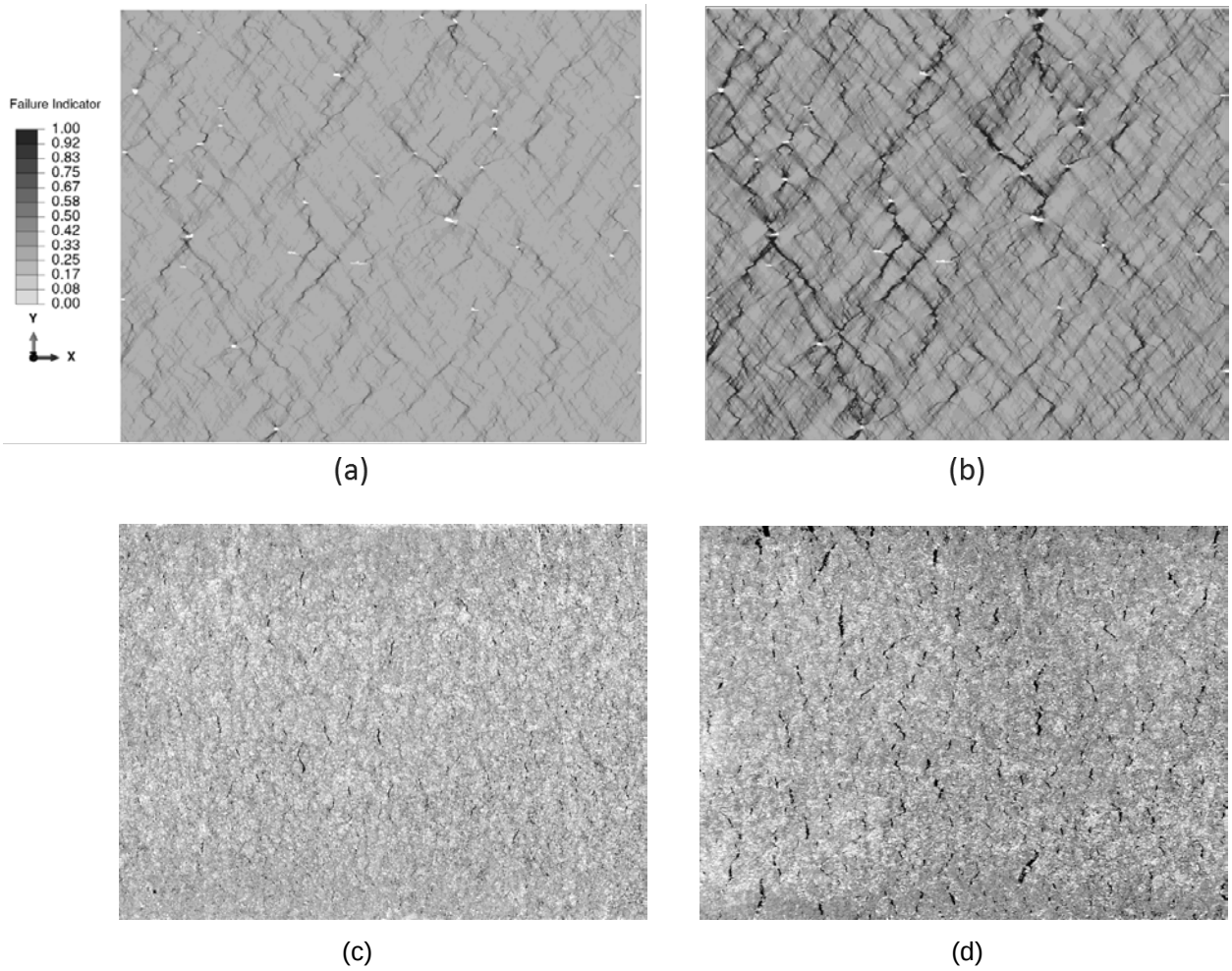

Figure 4. Predicted damage distribution and fracture patterns at (a) 0.04 and (b) 0.12 overall strains. Optical images of surface cracks on experimental tensile specimens strained to (c) 0.04 and (d) 0.125 overall strains. The predicted and observed crack patterns are similar.

Conclusions

During this report period, important progress has been made on finalizing our predictive capability for modeling ductile phase-toughened tungsten for plasma-facing applications by its experimental validation for tensile test analysis. Experimental tensile tests on W-Ni-Fe specimens were performed for this purpose. Current model predictions show good agreement with our recent experimental data with respect to stress-strain response, damage distribution, crack patterns as well as propagation directions in the studied W-Ni-Fe composite. In addition to crack bridging and crack meandering mechanisms, crack penetration into stronger W regions also contributed to retarding crack propagation leading to increased material strength and toughness. We will explore the latter mechanism in the analyses of hypothetical W-Ni-Fe microstructures to increase strength, toughness and ductility of W-Ni-Fe composites.

Future Work

We will complete our work on W-Ni-Fe composites by performing FE analyses of hypothetical W-Ni-Fe microstructures to increase strength and ductility of these composites. The analysis results will be reported in a journal paper.

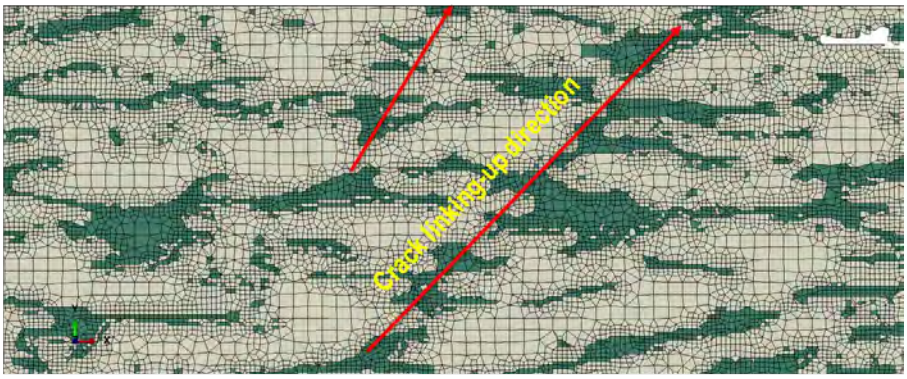

Gray: W; green: Ni-Fe

(a)

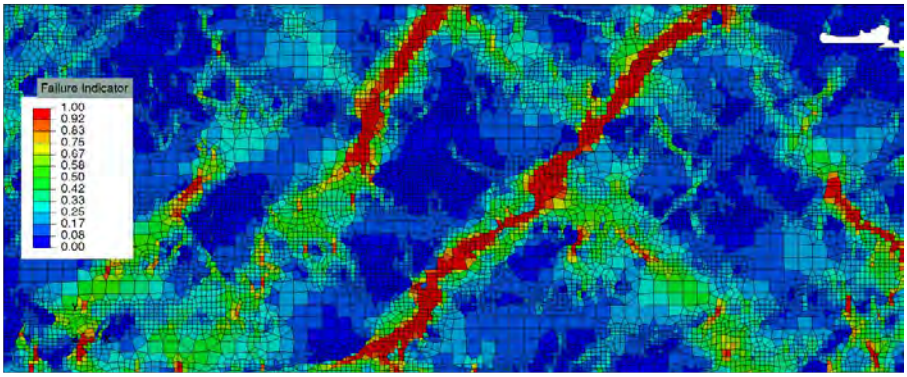

(b)

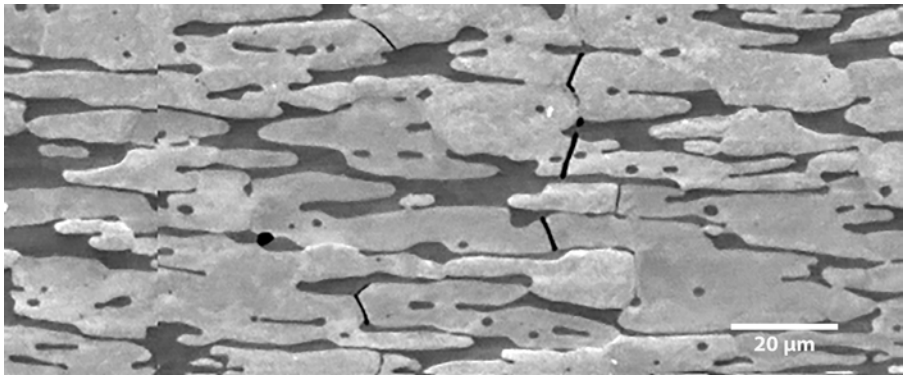

(c)

Figure 5. (a) A magnified view of a local area inside the microstructural domain (red arrows indicating crack propagation directions), (b) Predicted cracks formed by the linking-up of failed Ni-Fe and W elements, and (c) SEM image of cracks near the fracture path in tensile sample strained to failure.

References

[1] Nguyen, B.N., C.H. Henager, Jr, N.R. Overman, and R.J. Kurtz. 2018. A Multiscale Microstructural Approach to Ductile-Phase Toughened Tungsten for Plasma-Facing Materials. J. Nucl. Mater., 2018. 508: p. 371-384.

[2] Nguyen, B.N., C.H. Henager, Jr., and R.J. Kurtz. "Modeling Ductile Phase Toughened Tungsten for Plasma-Facing Materials by A Mulstiscale Microstructural Approach: Application to Nicken-Iron-Tungsten Composites." In Fusion Materials Semiannual Progress Report For the Period Ending June 30, 2018, FW Wiffen and S Melton, Editors, DOE/ER-0313/64, Vol. 64, pp. 158-165, Oak Ridge National Laboratory, Oak Ridge, TN.
[3] Deve, H.E., A.G. Evans, G.R. Odette, R. Mehrabian, M.L. Emiliani, and R.J. Hecht, Acta metallurgica et materialia, 1990. 38(8): p. 1491-502.
[4] Erdogan, F. and P.F. Joseph, J. Am. Ceram. Soc., 1989. 72(2): p. 262-270.
[5] Sigl, L.S., P.A. Mataga, B.J. Dalgleish, R.M. McMeeking, and A.G. Evans, Acta Metall., 1988. 36(4): p. 945-953.
[6] Rieth, M., J.L. Boutard, S.L. Dudarev, T. Ahlgren, S. Antusch, N. Baluc, M.F. Barthe, C.S. Becquart, L. Ciupinski, J.B. Correia, C. Domain, J. Fikar, E. Fortuna, C.C. Fu, E. Gaganidze, T.L. Galan, C. Garcia-Rosales, B. Gludovatz, H. Greuner, K. Heinola, N. Holstein, N. Juslin, F. Koch, W. Krauss, K.J. Kurzydlowski, J. Linke, C. Linsmeier, N. Luzginova, H. Maier, M.S. Martinez, J.M. Missiaen, M. Muhammed, A. Munoz, M. Muzyk, K. Nordlund, D. Nguyen-Manh, P. Norajitra, J. Opschoor, G. Pintsuk, R. Pippan, G. Ritz, L. Romaner, D. Rupp, R. Schaublin, J. Schlosser, I. Uytdenhouwen, J.G. Van Der Laan, L. Veleva, L. Ventelon, S. Wahlberg, F. Willaime, S. Wurster, and M.A. Yar, J. Nucl. Mater., 2011. 417: p. 463-467.
[7] Pitts, R.A., A. Kukushkin, A. Loarte, A. Martin, M. Merola, C.E. Kessel, V. Komarov, and M. Shimada, Physica Scripta Volume T, 2009. 2009(T138): p. 014001 (10 pp.).
[8] Mertens, P., T. Hirai, M. Knaup, O. Neubauer, V. Philipps, J. Rapp, V. Riccardo, S. Sadakov, B. Schweer, A. Terra, I. Uytdenhouwen, and U. Samm, Fusion Eng. Des., 2009. 84(7-11): p. 1289-93.
[9] Mertens, P., V. Philipps, G. Pintsuk, V. Riccardo, U. Samm, V. Thompson, and I. Uytdenhouwen, Physica Scripta Volume T, 2009. 2009(T138): p. 014032 (5 pp.).
[10] Gludovatz, B., S. Wurster, A. Hoffmann, and R. Pippan, Int. J. Refract. Met. Hard Mater., 2010. 28(6): p. 674-8.
[11] Zinkle, S.J. and N.M. Ghoniem, Fusion Eng. Des., 2000. 51-52: p. 55-71.
[12] V. Tvergaard, J. Mech. Phys. Solids, 1982. 30(6): p. 399-425.

9. FUSION SYSTEM DESIGN

No contributions this reporting period.

10. IRRADIATION METHODS, EXPERIMENTS AND SCHEDULES

10.1 PROGRESS OF LIGHT-ION TRANSMISSION IRRADIATION IN TUNGSTEN FOILS—Weilin Jiang, Giridhar Nandipati, Wahyu Setyawan, Charles H. Henager Jr., Richard J. Kurtz (Pacific Northwest National Laboratory)

OBJECTIVE

The aim of this study is to investigate void formation in tungsten using light-ion irradiation at elevated temperatures in a transmission geometry. Void distributions, including the possible formation of a void lattice, will be examined. The density and size distribution of voids will be determined as a function of irradiation parameters. The results will be compared to predictions by Object Kinetic Monte Carlo (OKMC) simulations with an intention to validate the computational approach.

SUMMARY

This report presents the progress and current status of our light-ion transmission irradiation study of polycrystalline tungsten foils at elevated temperatures. The choice of ion species and energy is based on the tungsten foil thickness and SRIM simulations. The dose rate and dose will be determined by the achievable beam current and reasonable irradiation duration. Tungsten foils of ~10 μm thickness have been prepared using mechanical grinding and are being further thinned with electrochemical flash polishing (FP). The focused ion beam (FIB) technique is not employed in this study to avoid beam damage. The transmission experiment is designed so that the level of the implanted species in the foil is less than 100 appm. In addition, a dedicated high-temperature holder of tungsten foils has been fabricated. The irradiated samples will be examined by Helium Ion Microscopy (HIM) and Scanning Transmission Electron Spectroscopy (STEM).

PROGRESS AND STATUS

Introduction

Our recent tungsten research efforts have primarily focused on the study of self-ion irradiation of monocrystalline and polycrystalline tungsten. The experimental procedures and major results have been documented in recent semiannual reports [1-3]. A high density of randomly distributed voids has been observed [3] in both monocrystalline and polycrystalline tungsten irradiated at 900 K to 1 dpa at 10^{-3} and 10^{-4} dpa/s. The voids are typically on the order of a few nanometers in diameter. In addition, a high density of dislocation loops has also been observed [2,3]. The loop distribution extends to a depth well beyond the ion projected range in the FIB-prepared specimens with FP. Surface damage on the tungsten foils due to Ga^{+} ion bombardment during the FIB process is expected and fast self-interstitial diffusion into the tungsten foil at room temperature is likely. In fact, our data [2] from Rutherford backscattering spectrometry under an axial channeling condition (RBS/C) shows that self-interstitials in tungsten are extremely mobile even at room temperature. The mobile interstitials could cluster and form dislocation loops in the tungsten foil. Instead of FIB, mechanical and electrochemical methods for preparation of thin tungsten foils can eliminate the artificial FIB damage. The MeV light-ion irradiation of tungsten with a smaller average primary knock-on atom (PKA) energy than that from fission or fusion neutron irradiation will be attempted in this study. To minimize the effects from the implanted species, transmission irradiation of tungsten foils will be used. The experimental data will be compared to predictions by OKMC simulations [4,5] with an intention to determine modeling parameters and validate the simulation results.

Experimental Procedure

The MeV light-ion irradiation of polycrystalline tungsten will be performed at an elevated temperature in a transmission geometry. The ion irradiation experiment is designed to (1) emulate neutron irradiation in tungsten at low dose rates and (2) minimize the introduction of implanted species during ion irradiation.

Table 1. Quick KP SRIM results and estimated irradiation conditions for polycrystalline tungsten foils

Ion Beam	1.5 MeV H^+	2.0 MeV H^+	4.0 MeV He^{2+}	5.0 MeV He^{2+}	6.0 MeV He^{2+}	6.0 MeV Li^{2+}
W Foil Thickness (μm)	6	10	4	6	8	3
Retention of Implanted Ions (appm)	90	60	60	60	50	60
Average Displacement Rate dpa/(ions/cm²)	3.9×10^{-20}	3.0×10^{-20}	3.2×10^{-19}	2.6×10^{-19}	2.2×10^{-19}	9.2×10^{-19}
Dose Rate (dpa/s)	10^{-7}	10^{-7}	10^{-6}	10^{-6}	10^{-6}	10^{-6}
Dose (dpa)	0.02	0.02	0.2	0.2	0.2	0.5
Irradiation Duration (h)	55.6	55.6	55.6	55.6	55.6	27.8
Ion Fluence (Ions/cm²)	5.1×10^{17}	6.6×10^{17}	6.3×10^{17}	7.6×10^{17}	9.0×10^{17}	5.4×10^{17}
Beam Current Density	410	530	1010	1220	1440	1740

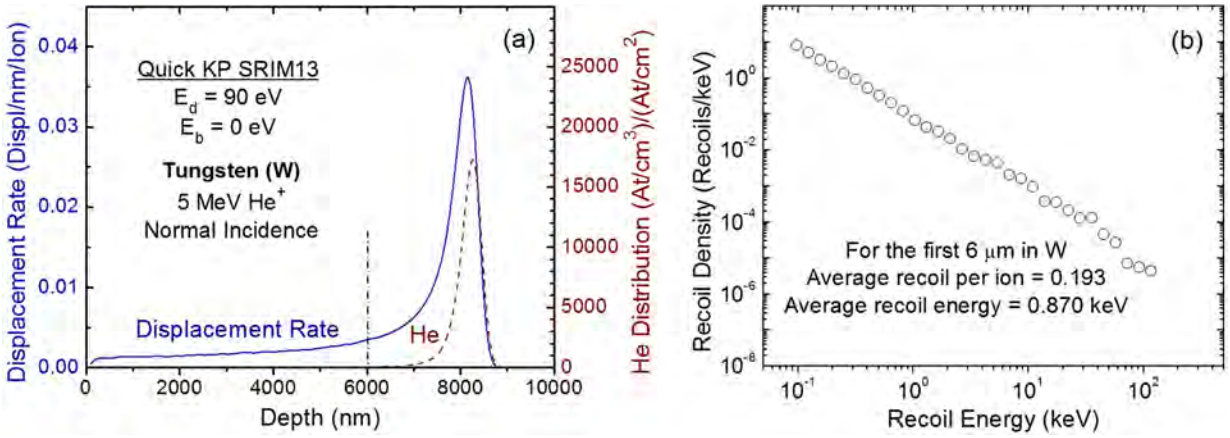

Figure 1. Quick Kinchin-Pease SRIM13 simulation results of 5 MeV Helium $(He)^+$ ion irradiation in tungsten (a) for depth profiles of the displacement rate and He atom distribution and (b) for recoil density distribution in a 6 μm thick tungsten foil. E_d: threshold displacement energy; E_b: lattice binding energy.

However, transmutation effects are not included in this initial study. Ion beams will be generated using the 3.0 MV NEC tandem ion accelerator at the Texas A&M University (TAMU).

Kinchin-Pease (KP) SRIM simulations for H^+, He^+ and Li^+ ion irradiations in tungsten have been performed and the results are given in Table 1. Irradiation with 1.5 or 2 MeV H^+ ions produces a very low displacement rate on the order of 10^{-20} dpa/(ions/cm²). Even for a high beam current, the dose rate (dpa/s) is still small. For a typical beam condition, it takes 55.6 h to generate a dose of only 0.02 dpa in the tungsten foil. For 6 MeV Li^+ ion irradiation with a larger stopping power, a tungsten foil must be very thin (~3 μm or less) in order for a great majority of ions to penetrate. A higher energy beam, such as 9 MeV Li^{3+} or higher, would reduce Li retention in the foil, but the beam current would be too small for practical irradiations. Overall, MeV He^{2+} ion irradiation appears to be the most suitable way to achieve the desired dose within a

Table 2. List of impurities in 99.97 wt % pure tungsten manufactured by Plansee

Element	Typical max. value [µg/g]	Typical max. value [appm]	Guaranteed max. value [µg/g]	Guaranteed max. value [appm]
Al	1	6.8	15	102
Cr	3	10.6	20	71
Cu	1	2.9	10	29
Fe	8	26.3	30	99
K	1	4.7	10	47
Mo	12	23.0	100	192
Ni	2	6.3	20	63
Si	1	6.5	20	130
C	6	91.8	30	459
H	0	0	5	919
N	1	13.1	5	66
O	2	23.0	20	230
Cd	1	1.6	5	8
Hg	0	0	1	0.9
Pb	1	0.89	5	4.5
Total	40	217.49	296	2420.4

reasonable irradiation time without a significant amount of He retention in the tungsten foil. As an example, the SRIM results from 5.0 MeV He^{2+} ion irradiation are shown in Figure 1a. For a 6 µm thick tungsten foil, a great majority of the He^{2+} ions will pass through the foil. Based on the SRIM simulation (Table 1), the atomic displacement rate at 3.0 µm is 2.6×10^{-19} dpa/(ions/cm^2). For a dose rate of 10^{-6} dpa/s, the corresponding He^{2+} beam current over an area of 1 cm^2 will be 1.22 µA. For a total dose of 0.2 dpa or an ion fluence of 7.6×10^{17} He^{2+}/nm^2, the corresponding irradiation duration will be 55.6 h, which is achievable. Under the irradiation conditions, the retained He concentration in the middle of the foil (3.0 µm) will be only 60 appm. The actual concentration could be even lower due to likely He out-diffusion and release from the foil during irradiation at elevated temperatures. In addition, SRIM simulation also indicates that the average PKA energy for 5 MeV He^{2+} ions in the first 6 µm thickness of tungsten is 0.870 keV (Figure 1b). This represents a small value compared to those from neutron irradiations from a fusion reactor (~45 keV) [5] and the high flux isotope reactor (HIFR) (~5 keV) [4]. We will test various ion beams and will select a suitable ion species and energy for irradiation at 973 K to multiple doses at a dose rate. This initial irradiation experiment is scheduled for late March 2019.

As reported previously [1], the samples are polycrystalline tungsten coupons with a purity of 99.97 wt%, obtained from Plansee. The grain size ranges from 1-5 µm [1]. There is a small fraction of grains that are smaller than 1 µm. The impurity concentrations in the samples are listed in Table 2 from the manufacturer's specification [6]. Typical major impurities include Mo (23.0 appm), C (91.8 appm), Fe (26.3 appm) and O (23.0 appm). Note that molybdenum is excluded from the calculation of the total impurities in tungsten. A number of ~10 µm thick tungsten foils have been prepared by mechanical grinding. Each of the tungsten foils was sandwiched between two gold rings (~3 mm in outer diameter) using a high-performance Ag paste. An example of the tungsten foil sample is shown in Figure 2. The tungsten foils are being further thinned down to ~6 µm using FP prior to ion irradiation. A high-temperature sample holder also has been fabricated

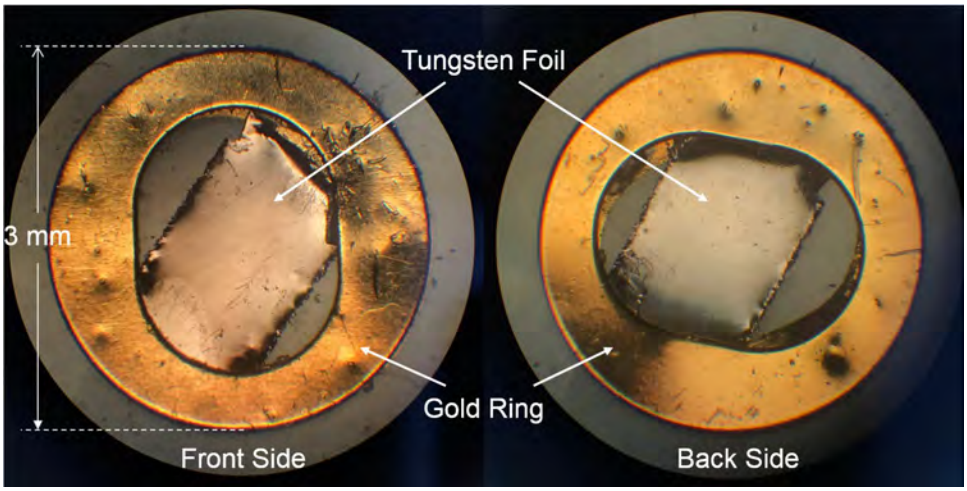

Figure 2. A mechanically ground tungsten foil sandwiched with two gold rings by applying a high-performance Ag paste.

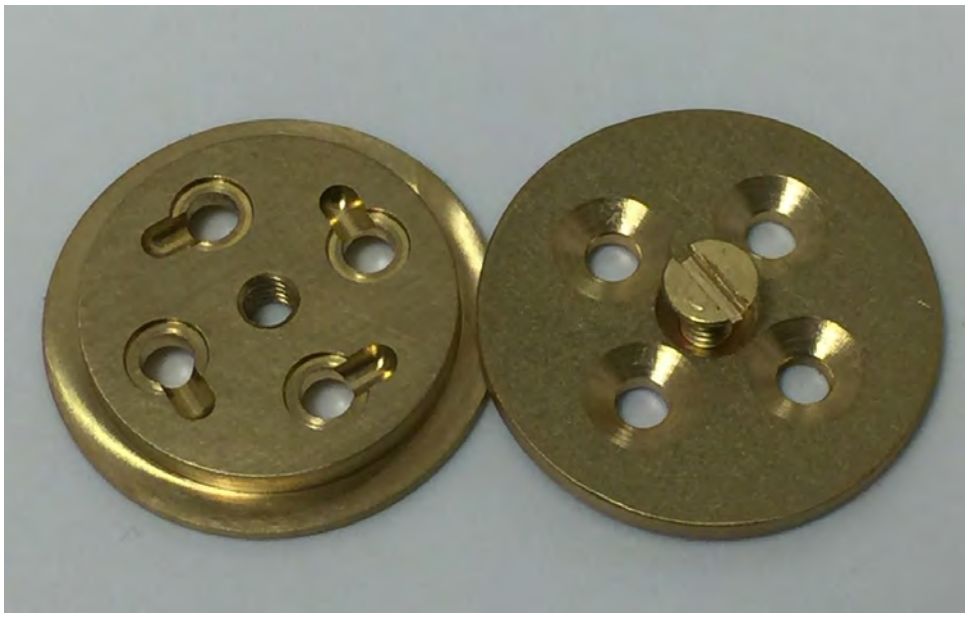

Figure 3. A TEM sample holder made of brass for ion irradiation at elevated temperatures.

for the ion transmission irradiation experiments at an elevated temperature, as shown in Figure 3, which is similar to a commercially available Al-alloy TEM grid holder. The customized holder is made of brass with a melting point of 1173 K and a thermal conductivity of 109 W/(m·K). Four samples can be mounted for simultaneous irradiation. Depending on actual irradiation conditions, selection of ion species and energy will be made based on Table 1. A good choice would be a 5.0 MeV He^{2+} ion beam with a current of ~1.22 μA over an area of 1 cm^2 if it can be generated from the ion accelerator facility at TAMU (Figure 4). Besides the reasons discussed above, the foil thickness of 6 μm is also appropriate for the grain size (1-5 μm).

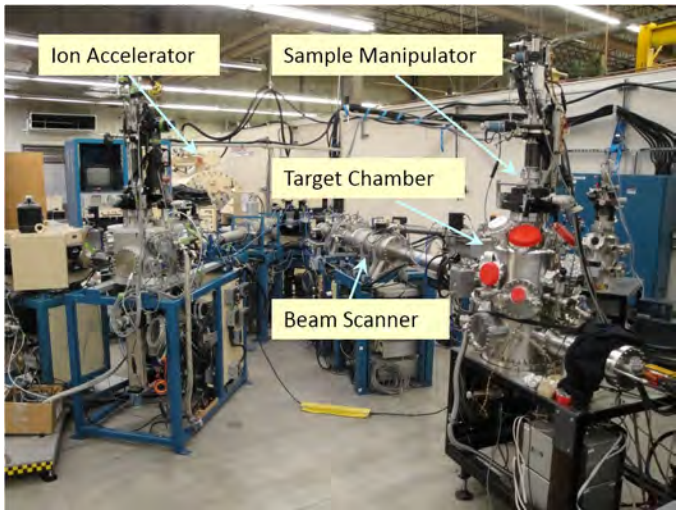

Figure 4. 3.0 MV NEC electrostatic tandem ion accelerator with 2 ion sources and 4 beamlines previously located at Pacific Northwest National Laboratory (PNNL) and now transitioned to the Texas A&M University.

Figure 5. He ion microscope with a spatial resolution of 0.35 nm, located at PNNL.

Results

The irradiated samples will be examined using an advanced HIM from Zeiss (Orion Plus) at PNNL (Figure 5) to determine if voids are visible and how they are spatially distributed. The HIM spatial resolution is 0.35 nm or better, which is comparable to TEM without the need for sample preparation. If the voids are not visible due to a lack of contrast, further thinning of the irradiated tungsten foils to electron transparency will be performed using FP. The samples will be examined using a Cs-aberration corrected JEOL ARM 200cF STEM at PNNL (Figure 6). The instrument is capable of sub-Å resolution for imaging. Various grains in the irradiated foil will be selected for HIM and STEM studies with a particular focus on grains with sizes below ~1 µm for comparison with the OKMC simulations. Based on our previous observations, voids are expected to be produced in tungsten under the irradiation conditions of this study. However, the precise void distribution is difficult to predict at this time. There are two possibilities that could occur: (1) void lattice formation in some grains and (2) random distribution of the voids in all grains.

If a void lattice is formed, the following results will be obtained, which could be used for comparison with OKMC simulations and possible model validation of grain size and dose effects. A void lattice is not expected to form in very small grains because both interstitials and vacancies will readily reach grain boundaries. It is also not expected to form in very large grains because there is a high probability for interstitials to combine with vacancies before they can reach grain boundaries. The void lattice is expected to form in medium-sized grains at sufficiently high doses and diffusion length of interstitials is on the order of grain size. Furthermore, the temperature should be so high that mono-vacancies are mobile and small vacancy clusters unstable. If the void lattice is observed, the lattice spacing, grain orientation and void size distribution will be determined to validate the OKMC model. Compared to FIB specimens, the mechanically ground and flash polished tungsten foils to be used in this study will provide a large area for microscopy studies, which is an advantage in the selection of small grains for examination. In a long term, other effects on damage accumulation will also be investigated, including dose rate and irradiation temperature effects. Note that the effects of irradiation temperature and dose rate are interdependent. If a random distribution of voids is observed, the density and size distribution of the voids will be determined as a function of grain size and dose, and later dose rate and irradiation temperature. Possible reasons why the void lattice does not form under the irradiation conditions will be identified.

Figure 6. JOEL JEM-ARM 200cF aberration-corrected scanning transmission electron microscope with EDS and EELS capabilities, located at PNNL.

Acknowledgements

This research was supported by Office of Fusion Energy Sciences, U.S. Department of Energy (US DOE) under Contract DE-AC05-76RL01830. We are grateful to Limin Zhang at Lanzhou University, China for preparation of tungsten foils, Alan Schemer-Kohrn at PNNL for flash polishing, and to Robert Seffens at PNNL for fabrication of TEM sample holders for ion irradiation at elevated temperatures.

References

[1] W. Jiang, K. Kruska, C. H. Henager, Jr., R. J. Kurtz, *Fusion Materials Semiannual Progress* Report for Period Ending December 31, 2016, DOE/ER-0313/61, U.S. Department of Energy, 115.

[2] W. Jiang, D. J. Edwards, G. Nandipadi, W. Setyawan, C. H. Henager, Jr., R. J. Kurtz, A. French, X. Wang, L. Shao, *Fusion Materials Semiannual Progress* Report for Period Ending June 30, 2017, DOE/ER-0313/62, U.S. Department of Energy, 125.

[3] W. Jiang, Y. Zhu, G. Nandipadi, W. Setyawan, D. J. Edwards, C. H. Henager, Jr., R. J. Kurtz, A. French, X. Wang, L. Shao, *Fusion Materials Semiannual Progress* Report for Period Ending June 30, 2018, DOE/ER-0313/64, U.S. Department of Energy, 93.

[4] G. Nandipati, W. Setyawan, H. L. Heinisch, K. J. Roche, R. J. Kurtz, B. D. Wirth, 2017; available at: https://arxiv.org/abs/1510.02732.

[5] G. Nandipati, W. Setyawan, H. L. Heinisch, K. J. Roche, R. J. Kurtz, B. D. Wirth, 2017; available at: https://arxiv.org/abs/1606.01308.

[6] https://www.plansee.com/en/materials/tungsten.html.

10.2 NEUTRON FLUENCE MEASUREMENTS AND RADIATION DAMAGE CALCULATIONS FOR THE MFE-RB-19J EXPERIMENT IN HFIR—L. R. Greenwood, B. D. Pierson, and T. Trang-Le (Pacific Northwest National Laboratory)

OBJECTIVE

Measure the neutron fluence and energy spectra during irradiations in HFIR (High Flux Isotopes Reactor) and calculate fundamental radiation damage parameters including dpa (displacement per atom) and gas production.

SUMMARY

The 19J experiment was irradiated in the removable beryllium (RB) position of HFIR with a 1 mm thick Gd liner. The experimental assembly was irradiated for cycles 466 through 469 starting on June 14, 2016 and ending December 9, 2016 for a total of 8001 MWD at a nominal power of 85 MW. Neutron dosimetry monitors fabricated by Pacific Northwest National Laboratory (PNNL) were inserted in the 19J experimental assembly at various elevations. After the irradiation, the neutron fluence monitors were recovered by Oak Ridge National Laboratory (ORNL) staff and sent to PNNL for analysis. The activated monitor wires were analyzed to determine activation rates that were used to adjust the neutron fluence spectrum at each irradiation position. The adjusted neutron fluence spectra were then used to calculate radiation damage parameters.

PROGRESS AND STATUS

Neutron dosimetry monitors were fabricated by PNNL for insertion in the 19J experimental assembly. The vanadium monitors measure 0.127 cm in diameter by 0.864 cm long. Each monitor has a 2-digit code stamped on the bottom to uniquely identify them. The monitors were filled with small wire segments of high-purity Fe, Ti, Nb, and 1% Co-V alloy from NIST. Each monitor was electron beam welded to maintain integrity throughout the irradiation. Following irradiation, staff at ORNL removed the monitors from the 19J assembly. The irradiated monitors were received at PNNL for analysis in October 2018. The identities of the monitors, as listed in Table 1, were verified using the 2-digit ID stamp on the bottom. The height above reactor centerline has an uncertainty of ± 0.7 cm. The heights in the assembly were provided by ORNL staff. Monitors 2U and 5H were received and identified for analysis. Unfortunately, the item that was received as monitor 8A was found to not be one of the PNNL fabricated vanadium monitors and appeared to be a solid metal cylinder, tapered on one end, with a low level of activity compared to the activities in our capsules.

Table 1. 19J neutron fluence monitors

Monitor	Height, cm
8A	-15.21
2U	2.71
5H	10.28

The monitors were gamma counted as received. The monitors were observed to have some external contamination and they were wiped with wet swabs to reduce the contamination level for further handling. A smear of one of the sample cans was gamma counted and showed activities of ^{60}Co, ^{54}Mn, ^{134}Cs, ^{137}Cs,

^{152}Eu, ^{154}Eu, ^{155}Eu, ^{46}Sc, ^{241}Am and a few weaker activities. The vanadium monitors were then opened using tubing cutting pliers and the individual wires were retrieved and gamma counted separately in order to look for possible interferences as well as to detect weaker nuclides that could not be detected in the whole monitor counts due to the high level of ^{60}Co activity. The ^{60}Co activities in the as-received monitors closely matched one wire segment, confirming that the activity was due to the 1% Co-V wire. The niobium wires were easily retrieved and weighed to confirm the identification prior to processing for x-ray analysis as described below. The iron wires were identified by observing that one wire had most of the ^{54}Mn activity. The wire weights were consistent with the pre-irradiation weights of the iron wire. The remaining ^{54}Mn activity seen on the whole capsule is due to the external contamination on the outside of the monitors. The titanium wire could not be cleanly retrieved and ^{46}Sc activity was found to be present in all of the wire segments removed from the vanadium monitors. For both monitors the sum of the ^{46}Sc activities in all the separated wires was used to determine this reaction rate. The sum of the ^{46}Sc activity appeared to match the activity in the gamma count of the entire monitor. However, it was difficult to detect ^{46}Sc in the count of the entire monitor due to the very high ^{60}Co activity. For capsule 2U, the ^{46}Sc activity could not be cleanly separated from the ^{60}Co activity such that this reaction rate could not be accurately determined. It should be noted that since the irradiation ended in December 2016, the ^{46}Sc activity decayed by more than eight half-lives, making it more difficult to detect ^{46}Sc in the presence of longer-lived, much higher activities of ^{60}Co, ^{54}Mn, and ^{94}Nb.

The nuclear reactions and activation products that were detected are listed in Table 2. The “90% neutron energy range” represents the energy range of the neutrons that produced 90% of the listed reaction; 5% of the activity was produced by neutrons with energies below the lower energy and 5% above the higher energy. The different energy ranges listed for the reactions are very useful in defining the neutron spectrum, as discussed later in this report.

Table 2. Nuclear reactions with half-lives and energy sensitivity ranges

Nuclear Reaction	Half-life	90% Neutron Energy Range, MeV
^{54}Fe(n,p)^{54}Mn	312 d	2.0 to 8.2
^{46}Ti(n,p)^{46}Sc	83.8 d	3.7 to 10.0
^{93}Nb(n,n')^{93m}Nb	16.1 a	0.66 to 5.0
^{59}Co(n,g)^{60}Co	5.28 a	Epithermal
^{93}Nb(n,g)^{94}Nb	20,300 a	Epithermal

The gamma detectors are calibrated using NIST traceable standards obtained from Eckert and Zeigler. Control counts are performed, every day that a detector is used, to check the continuing calibration of the energy, efficiency, and resolution. All nuclear data was adopted from the Nudat2 database at the National Nuclear Data Center at Brookhaven National Laboratory[1]. The weights of the individual wires were measured during fabrication and all results are reported as activity per gram of the elements with natural abundances using the pre-irradiation masses. The measured activities in Table 3 were corrected back to the end of irradiation time. The activities are corrected for nuclear burnup and gamma absorption to determine reaction rates using the SigPhi calculator from the STAYSL_PNNL software suite [2].

Table 3. Measured activities in Bq/g for the 19J irradiation; uncertainties are ±2% except for ^{93m}Nb at ±5% and ^{46}Sc at ±10%. Results are corrected to the end of irradiation time December 9, 2016. Corrections for decay during irradiation are included with the activation rates in Table 4.

ID	Height,cm	^{54}Mn	^{93m}Nb	^{94}Nb	^{60}Co	^{46}Sc
		Bq/g	Bq/g	Bq/g	Bq/g	Bq/g
2U	2.71	1.45E+09	2.34E+09	2.59E+07	1.34E+10	*
5H	10.28	9.22E+08	1.69E+09	1.66E+07	6.98E+09	4.88E+08

*Fluence wire not recovered or damaged such that data were not usable.

The ^{93m}Nb activities were determined by x-ray counting of the 16.6 and 18.6 keV x-rays using a low energy photon spectrometer (LEPS) detector. The high purity niobium wires were dissolved in a mixture of nitric and hydrofluoric acid using small Teflon beakers. A small aliquot (about 0.5%) of the solution was accurately weighed and dried on thin filter paper covered by 0.25 mil Mylar for LEPS counting. The very small mass and thin cover nearly eliminated concerns over x-ray absorption, backscatter, and fluorescence as discussed in American Society for Testing and Materials (ASTM) practice E1297 [3].

The saturated reaction rates are calculated from the measured activities in Table 3 by applying corrections for decay during irradiation, gamma absorption, and nuclear burnup of the target and product nuclides. These corrections are included with the BCF and SIG-PHI Calculator modules of the STAYSL_PNNL computer suite. (2) The irradiation history was provided by ORNL and is described briefly in the Summary section of this report. The BCF program breaks the irradiation up into periods of nearly constant reactor power and calculates the growth and decay of each activation product. Gamma absorption in the small wire segments is based on the XCOM database (see ref. [4]) as described in section 7.3 of ref [2]. Neutron burnup corrections for thermal neutron reactions use an iterative procedure using a ratio of the burnup reaction rates for the target and product nuclides. The uncorrected reaction rate is used to determine a correction and this procedure is iterated until convergence is achieved. The resulting thermal reaction rates are then used as the basis for calculating the burnup corrections for the threshold nuclear reactions using known thermal neutron cross sections and resonance integrals. For complete details regarding the iterative neutron burnup correction see Figure 28 of Reference [2]. The calculated saturated reaction rates are listed in Table 4.

Table 4. Saturated reaction rates in product atoms/(target atom – second)

ID	Height,cm	^{60}Co	^{54}Mn	^{94}Nb	^{46}Sc	^{93m}Nb
		± 2%	± 2%	± 2%	± 10%	± 5%
2U	2.71	4.08E-09	1.35E-11	4.68E-10	*	3.31E-11
5H	10.28	2.11E-09	8.60E-12	2.97E-10	1.20E-12	2.39E-11

*data not usable

The saturated reaction rates are equal to the integral of the neutron activation cross section times the time-averaged neutron flux over all neutron energies. At each irradiation position we thus have at most six integral equations that are solved simultaneously using a generalized least-squares procedure in the STAYSL_PNNL computer suite. The neutron activation cross sections were adopted from the IRDFF database compiled by the Nuclear Data Section of the International Atomic Energy Agency [5]. The input

neutron spectrum was provided by Charles Daily at ORNL (see Figures 1 and 2, blue lines) [6]. The input to STAYSL_PNNL consisted of the measured saturated reaction rates in Table 4, the input neutron spectrum, the irradiation history, and the IRDFF neutron activation cross sections including all known uncertainties and covariances. Matrix inversion was then used to determine the adjusted neutron flux spectrum and uncertainties including the complete cross-section covariance matrices and a Gaussian formalism-based flux covariance matrix. The results are presented in Table 5 and the neutron spectral adjustments are shown in Figures 1 and 2. The neutron fluence values are listed in Table 5.

Table 5. Neutron fluence values (n/cm^2) from the STAYSL_PNNL spectral adjustment

ID	Height,cm	Thermal		Epithermal		> 0.11 MeV		> 1 MeV	
		< 0.5 eV	±%	0.5 eV to 110 keV	±%		±%		±%
2U	2.71	1.01E+20	28	5.49E+21	6	3.55E+21	6	1.37E+21	5
5H	10.28	5.83E+19	28	3.35E+21	6	2.39E+21	6	9.38E+20	5

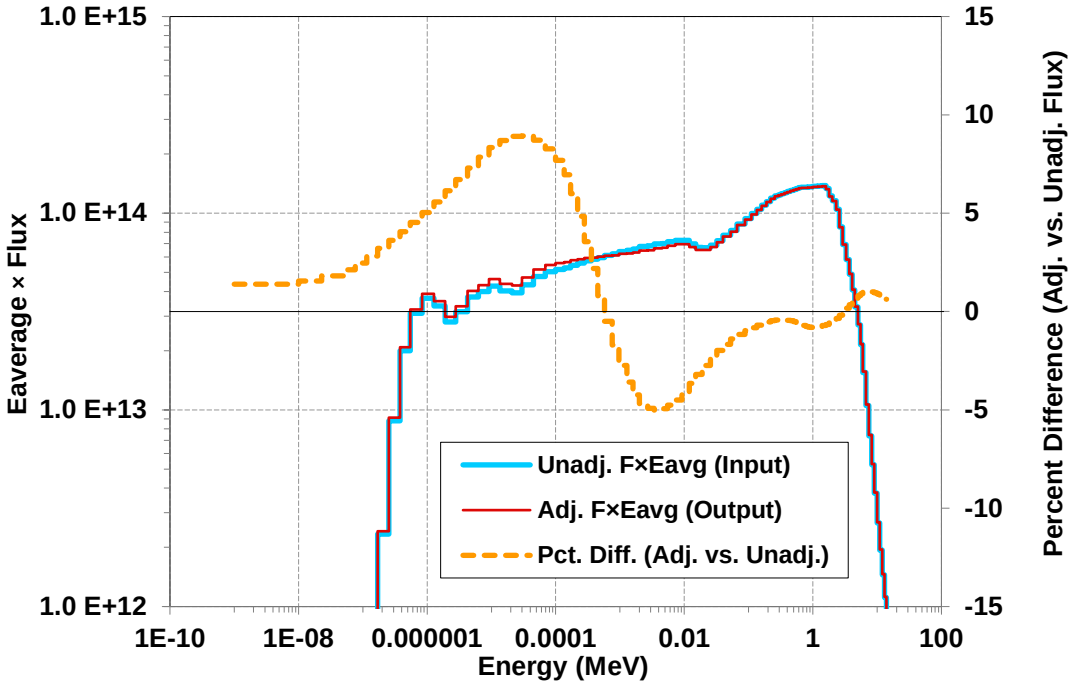

Figure 1. Neutron spectral adjustment with STAYSL PNNL for the 2U position at 2.71 cm. Flux per unit lethargy is shown both before and after adjustment. The dashed curve shows the size of the adjustment using the percent difference scale on the right side.

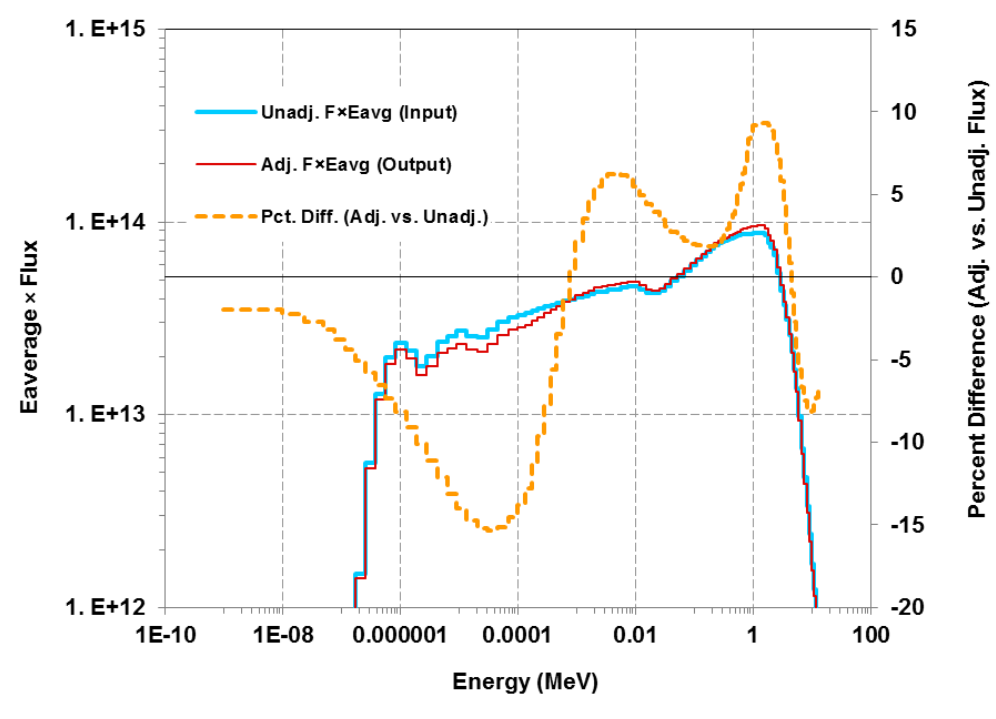

Figure 2. Neutron spectral adjustment with STAYSL PNNL for the 5H position at 10.28 cm. Flux per lethargy is shown both before and after adjustment. The dashed curve shows the size of the adjustment using the percent difference scale on the right side.

Radiation Damage Calculations

The adjusted neutron spectrum determined at each positon in the irradiation assemblies was used to calculate the dpa and helium production in various elements and alloys using the SPECTER computer code [7]. The calculated radiation damage parameters are listed in Table 6. The radiation damage calculations do not take into account nuclear transmutation that occurs during irradiation. In most cases the transmutation does not significantly change the dpa or helium production but may lead to changes in the alloy composition. Due to the Gd thermal filter in this experiment, transmutation effects are minimal. The dpa and helium values for nickel also include the extra contribution from ^{59}Ni. The 19J experiment is described in Reference 8 and the materials irradiated in the 19J experiment are provided in Reference 9. Based on this list, radiation damage calculations were performed for Fe, Ni, W, F82H, and SiC.

Table 6. Radiation damage parameters for the 19J experiment

Material	2U 2.71 cm		5H 10.28 cm	
	dpa	He,appm	dpa	He,appm
Fe	2.12	0.68	1.43	0.40
Ni*	2.35	9.62	1.58	5.15
W	0.58	0.0083	0.39	0.0050
F82H+	2.11	0.65	1.42	0.38
SiC	3.81	11.26	2.57	6.64

*****Ni dpa and helium values include contributions from ^{59}Ni.
+F82H composition 8Cr-2W-0.04Ta (balance Fe).

Fluence and Radiation Damage Polynomial Fits

The neutron fluence and radiation damage parameters can be well described by a polynomial function as shown by the trend lines on the plots. The form of the polynomial is given as equation (1) below where a is the maximum value, and b is the quadratic parameter. The fluence, dpa, and helium (appm) values at any location in the assembly can then be determined using the height, z in cm, and the coefficients listed in Table 7. The functions are symmetric about core midplane. The accuracy is limited since we only have two data points for the determination of the parameters. The heights of the monitors above reactor centerline have an uncertainty of ± 0.7 cm.

$$F = a\,(1 + b\,z^2) \qquad (1)$$

Table 7. Polynomial coefficients for Equation 1 to calculate neutron fluence and damage parameters

Neutron Fluence	**a**	**b**		
Thermal	1.04E+20	-4.17E-03		
Epithermal	5.65E+21	-3.85E-03		
>0.1 MeV	3.64E+21	-3.24E-03		
> 1 MeV	1.40E+21	-3.13E-03		
Damage parameter	**a dpa**	**b dpa**	**a He, appm**	**b He, appm**
Fe	2.17E+00	-3.23E-03	7.01E-01	-4.06E-03
W	5.94E-01	-3.25E-03	8.55E-03	-3.93E-03
F82H	2.16E+00	-3.25E-03	6.70E-01	-4.10E-03
SiC	3.90E+00	-3.23E-03	1.16E+01	-4.05E-03

Ackknowledgements

The authors would like to acknowledge Charles Daily and Joel McDuffee of ORNL for their assistance in providing detailed neutron spectral calculations for the 19J experimental assembly. Also, J. W. Geringer

and J. P. Robertson of ORNL provided many supporting documents and information about the 19J experiment.

References

[1] A. A. Sonzogni, *"Nudat 2.0: Nuclear structure and decay data on the internet,"* in AIP Conference Proceedings, 2005, vol. 769, p. 574.

[2] L. R. Greenwood and C. D. Johnson*, "Least Squares Neutron Spectral Adjustment with STAYSL PNNL,"* International Symposium on Reactor Dosimetry, EPJ Web of Conferences 106, 07001, 2016*.*

[3] ASTM E-1297-08 *Standard Test method for Measuring Fast-Neutron Reaction Rates by Radioactivation of Niobium (reapproved in 2013).*

[4] M. J. Berger et al., *"XCOM: Photon Cross Section Database (version 1.5)(2010),"* Natl. Inst. Stand. Technol. Gaithersburg MD, 2013.

[5] R. Capote, K. Zolotarev, V. Pronyaev, and A. Trkov, *"Updating and Extending the IRDF-2002 Dosimetry Library,"* Updat. Extending IRDF-2002 Dosim. Libr., J. ASTM International, 9, 197, 2012.

[6] C. Daily, private communication, Oak Ridge National Laboratory 2018.

[7] LR Greenwood and RK Smither*, SPECTER: Neutron Damage Calculations for Materials Irradiations,* ANL/FPP/TM-197, January 1985.

[8] J. L. McDuffee and J. W. Geringer, *The MFE-RB-19J HFIR Irradiation Experiment,* Fusion Materials Semiannual Progress Report for the Period Ending Dec. 31, 2016, DOE-ER-0313/61, pp 188-189, 2017.

[9] J. W. Geringer, J. L. McDuffee, C. M. Petrie, L. M. Garrison, R. H. Howard, N. O. Cetiner, D. A. Stringfield, R. G. Sitterson, *HFIR-MFE-RB-19J Specimen Loading Listing,* Fusion Materials Semiannual Progress Report for the Period Ending June 30, 2016, DOE/ER-0313/60, pp. 215-233, 2016.

10.3 DESIGNS AND SPECIMEN MATRICES FOR RE-IRRADIATION OF ISHI SAMPLES IN HFIR RABBIT CAPSULE ALONG WITH NEUTRON-ION BOOTSTRAPPING EXPERIMENTS—T. Yamamoto, G.R. Odette, P.B. Wells (University of California, Santa Barbara), D.J. Edwards, K. Kruska, R.J. Kurtz (Pacific Northwest National Laboratory), S.J. Tumey (Lawrence Livermore National Laboratory)

OBJECTIVE

The broad objective of this task is to carry out High Flux Isotope Reactor (HFIR) re-irradiation experiments using in-situ He injected (ISHI) tempered martensitic steels (TMS) specimens from JP-26 and 27 irradiations to examine microstructure evolution including the formation of bubbles, voids and dislocation loops up to ≈ 42 dpa and ≈ 2800 appm He at 400 and 500°C. In parallel, neutron-ion bootstrap irradiation experiments will be carried out to test the concept that would enable probing very high dose phenomena with combinations of ion and neutron irradiations.

SUMMARY

Matrices and loading arrangements are explored for HFIR rabbit capsules to re-irradiate ISHI discs from JP-26 and 27 irradiations to study microstructure evolution up to ≈ 42 dpa and ≈ 2800 appm He at 400 and 500°C to compensate for the loss of JP-28 ISHI experiment. The re-irradiation also enables advanced type ISHI that avoid low dose He/dpa transients. The capsules would also include wedge specimen ISHI experiments, multipurpose disc specimens and the first neutron irradiation of tungsten composites.

PROGRESS AND STATUS

Introduction

The He-dpa synergisms can cause severe degradation of fracture toughness and void swelling, that may greatly narrow the application window for the current candidate, TMS for fusion reactor (DEMO and beyond) structures that may experience up to 2000 appm He and 200 dpa [1]. Our earlier work proposed a "threshold" for most serious He-dpa synergistic effects in TMS alloys of ≈ 500 appm [1-4]. We have continued characterizing He bubbles, voids and other microstructures in TMS and a new class of material, nano-structured ferritic alloys (NFA) in He-dpa synergism study experiments, that include ISHI and dual ion beam irradiation (DII) irradiations, using transmission electron microscope (TEM) as the primary characterization tool [4-15]. As shown in Figure 1, DII at 500°C show that the swelling incubation dose (dpa_i) decrease linearly with He/dpa. The incubation dose is lower in 500°C ISHI neutron irradiations at the same He/dpa. However, the post-incubation swelling trends follow common broad trend [13,14], at least up to ≈ 15 (dpa) after the incubation at a rate of ≈ 0.1%/dpa.

Thus, adding swelling data points from ISHI experiments in JP-28/29 capsules at ≈ 40 dpa and 500°C would have been critically important to determine if swelling continues at a similar rate and to support swelling prediction models. Unfortunately, the 500°C ISHI experiments in JP-28/29 capsules ran at a significantly lower temperature than was designed [16]. Thus, the primary objective of this HFIR re-irradiation is to obtain swelling data at up to ≈ 42 dpa and 2800 appm He at 400 and 500°C by adding incremental dpa and He to preexisting JP-26 or JP-27 ISHI conditions.

In addition to gaining the incremental dpa and He, re-irradiation of NiAl-coated ISHI discs is advantageous, as illustrated in Figure 2. The ISHI first involves breeding Ni-59 (with no natural abundance) from Ni-58 (≈ 68% of natural abundance) through neutron capture (n_{th}, γ) reaction (Figure 2a) [1,5,6], and thus has a steep transient followed by a more gradual increase to a broad peak at ≈ 20 dpa (Figure 2b). The NiAl discs already irradiated to 5~40 dpa in JP26-29 experiments have bred sufficient fraction of Ni-59 to inject He into the adjacent new unirradiated samples at ≈ “steady sate” He/dpa ratio,

more relevant to fusion reactor environment. Note, Figure 2b is an example for 1 μm thick NiAl coating; changing the coating thickness (as an adjusting) allows for a wide range of He/dpa ratios.

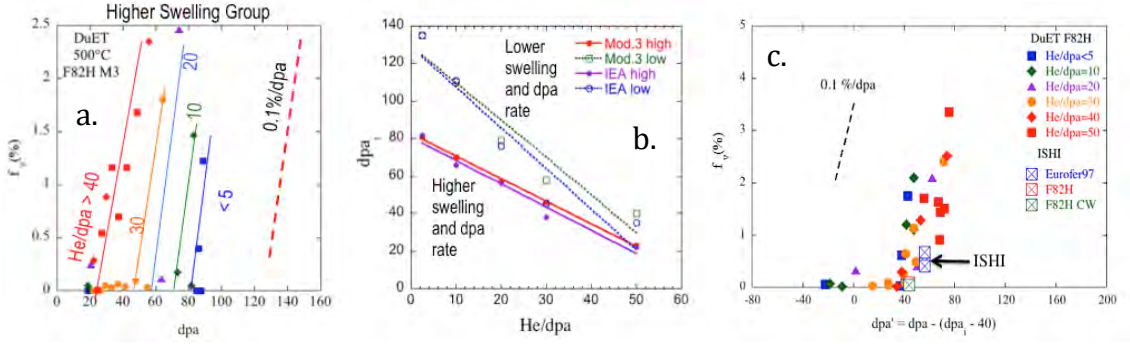

Figure 1. Summary of DII irradiation experiments showing a) void volume fraction, f_v, trends at various He/dpa ratio; b) systematic decrease in incubation dpa, dpa_i, with increasing He/dpa; and c) broadly common post-incubation swelling behavior regardless He/dpa including HFIR ISHI experiments [14,15].

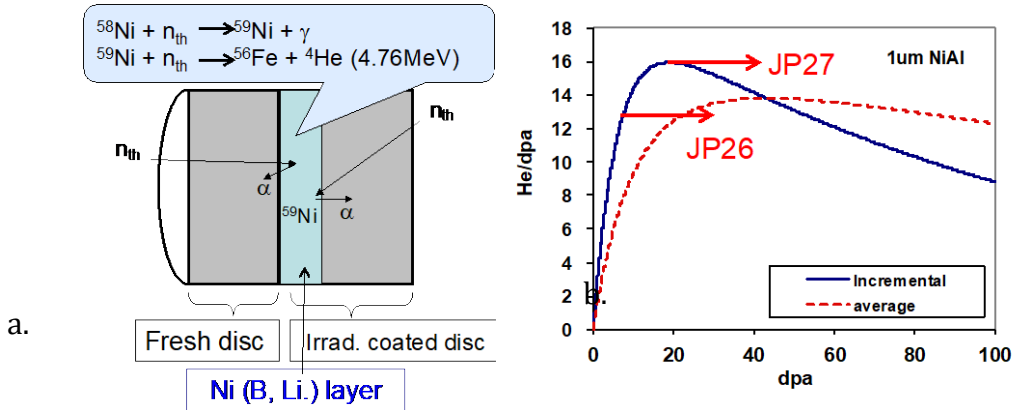

Figure 2. a) Schematic design of ISHI experiments [5]; and b) history of He/dpa ratio from 1 μm thick NiAl coating.

Another objective of the work is to test neutron-ion irradiations *bootstrapping* concept. This new approach is ultimately aimed at providing insight on swelling that may occur up to 200 dpa. The work will be guided by hypotheses derived from the current understanding of irradiation effects, resulting from many decades of international research. The key concept is that, the initial development of irradiation microstructures, in lower *nucleation* dose regimes, often has a dominant effect at higher doses. Irradiation tolerance is provided by high sink strengths that annihilate excess vacancies and self-interstitial atoms (SIA) and distribute He in fine bubble sinks. After an initial transient, the sink microstructure is generally stable, or evolves only slowly, and may reach a quasi-steady state, at least up to the point of new threshold instability caused by a limited and definable set of mechanisms. Such instabilities primarily include precipitate coarsening and dislocation, sub-grain, lath and fine grain recovery (loss of high sink strength). Note, these instabilities themselves can also lead to the degradation of critical mechanical properties, and at higher temperatures irradiation and thermal instability processes may interact. The He bubbles and dislocations play a key role in the void swelling. The growth of bubbles to a critical size where they convert to voids (or stress driven grain boundary creep cavities) and their subsequent growth is perhaps the major instability of concern.

The implication to fusion is that, once a population of voids formed by bubble conversion, subsequent swelling occurs by continued growth involving rather simple biased partitioning of vacancies and SIA to a relatively stable background sink structure. The partitioning and void growth can be studied by additional

increments of neutron and/or ion irradiations. Strong evidence supporting our hypothesis is the observation of approximately constant post incubation void swelling rates in both austenitic (≈ 1%/dpa) and ferritic (0.2% dpa) steels [17]. This leads to a *bootstrapping* concept for using ion irradiations to reach higher dpa.

Thus, this research will explore the concept of *"seeding'* the microstructure by neutron irradiation, followed by an increment of ion irradiation dose to higher and, eventually, very high dpa. To test this hypothesis, the neutron plus ion condition will then be compared to a neutron only irradiation to the same dose. This bootstrapping approach is illustrated in Figure 3.

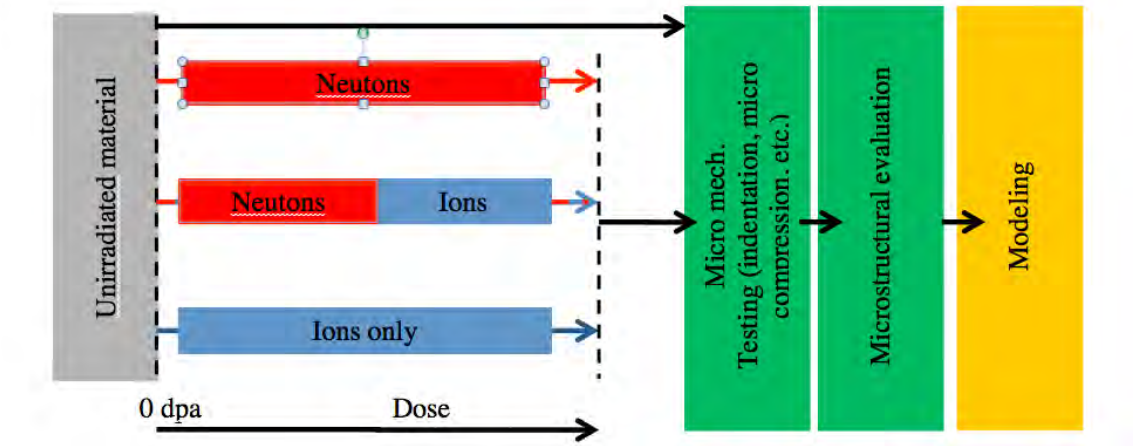

Figure 3. A schematic illustration of the neutron/ion bootstrapping irradiation approach.

Experimental Procedure

Design of HIFR re-irradiation Rabbit capsules

We have proposed re-irradiation experiments for two HIFR rabbit capsule irradiations at 400 and 500°C. Figure 4 shows an existing rabbit capsule design, where we utilized as a tentative base for the irradiations [18]. The design can hold 0.5 or 1.0 mm thick wafer specimens (part #7, 8, and 10) placed both sides of capsules with a total thickness of 1.5 mm between two layers of 0.5 mm thick SiC temperature monitors (#6 and 9) with a 6.2 mm wide and 5.5 mm high cross section. The stacks are pushed against the capsule wall by Spring (#11) placed at the center.

As is shown in Figure 5, the modified design takes sectional approach. The whole capsule consists of six 4 mm long and two 10 mm long sections having the same cross-sectional area as the base design. For three 4 mm long middle sections, two 1 mm thick specimen holders containing stacks of ISHI re-irradiation and fresh TEM discs replace the two 0.5 mm thick specimens (#7) and one 1.0 mm thick specimen (#10). Each stack has one NiAl coated He-injector re-irradiation disc paired with a disc that will also receive injected He. These discs are ≈ 0.2 mm thick and placed with ≈ 0.6 mm thick filler disc into two holes in each 1 mm thick holder. Thus, a 4 mm long section holds 4 pairs of He injector and specimen discs. This is schematically illustrated in more detail in Figure 6, with lists of injector-susceptor pairs for 500°C capsule. Blue highlighted rows show irradiated discs indicating particular specimen ID from JP's capsules and yellow-highlighted rows show unirradiated fresh TEM discs. The irradiated discs are distributed over the various sections so that each has reasonably low total dose rate for handling.

Figure 7 shows estimated He and dpa conditions that would be achieved in the 500°C ISHI re-irradiation experiments either in He injector and implanted discs, assuming the capsule receives 21 dpa of neutron dose. The open green diamonds indicate He-dpa conditions in the irradiated ISHI discs from JP-26 and 27 experiments. Each disc receives 21 dpa in the new irradiation with an amount of He depending on the injector NiAl thickness, as are indicated by the green arrows, to achieve final He and dpa shown in the red circles. Figure 7 also indicates ISHI for fresh susceptor discs by blue dashed arrows to reach various

He conditions at 21 dpa. The 400°C re-irradiation ISHI consists of similar set of irradiated JP specimens with unirradiated specimens, while the final He and dpa conditions are shifted slightly lower because the He and dpa received in JP-26 and 27 irradiations are lower at 400°C than at 500°C [5].

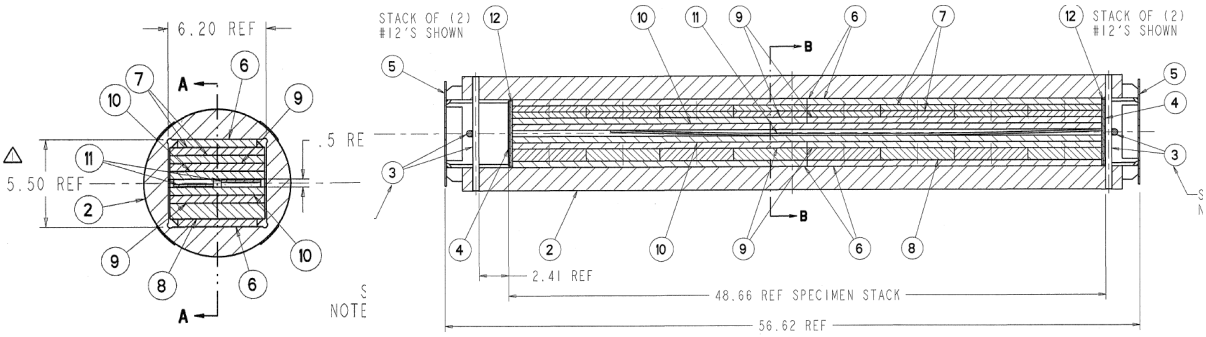

Figure 4. An existing rabbit capsule design used as a basis for the proposed new rabbit capsules, showing parts indicated by the numbers.

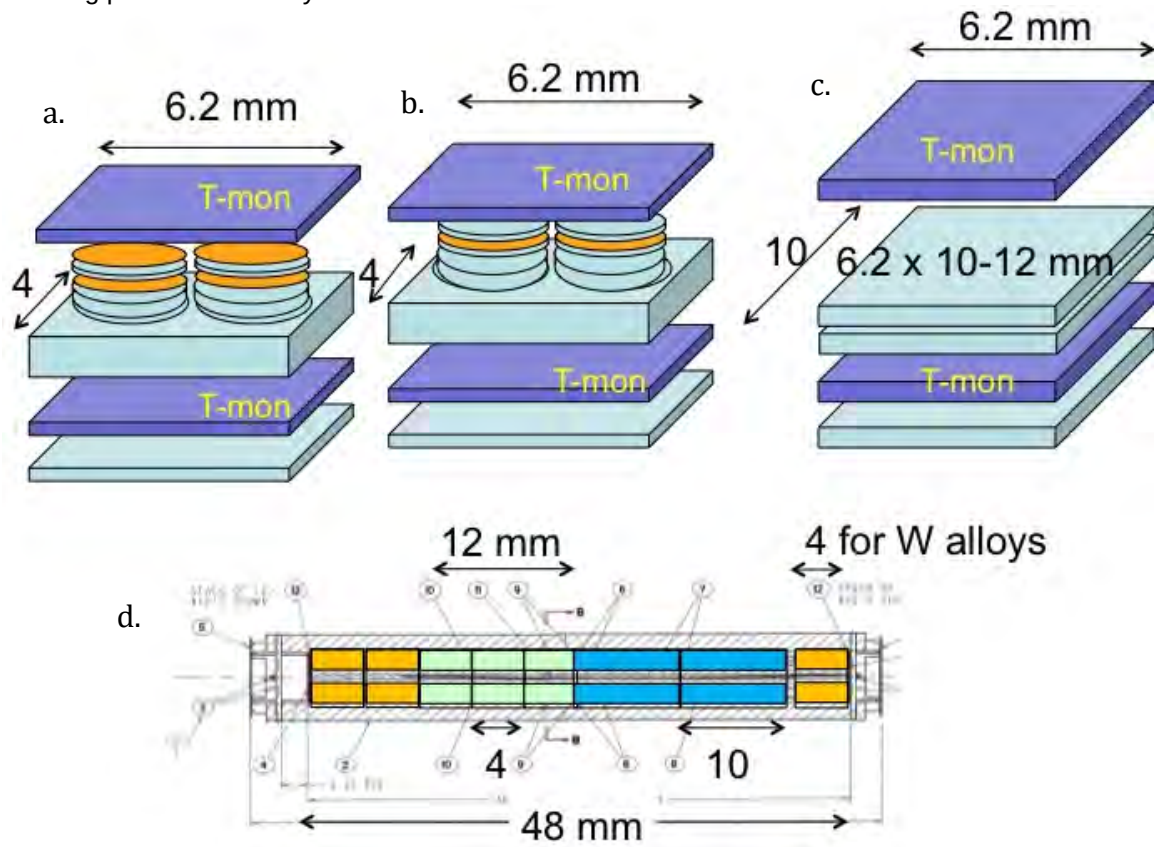

Figure 5. Three types of sample sections (a-c) along with W alloys section laid out over the 48 mm length of a rabbit capsule (d).

a.

Section 1	
SpID	Alloy
R26	Eurofer 97
	Eurofer 97
R56	Eurofer 97
UN57	F82H-mod.3+20%CW
O47	PM2000
	F82H IEA
ZS52	US-MA957
	MA957US

Section 2	
SpID	Alloy
R22	Eurofer 97
	Eurofer 97
H57b	Eurofer 97
	F82H IEA
H24	F82H-mod.3
	F82H-mod.3
R57	U14YW1150
	Eurofer 97

Section 3	
SpID	Alloy
R24	Eurofer 97
	Eurofer 97
H57a	Eurofer 97
	F82H-mod.3
H26	F82H-mod.3
UN27	F82H-mod.3+20%CW
ZQ52	F82H-XXX
UN56	F82H-mod.3+20%CW

b.

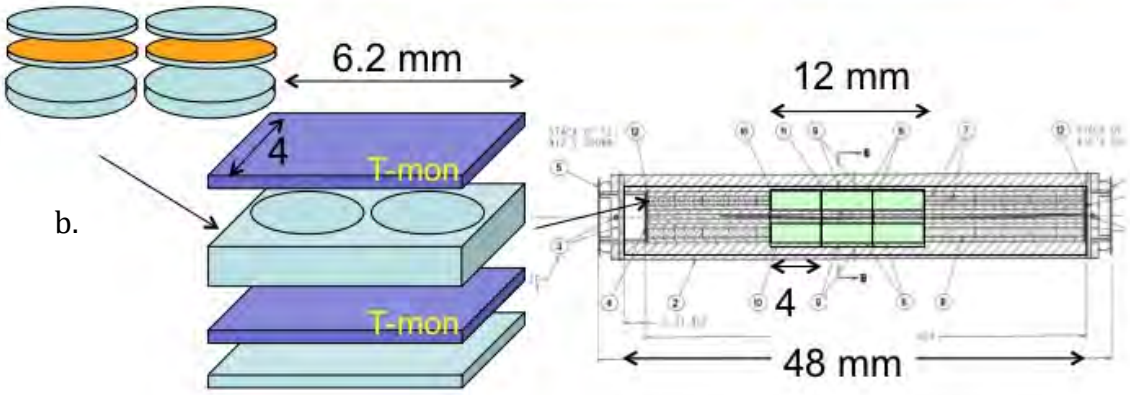

Figure 6. a) Lists of He injector-susceptor disc pairs for sections 1-3; and b) the disc loading schemes using 1 mm thick TEM disc holder.

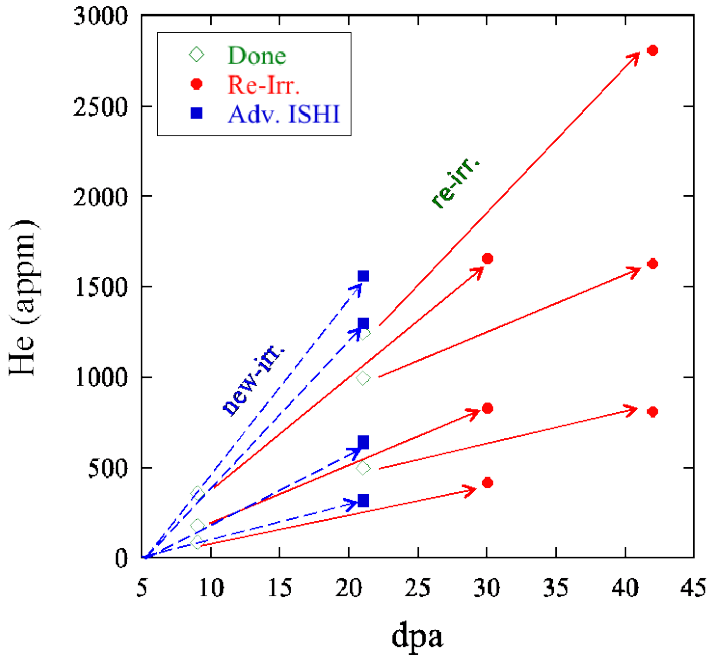

Figure 7. Target He-dpa conditions in the re-irradiation ISHI specimens (red circles), fresh and advanced ISHI specimens (blue squares) as well as earlier experiments (open diamonds).

The left end of the capsule in Figure 5 has two 4 mm long sections holding wedge type He injection experiments. Figure 8 shows schematic design of the wedge specimen with Ni foil He injector. Thick (thicker than emitted α particle range) injector foils inject He with profiles that linearly decrease with depth to the range in the target steel of ≈ 9.2 μm. For the target locations thicker than ≈ 18.4 μm like the locations E and F in Figure 8a, only ≈ 9.2 μm thick near-surface layers receive He with the linear profile shown in Figure 8b, where He concentration from the center of the target to the surface is plotted as a function of the thickness-normalized distance. If the target is thinner than twice the range (the tip side at location D), there is a region in the center where He from both surfaces crosses to create a constant He/dpa. The He in this region increases with decreasing the wedge thickness, reaching the amount at the surface the surface when the thickness is the same as the range (location B). The He concentration continues to increase as the wedge thickness decreases. The absolute level of He is calculated for 21dpa target position irradiation. Practically, pure Ni foils produce too high He concentration near the wedge tip, so the case for an ≈ 25%Ni alloy is shown in Figure 8b. The wedge specimens sandwiched by Ni (alloy) foils are loaded to TEM holder in the similar fashion to re-irradiation ISHI experiments as shown in Figure 8c.

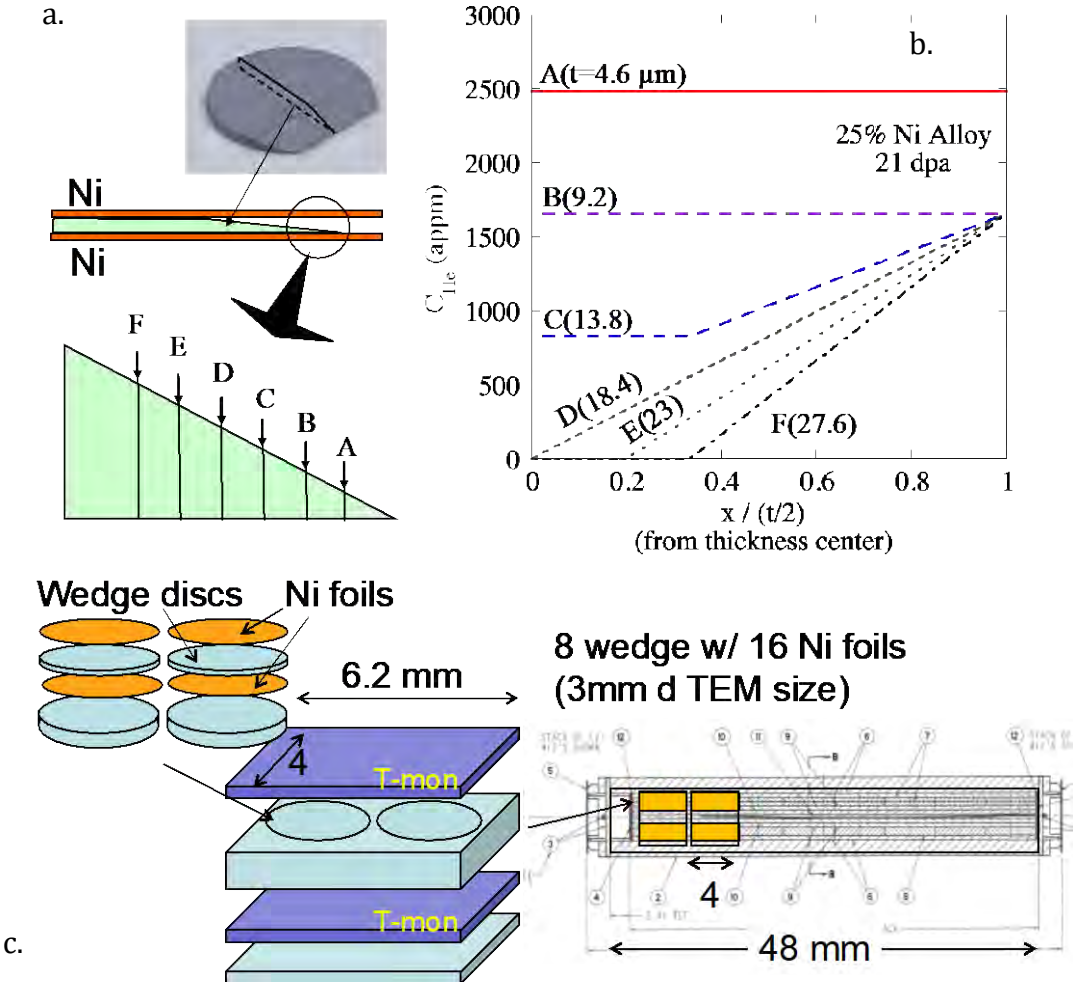

Figure 8. a) Schematic design of a wedge-shaped sample with Ni foil He injectors on the both sides; b) He concentration profiles at 21 dpa at the locations A ~ F of various thickness; c) loading of the wedge discs with Ni foil injectors.

The rest of the capsules corresponding the right half of Figure 5d are used for TMS mechanical property samples mainly used for shear punch test-based constitutive model analyses and a small section for tungsten alloy samples.

Table 1 summarizes the re-irradiation capsule loading at 500°C. The 400°C capsule consists of similar sets of re-irradiation ISHI, wedge ISHI, TMS mechanical and W specimens, while as has been noted above final He and dpa conditions in re-irradiation ISHI experiments are shifted lower due to the lower starting conditions in JP-26 and JP-27 at 400°C than 500°C.

Table 1. List of specimens for 500°C rabbit capsule with re-irradiation specimen IDs and section length

					Total:	48
Section	Objective	Type	Count	Sample ID	Alloy	Length
	Re-ISHI	TEM	8	R26	Eurofer 97	4
					Eurofer 97	
				R56	Eurofer 97	
				UN57	F82H-mod.3+20%CW	
				O47	PM2000	
					F82H IEA	
				ZS52	US-MA957	
					MA957US	
	Re-ISHI	TEM	8	R22	Eurofer 97	4
					Eurofer 97	
				H57b	Eurofer 97	
					F82H IEA	
				H24	F82H-mod.3	
					F82H-mod.3	
				R57	U14YW1150	
					Eurofer 97	
	Re-ISHI	TEM	8	R24	Eurofer 97	4
					Eurofer 97	
				H57a	Eurofer 97	
					F82H-mod.3	
				H26	F82H-mod.3	
				UN27	F82H-mod.3+20%CW	
				ZQ52	F82H-XXX	
				UN56	F82H-mod.3+20%CW	
		Wedge TEM	8	6	F2H IEA, mod.3, 20%CW	8
				2	Eurofer 97	
		SPT	8	2	MA957	20
		CPN 6.2 x 10		2	14YWT-1	
				2	NF616	
				2	HT9	
		W-TEM	4		W alloys	8

Design of neutron-ion bootstrapping experiments

Ion beam irradiations for neutron-ion bootstrapping experiments will be carried out for ISHI discs irradiated in JP-26 and 27 capsules. While very limited availability, there are a few redundant irradiated discs that, in parallel to the HFIR rabbit irradiations, can be irradiated as the whole disc in some ion-beam facilities including the CAMS accelerator system at Lawrence Livermore National Laboratory [19]. This facility is ideally suited for the proposed study because the large penetration depth (~7 μm) of high-energy (~80 MeV) Fe-ions allows for improved post-irradiation examination (PIE) [19, 20]. The ion irradiations will employ a "bootstrap" approach by incrementally extending the damage of specimens that have been previously irradiated to 9 and 21 dpa with neutrons at HFIR. This bootstrapping approach will involve beginning the ion irradiation with both the 9 and 21 dpa neutron-irradiated materials, as well as unirradiated alloys, in the target chamber. The specimens will then be removed at ≈10 dpa increments as schematically illustrated in Figure 9.

In order to avoid artifacts due to the implanted ions, PIE is ideally performed well in front of the ion deposition peak. We therefore define a "maximum damage" location in an irradiated specimen that corresponds to the point where the deposited ion concentration is 1% (≈ 5.5 μm) of the total. During the first stage of the experiment, both unirradiated and 9-dpa neutron-irradiated alloys will be irradiated with 80 MeV Fe ions to produce a dose increment of 12 dpa. Performing PIE at this location will enable direct comparison between the 21 dpa neutron-irradiated materials with materials irradiated to 21 dpa with a combination of neutrons and ions.

[1] PIE to be performed in front of the damage peak

[2] Specimen will be produced from future FIR irradiation

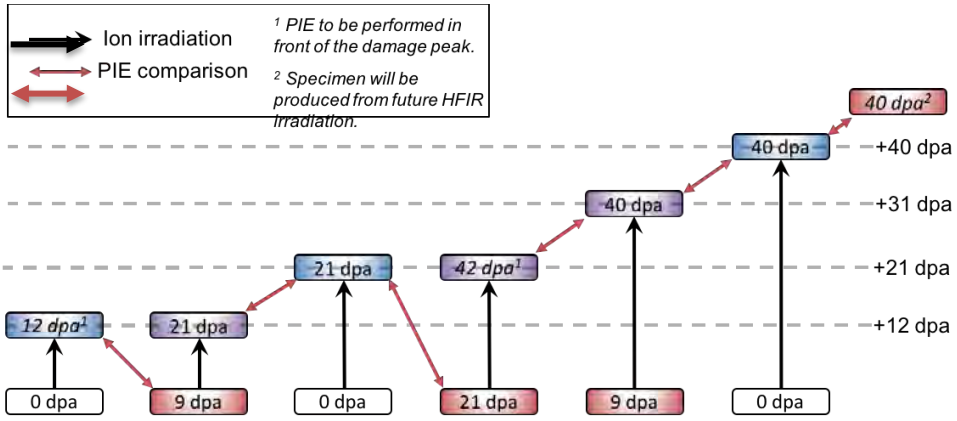

Figure 9. Schematic showing the proposed four-step bootstrap ion irradiation approach.

FIB lift out of ISHI samples with no redundancy for ion beam irradiations

Since not many alloy-dpa-He conditions are available with specimen redundancy to provide the whole disc samples for ion beam irradiations, the He injected part of key specimens will be lifted out using focused ion beam (FIB) machining. Another advantage of this approach is that, the lift-outs are not radioactive, so more ion beam facilities including dual-ion beam types become available for the irradiation experiments. Figure 10a schematically shows how the lift-outs are sampled in terms of the He injected regions in ISHI irradiated discs. The lift-outs are mounted sideways so relatively low (a few MeV) ion can reach the ISHI He injected region. Figure 10b shows a surrogate tempered martensitic steel sample lift out at Pacific Northwest National Laboratory (PNNL) to test a procedure from the FIB micromachining, through welding on to a substrate. The procedure has been optimized after many try outs.

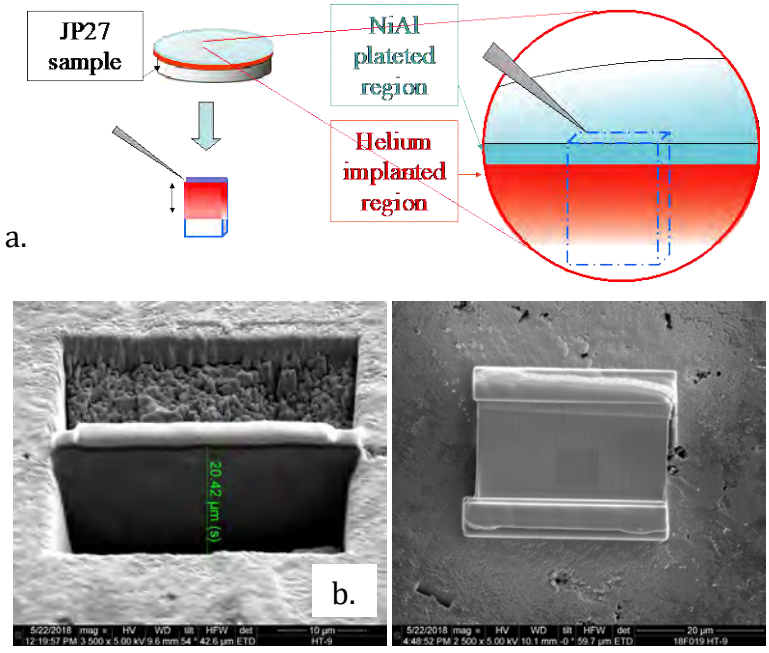

Figure 10. a) schematic design of lift-outs in terms of the He injected regions in ISHI irradiated discs; b) a surrogate tempered martensitic steel sample lifted out at PNNL to test an optimized lift-out to weld-mount procedure.

Future Work

The rabbit capsule design including W-alloy specimen matrices will be finalized with Oak Ridge National Laboratory (ORNL). Preparation of capsule will start in parallel at University of California, Santa Barbara (UCSB). The FIB lift-outs will be prepared from selected ISHI alloy-He-dpa conditions for bootstrap ion irradiations at PNNL.

Acknowledgments

The work was supported by the U. S. Department of Energy, Office of Fusion Energy Sciences, under the contracts DE-FG03-94ER54275 and DE-AC06-76RLO1830 for the part performed at UCSB and PNNL, respectively. The authors are also grateful to Dr. Yutai Katoh for kind advice and crucial information on HFIR rabbit capsule design.

References

[1] Y. Dai, G.R. Odette, T. Yamamoto, *The Effects of helium on irradiated structural alloys, in Comprehensive Nuclear Materials, R. Konings, T. R. Allen, R. E. Stoller, S. Yamanaka Eds. (2012) Elsevier.*
[2] G. R. Odette, T. Yamamoto, H. J. Rathbun, M. Y. He, M. L. Hribernik, J. W. Rensman, *J. Nucl. Mater.* 323 (2003) 313-340.
[3] T. Yamamoto, G. R. Odette, H. Kishimoto, J-W. Rensman and P. Miao, *J. Nucl. Mater.* 356 (2006) 27.
[4] Takuya Yamamoto, Yuan Wu, G. Robert Odette, Kiyohiro Yabuuchi, Sosuke Kondo, Akihiko Kimura, J. Nucl. Mater. 449 (2014) 190.
[5] T. Yamamoto, G.R. Odette, L.R. Greenwood, *Fusion Materials Semiannual Report 1/1 to 6/30/2005* DOE/ER-313/38 (2005) 95.
[6] T. Yamamoto, G.R. Odette, P. Miao, D.T. Hoelzer, J. Bentley, N. Hashimoto, H. Tanigawa, R. J. Kurtz, J. Nucl. Mater., 367-370 (2007) 399.
[7] R.J. Kurtz, G.R. Odette, T. Yamamoto, D.S. Gelles, P. Miao, B.M. Oliver, *J. Nucl. Mater.* 367-370 (2007) 417.
[8] G.R. Odette, M.J. Alinger, and B. D. Wirth, Annu. Rev. Mater. Res. 38 (2008) 471.
[9] T. Yamamoto, G.R. Odette, P. Miao, D. J. Edwards, R. J. Kurtz., J. Nucl. Mater. 386-388 (2009) 338.
[10] D.J. Edwards, R.J. Kurtz, G.R. Odette, T. Yamamoto, *Fusion Materials Semiannual Report 12/31/2009* DOE/ER-313/47 (2010) 59.
[11] G.R. Odette, P. Miao, D.J. Edwards, T. Yamamoto, R. J. Kurtz, Y. Tanigawa, J. Nucl. Mater. 417 (2011) 1001.
[12] T. Yamamoto, Y. Wu, G.R. Odette, K. Yabuuchi, S. Kondo, A. Kimura, *Fusion Materials Semiannual Report 6/30/2015* DOE/ER-313/58 (2015) 12.
[13] G.R. Odette, T. Yamamoto, Y. Wu, S. Kondo, A. Kimura, *Fusion Materials Semiannual Report 6/30/2015* DOE/ER-313/57 (2015) 8.
[14] T. Yamamoto, Y. Wu, G.R. Odette, S. Kondo, A. Kimura, *Fusion Materials Semiannual Report 6/30/2014* DOE/ER-313/56 (2014) 194.
[15] Takuya Yamamoto, Yuan Wu, G. Robert Odette, Kiyohiro Yabuuchi, Sosuke Kondo, Akihiko Kimura, *Fusion Materials Semiannual Report 6/30/2016* DOE/ER-313/60 (2016) 12.
[16] Takuya Yamamoto, Yuan Wu, G. Robert Odette, Dan Edwards, Rick Kurtz, *Fusion Materials Semiannual Report 12/31/2015* DOE/ER-313/59 (2016) 15.
[17] F.A. Garner, M.B. Toloczko, B.H. Sencer, J. Nucl. Mater. 376 (2000) 123.
[18] Y. Katoh, personal communication.
[19] N. Almirall, T. Yamamoto, D. Gragg, K. Fields, N. Cunningham, P. Wells, G. R. Odette, S. Tumey, T. Brown, DOE/ER-0313/59 (2015) 164.
[20] ER. Reese, N. Almirall, T. Yamamoto, S. Tumey, G.R. Odette, EA. Marquis, Scripta Mater. 146 (2018) 213.

10.4 HFIR IRRADIATION EXPERIMENTS—Y. Katoh, J.L. McDuffee, C. Bryan, J.P. Robertson (Oak Ridge National Laboratory)

SUMMARY

Neutron irradiation experiments were performed in support of the research and development of fusion reactor materials using various materials irradiation facilities in the High Flux Isotope Reactor (HFIR).

The HFIR operated for approximately 2.25 cycles between July 1 and December 31, 2018. Cycle 480 was completed on July 6 (2042.70 MWD), Cycle 481 on August 17 (2088.38 MWD), and Cycle 482 on September 28 (2079.28 MWD). Cycle 483 began on November 13, but there was an issue with the fuel and the reactor was shut down the same day.

During this time, up to 25 target zone rabbit capsules were in HFIR in a given cycle. The capsules are listed in Table 1 along with condensed information on material, specimen type, temperature, fluence, and period of irradiation. Three rabbit capsules completed the scheduled irradiation.

Table 1. HFIR fusion materials program rabbit capsules under irradiation in the second half of 2018

Experiment Designation	Primary Materials	Specimen Types	Irradiation Temperature (°C)	Max Exposure (dpa)	Number of Reactor Cycles
F13A5	FeCrAlY Steel	Bend bar	300	28	16
F13B4	FeCrAlY Steel	tensile	300	50	29
JCR11-05	SiC/SiC	bend bars	950	200	115
JCR11-07	SiC/SiC	Mini bend bars	950	100	47
JCR11-08	SiC/SiC	Mini bend bars	950	200	115
SCF8	SiC/SiC	Bend bars	600	100	45
SCF9	SiC/SiC	Bend bars	600	200	90
SCF11	SiC/SiC	Bend bars	950	100	57
ES01	EUROFER reference alloy	Tensile/MPC**	220	20	12
ES02	EUROFER reference alloy	Tensile/MPC**	240	20	12
ES03	EUROFER reference alloy	Tensile/MPC**	275	20	12
ES04	EUROFER reference alloy	Tensile/MPC**	300	20	12
ES05	EUROFER reference alloy	Tensile/MPC**	325	20	12
ES06	EUROFER reference alloy	Tensile/MPC**	350	20	12
ES07	EUROFER reference alloy	Tensile/MPC**	375	20	12
ES11	EUROFER reference alloy	Bend Bar	220	20	12
ES12	EUROFER reference alloy	Bend Bar	240	20	12
ES13	EUROFER reference alloy	Bend Bar	275	20	12
ES14	EUROFER reference alloy	Bend Bar	300	20	12
ES15	EUROFER reference alloy	Bend Bar	325	20	12

Experiment Designation	Primary Materials	Specimen Types	Irradiation Temperature (°C)	Max Exposure (dpa)	Number of Reactor Cycles
ES16	EUROFER reference alloy	Bend Bar	350	20	12
ES17	EUROFER reference alloy	Bend Bar	375	20	12

*Completed irradiation this reporting period.
**MPC = Multi-Purpose Coupon.